Evolution and nucleosynthesis of Asymptotic Giant Branch stars and accreting White Dwarfs

Inauguraldissertation

zur

Erlangung der Würde eines Doktors der Philosophie

vorgelegt der

Philosophisch-Naturwissenschaftlichen Fakultät

der Universität Basel

von

Umberto   Battino

aus Italien

Basel, 2017

Genehmigt von der Philosophisch-Naturwissenschaftlichen Fakultät

auf Antrag von

Prof. Dr. F.-K. Thielemann, Prof. Dr. Norbert Langer

Basel, den 15.09.2015

Prof. Dr. Jörg Schibler
Dekanin/Dekan

Il tempo corre sul filo, segnando il nostro cammino... So gia' che vuole averla sempre vinta lui

I would like to acknowledge every single person, face and smile I had the pleasure to meet all along this wonderful 5 years in Basel. In particular and first of all Prof. Dr. F.-K. Thielemann, it was a great honour meeting him... and simply unbelievable having the opportunity to actually work with him. Thanks to Marco Pignatari and Prof. Falk Herwig from University of Victoria for pushing me to do my best and teaching me how research works. Thanks to all the Unibas staff, students, researchers for all the great moments which were essential to make this experience simply unique. I would like to dedicate this thesis to my loving parents, to my friends, to all the

people who trusted in me even when I was not doing it myself... To all my colleagues I had the pleasure to discuss the beautiful topic contained in these pages drinking a cup of coffee or a pint of beer together... To all the girls I met and loved on which the words 'I am an Astrophysicist' made a remarkable effect... and to all the men and women who shares the same wonder and curiosity about the Nature and Universe like me: let's go on with this travel. My friend Nobuya would say 'Minchia!' at this point. Ladies, and gentlemen... thank you!

Duello duro col tempo, con il passato e il presente... E pure oggi mi dovro' affilare le unghie
(Litfiba, 'Prendi in mano i tuoi anni').

Umberto Battino

Declaration

I hereby declare that except where specific reference is made to the work of others, this dissertation is my own work and contains nothing which is the outcome of work done in collaboration with others, except as specified in the text and Acknowledgements.

<div align="right">

Umberto Battino

April 2017

</div>

Acknowledgements

Abstract

Type Ia supernovae (SNIa) are luminous stellar explosions which mark the fatal disruption of white dwarfs in a binary system. They are the major producers of Iron group elements in the solar system and also give relevant contribution to the alpha-elements Silicon, Solfur, Calcium and Titanium. Within specific conditions SNIa may also produce about 30 proton-rich isotopes heavier than iron. It is controversial what is the relevance of this p-process component for the abundance of these isotopes in the Galaxy and in our solar system. Its efficiency depends on the products of neutron capture processes active during the accretion phase to reach the Chandrasekhar mass. The aim of this thesis is to provide for the first time comprehensive stellar simulations for investigating the possibility of producing this seeds distribution for p-process nucleosynthesis, calculating it modelling the accretion phase onto a white-dwarfs increasing mass toward the Chandrasekhar limit. The main stellar model properties during the accretion phase are not so different from the asymptotic giant branch phase, before the star becomes a WD and the accretion phase starts. We have used the same stellar code MESA (revision 4219) to produce AGB stellar models, implementing the best known physics and producing eleven one-dimensional AGB stellar models with initial mass M = 2 and 3 solar masses, and with initial metal content Z=0.01 and Z=0.02. The convective boundary-mixing below Thermal Pulses and the Third-Dredge Up is included directly in stellar calculations to take into account Kelvin-Helmholtz instability and gravity waves. Rotation and magnetic field are not included. The same parameterization adopted for AGB models was consistently used for the accretion models, calculating 4 WD models with initial mass 0.856, 1.025, 1.259 and 1.376 solar masses accreting Z=0.01 metal content material. Post-processing calculations are finally done with the Mppnp NuGrid code.

Table of contents

List of figures

List of tables

Chapter 1

Introduction

Low-mass and intermediate-mass stars (M < 8 M$_\odot$) are fundamental contributors for the chemical evolution of the Galaxy. During their advanced evolutionary stage called Asymptotic Giant Branch (AGB) phase, these stars are characterized by recurrent He-shell flashes, or Thermal Pulses, triggering a finite amount of mixing across convective boundaries between the envelope and the underlying He-rich regions below, called He-intershell [72]. Thanks to this mixing between the He intershell and the stellar envelope, AGB stars contributed to the creation of most of the C and N observed today in the solar system [110, 213].In the same way, heavy elements like e.g. Ba, La and Pb are made by the slow neutron capture process [or s process,e.g., 101] in the He intershell and mixed with the stellar surface, and together with other lighter elements they are scattered in the interstellar medium by the powerful AGB stellar winds.

Despite the efforts in the past decades, the mechanisms driving the convective boundary mixing in the He intershell during the AGB phase are still matter of debate, and this poses a major limitation to our understanding of how these stars work. This is the first main topic discussed in this thesis, in Chapter 2. Crucial questions that we will try to answer are: what are the dominant physical mechanisms driving convective boundary mixing during the AGB phase? What is their impact on the chemical production in these stars? How do the stellar models including such mechanisms compare with stellar observations?

Once a star has left the AGB phase, the central remnant starts to evolve to become a CO White Dwarf (WD), or a ONeMg WD if the initial mass is large enough to start central C-burning off-center [e.g., 97]. If the star is in a binary system with another star, it may starts to accrete H-rich and He-rich matter from the stellar companion. For sufficiently high accretion rates, the CO WD may eventually reach the Chandrasekhar mass and become the progenitor of thermonuclear supernovae [SNe Ia 79]. SNe Ia are

responsible for the production of most of the iron-group elements in the solar system, and for a significant fraction of intermediate-mass elements like Ca and Ti [e.g., 211]. Recently an old scenario was reconsidered, in which, together with these elements, SNe Ia can also produce heavy proton-rich nuclei by activating the p process [12] in the most external SNIa ejecta [83, 84, 217]. A fundamental assumption for this scenario is to have s-process rich material in the outer layers of the SNIa progenitor.

Detailed stellar evolution calculations of these stages including modern treatment of convective boundary mixing are missing. This is the second main topic discussed in this thesis, in Chapter 3. Crucial questions that need an answer are: what are the main features of stellar evolution during the accretion stage up to the Chandrasekhar mass? what type of neutron capture nucleosynthesis is activated during the accretion stage, if any? What distribution of heavy elements made by neutron captures will act as a seed for the following p process in the SNIa explosion?

One of the main goals of this work is to better understand the production of heavy elements in stars. Through various stages of hydrostatic burning massive stars (M > 8 M$_\odot$) develop an onion skin structure with a Fe core surrounded by shells of different composition, changing from Si-rich to H-rich moving toward the stellar surface [141]. The different elements up to Fe can be made by following fusion reactions and charged particle reactions [e.g., 10, 209, 231, 234]. Today we know that it is possible to make elements heavier than Fe also by charged particle reactions in extreme explosive conditions in core-collapse supernovae, eventually up to the Pd-Ag mass region. These processes can be activated in $\alpha-$rich freezout [232], or in the neutrino-driven winds on the top of the forming neutron star [8, 51, 56, 187, 210]. Nevertheless, it is still unclear what is the role of these processes on the abundances observed in old stars formed in the early galaxy [e.g., 66, 67, 175, 214], on the galactic chemical evolution and on the abundances in the solar system. Still today, the old paradigm that neutron capture processes are the dominant nucleosynthesis sources for the elements heavier than Fe is confirmed by stellar simulations and observations.

1.1   Neutron-capture nucleosynthesis and the s-process in AGB stars

The basic form of the process of slow neutron addition as a mechanism for converting iron to heavier elements was first discussed by Cameron [31]. Later, Burbidge et al. [28] and Cameron [32] laid out a general framework for the formation of heavy nuclei. Analyzing solar system abundance distribution (see figure 1.1), Burbidge et al. [28]

determined that heavy nuclei were formed in three distinct nucleosynthetic processes, which they defined as r, s and p-processes.
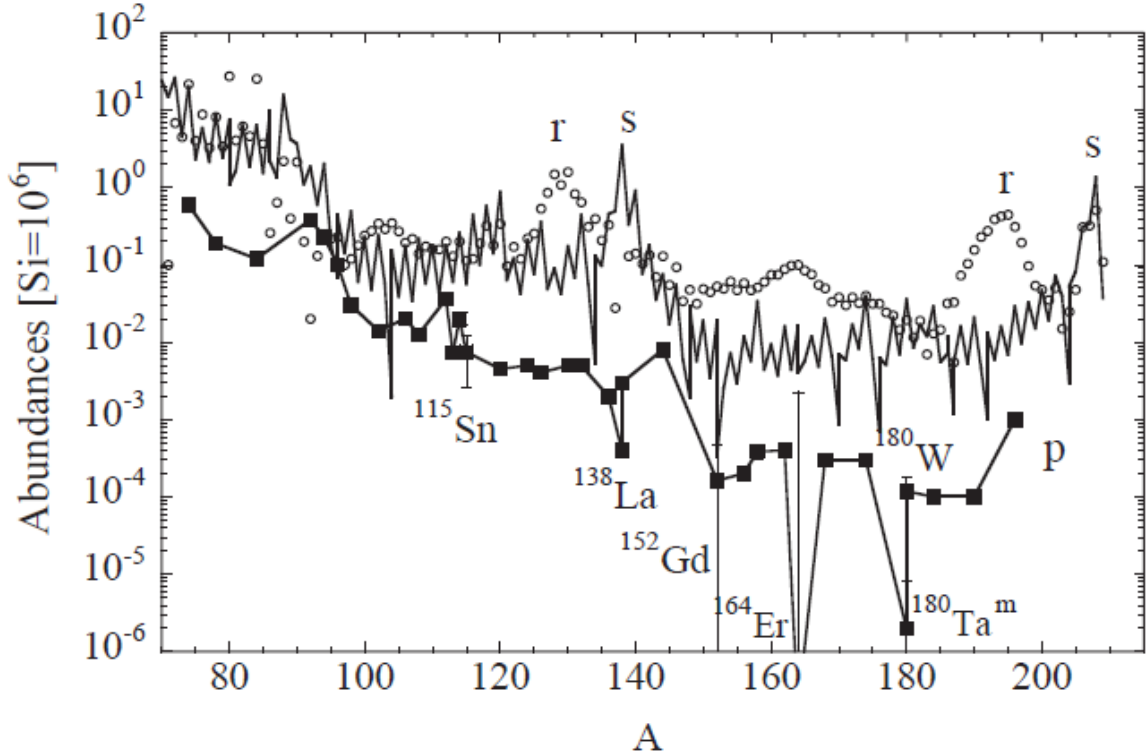
Fig. 1.1 Decomposition of solar system abundances into the *s*-process component,the *r*-process component and the *p*-process component [12].

Beyond Fe, about half of the heavy isotope abundances are made by the *s*-process , while the other half is made by the rapid neutron capture process, or r process [210]. The pattern of the solar "residual" *r*-process abundances (see figure 1.1) obtained by subtracting the *s*-process distribution from the solar abundances [9, 19] was shown to be consistent at least in first approximation with the r-process abundances observed in very old metal poor stars [197]. The r process is characterized by high neutron densities $N_n > 10^{20}$ cm^{-3}, which can be obtained only in explosive conditions. According to the most established scenario up to few years ago, the high neutron number density required was obtained in the neutrino-driven winds associated with the proto-neutron star formation in core-collapse supernovae [207]. Although the wind naturally ejects some amount of material enriched in heavy elements over a period of 1 s [8], the current neutrino-driven wind models have difficulties in providing the required *r*-process conditions, with entropies not sufficiently high to produce the heaviest r-process nuclei.

Recent hydrodynamic simulations for core-collapse supernovae support the idea that these entropy constraints can be fulfilled in the late phase when a reverse shock is forming, but at times when temperatures decrease to too low values for an r-process to operate [210]. Therefore, nowadays other scenarios are discussed, among others polar jets from rotating magneto-hydrodynamical explosions of core-collapse supernovae [147, 228], neutron-rich matter ejected from merging neutron stars [54, 162] and neutron-star-black hole mergers [205]. For a review of the different scenarios and r-process results see Thielemann et al. [210].

The s-process is characterized by a series of neutron capture nuclear reactions that occurs at relatively low neutron density: the s-process nucleosnthesis path evolves along the valley of stability in the chart of nuclei, since the neutron capture timescale of radioactive nuclei is typically slower than the β-decay timescale, and it decays to its stable isobar before a neutron is captured [101]. An example of s-process path is shown in figure 1.2, in the mass region between Kr and Mo. In figure 1.2, isotopes like ^{80}Kr and ^{82}Kr are defined as s-only isotopes and the only neutron-capture process responsible for their production is the s-process, since they are shielded by their stable isobars (in this case ^{80}Se and ^{82}Se, respectively) from any r-process contribution. From figure 1.2 it is also possible to see that the neutron-capture path on radioactive nuclei may change when the timescale of neutron capture becomes comparable to the β-decay. In this case, a branching is opened in the s-process path [see for instance the case of ^{85}Kr in the figure, and 1]. The study of s-process branching points can provide crucial information about the stellar conditions during the s-process activation in stars, by comparing stellar observations with theoretical stellar model predictions [e.g., 19, and references therein]. In chapter 2 we will discuss further the s-process branching points in our analysis.

The typical neutron density range of the s-process in stars is $10^7 \lesssim N_n \lesssim 10^{13}$ (where N_n is the neutron density expressed in cm^{-3}). The temperature range associated to the s-process activation in stars is $10^8 \lesssim T \lesssim 10^9$ K. These conditions are obtained in different types of stars.

Most of the s-elements in the region $60 \leq A \leq 90$ are produced by massive stars; among the solar system abundances, these form the so-called weak s-process component [100, 101, 166, 176, 177, 208]. In massive stars, the main neutron source for the s process is the ^{22}Ne(α,n)^{25}Mg reaction [34, 116, 163]. Depending on the initial mass of the star [e.g., 173] and on the ^{22}Ne+α rates [102, 166], some ^{22}Ne may be left in the He-burning ashes, which is activated later in the subsequent shell C-burning conditions
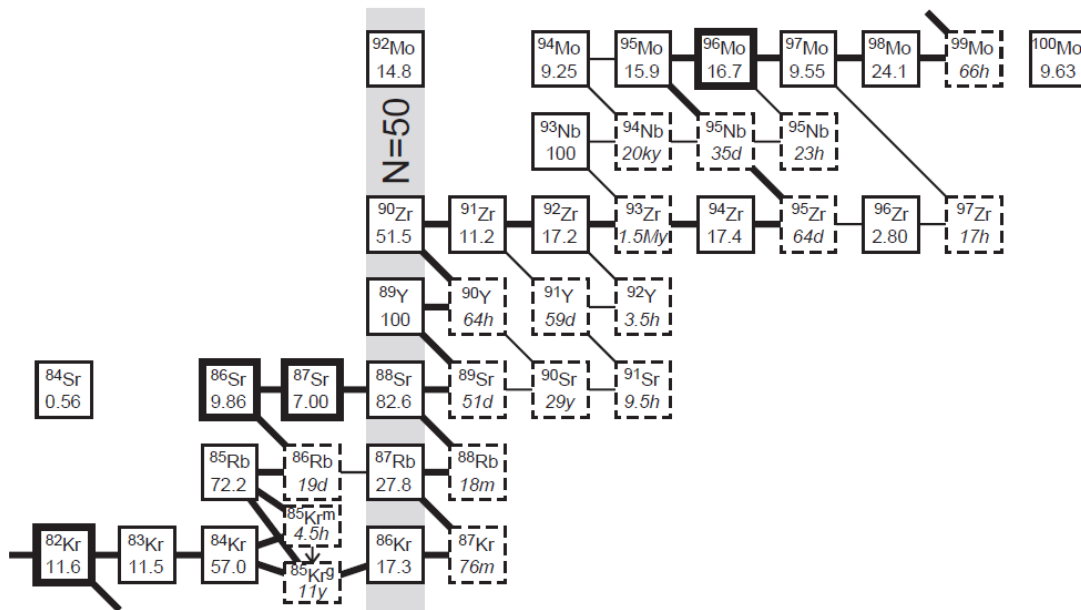
Fig. 1.2 Picture from Lugaro et al. [132] showing the *s*-process nucleosynthesis path in the region of strontium, zirconium, and molybdenum. Thick lines connecting isotopes show the main flow of the *s*-process thinner lines show branches; *s*-only isotopes are in bold and unstable isotopes are outlined with dashed lines.

[176, 180]. The elements produced most efficiently by the weak s-process are copper, gallium and germanium [166, and references therein].

For abundances with A$\gtrsim$90, the main astrophysical circumstance in which s-process takes place is in the AGB phase, which is the final evolutionary stage of low- and intermediate-mass stars before losing all their envelope through stellar wind and forming a Planetary Nebula [115, 184]. In the solar system isotopic abundances, the s-process distribution for A$\gtrsim$90 can be divided into main s-process component (between Sr and Pb) and strong s-process component (which includes about half of the solar ^{208}Pb). The main component is made by AGB stars with metallicity close to solar, while the strong component is mostly due to the galactical chemical contribution from much older and more metal-poor AGB stars [22, 59]. The s-process properties of metal-poor AGB stars are not very different from those of younger and more metal-rich objects. The more efficient production of Pb in metal-poor AGB stars is due to the lower amount of Fe seeds, which increases the number of neutron captures per Fe seed and makes the production of heavier s-process isotopes more efficient.

Most of the neutrons for the s-process in AGB stars are due to ^{13}C(α,n)^{16}O neutron source, activated in the radiative ^{13}C-pocket in the He intershell stellar region [203]. The physics mechanisms driving the formation of the ^{13}C-pocket are still matter of debate [see 72, and references therein] and will be discussed in this work.

Neutrons are also made from the ^{22}Ne(α,n)^{25}Mg source, partially activated at the bottom of the He intershell during the Thermal Pulses [e.g., 29, 38, 104, 168, 202]. Whereas the contribution to the total amount of neutrons is smaller compared to the ^{13}C neutron source, the activation of the ^{22}Ne(α,n)^{25}Mg generates higher neutron densities above 10^{10} neutrons cm^{-3}, leaving its fingerprints in the final s-process AGB stellar yields [e.g., 38, 59, 202].

The production of the s-process elements has been directly observed on a large sample of intrinsic or extrinsic AGB stars at different metallicities [e.g., 2, 29, 197, 235, and references therein], in grains of presolar origin condensed in the winds of old AGB stars and found in pristine carbonaceous meteorites [e.g., 14, 129, 130, 133, 236], in post-AGB stars [e.g., 43, 182, 185, 186, 218] and in ionized material of planetary nebulae around their central remnant star after the AGB phase [e.g., 154, 194, 200, 201].

The possibility to compare stellar models predictions with such a large variety of independent observations together with the needs for galactic chemical evolution [e.g., 214] has triggered the production of different sets of AGB stellar yields [e.g., 21, 38, 104, 134]. Indeed, s-process nucleosynthesis is extremely sensitive to the thermodynamic conditions, abundances and convective boundary mixing mechanisms

in the parent AGB stars, providing fundamental constraints to the macro- and micro-physics inputs used to produce theoretical stellar AGB models [e.g., 72]. In particular, the convective boundary mixing (CBM) below Helium-intershell during the convective TPs affects the abundances of the most abundant species (e.g., ^{4}He, ^{12}C and ^{16}O), and therefore the thermodynamic evolution and all the nucleosynthesis reactions in the He intershell during the AGB phase [e.g., 74, 133]. On the other hand, the CBM below the envelope after the convective thermal pulse, during the so-called Third Dredge Up event (TDU, see chapter 2), directly affects the formation of the ^{13}C-pocket. While the existence of the radiative ^{13}C-pocket is a well-established scenario in stellar nucleosynthesis, the assumptions made in hydrostatic one-dimensional stellar models do not allow to simulate directly the physics mechanisms responsible for the CBM. Guidance from hydrodynamics simulations is needed to include simpler CBM parameterizations.

Five physics mechanisms have been considered in AGB stars during the TDU: semi-convection [86], overshooting [74], rotation-driven instabilities [120] internal gravity waves [45, hereafter De03] and magnetic buoyancy [30, 152]. Limitations in distinguishing between these scenarios include also the uncertainty of their implementation in hydrostatic models, leading to different nucleosynthesis results to compare with observations. For instance, starting from indications of hydrodynamics simulations by [55], different implementations in stellar models lead to different ^{13}C -pockets with *s*-process production of heavy elements changing by at least one order of magnitude [39, 74, 133].

Convection always causes gravity waves propagation across the convective boundary, as also remarked by [75] (hereafter He07) where a new set of multi-dimensional hydrodynamical simulations for the TP was provided, considering the whole He-intershell. In these simulations, He07 showed the overlap of two different convective boundary-mixing contributions at the bottom of the TPs, a first steeper profile due to Kelvin-Helmholtz instability and a second slower decrease due to gravity waves. This is the dominant situation that arises when simulating TP events. Considering the mixing processes occurring under the convective envelope during TDU, the role of gravity waves on the ^{13}C-pocket formation have been discussed by De03.

In Chapter 2, the physics prescriptions by He07 and De03 will be adopted and their impact on the AGB stellar evolution and nucleosynthesis will be discussed.

1.2   The p-process

The p process is responsible for the formation of proton-rich isotopes heavier than Fe. The 35 p-nuclei [although today few of them should not be considered as p-process nuclei anymore, see 48] are bypassed both by the s- and the r-process. The p-process is characterized by sequences of proton captures and/or photodisintegration reactions on seed nuclei, resulting in the production of p-nuclei [12, 140].

Meyer [140] explored the conditions required for the p-process considering an environment at a fixed temperature $T_9=1$ (hereafter, $T_9=10^9$K) and target nuclei with atomic number $10 \lesssim Z \lesssim 80$. The timescale of a (γ,p) or a (γ,n) reaction is grater than 10^{10} seconds even considering a mass density in protons of 10^6 g/cm^3, while proton capture reactions are characterized by timescales always at least 10^5 times shorter. If an astrophysical site could maintain a mass density in protons of 10^6 g/cm^3 for 10^5 seconds at T9=1, the proton-rich isotopes of all elements up to platinum (Z=78) could capture a proton. The timescale for proton capture reactions decreases if the setting has a higher density in protons available. The proton capture rates also increase with temperature because the reactants have a higher relative kinetic energy compared to the Coulomb barrier than at lower temperatures. If we increase the temperature we see that the timescale for proton capture decreases, but so does the timescale for photo-disintegration reactions, which at some point becomes predominant. For example, if we consider T9=3 and a mass density in protons of 10^6 g/cm^3, photodisintegration reactions always have shorter timescales than proton capture reactions for $Z > 70$. If a system is evolving towards nuclear statistical equilibrium (hereafter NSE), nuclei that are more massive than the nucleus with the highest binding energy per nucleon will tend to disintegrate nucleons to increase the number of macroscopic states available to the system [140]. If thermodynamic conditions favour proton-captures, a large supply of protons must be available for a long time, thus putting severe constraints on hypothetical astrophysical sites. If the proton-capture process occurs at higher temperatures, disintegration reactions will dominate the flow and prevent capture to higher mass. Therefore, any astrophysical stellar site in which high temperatures and sufficiently short timescales lead to incomplete melting of seed heavy nuclei can produce p-nuclei [140]. For this reason, SNe Ia and core-collapse supernovae are potentially both hosts of the p process. If the p-process consists of sequences of photo-dissociations and β decays, it is usually called γ-process [233]. This occurs in explosive O/Ne burning during CCSN explosions and reproduces the bulk of p-isotopes within a factor 3 [180]. However, this scenario in CCSNe suffers from a strong underproduction of the most abundant p-isotopes (^{92}Mo, ^{94}Mo, ^{96}Ru and ^{98}Ru), and destroys ^{113}In and ^{115}Sn due

to lack of seed nuclei with A>90 [48, 172]. SNe Ia has been proposed as candidates for a complementary p-process production. In particular, in the Travaglio et al. [217] ^{92}Mo, ^{94}Mo; ^{96}Ru and ^{98}Ru were produced at the same level of the heavy isotopes.

1.2.1　Core-collapse supernovae as p-process sites

CCSNe results from the internal collapse and violent explosion of a massive star. The presence of hydrogen in its spectrum is what distinguishes a type II supernova from other classes of supernova explosions. In a typical type II supernova, the newly formed neutron star has an initial temperature of about 100 billions Kelvin; 10^4 times the temperature of the Sun's core. Much of this thermal energy must be spent for a stable neutron star to form, and this is accomplished by a further emission of neutrinos releasing about 10^{46} Joules. Later on, about 10^{44} Joules are re-absorbed by the stalled shock, producing an explosion [95]. Arnould [11] computed the p-process in the hydrostatic O-burning phase in stars. The timescales are longer in this site than in the SN site and would allow for more proton capture. In this site, temperatures are high enough for disintegrations (especially (γ,n) reactions) to be important. A major challenge for this model is to eject the new p-nuclei without significantly modifying their abundances during subsequent SN explosion. Woosley and Howard [233] computed the p-process in the ejected O/Ne shell in CCSNe. The supernova shock heats up this shell and activates the γ-process, where photodisintegrations are driving the nucleosynthesis of p-process nuclei. The inner regions of the O/Ne shell will achieve the highest temperatures (T $\geq 3\times10^9$K) and thus get closer to the NSE. These regions make the lightest p-nuclei. Outer regions produce the heavier p-nuclei because photodisintegration is less complete, due to the lowest temperatures in the SN shock. In particular, intermediate-mass ($50 \leq$ N ≤ 82) and heavy (N ≤ 82) p-nuclei are made in the temperature ranges $2.7 \leq$ T$_9 \leq 3$ and T$_9$ ≤ 2.5 respectively. Rapp et al. [178], Rauscher [179], Rauscher et al. [180], Rayet et al. [181] carried out detailed p-process nucleosynthesis simulations in CCSNe. All of these works confirm for the p-isotopes serious deficiencies for the p-process isotopes of Ru and Mo and in the 150<A<165 atomic mass region (see Fig. 1.3). On the other hand, [169] showed that a comparable production of ^{92}Mo, ^{94}Mo, ^{96}Ru and ^{98}Ru isotopes compared to other p-process isotopes can be obtained, if a much higher ^{C12}C+^{12}C rate is used compared to the standard rate by [33]. A strong C-fusion rate indeed allows to increase the s-process production, which is seed for the following γ process. On the other hand, the γ process contribution to the p-nuclei strongly depends on the initial metal content, being significant only around solar metallicity.
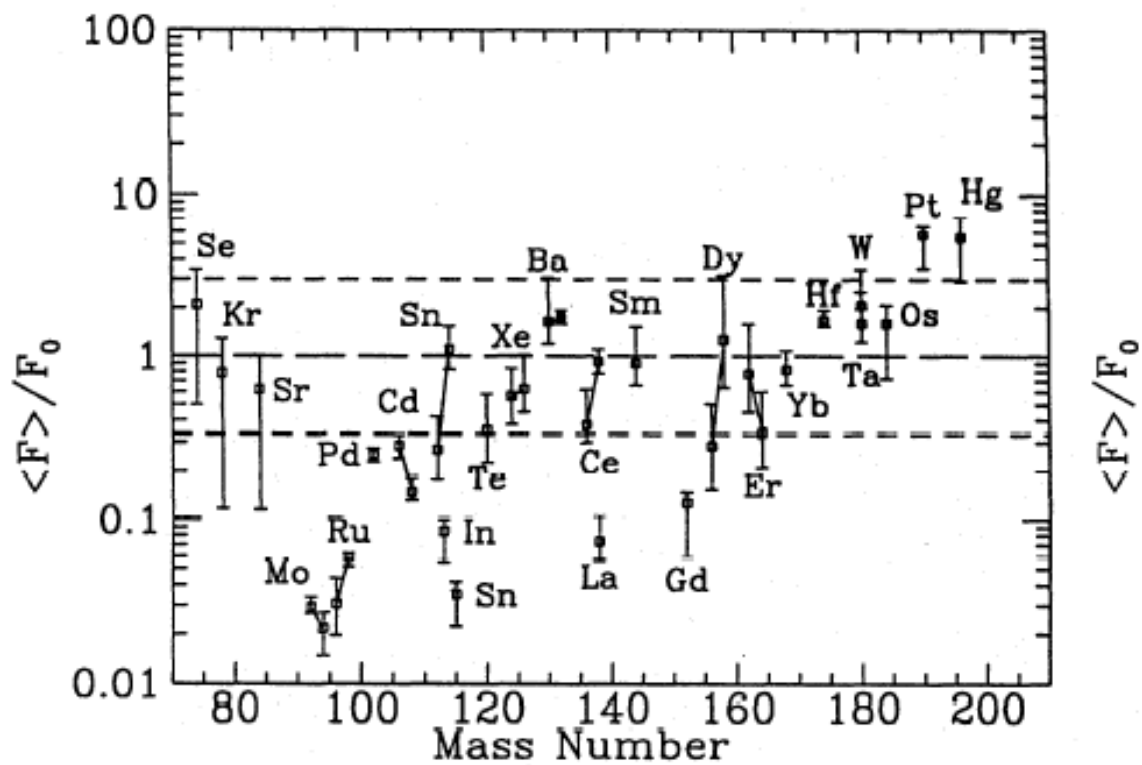
Fig. 1.3 *p*-process calculation in Type II Supernovae - results from Rayet et al. [181].

Alternative scenarios were proposed complementing the γ process in CCSNe. Woosley et al. [230] explored of the impact of neutrino-interaction with the ejected material, showing that the production of ^{138}La and ^{180}Ta may be strongly increased. Wanajo [222] proposed that neutrino-driven winds in CCSNe can be one of the possible sites for *p*-nuclei production through the rapid-proton-capture-process or *rp*-process, which is expected to take place in proton-rich compositions with sufficiently high temperature, and which leads to the production of proton-rich isotopes beyond iron. However, there are a number of nuclei with β-decay timescales of a few minutes on the *rp*-process path. These "waiting point" nuclei inhibit the production of heavy proton-rich nuclei beyond the iron group in CCSNe. The situation changes when neutrino-induced reactions are taken into account. Pruet et al. [174], Wanajo [222] have shown that such "waiting points" are bypassed by neutron capture reactions even in proton-rich environments. This is due to the continuous supply of neutrons from the anti-electron neutrino absorption by free protons in the early ejecta that are subject to intense neutrino flux. As a consequence, the *rp*-process takes place, leading to the production of proton-rich nuclei beyond the iron group. This last case is called νp-process [56]. Arcones and Montes [8] performed a two-dimensional simulation of SNII explosion, showing that, when the consequent external layers expansion becomes slower, the matter stays exposed to high neutrino fluxes for a longer time, increasing the efficiency of the ν-process. Other types of core collapse supernovae were investigated, as the electron-capture type Supernovae explored by Wanajo et al. [223].

1.2.2 High energy astrophysical sources as *p*-process sites

Other astrophysical sites besides standard core-collapse events can be the scene of neutrino induced *rp*-processes. Among these are the disk winds formed around a black hole, which are associated to γ-ray bursts, or the area around a neutron star, with possible super-burst as consequence. Schatz et al. [192] showed that photo-disintegration triggered conversion of heavy *rp*-nuclei into iron group nuclei can dominate the energy release in super-bursts that originate from a carbon flash in the ashes of a type I X-ray bursts. Therefore, X-ray bursts must produce a large amount of *rp*-nuclei to allow subsequent super-burst to happen and to explain their duration, energetics and spectral evolution. Type I X-ray bursts are flashes of accumulated H on an accreting neutron star. X-ray bursters exhibits periodic luminosity bumps peaked in the X-ray regime. These objects are made up of an accreting compact object and a 'donor' star. X-ray bursters differ from other X-ray variable objects since they show a fast rise in luminosity (1-10 seconds) followed by spectral softening [193]. The integrated flux of such events

is of the order of 10^{39-40} ergs, to be compared to the steady luminosity which is of the order 10^{37} ergs for accretion onto a neutron star. The ratio of the burst flux to the persistent flux ranges from 10 to 10^3. The timescales of those burst range from hours to days, even if more extended recurrence times and and weak bursts with recurrence times lower than 30 minutes are observed in some cases. To date, the thermonuclear explosion of hydrogen-rich material on accreting neutron stars makes these sites likely candidates for the occurrence of the *rp*-process. Schatz et al. [191] proposed that this type of transmutations could produce a substantial amount of *p*-nuclides, and could be a source of the *p*-isotopes Mo and Ru in the solar system content. However, a small amount of nucleosynthesis products is expected to be ejected, and its contribution to the Galactic chemical evolution is likely to be negligible [112, 191].

1.2.3 Type Ia supernovae as *p*-process sites

A SNIa is the result of the violent thermonuclear explosion of a white dwarf after having accreated mass from a companion star in a binary system reaching and overcoming in this way the critical Chandrasekhar mass. Since a few years ago, no clear consensus had been reached on whether the star explodes as a result of a subsonic nuclear deflagration that becomes strongly turbulent [27, 91], or a supersonic detonation, or whether this turbulent flame phase is followed by a delayed detonation during the expansion [107]. Today it seems that suitably tuned delayed detonations satisfy all the constraints given by SNIa spectra, light curves, and nucleosynthesis. A white dwarf is the remnant of a low or intermediate mass star that has completed its normal life cycle and has ceased nuclear fusion. However, CO white dwarfs are capable of further fusion reactions that release a great amount of energy if their temperatures rise high enough. Two are the most accepted explanations for a SNIa creation: a white dwarf that accretes mass in a binary system at the proper rate for a sufficiently long time to grow to nearly the Chandrasekhar Mass (1.39 $M_\odot$) at which it ignites carbon burning at or near its center (Single degenerate scenario, Whelan and Iben [227]) or the collision/merging of two white dwarfs resulting again in a final explosion (Double-degenerate scenario, Webbink [224]). At the onset of the explosion a thermonuclear energy runaway occurs, reaching almost 10^{10} $L_\odot$ [80]. SNe Ia peak luminosity is up to 20 times greater than typical CCNSe like SN Type-II [142]. This has important consequences concerning the production of Fe peak elements, which are produced more efficiently in SNe Ia than in SN II, as it can also be inferred from the corresponding higher luminosity. SNe Ia are responsible of about 70 % of the solar Fe amount, while the remaining 30% is attributed to CCSNe [138].

The p-process is expected to take place in the outermost zones of SNe Ia. Howard et al. [84] considered both solar abundances as seeds for the p-process as well as s-enhanced seeds considering the Khokhlov delayed detonation model. They obtained an efficient p-process production. In this case, the p-process is activated on the surface of a degenerate CO white-dwarf when it undergoes a type Ia supernova explosion. With an initial solar system-like composition of s- and r-process elements, they observed an insufficient galactic yield of p-nuclei. On the other hand, if the outer layer of CO white dwarfs became s-process rich during He shell flashes, a p-process component with average enrichment of 10^4 was obtained. When these stars undergo explosive disruption, there is a region near the surface where the temperature lies in the range $2.4 \lesssim T9 \lesssim 3.2$. At these temperatures, the enhanced s-process seeds are efficiently transmuted into p-isotopes (including light p-isotopes) on a time scale of much less than 1 second. The significant enhancement of the seed nuclei in the mass region $A \gtrsim 96$ was a key feature of Howard et al. work that could allow them to produce most of the light mass p-nuclei, with the exception of an overproduction of Se^{74}, Kr^{78} and Sr^{84} and underproduction of Mo and Ru isotopes, in particular ^{94}Mo and ^{96}Ru, even if not in such a dramatic way as in the case of a SN II explosion. More precisely, ^{94}Mo and ^{96}Ru were underproduced by a factor between 7 and 8 compared to the other p-process nuclei. For comparison, Rayet et al. 1995 obtained an underproduction by a factor of about 50 for these isotopes in the p-process in CCSN.

Goriely et al. [63] found that the He-detonation in CO white dwarfs is accompanied by an efficient p-process and triggers a variant of the rp-process, the pn-process, which develops in the presence of neutrons and with less protons than in classical rp-processes. The nuclear flow associated with this variant of the rp-process lies much closer to the valley of stability compared to the classical rp-process. This results from the lower proton and nonzero neutron concentration encountered in the He-detonation. Most of the p-nuclides, including the puzzling cases of Mo and Ru isotopes, are found to be Co-produced in these conditions in quantities close to the solar ones. Unfortunately they were underproduced (except ^{78}Kr) with respect to the Ca to Fe species, which means that at the moment this scenario does not seem to be relevant for the chemical inventory of the p-process nuclei in the galaxy. More recently, Kusakabe et al. [114] calculated the p-process in the C deflagration model for SNe Ia, using the W7 model [150]. Initial abundances of s-nuclei were obtained by calculating the s-process nucleosynthesis that they expected to occur in the repeating He shell flashes on the CO white dwarf during mass accretion. In practice, they derived the s-seed distribution assuming an exponential distribution of neutron exposures with two choices of the mean exposure

$_{\tau 0}$= 0.30 mb^{-1}, which reproduces the main component in the solar system [9], or $_{\tau 0}$ =0.15 mb^{-1}, which results in an s-process distribution decreasing with atomic mass number. These two particular choices of seeds distributions were justified by the expectation that the s-process nucleosynthesis proceeds through the neutron source reactions of ^{22}Ne $(\alpha,n)^{25}$Mg as well as of ^{13}C$(\alpha,n)^{16}$O assuming physical conditions similar to the AGB scenario. It was found that in all cases more than 50% of p-nuclides are Co-produced at almost the same degree of enhancement with respect to their solar abundances. They also showed that the effect of variable C/O ratio in the initial composition of the CO WD on the final p-nuclei yields is marginal. On the contrary, they confirmed that the effect of initial abundances of s-process nuclei on the p-process is crucial to calculate the final p-process yields. Travaglio et al. [217] presented 2D SNIa simulations, starting at the onset of the explosion. As seed distribution for the p-process, they assumed an s-process distribution similar to the main s-process component, obtained from AGB models simulations by varying the ^{13}C concentration in the pocket from 0 up to a factor of two times the standard value of 4×10^{-6} $M_{\odot}$ of ^{13}C (Gallino et al. [59], ST case). The multidimensional SNIa simulations assume instant burning of the C + O material once crossed by a deflagration or detonation front. A number of lagrangian tracer particles that record thermodynamic trajectories was passively advected with the hydrodynamic flow in the explosion simulation. In this way, they obtained for the first time a complete p-process distribution, with similar enhancements relative to ^{56}Fe, including the puzzling light p-nuclei ^{92}Mo, ^{94}Mo; ^{96}Ru and ^{98}Ru. They found that only the isotopes ^{113}In, ^{115}Sn, ^{138}La, ^{152}Gd, and ^{180}Ta diverge from the average p-process production. Among them, ^{152}Gd and ^{180}Ta have an important contribution from the s-process in AGB stars [9] or from the neutrino process in the SNe II [223, 230]. Both ^{113}In and ^{115}Sn are not fed by the p-process nor by the s-process [48]. A fundamental assumption for this scenario is the s-process distribution in the outer accreted layers of the SNIa progenitor. Travaglio et al. [217] assumed seeds distributions and resulting p-nuclei nucleosynthesis results are shown in Fig. 1.4 and 1.5.

One of the main goals of this work is to calculate consistently for the first time the distribution of the seeds nuclei heavier than Fe needed to simulate the p-process in SNe 1a. In order to do that, we simulated the last phases of the accretion on the WD, before the progenitor reaches the Chandrasekhar mass. Chapter 3 will explore the neutron-capture nucleosynthesis of heavy elements in these conditions, in order to verify if the seeds needed for an efficient p-process activation during the SNIa explosion are realistic. One of the main limitations is the lack of observational constraints of
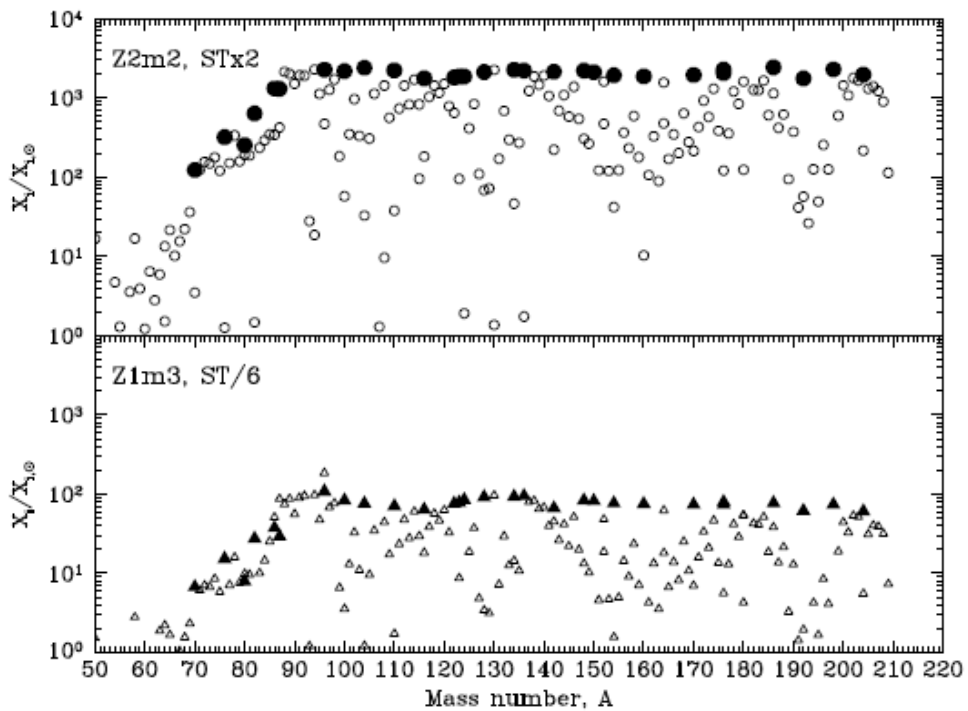
Fig. 1.4 Distribution of initial seed calculated assuming an AGB-like process for their production and adopted by Travaglio et al. [217]. Abundances are shown relative to the solar for Z = 0.02, with the STx2 case of Gallino et al. [59], in the upper panel, and for Z = 0.001, ST/6 case, in the lower panel. Filled dots and triangles are for *s*-only isotopes.
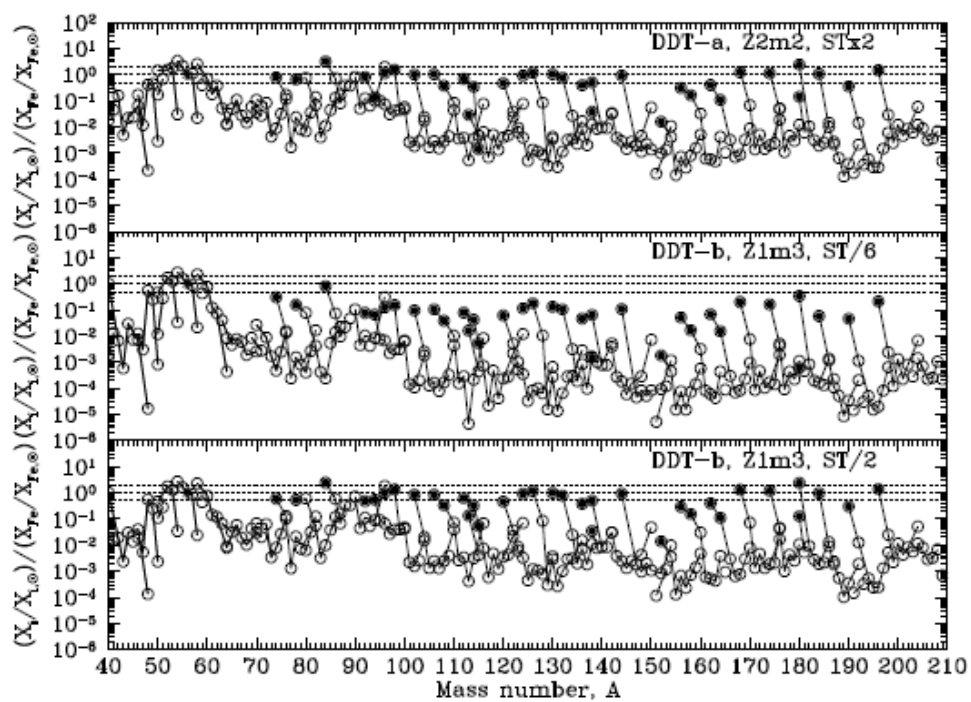
Fig. 1.5 Production factors, normalized to Fe, of *p*-nuclei obtained using 51200 tracer particles in the two-dimensional DDT-a and DDT-b models of Travaglio et al. [217]. The *s*-process enrichment is specified by the labels.

the accretion-phase in a single-degenerate scenario to calibrate our 1D simulations. On the other hand, the physical conditions that lead to the He-flash both during the accretion phase and during AGB evolution are similar, relying on the accumulation of H-burning ashes on the top of the He-rich intershell. Nevertheless, the AGB phase is can be constrained by an large amount of observational data. The same stellar code and physics prescriptions used for the simulation of AGB stellar evolution and nucleosynthesis have been applied also to the simulations of the accretion phase (chapter 2).

Chapter 2

AGB stars evolution and nucleosynthesis

2.1 Preliminary introduction to stellar simulations

After the exhaustion of H in the core at the end of the Main Sequence phase, in low-mass stars H starts to burn in an outer shell while the star is evolving along the Red Giant Branch. If the mass of the star is large enough, the central conditions allow to ignite He-burning and the star evolves to the Horizontal Branch until also the central He is consumed and a degenerate CO core is formed. The major production of energy to sustain the stellar structure is provided by the He shell, and by the H shell few 10^4 Kilometers outward, just below the stellar convective envelope. In this phase the star evolves along the AGB [72, 104]. Because of the different energy generation rates and instabilities caused by nuclear burning proceeding in thin shells, the star undergoes a series of pulses, with burning oscillating between the H and He-shell. H burning in the outer shell leads to the deposition of He onto the quiescent He shell, which contracts and heats up due to the addition of mass and eventually reaches the conditions necessary for the He to abruptly ignite creating an He-Flash. The rapid release of energy during the shell flash causes the outer H-burning shell to expand and cool down, hence interrupting the H-burning. After the shell flash, the He-burning continues trough the He-shell depositing the CO ashes onto the core until the He-shell is depleted.

These recurrent thermal pulses or TPs are caused by a combination of thin-shell instability and partial-degeneracy [72, 108]. Thin-shell instability occurs when nuclear burning happens in a spherical shell. Let us consider a shell of mass δm, temperature T and density ρ, lying between a fixed inner boundary r_0 and an outer boundary r,

such that $l=(r-r_0) \ll r_0$. If the shell is in thermal equilibrium, then the rate of nuclear energy generation within the shell is equal to the net rate of heat flow out of the shell. If the nuclear energy generation increases, then the shell will expand and lift the layers above it. Depending on the thickness of the shell and the equation of state of the gas, this can result in an instability. Hydrostatic equilibrium requires:

$$\frac{dP}{P} = -4 \times \frac{dr}{r} \tag{2.1}$$

Since

$$\delta m = 4\pi r^2 l \rho \tag{2.2}$$

we obtain

$$\frac{d\rho}{\rho} = \frac{dr}{l} = -\frac{dr}{r}\frac{r}{l} \tag{2.3}$$

and

$$\frac{dP}{P} = -\frac{d\rho}{\rho}\frac{l}{r} \tag{2.4}$$

Considering a generic equation of state of gas in the form

$$P = C\rho^a T^b \tag{2.5}$$

We find

$$(4\frac{l}{r} - a)\frac{d\rho}{\rho} = b\frac{dT}{T} \tag{2.6}$$

Therefore, $a \leq \frac{4l}{r}$ is required by thermal stability. On the other hand, a sufficiently thin shell can always violate this condition for any value of a, at which point an expanding shell will result in an increase of temperature, which will increase the nuclear burning rate [17]. Degeneracy condition is met when free particles (in our case electrons, i.e. fermions) are limited to a finite volume and can take only a discrete set of energies, called quantum states. Being fermions, electrons obey the quantum mechanical principle known as the Pauli Exclusion Principle: two electrons cannot share the same quantum state. At the lowest total energy, all the lowest energy quantum states are filled. Electrons want to sit in the lowest possible energy state. They cannot all do that. So the higher the density, the more the electrons have to exist in higher and higher energy states. Therefore, more energy means more motion, which is translated into higher pressure. If the gas is completely degenerate, we obtain an equation of state which is given by:

$$P_e \approx \rho^{5/3} \tag{2.7}$$

Notice that there is no temperature dependence [108].

During the AGB phase, He is accumulated below the H-shell through H-burning, compressing and heating the He-intershell. Therefore, temperature keeps rising. When the temperature is high enough, He can begin to fuse together to form C via the triple-α reaction rate. However, the core is degenerate, so that when temperature rises, pressure does not: the core cannot expand and cool. Therefore, energy rising causes temperature rising which in turn makes energy rise and so on, causing in this way a nuclear energy runaway known as He flash.

Once the energy feedback generated by the convective TP is decreased, the H-shell re-ignites and begins again to refill the He-shell. These burning-oscillation cycles characterize the whole AGB phase, which lasts for a few 10^6 years. During this phase, each expansion and cooling of the envelope as a consequence of a TP event causes an increase of the envelope opacity, thus making the convection more efficient and eventually penetrating into the C-rich intershell, dredging-up freshly syntetized C and s-process elements. This event is called TDU. In this way, the stellar envelope is more and more enriched in C and heavy s-process elements that will pollute the surrounding interstellar medium trough stellar winds (see also discussion in Chapter 3.1). AGB stars are the main contributors of the Solar-System amount of C and half of the elements between Fe and Bi [59, 215]. The recurrent expansion and the consequent cooling down together with the increasing C enrichment, leads to recurrent shocks dust formation in the outer stellar atmosphere. The combination of these two facts results in a sufficiently high mass-loss rate which leads to the ejection of the envelope [24, 25]. Once the entire AGB stellar envelope is lost via stellar winds, the post-AGB evolution starts and the star evolves through the proto-planetary nebula and the planetary nebula phase [e.g., 220]. Finally, after the nebula also disappears because is too far away and lost in the interstellar medium, the stellar remnant cools down along the White Dwarf path.

As it is mentioned in the introduction, the AGB evolution and nucleosynthesis is regulated by the CBM at the He-shell boundaries and between the envelope and the He intershell. The correct treatment of these mechanisms in the stellar simulations is crucial for stellar nucleosynthesis, since they are responsible for the formation of the radiative ^{13}C-pocket, the main contributor to s-process nucleosynthesis in AGB stars via the ^{13}C(α,n)^{16}O reaction. As today, the answer to what are the physics mechanisms producing CBM during the AGB is still controversial. Multi-dimensional hydrodynamics simulations by He07 highlighted the relevance of Kelvin-Helmholtz instabilities and gravity waves (hereafter IGW, following the naming scheme of De03) below the TPs.

To answer these puzzles, in this work I present eleven one-dimensional AGB stellar models with initial mass M = 2 and 3 solar masses, and with initial metal content Z=0.01 and Z=0.02. Consistently with He07 results, the CBM below TPs and the TDU is included directly in the stellar calculations to take into account Kelvin-Helmholtz IGW. Other physics mechanisms, such as rotation [e.g., 76**?**] and magnetic field, are not included.

2.2 Computational tools: Stellar codes

2.2.1 Stellar Evolution Calculations – MESA

All the new stellar models presented in this work were computed using the stellar code `MESA` [`MESA` revision 4219, 160].

The solar distribution used as a reference is given by [65]. The CO-enhanced opacities are used throughout the calculations, using OPAL tables [87]. For lower temperatures, the corresponding opacities from [52] are used. The Reimers formula [183] with $\eta_R = 0.5$ is used for the mass loss up to the end of the RGB phase. Along the AGB phase, the Blöcker [23] formula is used instead, with $\eta_B = 0.01$ for the O-rich phase, $\eta_B = 0.04$ and $\eta_B = 0.08$ for the 2 and 3 $M_\odot$ models respectively after the TDU event that makes the surface C/O ratio larger than 1.15. This choice is motivated by observational constraints, as for example the maximum level of C enhancement seen in C-rich stars and planetary nebulae [72], as well as by hydrodynamics simulations investigating mass loss rates in C-rich giants [139]. For the simulations the `MESA` nuclear network *agb.net* is used, including the pp chains, the CNO tri-cycle, the triple-α and the α-capture reactions ^{12}C $(\alpha, \gamma)^{16}$O ^{14}N $(\alpha, \gamma)^{18}$F $(e^+\nu)^{18}$O , ^{18}O $(\alpha, \gamma)^{22}$Ne ^{13}C $(\alpha, n)^{16}$O and ^{19}F $(\alpha, p)^{22}$Ne . I use the NACRE [7] reaction rate compilation for most reactions. For the ^{12}C $(\alpha,\gamma)^{16}$O the rate by [113] is adopted, ^{14}N $(p, \gamma)^{15}$O is by [89] and the triple-α by [58].

Convective mixing follows the standard mixing length theory [36], taking into account also CBM treatment. For `MESA` simulations the convective boundary mixing is computed by default using the exponential overshooting of [70]:

$$D(dr) = D_0 \times \exp^{-2dr/f_1 Hp_0} \tag{2.8}$$

where dr denotes the geometric distance from the edge of the convective zone. The term $f_1 \times Hp_0$ identifies the scale height of the *overshoot* regime. The values D_0 and

Hp$_0$ are respectively the diffusion coefficient D and the pressure scale height at the convective boundary.

In order to consider also the gravity waves contribution discussed by [75], a second slower decreasing mixing coefficient is included in a number of new AGB models presented in this work. This coefficient is defined as:

$$D_2 = D_0 \times \exp^{-2dr_2/(f_1 \times Hp_0)}. \tag{2.9}$$

with length scale = f$_2$ × Hp$_0$, which is adopted for distances dr > dr$_2$.

Therefore, for dr $\lesssim$ dr$_2$ in this new scheme the mixing coefficient is given by:

$$D(dr) = D0 \times \exp^{-2dr/f_1 Hp_0} \tag{2.10}$$

For dr > dr$_2$:

$$D(dr) = D_2 \times \exp^{-2(dr-dr_2)/(f_2 \times Hp_0)} = D_0 \times \exp^{-2dr_2/(f_1 \times Hp_0)} \times e^{-2(dr-dr_2)/(f_2 \times Hp_0)} \tag{2.11}$$

That becomes:

$$D(dr) = D_0 \times \exp^{-2(dr_2/(f_1 \times Hp_0)+(dr-dr_2)/(f_2 \times Hp_0))} \tag{2.12}$$

As discussed in Herwig [70], this exponential decay starts before reaching the convective Schwarzschild boundary, at a distance f$_1$ × Hp_0 from the estimated location where the adiabatic temperature gradient is equal to the radiative gradient. This new implementation can be defined by the three parameters f$_1$,f$_2$ and D$_2$, where f$_1$ defines the Kelvin-Helmholtz instability slope, and D$_2$ and f$_2$ the efficiency and the slope due to the gravity waves contribution. A schematic description of this formalism is given in Fig. 2.1. This new CBM scheme is only applied during the AGB phase, since the physics behind our CBM scheme has been specifically studied in this phase, whereas during all the previous stellar evolution stages the default overshooting is applied [70].

The list of complete stellar models is given in Tab. 2.1 with the models names and the CBM parameterization. A detailed description of the scheme used to assign model names and other details can be found in section 2.2.2. In Section 2.5.1 the criteria to select f$_1$,f$_2$ and D$_2$ at the two He intershell convective boundaries are provided.

Fig. 2.1 Schematic description of the double-exponential CBM applied in this work. The red line is the standard overshooting mixing coefficient profile following the single-exponential decaying. This profile is dominated by a single 'f' parameter that determines the slope of the mixing profile: the lower the 'f' value, the steeper the profile is. In order to account for the gravity-waves mixing effect, in this work we apply a second, slower, decay (green line) that takes over the first as soon as the mixing coefficient is equal or lower than a 'D_2' value, whose slope is determined by the 'f_2' parameter.

All the AGB stellar models in Tab. 2.1 include the mixing contribution due to molecular diffusion. We assume that the molecular diffusivity is equal to the molecular viscosity, because both of them are proportional to a product of the mean free path and mean velocity of the same particles. On the contrary, we do not consider the radiative viscosity as a component of the microscopic diffusivity, because it describes the exchange of momentum between photons and particles, and therefore it is proportional to the photon mean free path and the speed of light. The default MESA revision used for this work allows to include radiative viscosity as microscopic diffusion term, according to Morel and Thévenin [146]. For this work, also according to [3], we only consider the molecular viscosity term, using the following expression [198]:

$$\nu_{\mathrm{mol}} = 2.21 \times 10^{-15} (1 + 7X) \frac{T^{5/2} \times A^{1/2}}{\rho \times Z^4 \times Log\Lambda}. \tag{2.13}$$

where Λ is the Coulomb integral, with values ranging from 15 to 40 depending on the composition stellar layers. With the present implementation, the impact of molecular diffusion on final elemental abundances is $\lesssim 5\%$. On the contrary, the impact on s-process nucleosynthesis is severe if the controversial implementation from Morel and Thévenin [146] is adopted, strongly increasing the ^{14}N diffusion into the ^{13}C pocket and completely suppressing the s-process production by the ^{13}C(α,n)^{16}O neutron source. While we may rule out the implementation by [146] (we refer to the discussion in Alecian and Michaud [3] for more details), the role of molecular diffusion during the AGB phase deserves further investigation.

2.2.2 Stellar models: list and main parameters settings

In table 2.1 the list of models analyzed during this thesis, together with their main parameters settings, is presented. In the first line of the table, the parameters of our reference model M3.z2m2.st (with the final *st* standing for *standard*) are shown. Its main feature, which makes it differ from the other models, is the single exponential slope used in describing the CBM in order to effectively compare it with Pi13. The 10 models following the reference model can be joined into 3 different groups, their respective labels changing accordingly. The first group collects the main stellar grid made up of 4 models combining 2 initial masses (2 and 3 $M_\odot$) and 2 initial metallicities (0.01 and 0.2), more precisely: M2.z1m2, M2.z2m2, M3.z1m2 and M3.z2m2. Following them are the two *hCBM* models, whose only major difference from the main grid is a higher CBM under the convective envelope (check the difference in D2* and f2*

Table 2.1 List of AGB stellar models and their relevant parameters: initial mass, initial metallicity and CBM parameterization. The CBM parameterization can be given by a single exponential decreasing profile (sf), consistently with Pi13, or by a double exponential decreasing profile (df) introduced in this work, with or without limiting the mixing length to the size of the convection zones (clipping). The CBM parameters are given below the TP (f1, D2 and f2) and below the TDU (f1*, D2* and f2*).

name	mass [$M_\odot$]	metallicity	CBM	f1	D2	f2	f1*	D2*	f2*	clipping
M3.z2m2.st	3.0	0.02	sf	0.008	-	-	0.126	-	-	yes
M3.z2m2	3.0	0.02	df	0.024	10^5	0.14	0.014	10^{11}	0.25	yes
M3.z1m2	3.0	0.01	df	0.024	10^5	0.14	0.014	10^{11}	0.25	yes
M2.z2m2	2.0	0.02	df	0.024	10^5	0.14	0.014	10^{11}	0.25	yes
M2.z1m2	2.0	0.01	df	0.024	10^5	0.14	0.014	10^{11}	0.25	yes
M3.z1m2.hCBM	3.0	0.01	df	0.024	10^5	0.14	0.014	10^{12}	0.27	yes
M2.z2m2.hCBM	2.0	0.02	df	0.024	10^5	0.14	0.014	10^{12}	0.27	yes
M3.z2m2.he07	3.0	0.02	df	0.010	10^5	0.14	0.014	10^{11}	0.25	no
M3.z1m2.he07	3.0	0.01	df	0.010	10^5	0.14	0.014	10^{11}	0.25	no
M2.z2m2.he07	2.0	0.02	df	0.010	10^5	0.14	0.014	10^{11}	0.25	no
M2.z1m2.he07	2.0	0.01	df	0.010	10^5	0.14	0.014	10^{11}	0.25	no

between models with same initial mass and metallicity) in order to test the impact of the CBM parameters uncertainty on TDU and ^{13}C-pocket formation. The last group is formed by the *he*07 models. Crucial differences from our main grid are: the lower f1 parameter, in order to be fully consistent with He07 recommended values, and the absence of the *clipping*. From MESA revision 3713 on, it is introduced by default the limitation (or clipping) of the mixing length to the length of the convection zone. However, this feature is disabled in models with no clipping. Through the comparison of the *he*07 models with the main grid we want to check the consistency them both from an evolutionary and from a nucleosynthetic point of view.

Finally, an overview of the global stellar properties of each model is given in table 2.2.

In addition to the initial stellar mass and initial metallicity, the H-free core mass at the first TP, the approximated mean luminosity, the approximated mean radius, the number of TP's, the number of TP's with TDU, the time at first TP, the maximum dredged-up mass after a single TP, the average interpulse duration of TPs, the total mass lost during the evolution and the maximum temperature during the TPAGB phase are given. In particular, the dredged-up mass after a single TP and the maximum temperature during the TPAGB directly influence the total *s*-enrichment of the envelope and the activation of *s*-process branchings respectively.

Table 2.2 AGB stars properties.

Name	M_{ini} [$M_\odot$]	Z_{ini}	m_c [$M_\odot$]	$logL_*$ [$L_\odot$]	R_* [$R_\odot$]	N_{TP}	N_{TDUP}	t_{TPI} [$10^6 yr$]	ΔM_{Dmax} [$10^{-2}M_\odot$]	M_D [$10^{-2}M_\odot$]	t_{ip} [yr]	M_{lost} [$M_\odot$]	$T_{PDCZ,max}$ [K]
M2.z1m2	2.00	0.01	0.495	3.47	169	24	12	1.265E+03	0.8	6.348	164516	1.38	8.476
M2.z2m2	2.00	0.02	0.515	3.59	229	24	12	1.357E+03	0.7	5.563	112625	1.34	8.394
M3.z1m2	3.00	0.01	0.640	3.97	308	13	12	4.092E+02	1.2	9.324	57740	2.33	8.480
M3.z2m2	3.00	0.02	0.588	3.89	302	21	18	4.798E+02	1.3	12.983	67556	2.36	8.487
M2.z2m2.hCBM	2.00	0.02	0.514	3.58	223	21	12	1.357E+03	0.7	4.897	122534	1.35	8.487
M3.z1m2.hCBM	3.00	0.01	0.645	3.98	310	12	11	4.125E+02	1.4	9.874	58824	2.33	8.488
M3.z2m2.st	3.00	0.02	0.593	3.87	300	14	11	4.835E+02	1.0	7.188	69414	2.35	8.400
M2.z1m2.he07	2.00	0.01	0.497	3.48	170	25	13	1.279E+03	0.4	3.748	146344	1.36	8.460
M2.z2m2.he07	2.00	0.02	0.510	3.58	223	27	14	1.406E+03	0.4	3.243	107980	1.32	8.463
M3.z1m2.he07	3.00	0.01	0.647	3.99	312	15	14	4.127E+02	0.7	6.426	46333	2.30	8.247
M3.z2m2.he07	3.00	0.02	0.592	3.85	281	23	19	4.818E+02	0.8	7.129	58434	2.34	8.471

M_{ini}: Initial stellar mass.
Z_{ini}: Initial metallicity.
m_c: H-free core mass at the first TP.
L_*: Approximated mean Luminosity.
R_* : Approximated mean radius.
N_{TP}: Number of TP's.
N_{TDUP} : Number of TP's with TDUP.
t_{TPI}: Time at first TP.
ΔM_{Dmax}: Maximum dredged-up mass after a single TP.
t_{ip} : Average interpulse duration of TPs.
M_{lost}: Total mass lost during the evolution.
$T_{PDCZ,max}$: Maximum temperature during the TPAGB phase.

2.3   Nucleosynthesis Post-Processing Calculations – MPPNP

The multi-zone post-processing code `mppnp` is described in detail in [168]. The network includes up to about 5000 isotopes between H and Bi, and more than 50000 nuclear reactions. A self-controlled dynamical network defines the number of species and reactions considered in calculations, based on the strength of nucleosynthesis flows producing and destroying each isotope. Rates are collected from different data sources: European NACRE compilation [7] and [88], or more recent if available [e.g., 58, 90, 113]. In particular, for the ^{13}C$(\alpha,n)^{16}$O and ^{22}Ne$(\alpha,n)^{25}$Mg rates [69] and [94] are used, respectively. For experimental neutron capture rates of stable isotopes and available rates for unstable isotopes I use mostly the Kadonis compilation (`http://www.kadonis.org`). Exceptions relevant for this work are the neutron-capture cross sections of ^{90,91,92,93,94,95,96}Zr: the new rates by [135] were used instead, based on recent experimental measurements. For stellar β-decay and electron-capture weak rates I use [57], [153], [118] and [62], according to the mass region. Rates are taken from JINA reaclib library [41] if not available from one of the resources mentioned above.

2.4   Choosing the `MESA` revision and impact of the new nuclear reaction network

For this work, I used the `MESA` stellar evolution code revision 4219. In this section I compare the results of this choice with a previous MESA revision, 3372, that was used by Pignatari et al. [168] (here and after Pi13). These two different revisions are examined both in the HR and Kippenhahn diagrams. An HR diagram shows the evolution of the star in absolute magnitude or luminosity with respect to its effective temperature. A Kippenhahn diagram shows the evolution of the internal structure of a star in mass coordinates as a function of time.

In Fig. 2.2 and Fig. 2.3 the HR and Kippenhahn diagrams of two models with initial mass $M = 3\,M_\odot$ and initial metallicity Z=0.02, from pre-main sequence to the tip of the AGB phase, are shown: the model M3.z2m2.st (Tab. 2.1), calculated with the `MESA` rev. 4219, and its analogous stellar model from Pi13. For both models all the prescriptions regarding mass loss, nuclear reaction rates, convective boundary mixing parameters, resolution, timesteps, opacities and atmosphere description are the same. In particular, the CBM is included with same parameterization. As already mentioned, the only relevant difference is the MESA revision. In Fig. 2.2, the HR diagrams are extremely similar until the start of the AGB. Then, the two models tend to give different results. The different behavior is observed also in the C/O ratio at the surface during the AGB phase (see Fig. 2.3). This is due to specific modifications adopted since `MESA` rev. 3713, which are related to the handling of single convection zones of the order of 10^{-3} $M_\odot$, where the radial extent of the zone is so small that the normal calculation for mixing length gives a distance that is larger than the size of the zone. Therefore, from rev 3713 on (including rev. 4219) the mixing length is restricted to values smaller than the height of the zone. The main impact for our analysis is that small convection zones, which are present in particular under the PDCZ during a TP event, are mixed more weakly because of the mixing scale length being limited to the size of the zone, and therefore the He-intershell tends to be less enriched in O than with older `MESA` revisions.

This is shown in Fig. 2.5, where the evolution of He, C and O abundances in the He Intershell is shown for model M3.z2m2.st, **M3.z2m2.he07** and the analogous model in Pi13. Note that M3.z2m2.st is the only model including clipping (see table 2.1 for more detail about models parameters). The ^{4}He abundance in the He-intershell of model M3.z2m2.st is 30% higher compared to Pi13, while ^{12}C and ^{16}O are smaller. On the other hand, M3.z2m2.he07 is more similar to the results of Pi13, showing a good
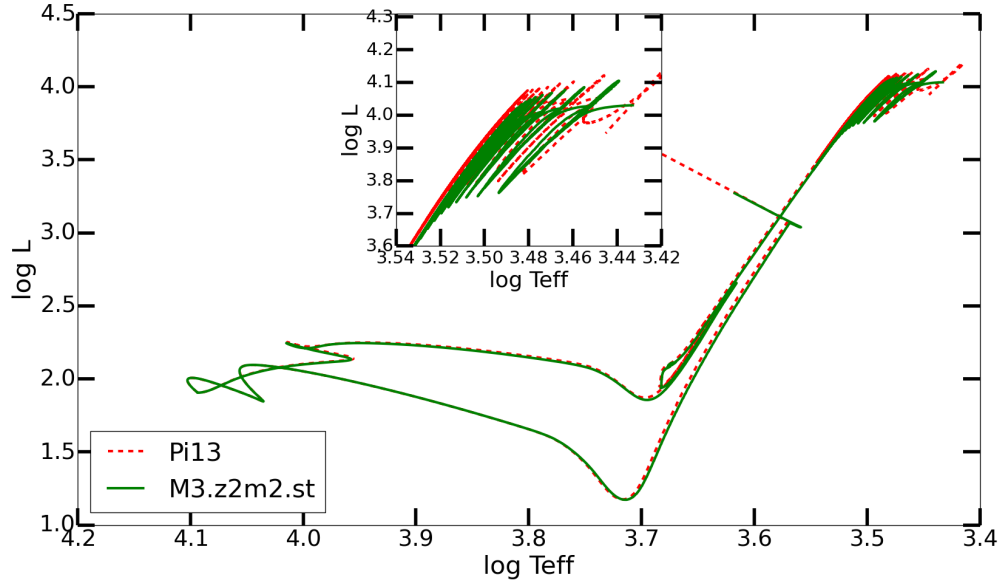
Fig. 2.2 HR diagrams for M3.z2m2.st and the analogous model calculated with `MESA` rev. 3372 (as in Pignatari et al. [168])
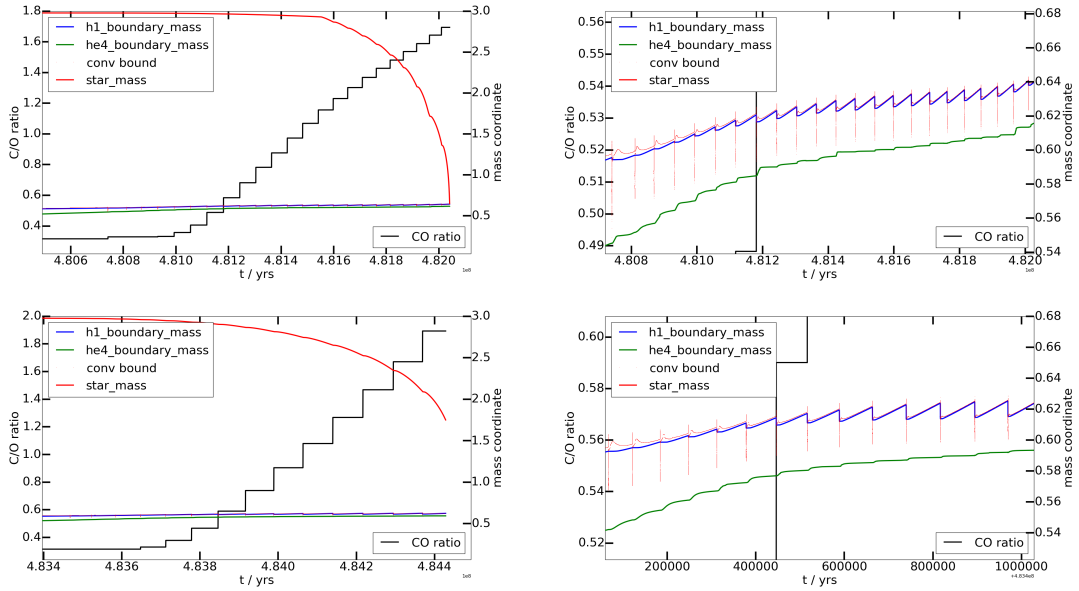
Fig. 2.3 Upper panels: Kippenhahn diagrams of the Pi13 $3\,M_\odot$ case at solar metallicity calculated with rev. 3372. The whole AGB phase is presented in the plot on the left panel, and zoomed in the He-intershell in the right panel. Lower panels: As in the upper panels, but for model M3.z2m2.st.

agreement all along the AGB evolution. For M3.z2m2.st the final mass fractions of ^{4}He, ^{12}C and ^{16}O in the He intershell are 0.55, 0.35 and 0.045, respectively, while for the 3 $M_\odot$ star model adopting the older `MESA` revision are 0.40, 0.40 and 0.15. Finally, we obtain 0.44, 0.34, and 0.16 for the model M3.z2m2.he07. Therefore, the clipping is the main source of the differences seen in Fig. 2.5. While this choice may be irrelevant in other stellar mass regimes, it appears to be crucial for AGB simulations. This is affecting the parameterization of physics mixing mechanisms in 1D models, and it is not clear a priori what is the best solution. However, hydrodynamics simulations give a clear indication that the clipping implementation used in the last MESA revisions should be switched off, as we did in the set of AGB models labeled he07. In He07, the mixing parameters extrapolated for the parameterization in 1D models f_1,f_2 and D_2 should be more considered as upper limits. Indeed, an overestimation of the CBM efficiency can be expected in case of hydrodynamics simulations not fully resolved.

In order to obtain similar C and O concentrations in the He intershell, the models with the clipping activated demand an f_1 larger than the upper limit given by hydrodynamics simulations. Based on these considerations, the set of AGB models labeled he07 are more realistic in terms of physics setup. On the other hand, I will show in the next sections that once similar He, C and O abundances are present in the He intershell, similar s-process nucleosynthesis results are obtained during the AGB phase, independently of the physics setup that leads to these He, C and O concentrations.

Fig. 2.3 compares the evolution of models Pi13 and M3.z2m2.st. In addition to the usual mass-coordinate on the y-axis, also the surface numerical C/O ratio is shown, following in this way the progressive formation of the C star (which is achieved once the surface C/O is larger than 1). It should be noted that the C/O ratio evolves with a step-like behavior, where each step-up of the C/O value corresponds to a TDU event that brings freshly syntetized C from the intershell to the surface. Important points to consider are the following: 1) with the new revision, less TPs are made compared to the old revision. In particular, the Pi13 model has 23 TPs, with 19 TDU events, while M3.z2m2.st has 17 TPs and 14 TDUs respectively; 2) TDUs are more efficient in M3.z2m2.st compared to the older revision. Point (1) and (2) are connected, since more efficient TDUs allow the AGB envelope to become C-rich earlier, and therefore to be consumed by stellar winds at earlier times. The final surface C/O ratio reached in the 3 $M_\odot$ star model by Pi13, M3.z2m2.he07 and M3.z2m2.st is equal to 1.7, 1.6 and 2.2 respectively. Compared to Pi13, in this work I am using an updated nuclear reaction network, including few different neutron capture reaction rates: the new cross sections for ^{20,21,22}Ne by [68], ^{62,63}Ni by [124], and ^{90,91,92,93,94,95,96}Zr [135, 206, and

references therein]. The only exception is model M3.z2m2.st, that was calculated using the same nuclear reaction network of Pi13.

While none of the rates mentioned above has a relevant impact on stellar evolution or on the total s-process production, the new Zr cross section affects the s-process branching at ^{95}Zr during convective TPs. This aspect is crucial since ^{96}Zr is produced via a branching at the unstable ^{95}Zr only if the neutron density exceeds 5×10^8 neutrons cm^{-3}. Data from single SiC grains show deficits in the ^{96}Zr/^{94}Zr ratio with respect to the solar values and point to a marginal activation of ^{22}Ne neutron source in the grain parent stars [136]. For this reason, we also provide here below the results for the $3\,M_\odot$ star model described by Pi13, but using the same nuclear reaction network adopted for this work (model Pi13.newnet). Fig. 2.4 shows the differences arising from the nucleosynthesis calculations of the three models. Due to the lower number of TDU, the M3.z2m2.st shows a milder s-process enrichment at both the Sr peak and the Ba peak (where ls ($light-s$) and hs ($heavy-s$) represent the production at the two neutron magic peak in logarithmic notation, Luck and Bond [131]), only partially compensated by the larger TDU efficiency as we mentioned earlier. On the other hand we obtain similar [hs/ls] ratios, defined as the average logarithmic ratio normalized to solar ([hs/ls]=log(hs/ls)$-$log(hs/ls)$_\odot$). A similar definition is given to the [ls/Fe] and [hs/Fe] indices. The evolution of the Zr isotopic ratios shows strong differences. The comparison of the results obtained by the Pi13 model and the Pi13.newnet model shows that the use of new Zr neutron capture cross sections (and in particular of the ^{95}Zr cross section, that is more than a factor of two lower than the rate used by Pi13) allows to obtain much lower ^{96}Zr/^{94}Zr ratios. On the other hand, adopting the same nuclear reaction network of Pi13, M3.z2m2.st shows milder s-process signatures by, on average, 0.1 dex compared to Pi13 and Pi13.newnet models, due to the lower amount of TPs and to the lower temperatures obtained at the bottom of the convective TPs. This is an effect of the larger ^{4}He abundance in the He intershell of M3.z2m2.st, allowing the He-burning activation at lower temperatures (see e.g., Fig. 2.5). Interestingly, the new Zr cross sections have a larger impact on the final Zr isotopic ratios than the stellar model uncertainties. The ^{96}Zr/^{94}Zr ratio is considered an indicator of the ^{22}Ne(α,n)^{25}Mg efficiency at the bottom of convective TPs [e.g., 133]. I will come back to the s-process signature on Zr isotopes in the following sections.

Concluding, significant differences were obtained during the AGB evolution using the two different `MESA` revisions, despite the fact that the same physics parameterizations were adopted. I showed that the main source of these differences comes from the different handling of small convective zones in the setup of the two revisions. A priori it

is not clear what is the best implementation for 1D models. However, hydrodynamics simulations clearly indicate that the no-clipping setup (Tab. 2.1) should be favored. Thanks to the example of the Zr isotopes, we have seen that nuclear uncertainties are crucial: they might be locally more relevant than stellar uncertainties, assuming that it is possible to disentangle their complementary contributions.

2.5   Stellar models - CBM in the He intershell and the ^{13}C-pocket

Most of the metals made by low-mass and intermediate-mass stars are made during the AGB phase in the He intershell region. Its nucleosynthesis products like C and s-process abundances are brought to the stellar surface by recurrent TDU events. The AGB stellar yields carry the signature of the relevant physics processes in the He intershell, challenging our understanding of these stars [72, 204]. On the other hand, independent observations are available to verify the results of theoretical stellar models. I will compare the results obtained with part of these observations in §3.4. For this work, I calculated a set of models considering two initial masses and two initial metallicities: M = 2, 3 $M_\odot$ and Z = 0.02, 0.01. As mentioned in the previous sections, the CBM included at the He-intershell boundaries has a crucial impact on AGB stellar evolution and nucleosynthesis. In this section, the CBM setup at the He-intershell boundaries and the main features of the stellar models are described.

2.5.1   CBM below the convective TP

Based on hydrodynamics simulations of the AGB He flash, He07 showed that Kelvin-Helmotz instabilities are crucial to shape the CBM below the convective TP. He07 obtained that convective motions induce a rich spectrum of IGW in the neighboring stable layers, triggering more mixing across the convective boundary. Three parameters are needed to fit such complex CBM profiles in one-dimensional hydrostatic models, f_1, D_2 and f_2 (see §2.2.1). He07 extracted the following values: f_1=0.01, D_2=10^5, f_2=0.14. Moreover, He07 quantified the uncertainty affecting the f_1 and f_2 parameters, mainly derived from the adoption of different heating rates, number of dimensions and computational codes: in particular, it resulted that $0.004 \leq f_1 \leq 0.016$, as it is visible in Fig. 2.6 (central panel). Left and right panels show the same kind of results for the f_2 parameter and the single slope formalism case respectively. Focusing more on how RAGE results for the f_1 value evolve as a function of resolution in the central panel, it
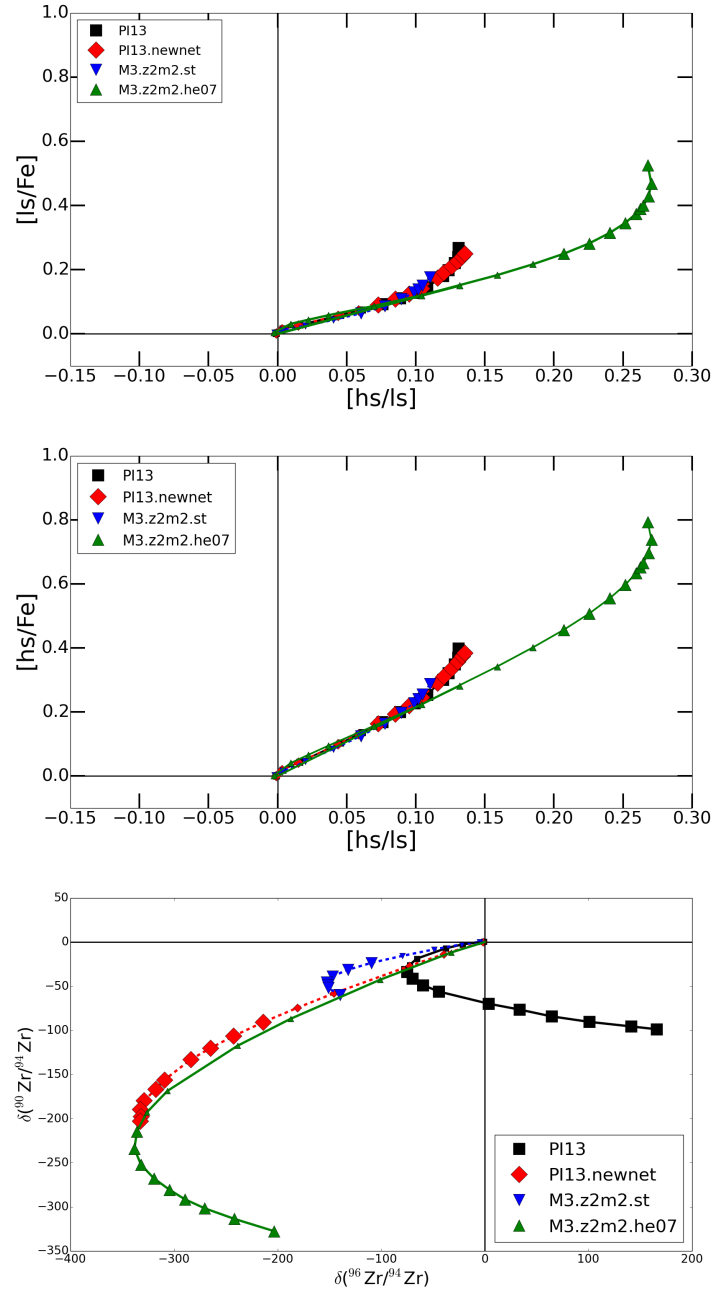
Fig. 2.4 Comparison between the nucleosynthesis products of the same models in figure 2.5 and model PI13.newnet. The evolution of the [ls/Fe] ratio (upper panel) and of the [hs/Fe] ratio (middle panel) are shown in comparison with the [hs/ls] ratio. In particular, each marker represents a TP during the AGB phase. Larger markers are used when the surface C/O ratio exceeds 1. In the lower panel the evolution of $\delta(^{90}\mathrm{Zr}/^{94}\mathrm{Zr})$ and $\delta(^{96}\mathrm{Zr}/^{94}\mathrm{Zr})$ ratios are shown for the same models in the previous panels. The isotopic ratios are shown in $\delta=((\mathrm{ratio/solar})\text{-}1)\times1000$.
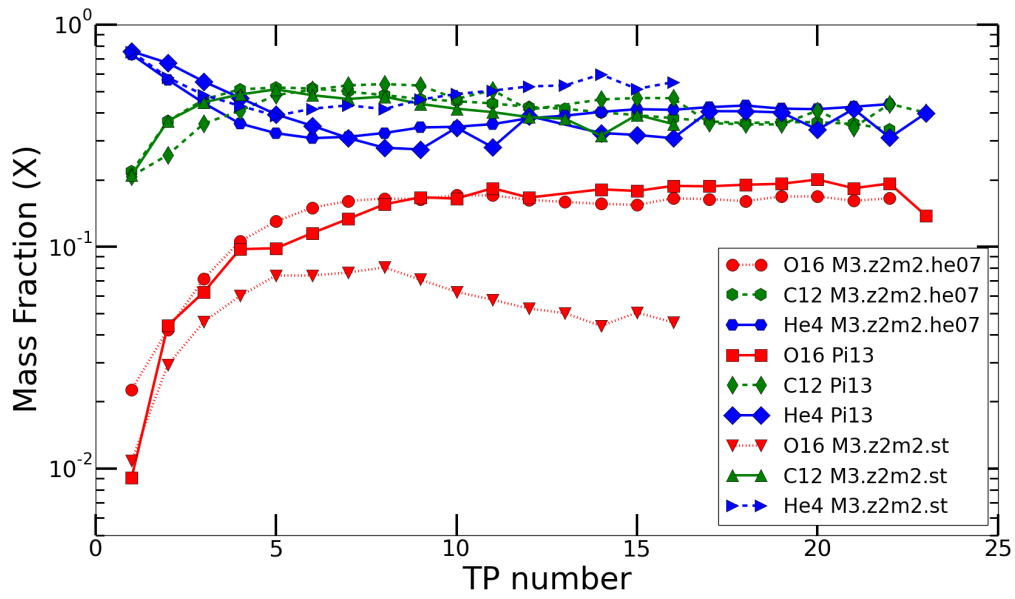
Fig. 2.5 He, C and O abundances evolution in the He Intershell as a function of the TP number along the AGB evolution of M3.z2m2.st and the analogous model calculated with `MESA` rev. 3372 (as in Pignatari et al. [168]). We also included M3.z2m2.he07 model to get the impact of mixing-length clipping during the TP by comparing it with M3.z2m2.st (see text for more details).

should be noticed that a further increase in resolution could result in even lower values for f_1. I therefore started from He07 values and tested the impact of each one of the three parameters on the intershell nucleosynthesis of He, C and O, which represent the main observational constraints to be matched. Fig. 2.7 shows the impact of the D_2 parameter, whose logarithm turns out to have a linear relation with the O abundance for values higher than 6. No impact is seen for lower values of D_2. A linear relation with O has been found also for the f_1, which resulted to be the parameter with the highest impact in the description of this scenario.
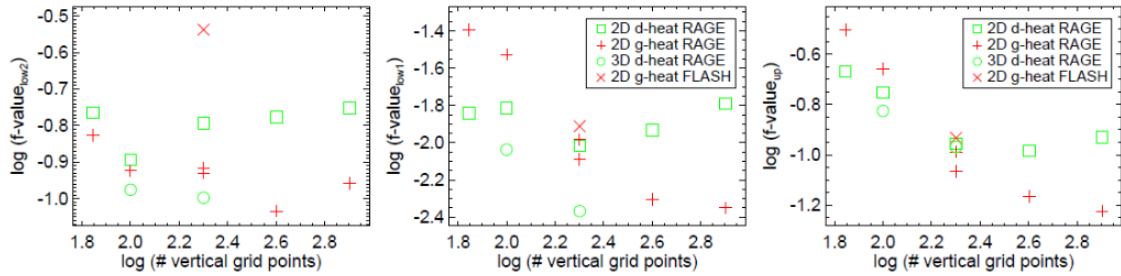
Fig. 2.6 f-values over number of vertical grid points for f_2 and f_1 values to describe CBM under the PDCZ during TP with a double-exponential slope (left and center panel respectively) and the single slope formalism case in the upper overshoot region (right panel). The plots represent results from Herwig et al. [75] and combine data for two heating rates, several 2D runs and two 3D models, runs with the RAGE code and one simulation with the FLASH code.

According to Tab. 2.1, with the exception of model M3.z2m2.st (§2.4), below the TP f_1=0.024, D_2=10^5 cm^{2}s^{-1}, f_2=0.14 were used for all the models, i.e. the values given by He07 but with a f_1 higher by a factor of two. I use this larger value to reproduce
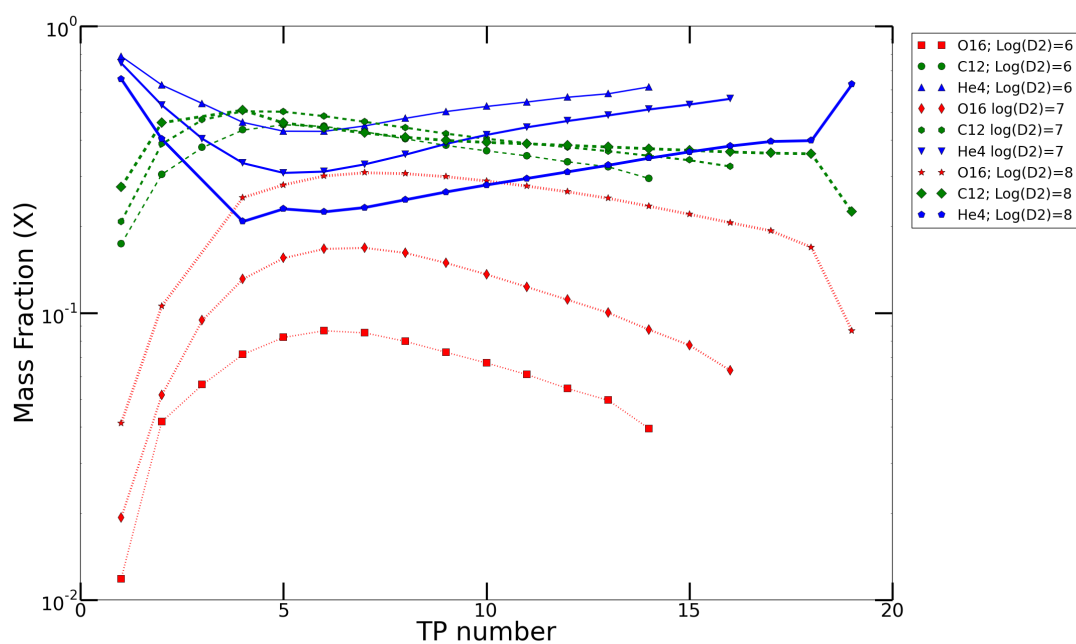
Fig. 2.7 Evolution of He, C and O mass fraction in the He-intershell during AGB evolutions in stellar models adopting different D_2 parameter values in describing the CBM at the bottom of the PDCZ during TP events. All the other CBM parameters are fixed to He07 values.

the full range of the observed O abundances in post-AGB H-deficient stars (see §3.4 for more details). For instance, by using He07 parameters we obtain for the M=3M$_\odot$ Z=0.02 a final He, C and O of 55%, 29% and 6% respectively, compared to 48%, 31% and 13% for model M3.z2m2. Note that the f$_1$=0.024 value has been determined with a `MESA` revision with the peculiar treatment of small convection zones during TP under the He intershell discussed in §2.4. In the upcoming sections it will be shown that the results obtained with older `MESA` revisions (i.e., without limiting the mixing length to be smaller than the height of the zone) adopting He07 parameterizations are similar to those obtained with our newer revision using the parameters previously described, demonstrating in this way the consistency of our parameterization with hydro-simulations results. For the same reason also the uncertainty interval previously specified should be shifted to values higher by a factor of two as well, becoming $0.008 \leq f_1 \leq 0.032$.

The D$_2$ and f$_2$ parameters were not modified here. We found that the parameter f$_2$ has a negligible impact on the evolution and composition of the He intershell with D$_2$=10^5. The parameters D$_2$ and f$_2$ become relevant only for D$_2 \gtrsim 10^6$ cm^{2}s^{-1}, two orders of magnitude higher than the indications by He07 results. For this reason, according to these simulations, Kelvin-Helmotz instabilities are the most relevant physics mechanism to consider below the convective TP for AGB stellar evolution, while IGWs have a minor impact.

2.5.2   CBM below the convective envelope during TDU: the formation of the ^{13}C-pocket

The CBM below each TDU during the AGB phase causes a decreasing profile of protons in the He-intershell material, due to a finite amount of proton diffusion from the convective envelope to the He intershell. This profile is the product of the physics mechanisms triggering the CBM, and will have direct impact on crucial features of the radiative ^{13}C-pocket. The H/Y(^{12}C) ratio (where Y(^{12}C) is the ^{12}C concentration in the He intershell) defines the boundary between the ^{13}C-pocket and the ^{14}N-pocket above. The proton capture rates involved in the production and in the depletion of ^{13}C in these stellar radiative layers and the amount of ^{12}C define where the condition X(^{13}C)>X(^{14}N) is satisfied [e.g., 64, 133]. The ^{14}N-pocket is also ^{13}C rich, but the neutrons made by the ^{13}C(α,n)^{16}O reaction are mostly captured by the poison reaction ^{14}N(n,p)^{14}C, thus reducing the s-process efficiency [e.g., 37, 59]. In the present models, the upper boundary of the ^{13}C-pocket is given by H/Y(^{12}C) $\sim$ 0.4. During the TDU,

this ratio is obtained for a mixing coefficient $D \sim 10^7 cm^2 s^{-1}$. For comparison with other models, see the discussion in [133], [64] and [40]. For $H/Y(^{12}C) \lesssim 0.4$ the ^{13}C-pocket forms, with a decreasing abundance of ^{13}C moving toward the center of the star. The s-process production in the He-intershell layers with concentration of ^{13}C $X(^{13}C) \lesssim 10^{-3}$ becomes negligible. The size of the ^{13}C-pocket (i.e. the ^{13}C-rich mass region with $X(^{13}C) > X(^{14}N)$ and $X(^{13}C) \lesssim 10^{-3}$) is crucial for the s-process production. In this work, at the bottom of the AGB envelope during the TDU we have used the same double-exponential formalism used at the bottom of the convective TPs (see the previous section). As a guidance to derive the D_2 and f_2 parameters to include in the initial setup of the AGB stellar models, we compared the mixing coefficient given by the double-exponential profile with the De03 IGW mixing coefficent. In particular, we are mostly interested in fitting the results of Denissenkov et al. for mixing coefficents within the range relevant for the ^{13}C-pocket ($D \lesssim 10^7 cm^2 s^{-1}$). The results are shown in Fig. 2.8. I used as default $D_2 = 10^{11} cm^2 s^{-1}$, consistently with the maximum mixing coefficient given by IGW according to De03, and $f_2 = 0.25$ (see also Tab. 2.1). The f_1 parameter affects only marginally the size of the ^{13}C-pocket, since in my models it defines the H profile below the TDU for $D \gg 10^7 cm^2 s^{-1}$. In general, by increasing (decreasing) f_1 the position of the ^{13}C-pocket is shifted downward (upward) in the He interhell layers. This parameter may affect instead the overall TDU efficiency, and thus the amount of C and s-process material dredged-up to the surface of the AGB star.

For this work, f_1 is equal to 0.014 by default, consistently with the explonential decay parameter used during the AGB interpulse phase in Pi13, while the impact of the D_2 and f_2 parameters on the size of the ^{13}C-pocket is analyzed. As an example, Fig. 2.9 and Fig. 2.10 show the ^{13}Cpocket size resulting from the model M2.z2m2 as a function of D_2 and f_2 after the 3rd and 5th TDU. In order to produce the results of this test, I recalculated the stellar structure from the end of the previous convective TP until the formation of the ^{13}C pocket. In these calculations, the parameter ranges $10^7 \lesssim D_2 \lesssim 10^{13}$ and $0.17 \lesssim f_2 \lesssim 0.29$ were explored. All the other stellar parameters were not changed. The typical ^{13}C-pocket size obtained by using the parameter setup by De03 is $\sim$ 7-8 $\times 10^{-5}$ $M_\odot$. The size of the ^{13}C-pocket tends to increase with the increasing of D_2 and f_2, up to a size of 1.5×10^{-4} $M_\odot$ with the largest D_2 and f_2 values in the figure. The colored area represents the range of f_2 still giving an acceptable fitting of the De03 calculations, and of D_2 assuming an uncertainty of one order of magnitude. the ^{13}Cpocket size that I obtain ranges from about 4×10^{-5} to $1.2 \times 10^{-4} M_\odot$. The impact of this uncertainty on the full AGB stellar simulations is studied in the models M2.z2m2.hCBM and M3.z1m2.hCBM, which are characterized by $D_2 = 10^{12} cm^2 s^{-1}$ and
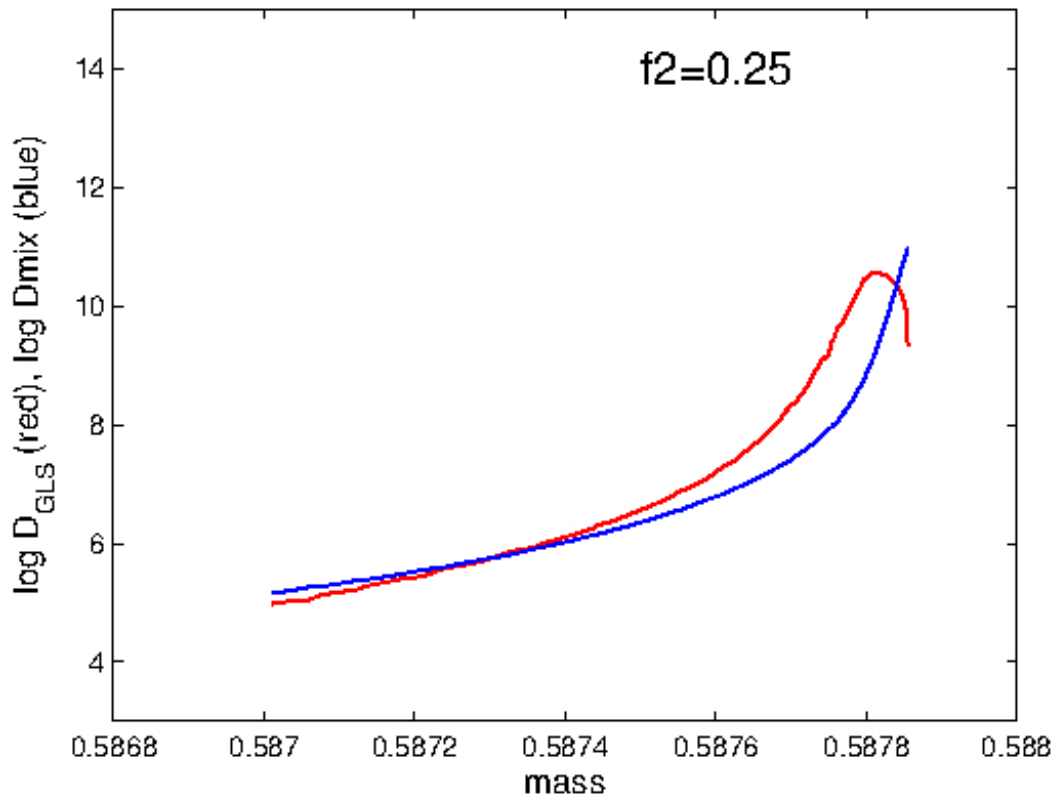
Fig. 2.8 Comparison between the internal gravity waves mixing coefficient profile derived by Denissenkov and Tout [45] (red line) and the CBM profile derived with the parameterization used in this work (blue line).

f_2=0.27. The same investigation has been performed at the 3rd TDU of the same model, giving consistent results. As an example, in Fig. 2.11 three snapshots of the abundance profiles of indicative species from model M3.z2m2 are reported, showing the maximum penetration of H in the He intershell during the 5th TDU (upper panel). After the TDU, a finite amount of H has diffused into the C-rich intershell, triggering the nuclear reaction chain ^{12}C(p,γ)^{13}N(β+)^{13}C leading to the ^{13}C -pocket full formation. At this point, neutrons produced by ^{13}C(α,n)^{16}O start to be released and captured by ^{56}Fe (refer to the plot to see how this starts to be depleted) and other Fe-peak isotopes, producing s-process species. Finally, the ^{13}C-pocket is totally consumed in the bottom panel, close to the end of the AGB interpulse period. From the top to the middle panel about 10^3 years have passed, while it takes around 10^4 years to reach the stage shown in the bottom panel. The following convective TP will mix the s-process products in the He intershell.
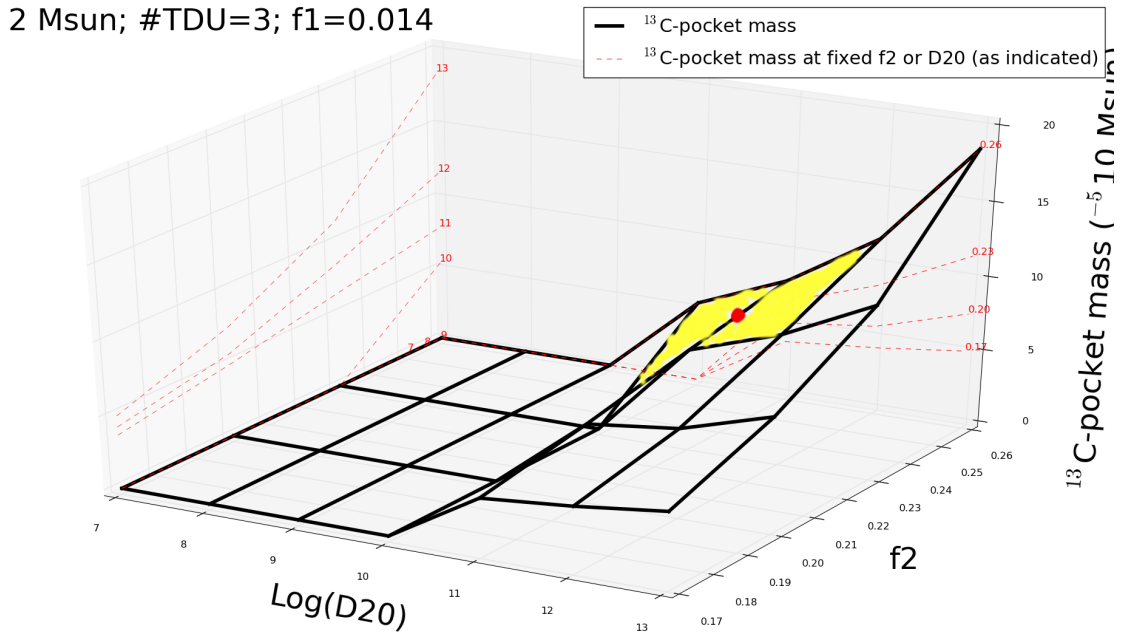
Fig. 2.9 ^{13}C-pocket size as a function of the CBM parameters associated with the 3rd TDU event. The red dot represents the tipical ^{13}C-pocket size obtained with our stellar models. The yellow area is the typical uncertainty that still affects its value.

2.5.3   AGB stellar models: summary of their main features

In the previous two sections, the CBM setup used to calculate the AGB stellar structures listed in Tab. 2.1 has been discussed. The main properties of these AGB models are
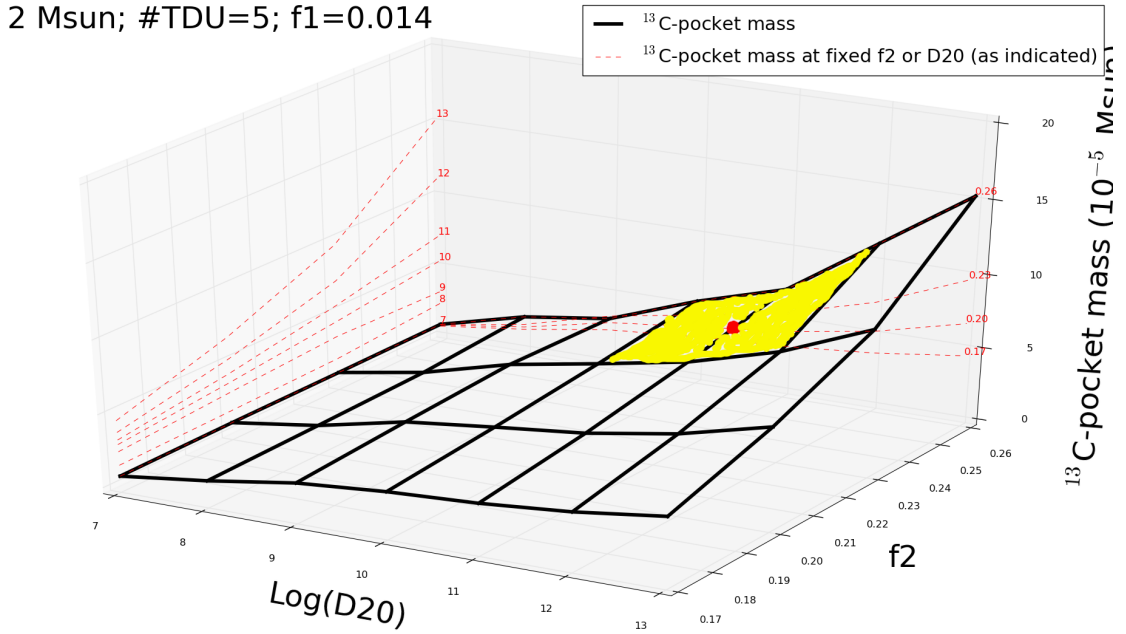
Fig. 2.10 Same kind of plot as in the previous figure, but for the 5th TDU.

summarized in Tab. 2.2 and A.2. In Fig. 2.12, top panel, we show the evolution of the C/O ratio at the stellar surface during the AGB evolution. The surface C/O ratio evolves similarly considering each model and its analogous He07 model. In particular, the He07 models show a C/O ratio lower by about 0.2, which corresponds to an avarage departure of 10% and is mostly due to a lower λ_{DUP} dredge-up parameter during the AGB phase. This latter parameter is shown in the middle panel and is defined as:

$$\lambda = \frac{\Delta M_{DUP}}{\Delta M_H} \tag{2.14}$$

where ΔM_H is the growth of the H-free core after each TP and ΔM_{DUP} is the dredged up mass. As expected, we obtain more efficient TDUs (i.e., higher λ_{DUP}) as the initial metallicity decreases [e.g., 121]. In the lower panel, the temperature at the bottom of the convective envelope at the deepest extent of TDU (T_{CEB}) is presented. The larger temperatures at the last TDUs for models with Z=0.02 compared to the models at Z=0.01 are due to the inverse correlation between the largest temperature at the bottom of the He-flash convective zone (T_{FBOT}) and T_{CEB}: the higher the TP luminosity, the more the He intershell will expand causing colder TDUs (T_{CEB} and T_{FBOT} for all the AGB models and all the TPs are provided in Tab. A.2). We also confirm the strong dependence of the interpulse period on the core-mass as already discussed by Paczynski [157]. This is obtained not only along the evolution of single
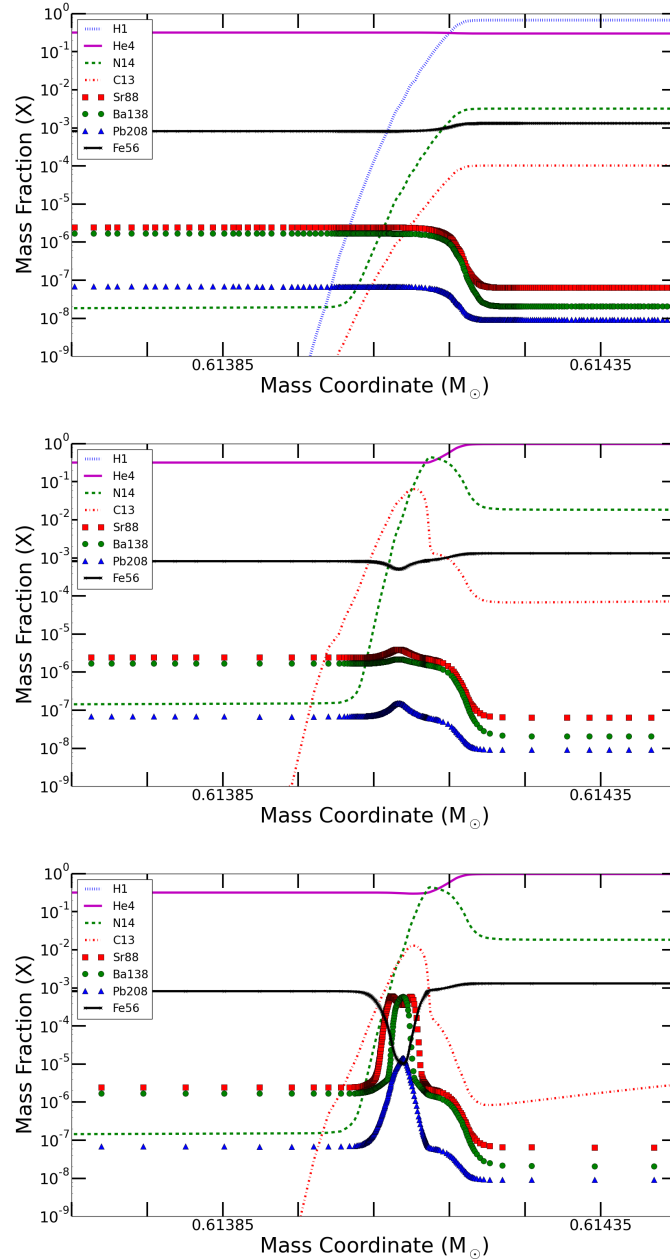
Fig. 2.11 Three different steps of ^{13}C-evolution in M3.Z2m2 are presented. The abundances of H, ^{4}He, ^{16}O, ^{13}C and ^{14}N are shown, together with the main Fe-seeds, ^{56}Fe and the heavy s-process isotopes of the different neutron magic peaks N=50 (^{88}Sr), N=82 (^{138}Ba) and N=126 (^{208}Pb). The top panel refers to the moment of maximum penetration of the TDU, which is followed by the radiative burning of the ^{13}C-pocket with the consequent neutron release and s-nuclei synthesis (middle and bottom panel).

models, but also from the comparison of the results between different models. The envelope mass is not important in this sense, since our 3 $M_\odot$ models have almost the same interpulse period of our 2 $M_\odot$ models when core masses are similar. The extension of the different thermal pulse episodes reflects the intershell thickness instead, being larger in the 2 $M_\odot$ models and smaller in the 3 $M_\odot$ ones as expected. Finally, all my models experience a large mass-loss increase as the star becomes C-rich, as a consequence of the higher opacities in such regime and of a higher bloecker-wind coefficient adopted during this phase as already discussed in section 2.2.1. In particular, a super-wind regime occurs after the last TDU event of each model, leading to the loss of an envelope mass ranging from about 0.7 to 1 $M_\odot$ and finally leaving the degenerate CO core surrounded by the He-intershell. In order to simulate the last TPs, the opacity is modified to prevent convergence problems related to the Fe opacity peak at the bottom of the envelope. Indeed, when the star is approaching the end of the TP-AGB, close to stripping the envelope from the CO core, unstable pulsations are set up, due to the effect of the Fe-group opacity bump at temperatures around 2×10^5 K, in a zone right below the surface. This becomes apparent in the large and irregular variations of effective temperature and luminosity in the HR diagram. This effect was identified by Dziembowski and Pamiatnykh [50] to explain β Chepheids pulsations: the authors dermined that a typical solar metal content suffices to explain the pulsation. In order to get through this phase in my stellar models, I need to lower the opacity to prevent the Fe bump is effective [96, 122].

2.6 Post-processing nucleosynthesis calculations and comparison with observations

In this section I discuss the nucleosynthesis results of our AGB models, in comparison with observations and stellar yields from other authors. The abundances for all the isotopes up to Bi have been calculated using the post-processing tool mppnp(§2.3). In addition to the stellar models in Tab. 2.1, other post-processing calculations have been performed on the same stellar structures, but using different reaction rate networks. The complete list of these tests is given in Tab. A.1 (see Appendix). Specifically, we tested the impact of the ^{14}N(n,p)^{14}C reaction rate (models labeled with *ntest*, where the default rate is multiplied by a factor of two) and of the neutron capture cross section ^{95}Zr(n,γ)^{96}Zr (models labeled with *zrtest*, where the default rate has been reduced by a factor of two). The ^{14}N(n,p)^{14}C is the main neutron poison in the ^{13}C-pocket. While there are several experimental results beyond 20 keV [221, and references therein],
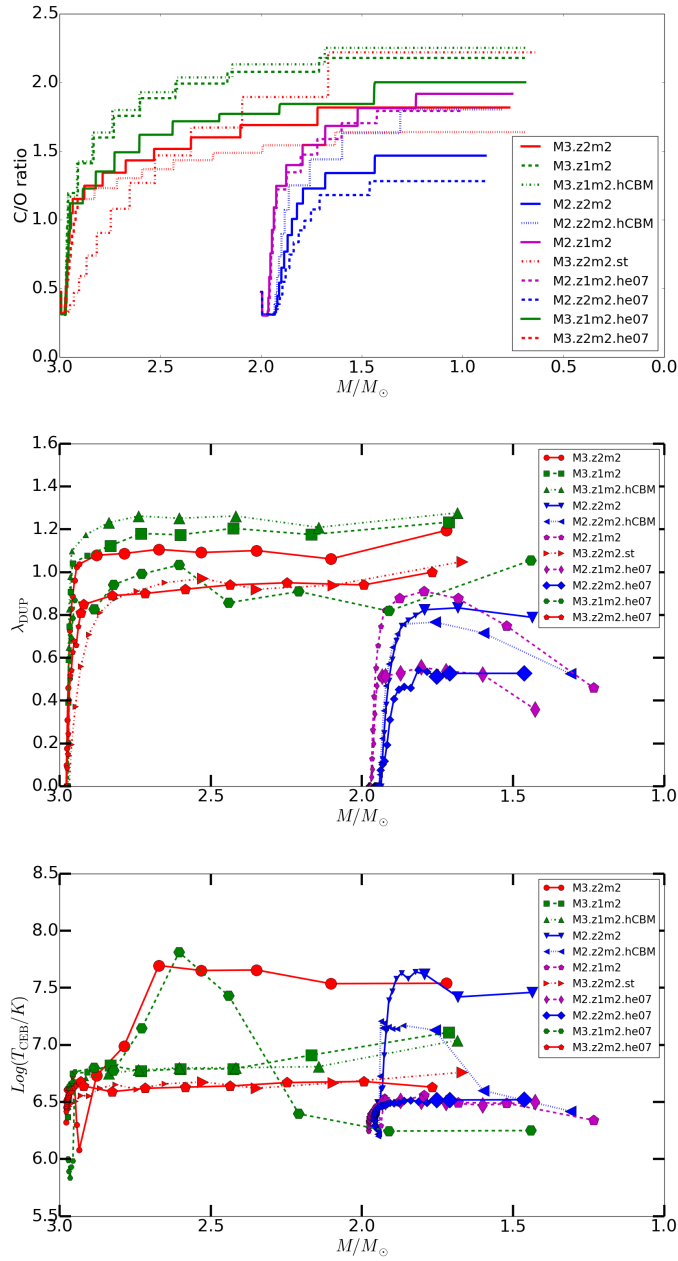
Fig. 2.12 Main stellar properties during the AGB phase. From top to bottom panel: C/O surface ratio, Dredge-Up Lambda parameter and Temperature at the bottom of the convective envelope during interpulse periods (in logarithmic scale). All those quantities are plotted against the total stellar mass.

there is only one available so far at energies ~ 8 keV, typical of the ^{13}C-pocket [111]. Beyond 20 keV, independent experiments gave rates changing within a factor of three. The Zr neutron capture cross sections have been updated by a number of works in the last years [135, 206, and references therein]. [135] provided a new evaluation of the ^{95}Zr(n,γ)^{96}Zr cross section based on the measurements on the neighboring Zr species. Its value is more than a factor of two lower compared to older rates [e.g., 15]. This rate is crucial for the s-process branching point at ^{95}Zr, leading to the production of ^{96}Zr. Zr isotopic ratios are observed in presolar SiC mainstream grains from AGB stars [16, 129], and provide an important diagnostic for the thermodynamics conditions at the bottom of convective TPs [e.g., 133]. Therefore, we have tested the impact of this reaction on the s-process Zr products by reducing its rate by a factor of two. The uncertainties of other reaction rates crucial for s-process nucleosynthesis in AGB stars, among which the ^{22}Ne(α,n)^{25}Mg, were not considered in this work. We refer to other works for details [e.g., 59, 105, 130, 167].

In §2.5.1 we defined the new CBM parameterization adopted at the boundaries of the He intershell to calculate the AGB stellar structures discussed here. We have already seen from Fig. 2.12 that all the AGB models become C rich before the end of the AGB phase, with final $1.4 \lesssim$ C/O $\lesssim 2.4$. In this section the s-process production in our AGB models is discussed. In Fig. 2.13 and 2.14, the evolution of the s-process indexes during the AGB evolution [131] are shown, where [ls/Fe] is representative of the surface abundance of s-process elements at the neutron shell closure N=50 (ls elements = Sr, Y, Zr), and [hs/Fe] of the elements at N=82 (hs elements = Ba, La, Nd, Sm). The ratio [hs/ls] is given by the relative s-process production at the two s-process neutron-magic peaks, independently from the absolute production of these elements [e.g., 29]. Compared to the model Pi13.newnet for a star with the same mass and metallicity (M = 3M$_\odot$, Z=0.02), the production is more efficient by 0.3-0.4 dex at the two s-process peak elements. This is due to the different CBM prescription used below the TDU compared to Pi13: the IGW parameterization allows to form ^{13}C pockets that are a factor of 3-5 larger compared to the overshooting CBM prescription used by Pi13. On the other hand, the two models have comparable concentrations of He, C and O in the He intershell (see §2.6.1). As a consequence, the [hs/ls] ratios are consistent within ~ 0.05 dex. The model M3.z1m2 and the associated test cases show a stronger s-process enrichment compared to the models with M=2M$_\odot$ and/or with higher metallicity. In particular, [ls/Fe] ~ 0.7 for M3.z1m2.hCBM.ntest, and [hs/Fe] ~ 0.95 for M3.z1m2 and M3.z1m2.hCBM.ntest.

From a comparison between each model and its analogue with He07 CBM (see Tab. 2.1), it can be seen that the results are consistent within 0.1 dex. This is because the set of AGB models he07 and the analogous models with no clipping but higher f_1 share enhanced C and O abundances in the He intershell (see discussion in §2.4 and 2.5.1). Therefore, our s-process results are not strongly affected by using these two different setups.

Most of the models show a final [hs/ls] > 0, with the exception of the models M2.z2m2.hCBM and M2.z2m2.hCBM.ntest, where [hs/ls] = -0.1 and -0.25 respectively. The models with more efficient IGW CBM are expected to host ^{13}C-pockets on average 50-70% larger compared to the default case. The consequent s-process enrichment in the AGB star envelope increases by $\lesssim 0.2$ dex for ls elements, while is quite comparable for hs elements (Fig. 2.14). In general, a larger ^{13}C-pocket allows to have a smoother decline of ^{13}C, and thus to produce lighter elements more efficiently and, consequently, lower [hs/ls] ratios. Therefore, while the total amount of s-process elements dredged-up in the AGB envelope is not drastically affected, the uncertainties associated with the IGW CBM setup in my models are affecting the relative production at the Sr peak with respect to the Ba peak. According to the discussion in §2.5.1, the parameters D_2 (i.e. the point where the IGW mixing efficiency dominates CBM) and f_2 need to be constrained by future hydrodynamics simulations with an uncertainty much lower than what was considered here. In Fig. 2.14, we also show the cases labeled as *reference_model.ntest*, where the only difference with respect to their reference models is the ^{14}N(n,p)^{14}C rate multiplied by a factor of two (Tab. A.1). By changing the ^{14}N(n,p)^{14}C rate, the impact is comparable to the uncertainties due to the IGW CBM setup: for the default models the rate increase reduces the [hs/ls] by about 0.05 dex, while for hCBM models the [hs/ls] ratio is reduced by 0.1 dex. In general, this is due to the poisoning effect of the rate, which reduces the neutron exposure and favors the production at the Sr peak in comparison to the models that use the lower rate. While the errors given by [111] are much lower than a factor of two, the large departure among different experiments at energies larger than 20 keV requires further experimental analysis. An accurate determination of the ^{14}N(n,p)^{14}C cross section at ~ 8 keV would allow to constrain more efficiently the physics mechanisms driving the formation of the ^{13}C pocket.

In the Appendix, we provide two more tables comparing our 2 and 3 $M_\odot$ models, Cristallo et al. [38] and [103] for the stellar yields. The yields values of C and O in Cristallo et al. [38] are visibly much lower than what we obtain, as a consequence of the absence of CBM under the PDCZ in their models.
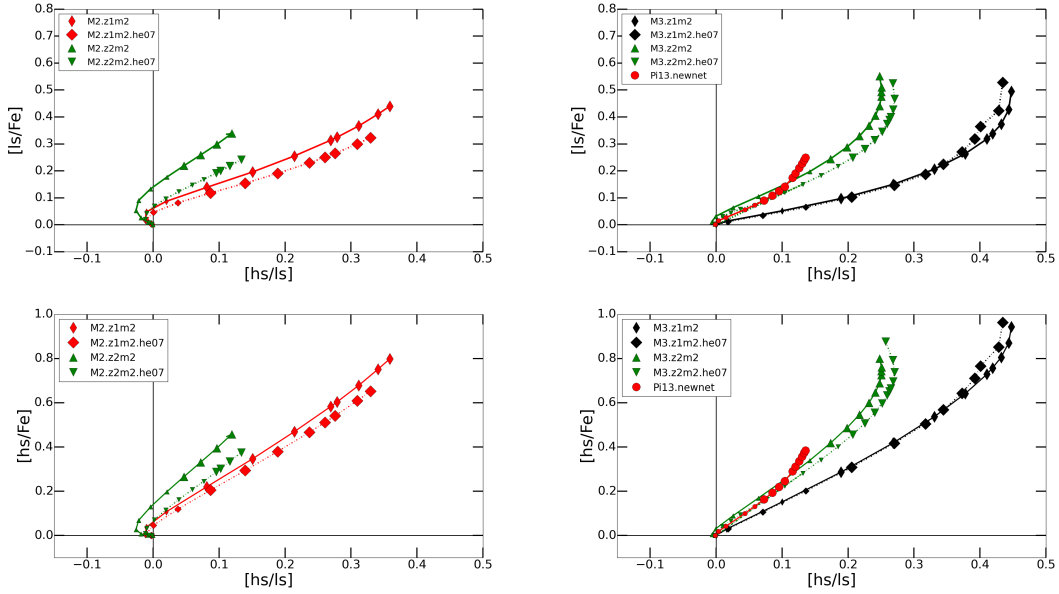
Fig. 2.13 The evolution of the [ls/Fe], [hs/Fe] and [hs/ls] ratios during the AGB evolution are shown for the models M2.z1m2, M2.z2m2, M2.z1m2.he07 and M2.z2m2.he07 (left panels) and PI13.newnet, M3.z1m2 and M3.z2m2, M3.z1m2.he07 and M3.z2m2.he07 (right panel). Each TDU event is indicated with small symbols for C/O < 1 in the AGB envelope, and with large symbols for C/O > 1.Also the observational data from Abia et al. [2] and Zamora et al. [235] are shown for comparison.
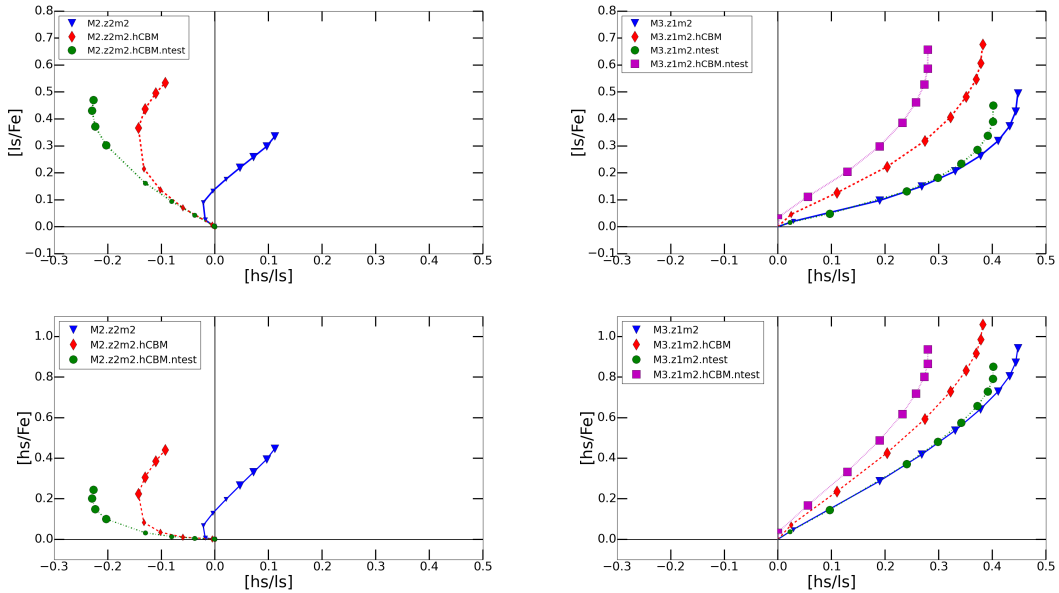
Fig. 2.14 As in Fig. 2.13, but the abundances obtained in reference model M2.z2m2 are compared with the models M2.z2m2.hCBM and M2.z2m2.hCBM.ntest; the results of the model M3.z1m2 are compared with the models M3.z1m2.ntest, M3.z1m2.hCBM and M3.z1m2.hCBM.ntest.

2.6.1   Comparison with spectroscopic observations of post-AGB H-deficient stars and planetary nebulae

About 10% of the AGB stars will experience a Late Thermal Pulse or Very Late Thermal Pulse event during their post-AGB evolution, becoming H-deficient stars [e.g., 73, 144]. Examples are the Sakurai's object [e.g., 77, and references therein], and the Fg Sagittae [61]. The observation of the surface abundances of stars like the PG1159 objects reveals the He-intershell abundances at late AGB stages, where the amount of the most abundant elements He, C and O are relics of the AGB stellar evolution phase. Therefore, they can be used as diagnostics for CBM during this earlier phase [e.g., 225, 226]. The observed range of abundances in mass fractions are $0.3 < \text{He} < 0.85$, $0.15 < \text{C} < 0.6$ and $0.02 < \text{O} < 0.20$. The CBM below the convective TPs allows to cover this range of abundances and the largest observed concentrations for C and O, independently on whether the physics mechanism driving the CBM is overshooting [e.g., 74] or Kelvin-Helmotz instabilities (this work). [123] partially reproduced the observed C and O enrichment in the He intershell, with a maximum O concentration of 5.9%, by including semi-convection in their calculations. While the observation of C and O in H-deficient stars is affected by relevant uncertainties [e.g., 13, 60], there are no controversial observations questioning the large spread of C and O abundances in post-AGB H-deficient stars, and the largest C and O enrichments that are observed. In Fig. 2.15, upper panel, the abundances of He, C and O are shown in the He intershell after each TP for models M2.z2m2, M3.z2m2, M2.z1m2 and M3.z1m2. The final C and O abundances are 0.4-0.5 and 0.2-0.1, respectively. Moreover, the linear dependence between O mass fraction and the adopted f_1 is confirmed. As a comparison, in Fig. 2.15, lower panel, we also report the abundances observed for PG1159 stars [225], which are consistent with the predicted He-intershell abundances shown in the upper panel. Along the post-AGB evolutionary phase, planetary nebulae (PNe) are still carriers of the abundance signature of the previous AGB phase [220, and references therein]. The abundances of elements such as O, Cl, Ar have been used in order to identify the initial metallicity of the PNe progenitor, assuming that their initial concentrations are not affected by AGB nucleosynthesis. However, evidence for O enrichment has been found first for PNe at low metallicity [e.g., 161], and lately for PNe with metallicities close to solar [44, 188]. In particular, [44] confirmed that the O enrichment calculated for AGB models including CBM at the bottom of the convective TP by Pi13 are compatible with observations for PNe with solar-like metallicity. Consistently with post-AGB H-deficient stars, this is another independent observational confirmation that CBM should be included during the AGB phase. On the other hand, stellar AGB models with

large C and O concentrations in the He intershell, typically yield s-process abundances with [hs/ls] larger compared to models without CBM [e.g., 22, 38]. In the past this has been considered a conundrum for AGB stellar evolution and nucleosynthesis. This point will be discussed later in this section. Furthermore, it is known that the ^{22}Ne$(\alpha,n)^{25}$Mg tends to be more efficient in models with CBM, causing a higher neutron capture efficiency at s-process branching points, among others at ^{95}Zr [e.g., 133]. Later in this section we will see that this point is controversial at the moment, and that for AGB models with initial mass M ≤ 2M$_\odot$ and with CBM at the bottom of the convective TPs the ^{22}Ne$(\alpha,n)^{25}$Mg does not efficiently activate the neutron-capture channel at the ^{95}Zr branching.

2.6.2   Comparison with spectroscopic data from AGB stars

In Fig. 2.17, the [hs/ls] ratios obtained from my models are compared with spectroscopic observations of galactic AGB stars [2, 235]. The results for the stellar models with the same initial mass from the FRUITY database are also shown [38]. The different [Fe/H] between the two theoretical data sets is due to the different reference solar metals distriburion adopted. In my models, CBM is considered below the convective TP, while this is not the case for the models in the FRUITY database. This implies that we obtain concentrations of ^{12}C in the He intershell up to a factor of two larger compared to models without CBM. As explained by [133], this causes a higher abundance of ^{13}C in the ^{13}C pocket and, as a consequence, a larger neutron exposure yielding a more efficient production of heavier s-process elements. This is the reason why my models tend to show a systematic larger [hs/ls] compared to AGB calculations by [38], and in general compared to all models without CBM [e.g., 21, 135]. Note that it is not only the CBM below the convective TP to define the evolution of the [hs/ls] ratio at the surface of the AGB star. Indeed, the s-process nucleosynthesis is affected by the complex interplay between CBM at both the two He intershell boundaries, and the selection of the nuclear reaction rates. In Fig. 2.14, we have shown that a different IGW CBM setup below the TDU combined with the uncertainty of the ^{14}N$(n,p)^{14}$C rate might reduce of up to ∼0.3 dex the final [hs/ls] ratio. In §?? we have quantified for the first time the effect of molecular diffusion, where with our present implementation the [hs/ls] is only marginally affected. On the other hand, the models shown in Fig. 2.17 do not include other relevant physics mechanisms such as rotation and magnetic field. For instance, [164] have recently shown that by considering rotation in AGB models the final [hs/ls] ratio tends to be reduced, compared to non-rotating models. Overall,
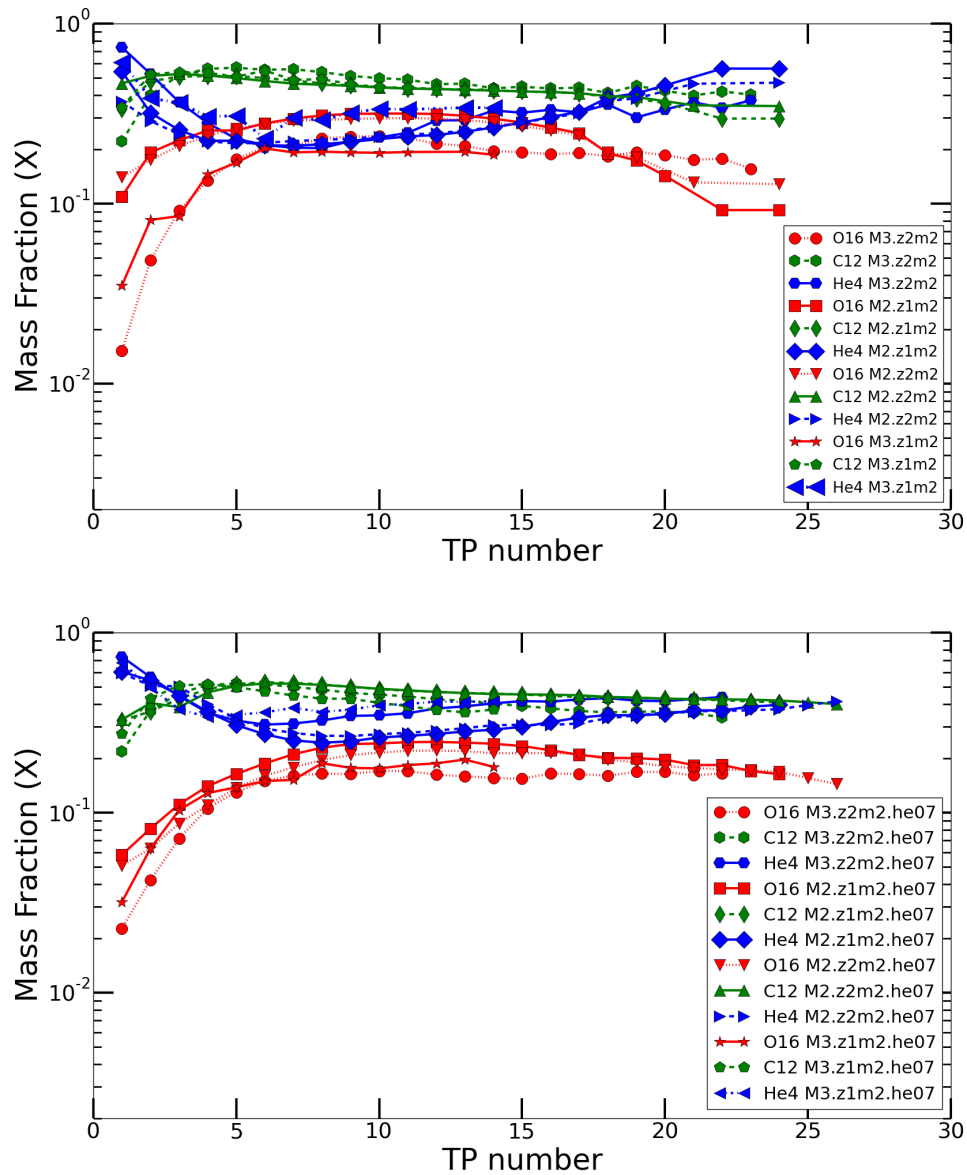
Fig. 2.15 He, C and O abundances evolution in the He Intershell as a function of the TP number along the AGB evolution for the AGB models M3.z2m2, M3.z1m2, M2.z2m2 and M2.z1m2 (upper panel), and for M3.z2m2.he07, M3.z1m2.he07, M2.z2m2.he07 and M2.z1m2.he07 (lower panel).
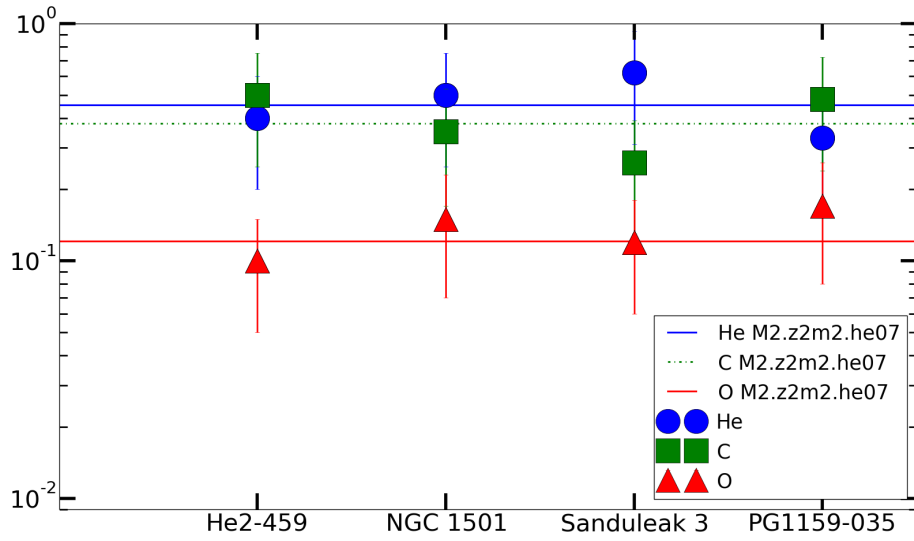
Fig. 2.16 He, C and O abundances observed for a sample of H-deficient post-AGB stars classified as PG1159 objects: He2-459, NGC1501, Sanduleak3 and PG1159-035. Observations are given by [225].Also the final intershell abundances from M2.z2m2.he07 are presented

both the two sets of models in Fig. 2.17 are consistent with observations. This is also due to the large observational uncertainties (reported in the figure).

In Fig. 2.18, my models are compared with spectroscopic observations for the [Rb/Fe] and the [s/Fe] ratio, given by the average production at the ls and hs s-process neutron-magic peaks. The [s/Fe] ratio is a diagnostic tool for the s-process efficiency, while the [Rb/Fe] ratio increases with the increasing of the efficiency of the ^{22}Ne $(\alpha,n)^{25}$Mg reaction during the TP [e.g., 117]. In particular, Rb is not made efficiently at neutron densities typical of the ^{13}C pocket, while at the high neutron densities during the TP the nucleosynthesis flow ^{84}Kr(n,γ)^{85}Kr(n,γ)^{86}Kr(n,γ)^{87}Kr(β^-)^{87}Rb allows to accumulate ^{87}Rb. In these conditions, ^{87}Rb is made more efficiently than ^{85}Rb and the s-process production of Rb is higher, because of the lower neutron capture cross section of ^{87}Rb compared to ^{85}Rb [e.g., 1]. As for Fig. 2.17, in Fig. 2.18 observational uncertainties pose a serious limitation to the diagnostic power of these observed abundance ratios. A large observational scatter is obtained for s-process and Rb enrichment. On the other hand, it needs to be clarified whether such a scatter is just due to uncertainties, or if, instead, it traces a real spread of s-process nucleosynthesis conditions in the He intershell of AGB stars. In my models, the [s/Fe] ratio changes
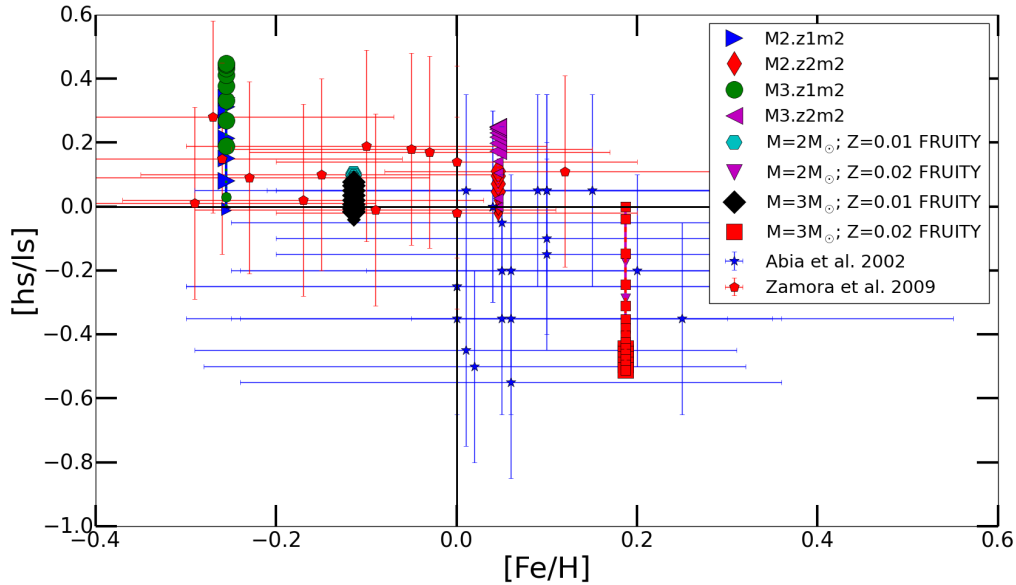
Fig. 2.17 Comparison of the [hs/ls] vs [Fe/H] obtained from my models with the distribution of observational data from Abia et al. [2] and Zamora et al. [235], including my models and F.R.U.I.T.Y. results.

between ~ 0.4 dex (M2.z2m2) and 0.8 dex (M3.z1m2.hCBM). They all show quite similar theoretical curves in Fig. 2.18, consistent also with results from the FRUITY models at Z=0.02. Yet, the s-process abundance evolution for the models at Z=0.01 by [38] shows a larger [s/Fe] up to [s/Fe]$\sim$1.3 dex, with a production of Rb comparable with the models at higher metallicity.

Moreover, as already observed from Fig. 2.13, we obtain again a visible similarity between each model and its He07 analogue.

The model Pi13.newnet has a final [s/Fe] ~ 0.3 and [Rb/Fe] ~ 0.1. As we mentioned in the previous sections, the IGW CMB allowed to obtain larger ^{13}C pockets compared to PI13, causing a higher s-process enrichment of the AGB star surface. As it is possible to see from Fig. 2.18, within the observational and stellar uncertainties these models can reproduce the observed range of [s/Fe]. Therefore, IGW provide a suitable mechanism to drive the CBM below the TDU, leading to the formation of the radiative ^{13}C pocket. Of couse this is not a definitive result. Multidimensional hydrodynamics simulations are required to constrain IGW efficiency in these conditions and to provide a consistent set of CBM parameters to include in one-dimensional AGB models.
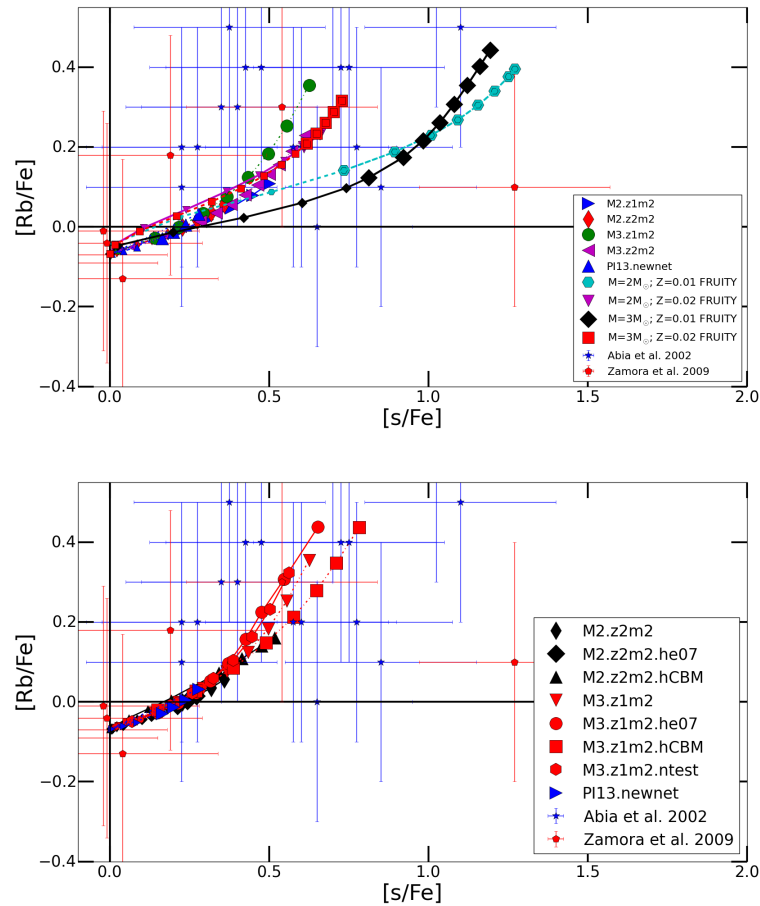
Fig. 2.18 Upper panel: [Rb/Fe] vs [*s*/Fe] of a sample of C stars by Abia et al. [2] and Zamora et al. [235]. Only stars with [Fe/H] >-0.3 were considered. My models and F.R.U.I.T.Y. database [38] results included. Lower panel: Test of the CBM impact on our results. In particular, considering model M3.z1m2 it turns out that a higher CBM efficiency during TDU allows to reproduce the abundances of *s*-process and Rb-rich stars inside the observational uncertainties.

2.6.3 Comparison with presolar-grains data

Different types of dust of presolar origin are found in primitive Caceous meteorites. Their isotopic abundance signatures are anomalous compared to solar material. Today we know that they were made in stars before the formation of the Sun, by different stellar sources. Their astrophysical relevance is due to the fact that they are pieces of old stars, and they still carry the peculiar abundance signatures of the stellar environments where they were forged [236]. The major stellar sources of presolar C-rich grains are core-collapse supernovae and AGB stars: nano-diamonds [4, 126, 156], SiC grains of type X [e.g., 18, 127] and of Type C [82, 170], and low-density (LD) graphite grains [e.g., 5] were made by core-collapse supernovae, while AGB stars are the astrophysical source of SiC grains of type mainstream [125, 132, 155] and of high-density (HD) graphite grains [e.g., 81, 93]. Other types of presolar C-rich grains are SiC classified as nova grains that are made in Novae and core-collapse supernovae [148] and SiC grains of Type AB, which may have many different stellar sources [6, 190]. Mainstream SiC grains are the most abundant type of presolar SiC grains [more than 90% 236]. They condensed in the envelope of C-rich AGB stars and were ejected into the surrounding interstellar medium by stellar winds. The condition to form in a C-rich environment (i.e., C/O>1) is crucial for the formation of C-rich grains. Thanks to high-precision laboratory measurements of their isotopic composition for heavy elements like Sr, Zr and Ba, it is possible to derive fundamental constraints about their parent AGB stars. In particular, theoretical stellar simulations can be compared with the inferred conditions in the He intershell, where the s-process is activated in AGB stars [e.g., 14, 16, 128–130, 133, 135]. In this section, the results of our stellar calculations are compared with measurements of isotopic abundances in mainstream SiC grains for Zr and Ba. Recently, [130] and [135] have reconsidered the measurements of Zr in mainstream SiC grains by [16]. The measured ^{96}Zr/^{94}Zr ratio in SiC grains is known to be a diagnostic for the activation of the ^{22}Ne$(\alpha,n)^{25}$Mg neutron source at the bottom of the convective TPs. This is due to the s-process branching point at ^{95}Zr, which needs high neutron densities to produce ^{96}Zr via direct neutron capture on ^{95}Zr [133]. [135] identified a positive correlation between the ^{92}Zr/^{94}Zr and ^{29}Si/^{28}Si ratios, suggesting that the observed spread of ^{92}Zr/^{94}Zr is a signature of the initial metallicity of the AGB progenitor. Furthermore, [130] suggested that this ratio can be used to constrain the internal structure of the ^{13}C-pocket. The same methodology is adopted by [128] by using new measurements for Sr and Ba. In particular, the comparison of AGB calculations with new measured ^{88}Sr/^{86}Sr and ^{138}Ba/^{136}Ba ratios is used to derive information about the size and ^{13}C concentrations in the ^{13}C-pocket. In Tab. A.3 the

final isotopic ratios obtained in the He intershell and in the AGB envelope are shown for our AGB models. In Fig. 2.19 and 2.20 the evolution of the Zr abundances at the stellar surface during the AGB evolution are shown. In Fig. 2.19, the models cover a large range of ^{96}Zr/^{94}Zr ratios, with $200 \gtrsim \delta(^{96}$Zr/^{94}Zr$)\gtrsim$-600. The physical factors with the largest impact on this quantity are the temperature at the bottom of the PDCZ, which is correlated to the CBM description at the bottom of such zone, and the neutron-capture reaction rates on Zirconium isotopes. Compared to Pi13 and the results by [132] obtained for AGB models including CBM at the bottom of the convective TPs, the negative δ values are mostly due to the new ^{95}Zr MACS by [135] (see also Fig.2.4). My models reproduce the observed scatter of $\delta(^{90}$Zr/^{94}Zr), while a relevant fraction of grains with low $\delta(^{91}$Zr/^{94}Zr) and $\delta(^{92}$Zr/^{94}Zr) ratios are not reproduced. As discussed by [130], Zr isotopic ratios can be used to test size and properties of the ^{13}C pocket. In my models, the ^{13}C pocket is made after each TDU consistently with the IGW CBM adopted to calculate the stellar structure, while the IGW CBM implementation is made by a simple fitting of the [45] simulations. This allows to provide a good indication of the size of the ^{13}C pocket due to IGW CBM, but the detailed shape needs to be constrained by hydrodynamics simulations. Furthermore, rotation and magnetic field are two fundamental pieces of physics still missing in my models, that will affect the ^{13}C pocket properties after its formation [for rotation, see 76, 164], and eventually the s-process Zr isotopic ratios [128]. Therefore, a crucial step forward to challenge the scenario where IGW CBM is the physics mechanism responsible for the formation of the ^{13}C pocket, will be to calculate how the pocket is modified by rotation and magnetic field during the s-process production.

Grains with $\delta(^{96}$Zr/^{94}Zr)<-900 are not reproduced by baseline AGB models [130, 135]. The models shown in Fig. 2.19 confirm the increasing trend of the ^{96}Zr/^{94}Zr ratio with the increase of the initial mass and with the decrease of the initial metallicity [130, 133, 135]. However, my AGB models cannot reproduce grains with $\delta(^{96}$Zr/^{94}Zr)<-600. Fig. 2.20 shows the impact of the ^{95}Zr(n,γ)^{96}Zr neutron capture cross section on our results. The cross section provided by [135] was reduced by a factor of two. In general, the use of the reduced rate allows to decrease the final ^{96}Zr/^{94}Zr ratio by $\delta \sim$200. Therefore, while the new ^{95}Zr(n,γ)^{96}Zr cross section helps to alleviate the overproduction of ^{96}Zr compared to ^{94}Zr, the observed range is not reproduced. From the nuclear physics point of view, the other reaction rate relevant for the ^{95}Zr branching is the rate of the neutron source ^{22}Ne(α,n)^{25}Mg. Once the combined uncertainties of the ^{95}Zr(n,γ)^{96}Zr and ^{22}Ne(α,n)^{25}Mg rates will be reduced by nuclear experiments, the ^{96}Zr/^{94}Zr will be a crucial diagnostic to constrain our simulations. From Fig. 2.19
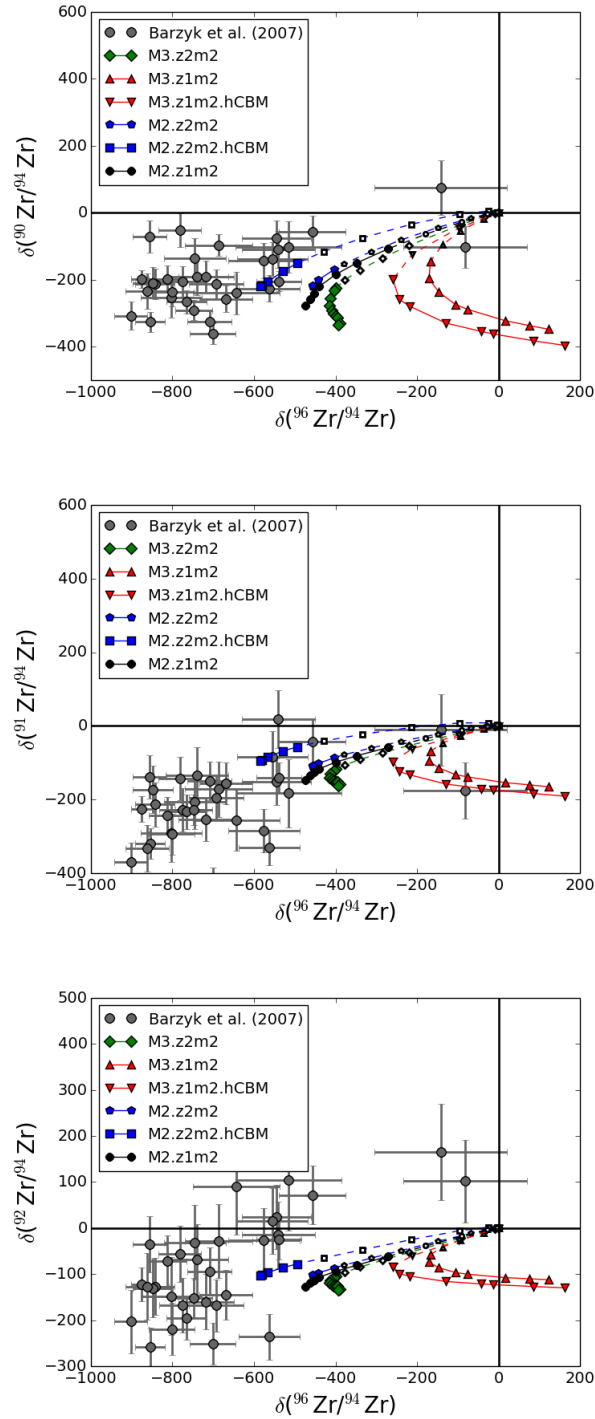
Fig. 2.19 Upper panel: $\delta(^{90}\text{Zr}/^{94}\text{Zr})$ vs. $\delta(^{96}\text{Zr}/^{94}\text{Zr})$ for the same models in figure 2.13 but also including the M2.z2m2.hCBM and M3.z1m2.hCBM to check the CBM impact. Middle panel: $\delta(^{91}\text{Zr}/^{94}\text{Zr})$ vs. $\delta(^{96}\text{Zr}/^{94}\text{Zr})$ for the same models in the upper panel. Lower panel: $\delta(^{92}\text{Zr}/^{94}\text{Zr})$ vs. $\delta(^{96}\text{Zr}/^{94}\text{Zr})$ again for the same models. In all these plots is visible how difficult is to reproduce observational data from grains with low $\delta(^{96}\text{Zr}/^{94}\text{Zr})$, even if a higher CBM efficiency during TDU seems to help as this is translated in a higher ^{94}Zr production.
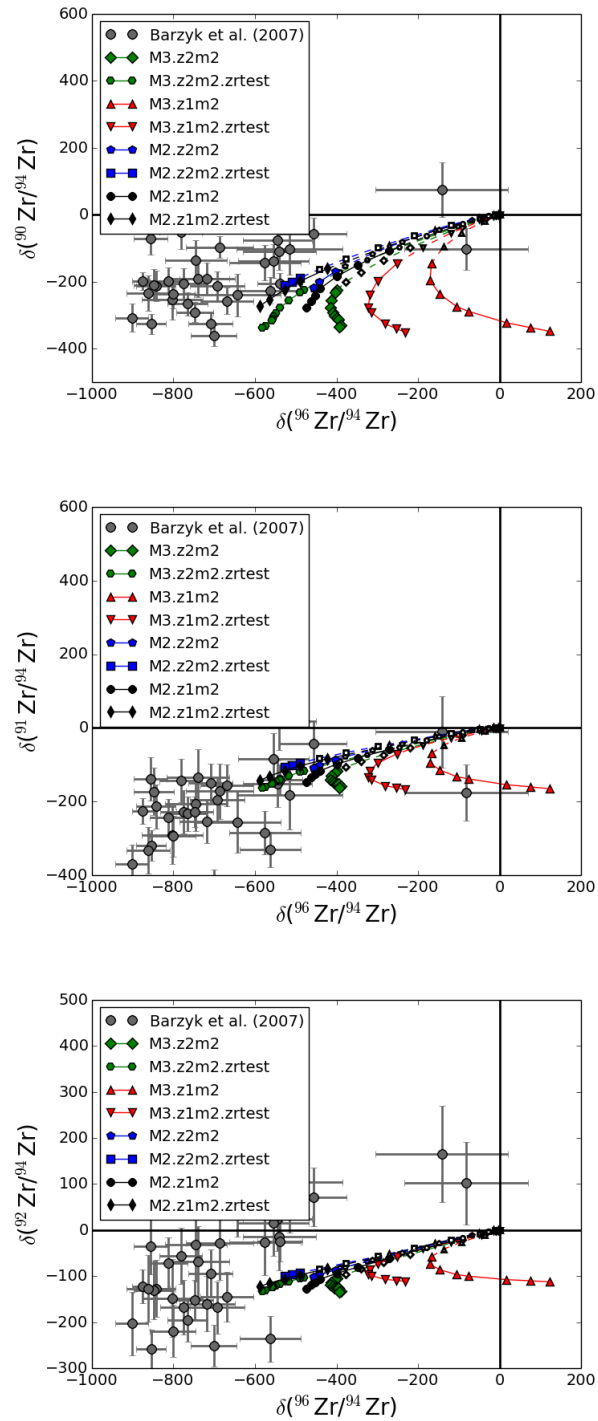
Fig. 2.20 Same kind of panels as in figure 2.19, but here showing the impact of ^{95}Zr(n,γ)^{96}Zr reaction rate. In particular we show what results dividing the reaction rate by a factor of two. It's noticeable the impact of the rate uncertainty that, together with the CBM one, can explain the SiC presolar grains here plotted.
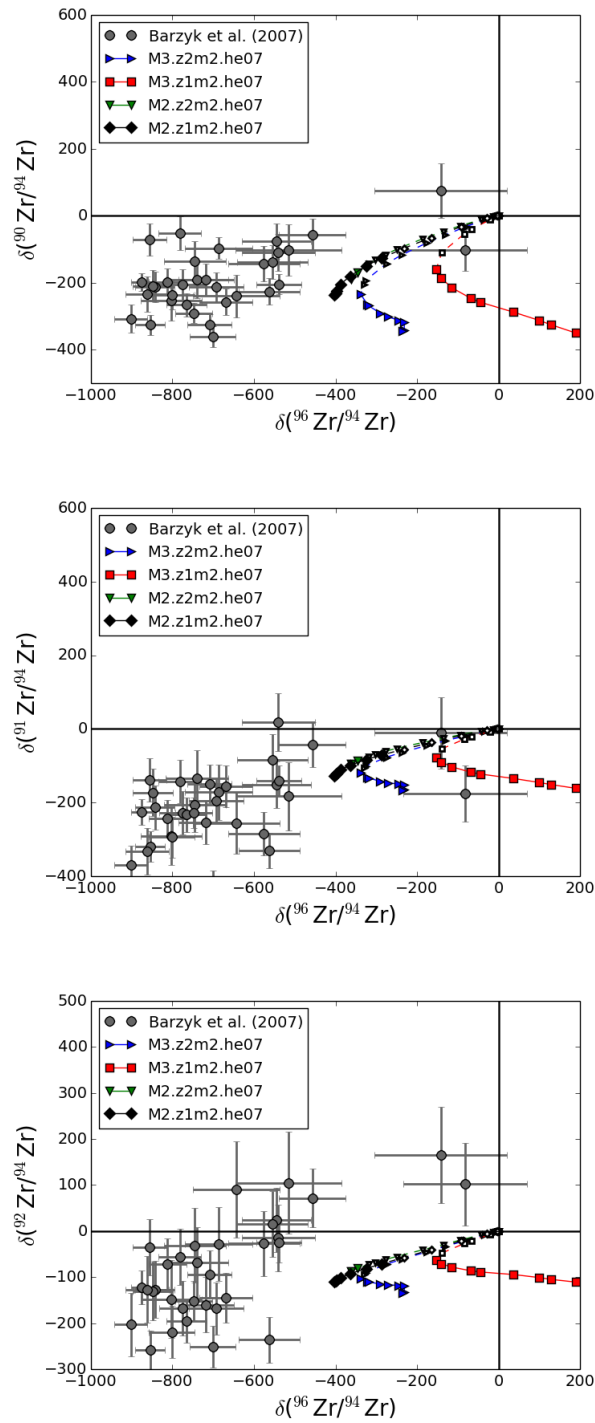
Fig. 2.21 As in figure 2.19, but the results are shown for the models calculated with the Herwig et al. [75] CBM prescriptions.

and Fig. 2.20, it appears that the impact of ^{95}Zr(n,γ)^{96}Zr is comparable with the variations between models M2.z2m2 and M2.z2m2.hCBM. These two models carry the impact of the uncertainty associated to the IGW CMB implementation in my models. This is due to the fact that model M2.z2m2.hCBM tends to have ^{13}C pockets larger than model M2.z2m2, changing the relative contribution to the total neutrons made from ^{13}C(α,n)^{16}O (producing ^{94}Zr but not ^{96}Zr) and from ^{22}Ne(α,n)^{25}Mg (eventually producing also ^{96}Zr). Furthermore, a larger s-process enrichment in the He intershell allows a more efficient pollution of the AGB envelope. Therefore, in my models the ^{13}C-pocket properties affect also the ^{96}Zr/^{94}Zr ratio. An additional aspect that deserves more discussion is the parameterization of the CBM at the bottom of the PDCZ. As mentioned in §2.5, He07 upper-limit parameter values were adopted in this work, with the f_1 value higher by more than a factor of 2. The same section also outlined the peculiar treatment of small convection zones made in our adopted `MESA` revision and in the following ones, in which the mixing length was forced to be smaller than the height of the zone, resulting in a less efficent CBM for the same CBM parameters. It is shown now how the CBM parameters with the `MESA` revision adopted in this work are consistent with the upper-limit values given in He07. First of all, the final He, C and O mass-fractions in the Intershell obtained with our M3.z2m2 model (48%, 31% and 13% respectively) are clearly comparable with the values obtained with the analogue model calculated without any forced-limit on mixing length and He07 upper-limit parameters (in this sections briefly referred to as 'He07 models'), i.e. 58%, 25% and 10%. These values can be compared with their analogous ones obtained by re-introducing the forced mixing-length limit, i.e. 55%, 29% and 6%. It should be noted in particular that O is the most sensitive element to such mixing-description. Moreover, each He07 model has the same number of TDU events, also considering the C-rich phase. The impact on δ(^{96}Zr/^{94}Zr) was also considered. As already said, this too depends on the CBM description at the bottom of the PDCZ. In general, the values from each model evolve in a similar way compared to its He07 analogous, also considering final values. The only exception can be identified comparing models M3.z2m2 and M3.z2m2.he07, where the final δ(^{96}Zr/^{94}Zr) values differ by more than 100. The Zr isotopic ratios for the He07 models are shown in Fig. 2.21, compared to the observed abundances in presolar grains.

From Tab. A.3, it appears that the final surface abundance for most of the models is quite representative of the He-intershell abundances, with the tendency to show a milder departure from the solar composition in the AGB envelope compared to the He intershell, due to the contribution from the pristine stellar composition. Concerning

the ^{96}Zr/^{94}Zr ratio, this trend is maintained for both positive and negative δ values. For instance, the model M3.z1m2.hCBM has final $\delta(^{96}$Zr/^{94}Zr) equal to +631 and +162 in the He intershell and in the AGB envelope, respectively. On the other hand, the model M2.z2m2.hCBM shows δ = -741 and -584. The model with the lowest δ values is M2.z1m2.zrtest, with -831 and -613. More efficient TDUs, or a larger number of them would have eventually allowed to reach lower final $\delta(^{96}$Zr/^{94}Zr) values.

If we look carefully at the theoretical evolution curves in Fig. 2.19 and 2.20, all the models with initial mass M=3 $M_\odot$ show a signature of efficient ^{96}Zr production due to the ^{22}Ne(α,n)^{25}Mg activation at the bottom of the convective TP, eventually leading to positive δ values. This picture is consistent with [133] and Pi13, where CBM at the bottom of the convective TPs makes the He intershell more He-poor, causing a stronger ^{22}Ne(α,n)^{25}Mg activation due to the larger temperatures compared to models without CBM. On the other hand, in our M=2 $M_\odot$ models the new ^{95}Zr(n,γ)^{96}Zr cross section strongly reduces the production of ^{96}Zr. Therefore, according to our simulations, AGB models with initial mass M$\lesssim$2 $M_\odot$ can have negative $\delta(^{96}$Zr/^{94}Zr)and, at the same time, C and O concentrations in the He intershell consistent with post-AGB stars and planetary nebula observations. However, for the 2 $M_\odot$stellar models the degree of pollution of the AGB envelope with He-intershell material seems to be not high enough to explain the abundances for all the presolar grains. In Fig. 2.22, the Ba isotopic ratios from our calculations are compared with the observations. The ^{138}Ba/^{136}Ba ratio decreases with increasing metallicity and with decreasing stellar mass. Furthermore, as also indicated by [129] and [128], the shape of the ^{13}C pocket affects the results. Also the uncertainty of the ^{14}N(n,p)^{14}C rate is relevant for the Ba isotopic ratios, since it is the main neutron poison in the ^{13}C pocket. In Fig. 2.22, we compare the results for the models M3.z1m2, M3z1m2.hCBM and M3.z1m2.hCBM.ntest (Tab. 2.1 and A.1). With the exception of the grains with the lowest $\delta(^{138}$Ba/^{136}Ba) and $\delta(^{135}$Ba/^{136}Ba), the observed range is reproduced by my models within the uncertainties, and the same conclusion can be drawn considering $\delta(^{137}$Ba/^{136}Ba).

In Fig. 2.23 we show the same kind of comparison as in Fig. 2.22, but this time time for our He07 models, confirming again the high similarity of the results.

Summing up, 2 $M_\odot$ AGB models that include CBM at the bottom of the convective TP and with C and O concentrations in the He intershell are presented in this work. Thanks to the recent update of the Zr neutron capture cross sections, these models are, for the first time, consistent with observations in post-AGB stars, with no efficient production of ^{96}Zr. The ^{96}Zr/^{94}Zr ratio was also shown to be affected by the ^{13}C pocket implementation. As indicated by [129], [130] and [128], observations of the s-process

signature in presolar grains from AGB stars may help to derive important constraints for the main features of the ^{13}C pocket. In the future, AGB models will need to include rotation and magnetic field, since, as shown recently by [164], rotation affects the ^{13}C pocket history once the ^{13}C pocket has formed. A more detailed description of the IGW CBM is crucial to fully test a scenario where gravity waves are the dominant physics mechanism responsible for the formation of the ^{13}C pocket.

2.7   AGB stars models: Discussion and summary

In this work I have presented eleven new AGB stellar models with initial mass M $= 2\,M_\odot$ and $3\,M_\odot$, and initial metallicity Z = 0.01 and 0.02. Additionally, other seven complete stellar runs have been calculated using the same stellar structures, but different rates for the reactions ^{14}N(n,p)^{14}C and ^{95}Zr(n,γ)^{96}Zr. The element distribution at the stellar surface after the last TDU event for these models is given in Fig. 2.24. In the lower panel it's possible to compare the results of Pi13 with our M3.z2m2, finding the confirmation of the larger *s*-process production (by about a factor of 4 at both Sr and Ba peaks) due to the larger ^{13}C -pocket obtainedin our models and at the same time the [hs/ls] index, characterising the slope of the *s*-process distribution is overall the same. In both panels, the difference between He07 models and their corresponding ones with *clipping* is about the same. The isotopic distribution is given in the Appendix, Fig. A.1 and Fig. A.2.

For the first time, these models study the impact of the following physics processes on AGB stellar evolution and nucleosynthesis: the CBM at the bottom of the convective TPs keeping into account Kelvin-Helmholtz and IGW instabilities, guided by He07 hydrodynamics simulations and by observations in post-AGB stars; the CBM below the TDU driven by IGW, according to De03; the molecular diffusion in the stellar layers where the radiative ^{13}C pocket forms and evolves.

The main results are the following. The Kelvin-Helmholtz instabilities at the bottom of convective TPs affect the AGB evolution and the He intershell abundances by allowing to accumulate C and O and reducing the He abundance. Our results are consistent with previous AGB simulations where overshooting was assumed to be the dominant CBM mechanism. In these models, the final C and O mass fractions in the He intershell are 0.4-0.5 and 0.2-0.1, respectively. Compared to Kelvin-Helmholtz instabilities, gravity waves have a marginal contribution. These results are obtained by applying a decreasing double-exponential profile of the mixing coefficient to my one-dimensional stellar models. The CBM parameters adopted for MESA calculations
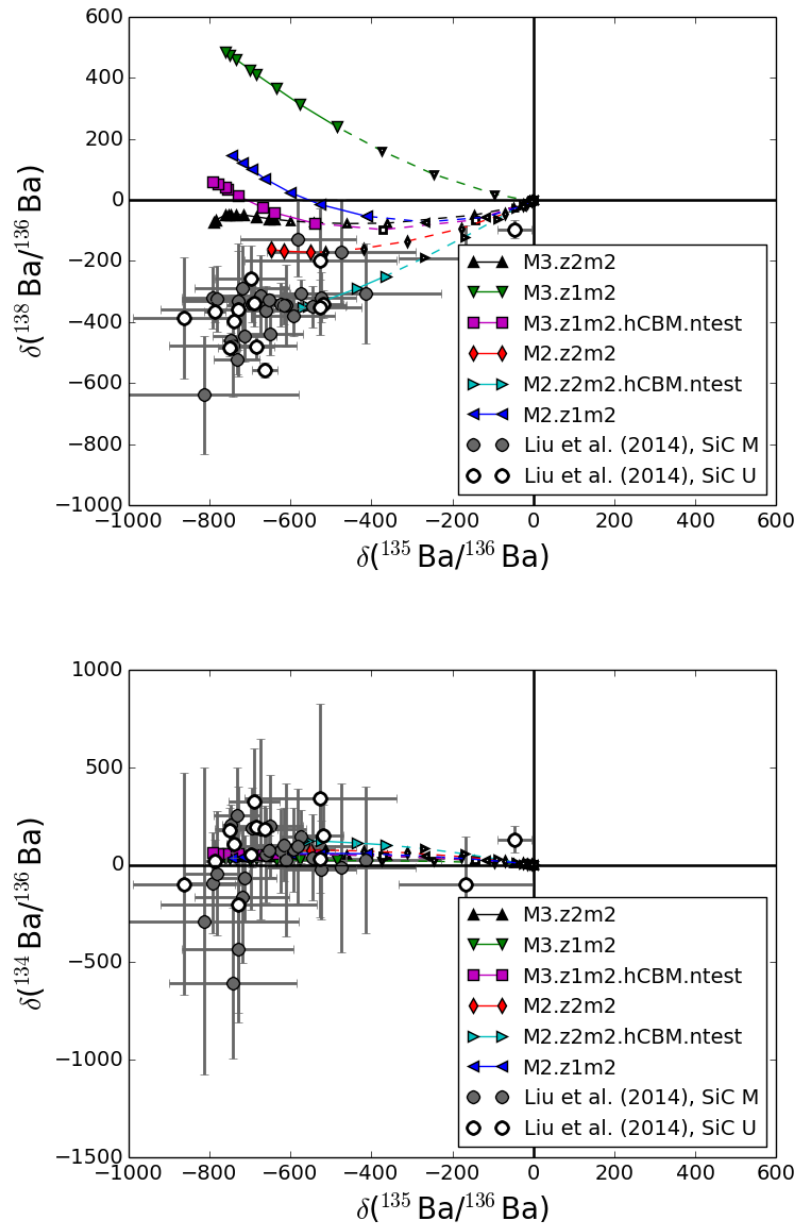
Fig. 2.22 Upper panel: $\delta(^{138}\text{Ba}/^{136}\text{Ba})$ vs $\delta(^{135}\text{Ba}/^{136}\text{Ba})$ for my models grid. Notice how the results from models are in agreement with the observations, given the tipical uncertainty of both CBM and ^{14}N (n,p) ^{14}C as well as the absence of rotation in these models, which is expected to lower the value of $\delta(^{138}\text{Ba}/^{136}\text{Ba})$. Lower panel: $\delta(^{134}\text{Ba}/^{136}\text{Ba})$ vs $\delta(^{135}\text{Ba}/^{136}\text{Ba})$ for the same models.
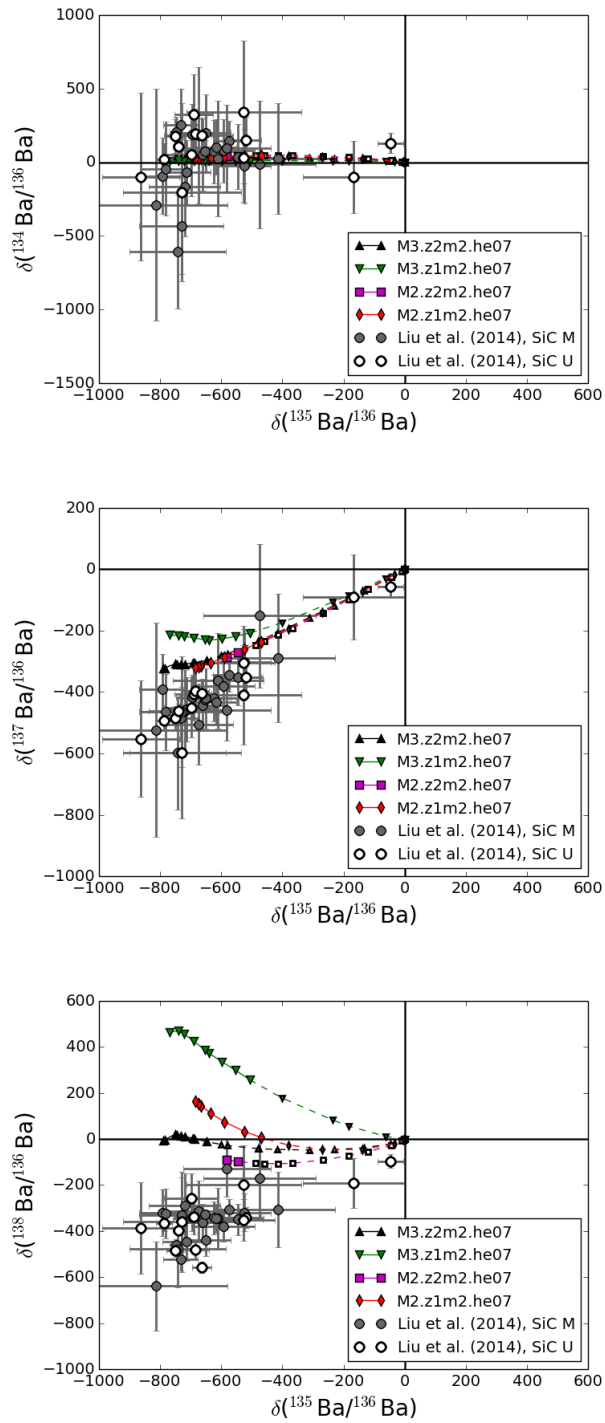
Fig. 2.23 Same as in Fig. 2.22, but the results are shown for the models calculated with the Herwig et al. [75] CBM prescriptions.
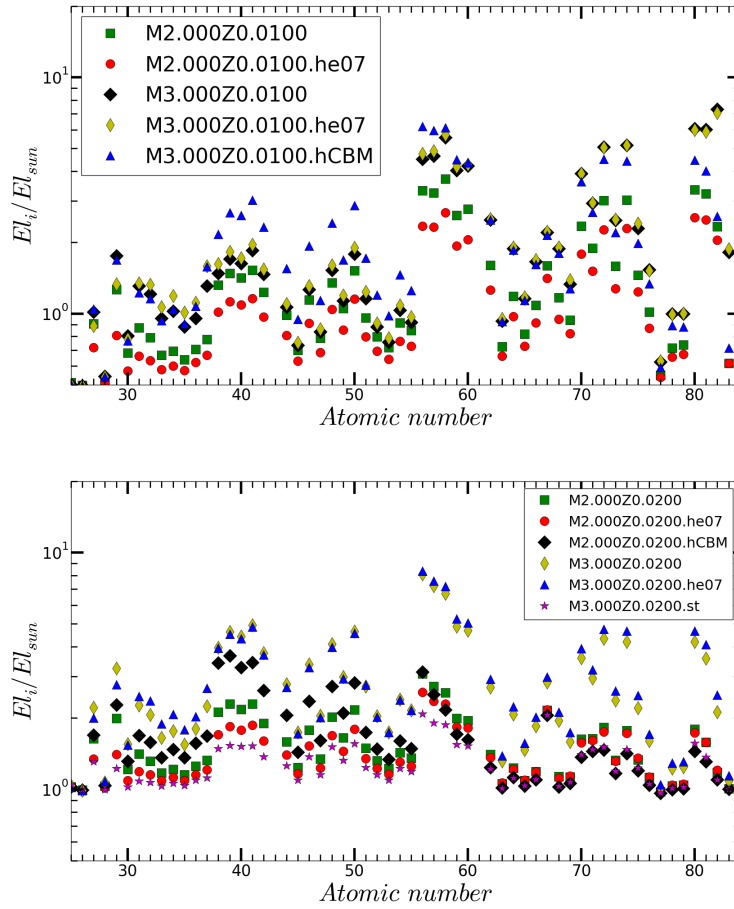
Fig. 2.24 Upper panel: Elemental abundance distribution after the last TDU event in out Z=0.01 models. Lower Panel: same as in the upper panel, but for models with Z=0.02

below convective TPs are f_1=0.024, f_2=0.14 and D_2= 10^5 cm^{2}s^{-1}.

Therefore, compared to the original prescriptions by He07, we have increased f_1 by a factor of two in order to be consistent with the observations in post-AGB stars.

While guidance from hydrodynamics simulations is crucial to build robust AGB stellar models, it is difficult to derive absolute recipes directly applicable to one-dimensional simulations without some preliminary work and additional guidance from observations. For instance, we have shown that different sets of parameters may be needed to get the same results by using different MESA code revisions. The same conclusions could possibly be derived by using different stellar codes. These differences need to be considered as intrinsic uncertainties of the one-dimensional stellar evolution. Following the discussion in section 2.4, it is worth emphasizing that it is not clear whether the default choices made for convection in MESA revision 4219 (used to calculate the AGB models in this work) are more correct than the previous setup in MESA revision 3372 (Pi13). Both cases are characterized by assumptions that are not unequivocally correct for the He-intershell conditions.

In our AGB models the IGW allow to form radiative ^{13}C pockets with size in the order of $10^{-4}\,M_\odot$, by using the following CBM setup below the TDU in MESA calculations: f_1=0.014, f_2=0.25 and D_2=10^{11} cm^{2}s^{-1}. This setup was obtained from fitting De03 results. However, the parameter f_1 does not affect the size of the ^{13}C pocket, which is dominated by the IGW parameterization (i.e., f_2 and D_2).

At the end of the the AGB evolution, an s-process production of 0.36 $<[s/\mathrm{Fe}]<$0.78 and -0.23 $<$[hs/ls]$<$0.45 is obtained. This is consistent with spectroscopic observations. The impact of the uncertainty in the IGW CBM parameterization for the ^{13}C pocket, and of the ^{14}N(n,p)^{14}C rate on the results is also . According to my models, an increase of the mentioned rate by a factor of two at a relevant energy of $\sim$8 keV reduces the final [hs/ls] by 0.05-0.1 dex. Comparable variations are obtained by using different IGW parameterizations. Therefore, the ^{14}N(n,p)^{14}C rate needs to be constrained with an uncertainty much lower than a factor of two in order to better explore the IGW scenario.

The s-process abundance signatures in presolar C-rich grains are the most challenging and constraining observations to study the s-process nucleosynthesis in AGB stars, and they also provide crucial information about the stellar conditions in the He intershell of the parent stars. Recent works compared new measurements in SiC mainstream grains and stellar AGB models predictions, and ascertained that the size and shape of the ^{13}C pocket can be indirectly studied by isotopic ratios of s-process elements like Sr, Zr and Ba. Thanks to the flexibility given by the use of AGB models

with parameterized ^{13}C pockets, [129], [130] and [128] tried to infer about the main properties of the pocket where the s-process takes place. On the other hand, [164] and [128] showed that a physics mechanism like rotation might affect the main properties and the nucleosynthesis in the ^{13}C pocket *after* its formation. This is due to e.g., the slow mixing of material (including ^{14}N and the s-process seed ^{56}Fe) from stellar layers located above the pocket into the thin regions where the s-process takes place. Qualitatively, the same effect is triggered by molecular diffusion in my models. Molecular diffusion does not have an impact in the typical timescales of the ^{13}C pocket formation. However, it might affect the ^{13}C-pocket at later stages. It has been shown shown that with the implementation of the molecular diffusion adopted in this work the impact on the final s-process abundances is marginal. However, by using the default MESA setup the s-process nucleosynthesis in the ^{13}C pocket would have been suppressed.

Therefore, the measurements in presolar grains may allow to infer about the physics mechanisms crucial for the formation ^{13}C pocket, but also about the physics events affecting the pocket along its evolution before the ^{13}C(α,n)^{16}O neutron source runs out of fuel. These information is wrapped together in the s-process abundance signatures in presolar grains from AGB stars. In order to use presolar grain data to answer the question of what the physical mechanisms for the formation of the ^{13}C-pocket are, AGB stellar models need to take into account processes with a delayed impact like rotation, magnetic field and molecular diffusion. This might be challenging, but the future guidance from multi-dimensional hydro-simulations will make it possible in the next few years, thus making AGB stars a unique laboratory to study different physics mechanisms in stellar environments.

Chapter 3

Production of the p-process seeds for thermonuclear supernovae in the single-degenerate scenario

3.1 Introduction

At the end of the AGB evolution, stars lose all their envelope entering the planetary nebula phase and cooling down as a WD. However, a fraction of those WDs that are part of a binary system can evolve differently, and eventually explode as SNe Ia. Several studies in the past tried to simulate the accretion of material on a central WD, since, depending on different details of the binary system and of accretion efficiency, they may generate different objects that are observed in the galaxy, like Novae [e.g., 98] and cataclismic variables [109]. If the star can reach the Chandrasekhar limit (1.39 $M_\odot$) by accretion, it will end its life as a SNIa [79].

Sion et al. [196] and Paczynski [158] investigated the long-term evolution in close binary systems of accreting WDs, focusing on H-shell flashes occurrence and on their dependence on the accretion rate. Paczynski [158] introduced a one-zone formalism that has been adopted later by e.g., Shen and Bildsten [195]. In this work, a stable H-burning condition on accreting WDs is studied, and the dependence of various H-burning regimes (unstable, nova-recurrent, stable burning and super-Eddington limit) on the accretion rate, on the metallicity of the accreted material and on the WD mass is defined.

In these studies, the evolution of the deeper He-burning layers is not followed in detail, and only the feedback to the He luminosity is considered (see also Nomoto et al.

[151], Ma et al. [137] and Starrfield et al. [199]). One of the first works to simultaneously simulate H and He flashes was that presented by Jose et al. [99], performing a numerical two-zone study. Later, Tornambé et al. [212] performed a similar study. In particular, he highlighted that during the accretion phase of WDs the He-flashes strongly reduce the capability of the star to retain the accreted mass, making it more difficult for the SNIa single-degenerate scenario to reach the Chandrasekhar mass.

Langer et al. [119] studied the evolution of close binary systems consisting of a main sequence star and a WD, resolving both the components of the binary system, but txreating the WD as a material point. With this setup, they investigated the properties of the systems as a function of the initial donor star mass, initial WD mass, initial period, and chemical composition. They obtained that, in order to reach the Chandrasekhar limit, the initial mass of the WD when the accretion starts should be about 0.7 $M_\odot$.

As mentioned in Chapter 3.1, SNe Ia are fundamental sources for galactical chemical evolution. They produce iron group elements in the ejecta exposed to the most extreme SN conditions [e.g., 26, 92]. In the ejecta exposed to less extreme conditions, intermediate mass elements like Si and Ca are made, as also confirmed from optical spectra of recent SNIa remnants [e.g., 53, 79, and references therein]. Finally, in the most external 0.2-0.3 $M_\odot$ ejected also the *p*-process nuclei from ^{74}Se to ^{196}Hg can be made.

Travaglio et al. [217] and more recently Travaglio et al. [216] obtain that almost all the *p*-nuclei are calculated with similar enhancement factors relative to ^{56}Ni, including the puzzling light *p*-nuclei ^{92}Mo, ^{94}Mo, ^{96}Ru and ^{98}Ru. As also pointed out by the authors, a crucial assumption for the this scenario is to have *s*-process rich material in the outer accreted layers of the SNIa progenitor. Indeed, the *p*-process products in SNe Ia can be made in large quantities only if there is a previous heavy-elements enrichment by neutron captures during the accretion stage, which will act as seed for the p process during the SNIa explosion. Furthermore, this enrichment should be located in the most external layers of the SNIa progenitor. If they are located too deep, the temperature conditions are too extreme and the SN shock will completely photo-disintegrate all abundances heavier than the Fe group, including the p-process isotopes.

Possible sources of *s*-process enrichment in the SNIa progenitor are the *s*-process abundances accumulated during the AGB phase before the formation of the WD [20, 59, 104]. I presented in Chapter 2 my results for the *s*-process in AGB stars. On the other hand, the *s*-process production made during the AGB phase will be

buried inside the progenitor at mass coordinate about 0.6-0.65 $M_\odot$ (see e.g., Tab. A.2). For typical SNIa explosions in the single-degenerate scenario, this region will be first convectively mixed during the simmering phase before exploding as SNIa, where a convective region grows at the WD center including up to about $1\,M_\odot$ over a timescale of ~ 1000 yr [171]. The s-process enrichment built in the AGB He intershell is mixed over the WD structure, with a strong dilution of heavy element enrichments. Furthermore, the same region will later experience α-rich freezout or incomplete Si-burning conditions during the SNIa explosion [211]. So, there will be no p-process material ejected from this stellar region.

Travaglio et al. [217] assumed that during the accretion phase the s-process material was accumulated in the external 0.2-0.3 $M_\odot$ of the SNIa progenitor, with a distribution typical of the main s-process component. Iben [85] proposed that heavy elements could be made in these conditions, where He-burning layers were burning with convective TPs below the accreting H-burning layers. They suggested the ^{22}Ne $(\alpha,n)^{25}$Mg as the main neutron-source during the following TPs events. That work was a first attempt to access and discuss this possibility, without actually simulating the accretion phase. Another interesting case prospective is the Helium-accreting scenario, which was recently considered by Piersanti et al. [165], who studied the thermal response of non-rotating WDs to direct accretion of helium. They explored the impact of different Helium accretion-rates on the WD structure, without investigating the nucleosynthesis coming from a SNIa event with a this kind of progenitor.

In the next sections of this chapter I will report the results of my calculations. I will present my simulations of solar-composition matter accreting WD models, and the neutron-capture nucleosynthesis of heavy elements during the accretion phase, testing the assumption of Travaglio et al. [217].

3.2   Accreting WD models: main stellar model properties and initial setup

The stellar models presented in this chapter are computed using the stellar code `MESA` [`MESA` revision 4219, 160].

The solar distribution used as a reference is given by [65]. For a description of the MESA code and the CBM implementations in these models, I refer to chapter 2.

Mass loss is only considered when Super-Eddington wind conditions are met,

which is triggered when the luminosity of the accreting WD exceeds the Eddington luminosity, defined as

$$L_{Edd} = \frac{4\pi \ GMc}{kap} \tag{3.1}$$

where M is the WD mass and kap is the opacity [137, 149, 195]. After the TP, the balance between the radiation and the gravitational forces is violated and a highly intensive mass loss rate results. Considering a pure ionized H plasma, a simple derivation of the Eddington limit is obtained by setting the outward radiation pressure equal to the inward gravitational force, thus giving:

$$L_{Edd} = 3.2 \times 10^4 \frac{M}{M_\odot} L_\odot \tag{3.2}$$

Once L_{Edd} is defined, if the stellar luminosity L exceeds L_{Edd} mass-loss is calculated according to Paczynski and Proszynski [159], who determined an analytical relation between the stellar luminosity and the mass outflow rate:

$$\frac{dM}{dt} = 1.67 \times 10^{18} gs^{-1}(\frac{L}{L_{Edd}} - 1) \tag{3.3}$$

For the simulations the following nuclear networks are adopted: 1) *wd-accr.net*, including 33 isotopes from protons to ^{26}Mg linked by nuclear-reactions including the pp chains, the CNO tri-cycle, the triple-α and the α-capture reactions ^{12}C $(\alpha, \gamma)^{16}$O ^{14}N $(\alpha, \gamma)^{18}$F $(e^+\nu)^{18}$O , ^{18}O $(\alpha, \gamma)^{22}$Ne ^{13}C $(\alpha, n)^{16}$O and ^{19}F $(\alpha, p)^{22}$Ne . We use the NACRE [7] reaction rate compilation for most reactions. For the ^{12}C $(\alpha,\gamma)^{16}$O we adopt the rate by [113], ^{14}N $(p, \gamma)^{15}$O is by [89] and the triple-α by [58]. This network is used for the main calculations in this chapter, presented in section 3.2.2; 2) *nova.net*, which includes 48 isotopes from H to Si^{30} coupled by 120 reactions. The same network was used by e.g., Denissenkov et al. [47], and, compared to *wd-accr.net*, it differs by not including He-burning reactions. This network is used for the tests presented in section 3.2.1; 3) *cno − extras.net*, including 13 isotopes from H to Mg^{24} coupled by 56 reactions. This network is used for the tests presented in section 3.2.1.

The initial WD models used to start the simulations are included in the MESA revision 4219, in the *data* folder. We did not calculate WD models since the simulations are focused on the accretion phase, that is quite independent from the WD interior structure [e.g., 137, 229]. For the models presented in section 3.2.1, we use the MESA WDs models 0.639from3.0z2m2.mod, 0.819from4.0z2m2.mod, 1.025from7.0z2m2.mod and 1.316from8.5z2m2.mod. For the models in section **??**, we use CO WDs with initial

mass $M = 0.639 \text{and} 0.856 \, M_\odot$. In the center they are made of about 30%, 68% and 2% on C, O and Ne respectively. They are characterized by an He-rich cap over the CO core, which is a relic of the He-burning layers on top of the CO core, with typical mass fractions $55\% \leq \text{He} \leq 65\%$, $35\% \leq \text{C} \leq 45\%$ and $2\% \leq \text{O} \leq 10\%$.

As shown in chapter 2, these are consistent with the results of the CBM adopted in this work. We also use the following ONeMg WDs: $M = 1.259 \, M_\odot$, with 60% O, 30% Ne, 7% C and 3% Mg, and $M = 1.376 \, M_\odot$, with 60% O, 37% Ne, and 3% Mg. WD models have all a central temperature of the order of 100 MK, which means that we assume that the WD has been formed recently and it did not spend a long time cooling down [see 137]. Notice that I use ONeMg WDs, that are not SNIa progenitors. As already mentioned, the central conditions are not relevant for the accretion simulations on the surface of the WD. On the other hand, it is plausible to use these WD models as progenitors assuming that they reached that mass by previous accretion, or by forming recently as hybrid WDs [46].

3.2.1 Models description: identification of different burning regimes

In accreting WDs, different burning regimes are possible, depending on the accretion rate, on the composition of the accreted material and so on. Five main accretion regimes are identified: strong H-shell flash regime, mild H-shell flash regime, steady H-burning regime, red-giant regime and super-Eddington wind regime. Supersoft X-ray sources have been proposed as observational signatures of accreting WDs in which steady burning of H is taking place [219]. Given a specific composition of the accreted material and assuming constant accretion rate, stable burning of H requires accretion rates within a narrow range. Below this range unstable H burning occurs, and above this range the stellar envelope expands to red giant size, or eventually a strong overflow or Super-Eddington wind is set for higher rates. Therefore, the highest probability to efficiently accrete material and reach the Chandrasekhar-mass limit is by adopting an accretion-mass rate within the steady H-burning regime. For such systems, theoretical stellar calculations found H-rich matter transfer rates ranging between 10^{-7} and $4 \times 10^{-7} \, M_\odot \, \text{yr}^{-1}$ [e.g., 151, 195].

The steady H-burning conditions were defined by considering only H burning and without including He-burning rates for deeper stellar layers. Nevertheless, it may be assumed that they still hold even if He-burning is also considered, provided that burning is dominated by reactions of the full CNO cycle [151, 195]. In this section, we

present a preliminary study done to identify these conditions with the MESA code. The main goal is to verify with our code setup the critical mass-accretion rate resulting in a transition from unstable to stable H burning as a function of the accreting WD mass, to apply for the following calculations.

The stellar models and their basic properties are presented in Table 3.1. All of the models are used starting from WDs of different masses, described in section 3.2. Those models denoted by *cbm*1 and *cbm*2 were calculated using *nova.net*, with the *cbm*1 models using the CBM prescription of Denissenkov et al. [47], i.e. a single-exponantial decay overshooting scheme with f=0.004 applyed to every convective boundary, and the *cbm*2 ones using the double-exponential decay formalism introduced in Chapter 2 with f_1=0.014 applied under the H-burning shell. Notice that this last case is equivalent to a single-exponential decay overshooting scheme with f=0.014, since the second decay is activated only when TDU conditions are achieved (see Chapter 2) and this cannot happen in this preliminary study, since the H-burning shell is never extinguished. Models denoted by *simple* were calculated using *cno − extras.net* and no CBM applied. Moreover, M0p639.Z1m2.Hburn.cbm2 and M0p639.Z1m2.Hburn.simple achieved H-burning with dm/dt=4×10^{-8} $M_\odot$ yr^{-1}, while in M0p639.Z1m2.Hburn.cbm1 I used dm/dt=5×10^{-8} $M_\odot$ yr^{-1}. In M0p856.Z1m2.Hburn.cbm1, M0p856.Z1m2.Hburn.cbm2 and M0p856.Z1m2.Hburn.simple dm/dt=1.1×10^{-7} $M_\odot$ yr^{-1} was identified, which increases to dm/dt=2.75×10^{-7} $M_\odot$ yr^{-1} in M1p316.Z1m2.Hburn.cbm1, M1p316.Z1m2.Hburn.cbm2 and M1p316.Z1m2.Hburn.simple. Finally, M1p025.Z1m2.Hburn.cbm2 and M1p025.Z1m2.Hburn.simple achieved H-burning with dm/dt=1.8×10^{-7} $M_\odot$ yr^{-1}, while in M0p639.Z1m2.Hburn.cbm1 I used dm/dt=2×10^{-7} $M_\odot$ yr^{-1}.

These calculations allow to explore the impact (if any) of different nuclear networks and CBM schemes. A summary of the results is given in figure 3.3. For comparison, I include also the models provided by Nomoto et al. [151] and Shen and Bildsten [195]. The results show that: 1) the details of the stable-burning accretion are only marginally affected by the CBM, or 2) by using different networks; 3) a good agreement is obtained between my calculations and Nomoto et al. [151] and Shen and Bildsten [195], despite using different stellar codes and simulations setup.

As indicated in the previous section, the accreted material has Z=0.01 metallicity. The results obtained above depend on the metallicity of the accreted material [195]. In the next section, I will use the fixed accretion rates indicated in table 3.2 consistently with the WD initial mass. From the table and from figure 3.3, the accretion rate needed to burn H steady increases with increasing WD mass, as expected [137, 195]. This will also imply a decrease of the interpulse period with the WD mass. Paczynski

Table 3.1 List of accreting WD models with critical stable H-burning conditions: initial mass, initial metallicity and CBM parameterization are given. The CBM parametrization is given by a single-exponential decreasing profile. The CBM parameter f is given below the H-burning shell. The nuclear network adopted is denoted by *cno* where *cno − extras.net* was used or *nova* where *nova.net* was used.

name	mass [$M_\odot$]	metallicity	f	network
M0p639.Z1m2.Hburn.simple	0.639	0.01	-	cno
M0p856.Z1m2.Hburn.simple	0.856	0.01	-	cno
M1p025.Z1m2.Hburn.simple	1.025	0.01	-	cno
M1p316.Z1m2.Hburn.simple	1.316	0.01	-	cno
M0p639.Z1m2.Hburn.cbm1	0.639	0.01	0.004	nova
M0p856.Z1m2.Hburn.cbm1	0.856	0.01	0.004	nova
M1p025.Z1m2.Hburn.cbm1	1.025	0.01	0.004	nova
M1p316.Z1m2.Hburn.cbm1	1.316	0.01	0.004	nova
M0p639.Z1m2.Hburn.cbm2	0.639	0.01	0.014	nova
M0p856.Z1m2.Hburn.cbm2	0.856	0.01	0.014	nova
M1p025.Z1m2.Hburn.cbm2	1.025	0.01	0.014	nova
M1p316.Z1m2.Hburn.cbm2	1.316	0.01	0.014	nova
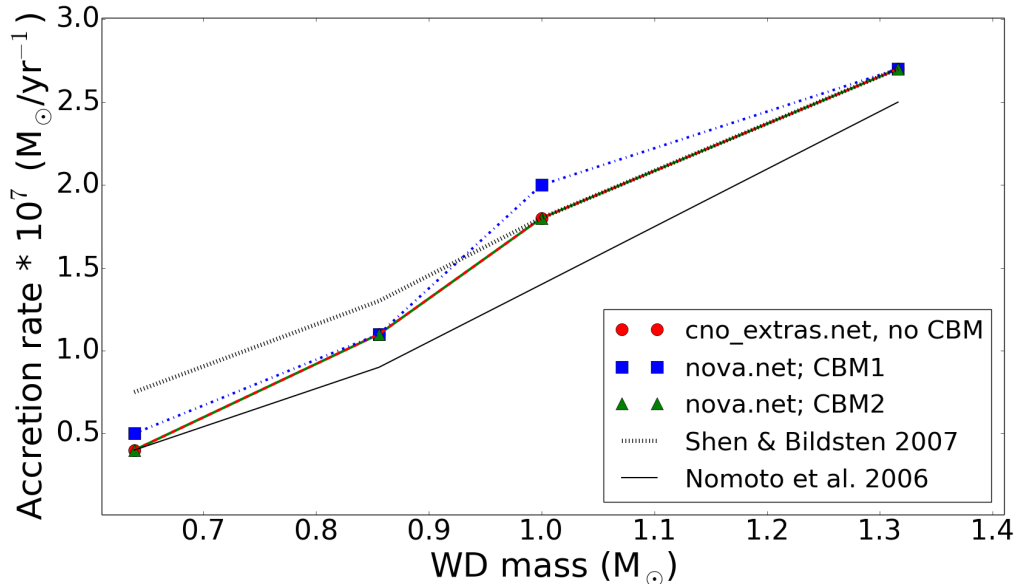
Fig. 3.1 Critical mass accretion rate resulting in a transition from unstable to stable H burning as a function of the accreting WD mass. All the accretion rates lower than the critical values result in unstable H burning, making the reaching of the Chandrasekhar limit more difficult. A comparison between our accretion models and the literature is also provided.

[157] found the same result in AGB stars, where in that case the relation is between the interpulse period and the CO core mass.

3.2.2 Models description: accretion models calculations

Once the accretion rate is defined in order for a given initial WD mass to have steady burning of H, the accreted material is burned via CNO cycle efficiently. The H-burning ashes are accumulated in the He-rich intershell just below the surface. The bottom of the He intershell is compressed and temperature rises until an He flash occurs, releasing large amounts of energy and developing a pulse-driven convection zone (hereafter PDCZ). Therefore, the accretion phase appears to have strong similarities with the convective TPs occurrence during the evolution of AGB stars, discussed in the previous chapter. The first qualitative difference is that during the AGB phase there is a large H-rich envelope on top of the He-burning region, while in this case there is no envelope.

Despite this, as also indicated by previous works [e.g., 106], during the accretion regular convective TPs occur in the He-burning layers. Thousands of TPs would be required in order to reach the Chandrasekhar-mass limit. However, I simulate only a limited number of TPs for each initial WD mass, to study the different conditions obtained along the accretion phase.

In table 3.2 the list of models analysed during this thesis, together with their main parameters setup, is presented.

All the models were calculated using the reaction network $wd-accr.net$ and a double-exponential mixing-coefficent decay formalism to include CBM [75]. Each model is characterized by a fixed accretion rate. dm/dt is $2.08\times10^{-7}\,M_\odot\,\mathrm{yr}^{-1}$ in M0p856.Z1m2, dm/dt is $3.16\times10^{-7}\,M_\odot\,\mathrm{yr}^{-1}$ in M1p025.Z1m2, dm/dt is $3.7\times10^{-7}\,M_\odot\,\mathrm{yr}^{-1}$ in M1p256.Z1m2 and dm/dt is $6\times10^{-7}\,M_\odot\,\mathrm{yr}^{-1}$ in M1p376.Z1m2.

Initial mass, metallicity, CBM parameters and number of TP simulated are given in the table.

Table 3.2 List of accreting WD models and their relevant parameters: initial mass, initial metallicity and CBM parameterization. The CBM parametrization is given by a double exponential decreasing profile. The CBM parameters are given below the TP (f_1, D_2 and f_2).

name	mass [$M_\odot$]	metallicity	f_1	D_2	f_2	TP `MESA`	TP MPPNP	Accretion rate ($10^{-7}\,M_\odot$)
M0p639.Z1m2	0.639	0.01	0.011	10^5	0.14	4	0	1.00
M0p856.Z1m2	0.856	0.01	0.011	10^5	0.14	4	4	2.08
M1p025.Z1m2	1.025	0.01	0.011	10^5	0.14	137	7	3.16
M1p259.Z1m2	1.250	0.01	0.011	10^5	0.14	4	4	3.70
M1p376.Z1m2	1.376	0.01	0.011	10^5	0.14	2	2	6.00

In table B.1 (see appendix), for each model the main stellar properties after each TP event are given. In addition to the mass coordinate at the top and bottom of the He-flash convective zone, for every TP the largest temperature (in logarithm) at the bottom of the flash-convective zone is presented. This is the most crucial stellar property from a nucleosynthetic point of view, since it directly determines the efficiency of the ^{22}Ne $(\alpha,\text{n})^{25}$Mg and the resulting neutron-density. Finally, the stellar mass at and after the TP is given, allowing to estimate the mass retention rate for each model.

3.3 Accretion-WD models: summary of their main features

As it is possible to see from table 3.2, a limited number of TPs is simulated for each model. The only exception is model M1p025.Z1m2, where 137 TPs are calculated to explore relevant changes of the TPs properties in a longer sequence, and to study if the accreting WD is actually increasing in mass.

Figure 3.2 shows the Kippenhahn diagram for a TP and a sequence of TPs of the model M1p025.Z1m2. The results of this model (and of all the models in table 3.2) confirm the calculations of Tornambé et al. [212]: the Eddington limit [189] is easily exceeded immediately after each He flash, ejecting almost all the matter accumulated during the previous interpulse phase. This reduces the efficiency of the accretion process toward Chandrasekhar mass. Despite these powerful winds, in figure 3.2 it is highlighted that the star is still growing in mass. Furthermore, higher WD mass will finally result in higher surface gravity, thus reducing the net amount of mass loss after the super-Eddington wind phase which follows every TP. According to the models presented here, the average net amount of mass loss in M0p856.Z1m2 is around 0.006 $M_\odot$, while it is around 0.001 $M_\odot$ in M1p025.Z1m2 model (figure 3.2), 2×10^{-4} $M_\odot$ in M1p256.Z1m2 and 10^{-5} $M_\odot$ for M1p376.Z1m2.

Based on the WD mass increase all models, a WD with at least an initial mass of M $\sim$ 1.1 $M_\odot$ wouldbe able to reach the Chandrasekhar limit. This estimate can be done looking at figure ??, where the retention efficiency, defined as the total mass difference before and after the mass loss by super-Eddington wind after each TP, as a function of the initial WD mass is shown. A stellar donor as a companion is needed with an initial mass lower than the progenitor star from which a WD of a given mass comes from, allowing to have enough material accreted before finishing the mass reservoir in
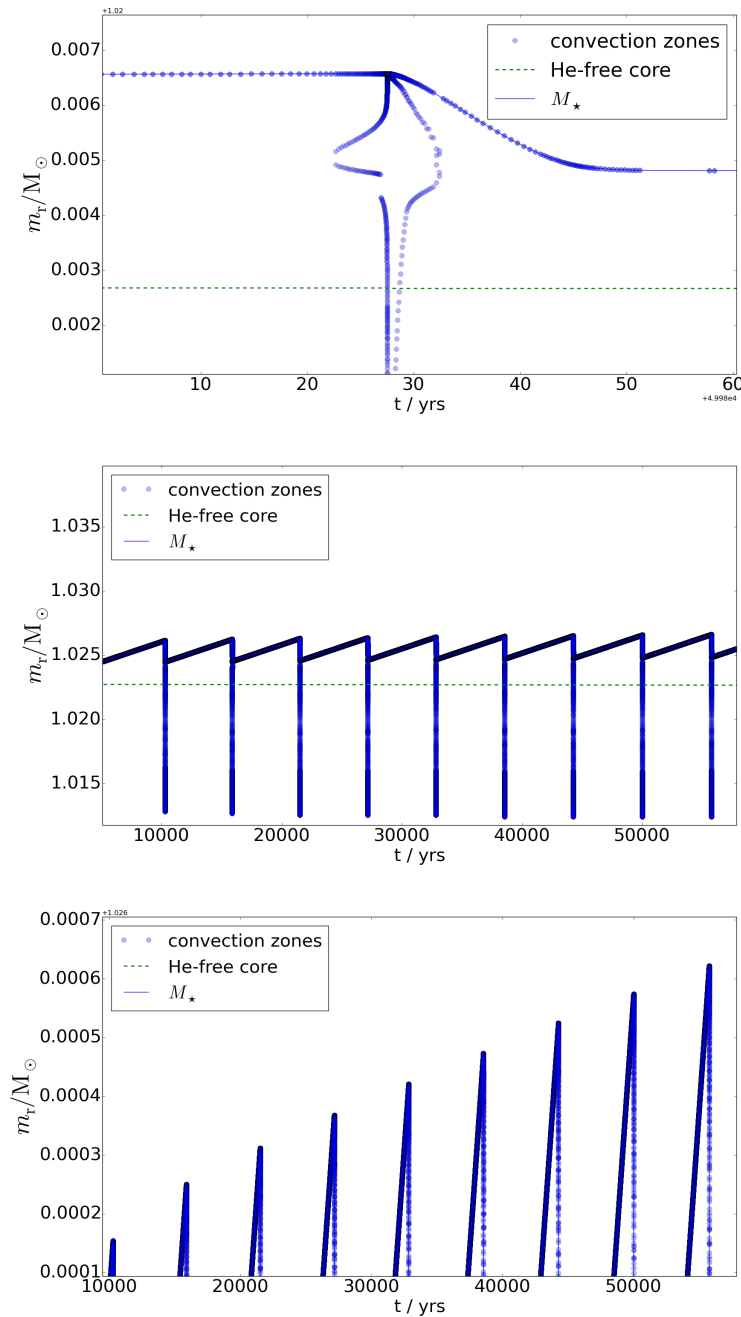
Fig. 3.2 Upper panel: Kippenhahn diagram of a typical He-flash event during the accretion phase of our 1 M$_\odot$ accreting WD model. Indicated are the convective boundaries of the TP, and the surface of the star. The fast mass loss is due to the super-Eddington wind after the He flash, and it is indicated by the reduction in mass of the star. The He-free core is also indicated. Middle panel: Kippenhahn diagram of a sequence of He flashes. Lower panel: A zoom of the plot in the middle panel, showing the WD mass increase during the accretion. The fast mass loss after each TP is visible.

the binary companion. A simple integration of the parabolic fit obtained shows that a WD with an initial mass lower than $\sim 1.1\ M_\odot$ and accreting Z=0.01 material would not be able to reach the Chandrasekhar mass. Notice how ,lowering the metallicity of the accreted material to Z=0.001, the retention efficiency increases by around a factor of two for all initial masses higher than $1\ M_\odot$: In this case, the resulting minimum WD mass required to reach the Chandrasekhar limit passes from $1.1\ M_\odot$ to $0.86\ M_\odot$. On the other hand, in our simulations we resolve the accreting WD structure but we do not simulate the evolution of the donor, using instead a constant rate accretion on the WD surface. Langer et al. [119] computed the evolution of binary systems formed by a main sequence star and a WD star, including orbital separation and accretion rates. With this different approach, Langer et al. [119] obtain that the minimum WD mass to reach the Chandrasekhar limit is M=0.7 $M_\odot$.
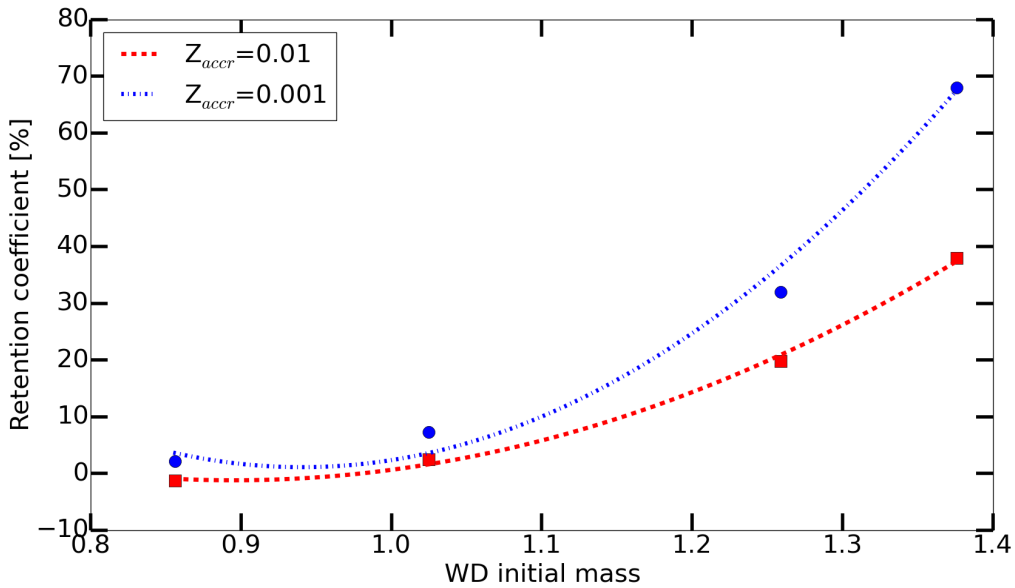
Fig. 3.3 Retention efficiency as a function of the initial WD mass. A parabolic fit has been derived for two different accreted material metallicities, showing in this way hi the the quantity of retained material increases lowering the metal content of the donor.

In figure 3.4 the Kippenhahn diagram for three convective TPs of different models are shown. As in figure 3.2, the strong mass loss is clearly visible, forcing the structure to lose most of the mass accreted in the last interpulse phase. The highest energy generation coincides with the highest downward extension of the PDCZ. It is also interesting to observe that the energy generation from He burning continues to be significant also when the H-burning has already started. The abundance profiles of

indicative isotopes for the same TPs are shown in figure 3.5. Figure 3.5 shows the mixing coefficient, including convection and CBM. In particular, the extra-mixing due to IGW (see chapter 2) penetrates down to the core. However, the results indicate that the mixing timescale due to this term is not relevant because of the low D_2; this same result was obtained also for the TP-AGB stars.

Despite the mass increase of about $0.4\,M_\odot$ between M0p856.Z1m2 and M1p259.Z1m2, the Kippenhahn diagrams and the abundance profiles look quite similar. However, as already mentioned earlier in this section, there is one important difference: the mass lost by super-Eddington wind decreases by increasing the WD mass. But there are also other important differences that become crucial from the nucleosynthesis point of view.

In figure 3.6, the evolution of temperature and density at the bottom of the PDCZ (T_{FBOT}, see table B.1) with respect to the WD mass is shown. The temperatures T_{FBOT} are taken from one TP, but they are representative of others TPs calculated with the same WD mass. Indeed, according to table B.1, the T_{FBOT} variation is marginal. Even for the more extended M1p025.Z1m2 model, T_{FBOT} variation is less than 3%. In figure 3.6, the logarithm of the temperature linearly increases with the WD mass. This trend is consistent for all the mass range explored. The main reason of the temperature increase with the progenitor mass is the thin shell instability and partial degeneracy described in §2.5.1: the higher the accreting WD mass, the lower the shell thickness will be, making thin shell instability more efficient, as the expanding shell pushed by triple α will need more time to reach a thickness high enough to restore hydrostatic equilibrium, giving more time for the temperature to rise. A similar trend is also visible for the density.

I have mentioned that the thickness of the He intershell decreases with the increase of the WD mass. This statement is shown in figure 3.7. Between models M0p639.Z1m2 and M1p376.Z1m2, the mass of the He intershell decreases by almost three orders of magnitude, from few $10^{-2}\,M_\odot$ (wich is consistent with the TP-AGB simulations in chapter 2) down to a few $10^{-5}\,M_\odot$. In figure 3.7, it is also reported the amount of H-rich mass that is not processed by H burning before the next convective TP will occur. Its mass is reduced from M $\sim 10^{-4}\,M_\odot$ for model M0p639.Z1m2 to M $\sim 10^{-7}\,M_\odot$ for model M1p376.Z1m2. These last numbers need to be compared to the mass accreted during the same interpulse phase, that is comparable to the He-intershell mass. This means that at the onset of the convective TP, only few per cent of the H-rich material accreted still has to burn. In general, for the mass range explored in our simulations and for all the convective TPs, the size of the He intershell mass is about two orders of magnitude larger than the unburned H-rich material. These
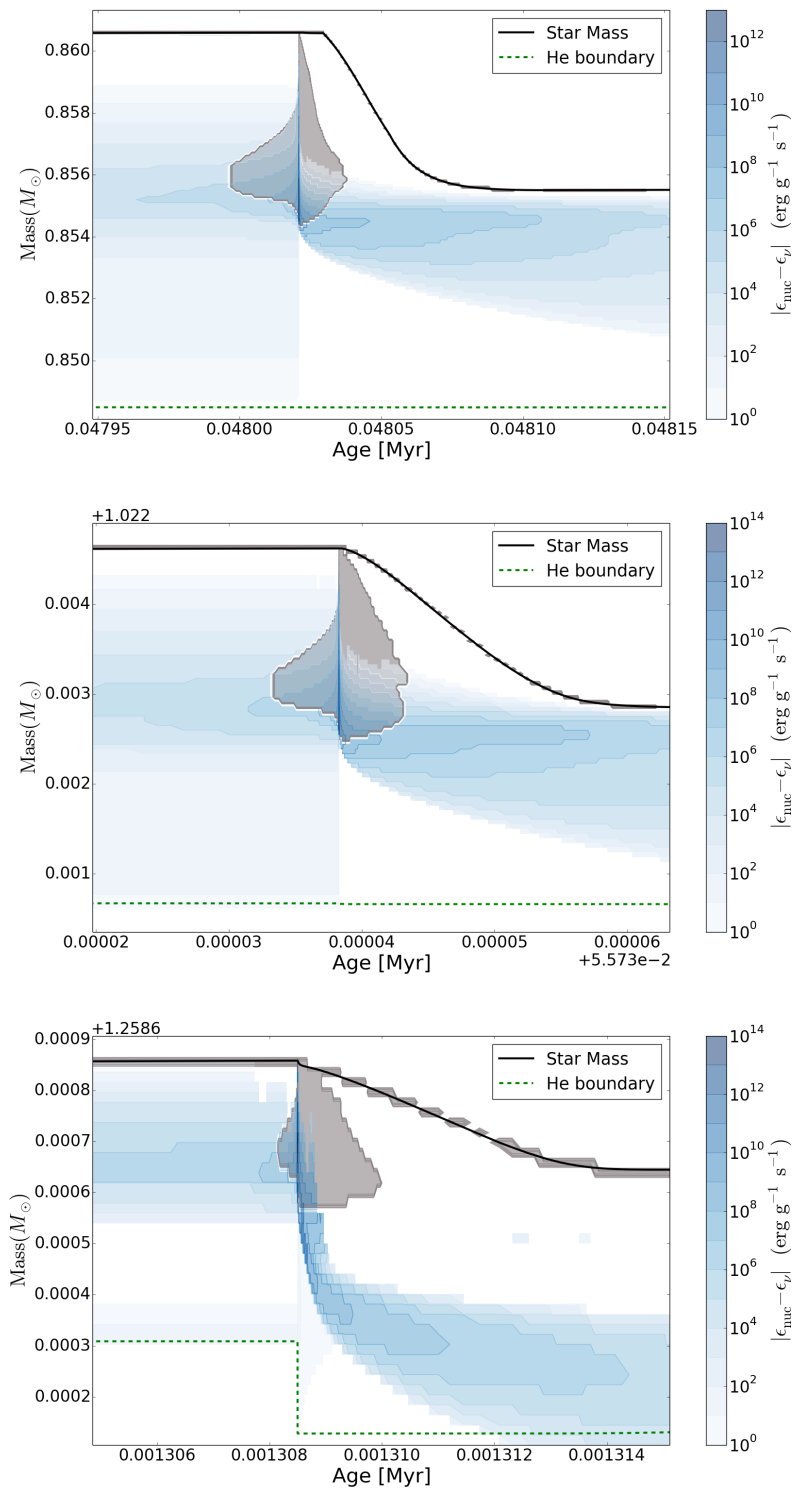
Fig. 3.4 Kippenhahn diagram of a convective TP for the models M0p856.Z1m2 (top panel), M1p025.Z1m2 (middle panel) and M1p259.Z1m2 (bottom panel). The energy generation (blue shaded areas) and convective zones (grey-shaded areas) are indicated.
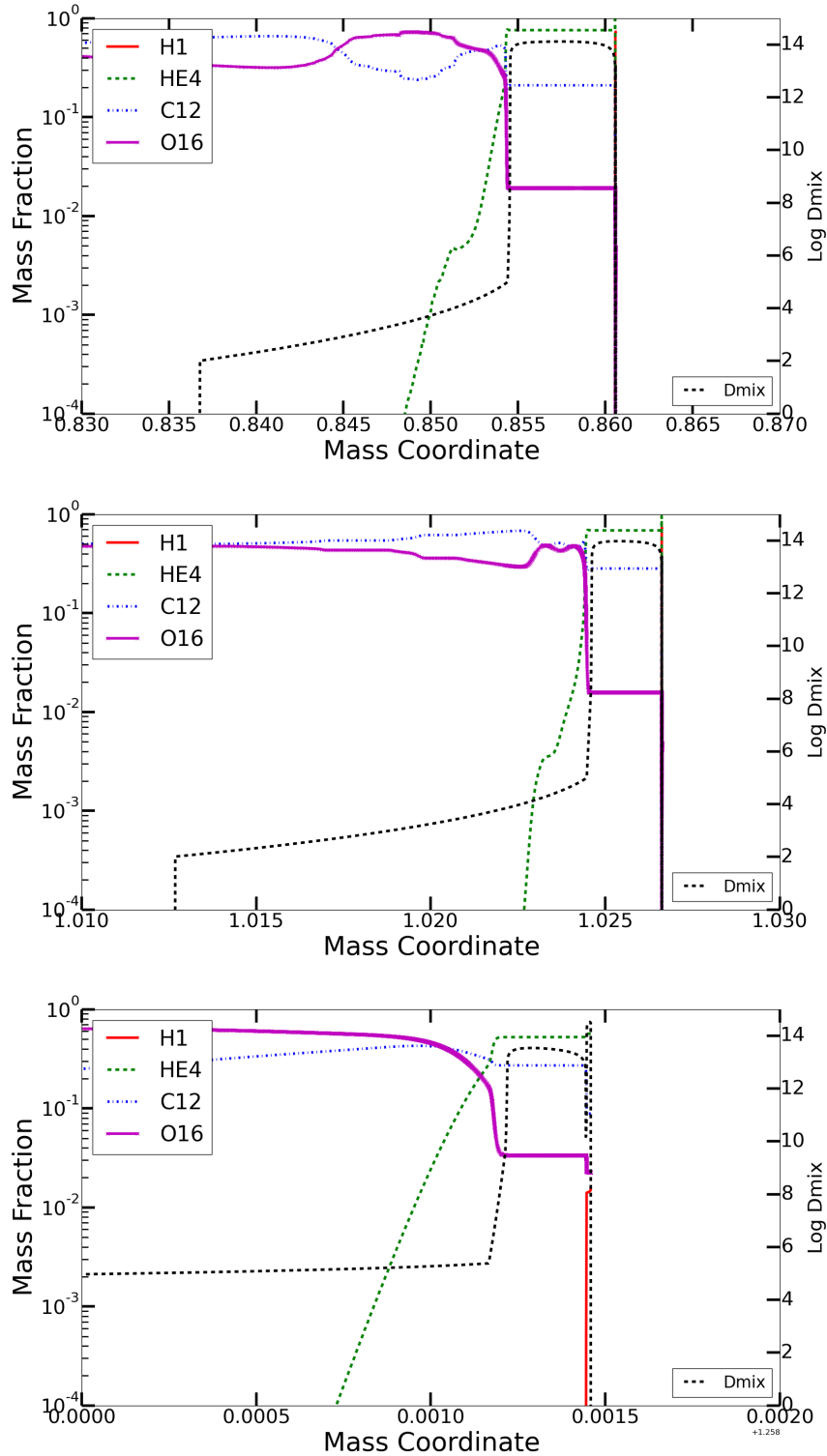
Fig. 3.5 Abundances profiles of H, ^{4}He, ^{12}C and ^{16}O are shown for the convective
TPs in figure 3.4. The mixing-coefficient is also reported, including the CBM profile
extending down to the core.
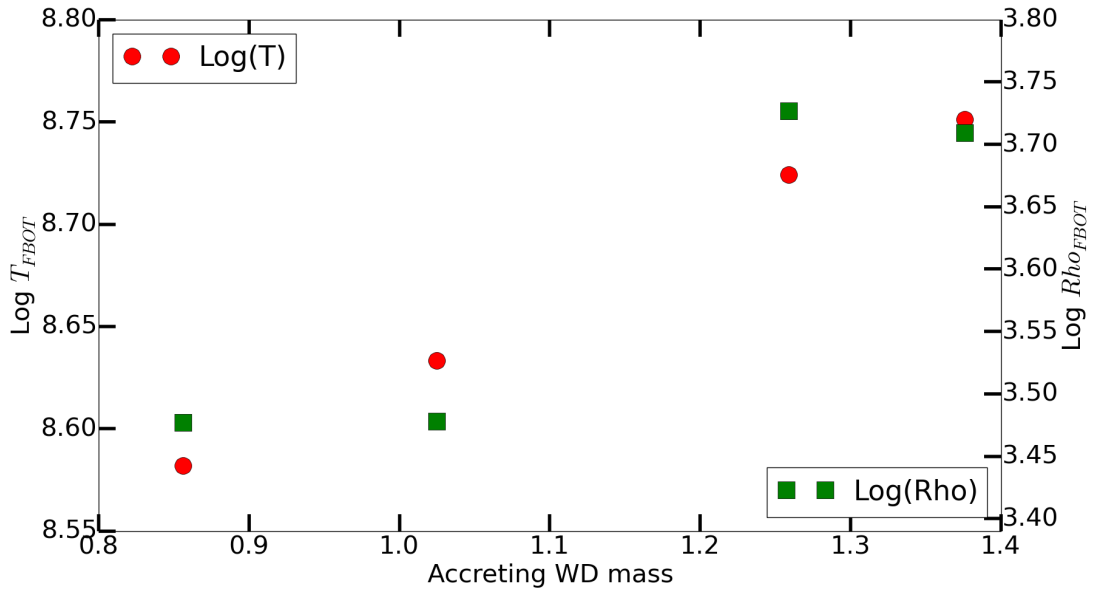
Fig. 3.6 Temperature and density at the bottom of the TPs with respect to the WD mass for the models M0p856.Z1m2, M1p025.Z1m2, M1p259.Z1m2 and M1p376.Z1m2.

proportions are similar to those found in the very late thermal pulse (VLTP) or late thermal pulse (LTP) events in post-AGB stars. A famous star experiencing a VLTP is the Sakurai's object [e.g., 77, 143]. I will come back to this point in the next section: also TPs during the accretion phase may indeed cause the ingestion of H, still present at the surface of the star (figure 3.7).

3.3.1   The model M1p025.Z1m2: extended stellar calculations

As reported in table 3.2, model M1p025.Z1m2 includes 137 convective TPs. This is the longest accreting WD model in the set presented in this thesis. For lower WD masses, I only simulate a small number of TPs. Indeed, the production of p-process isotopes in SNIa deeper than $M \sim 1\,M_{\odot}$ is not relevant, due to the simmering phase and the SN shock temperatures, which are too high to make p-process isotopes [217]. For higher WD masses, convergence criteria for stellar calculations become more and more difficult to achieve, and require more computing time. For example, with the simulations setup adopted in this work, a typical TP of the M1p025.Z1m2 model is calculated in about 7000 timesteps. More than 25000 timesteps are needed to complete a TP of the M1p376.Z1m2 model. The larger number of timesteps needed can be explained by the higher temperatures at the bottom of the PDCZ. For both simulations,
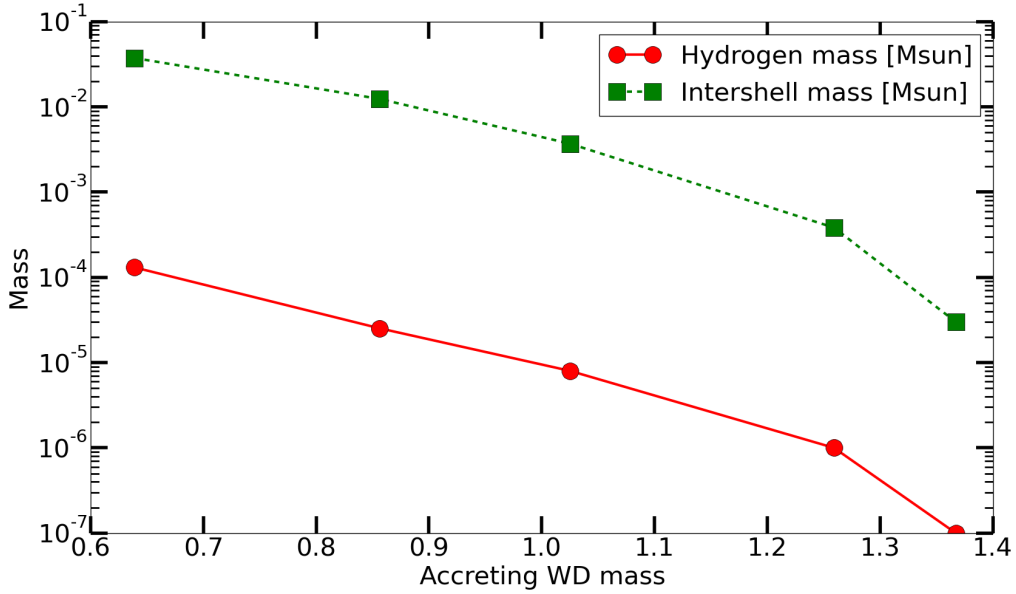
Fig. 3.7 Mass of the H-rich material accumulated at the surface of the star and He Intershell mass at the onset of the convective TP are shown, as a function of the accreting-WD mass.

the accretion interpulse phase is the most difficult to resolve, with up to 10^4 mass zones needed. The largest resolution down to $10^{-13}\,M_\odot$ is required to have convergence in the top layers where accretion and H burning is taking place. These limitations are more severe for larger WD masses and larger accretion rates.

The simulations details for different TPs of M1p025.Z1m2 are given in table B.1. Here only the numbers for the first seven TPs and the last three are reported. Their variation during the evolution is extremely slow, and local variations between TPs are not relevant. While in general the thermodynamics conditions at the bottom of the TP and the amount of mass lost after each TP event are not changing significantly during the evolution of the M1p025.Z1m2 model, I obtain an interesting evolution for the He intershell.

As shown in the Kippenhahn diagram of Fig. 3.8, upper panel, the He intershell before each convective TP is made of H-burning ashes, produced during the interpulse phase, and of older material in the He intershell that was exposed and affected by previous TPs events. These two zones will be mixed by the following TP. In the lower panel of Fig. 3.8, the evolution of the fraction of H ashes and older He-inteshell material for the sequence of TPs is given. Typical total mass of the He intershell is given in Fig. 3.7. The He intershell component becomes more relevant with increasing the TP

number: it accounts of about 50% of the material affected by the first TP event, and about 80% of the last TP in the simulations. The evolution of the intershell component in Fig. 3.8, $I(x)$, can be expressed with a polynomial-fit of the amplitude-evolution as a function of the TP number (x):

$$I(x) = 2.57e^{-15}x^7 - 1.40e^{-12}x^6 + 3.14e^{-10}x^5 - 3.85e^{-8}x^4 + 2.90e^{-6}x^3 - 0.0002x^2 + 0.007x + 0.49$$

$$(3.4)$$

The H-ashes component is simply given by $1 - I(x)$. The main reason of this variation is that the initial WD progenitor was calculated from the previous AGB phase, which, despite the many similarities, has also a number of basic differences compared to the accretion stage. This means that the common assumption that the progenitor structure is not relevant for the evolution properties during the WD accretion stage is not entirely true. Furthermore, the WD progenitor is calculated with a different simulation setup compared to the one adopted here, which makes the analysis more difficult.

While the general TP properties are not affected over 137 TPs (table B.1), these variations need to be considered as potential source of uncertainty, affecting also the nucleosynthesis calculations (see next section). The He intershell tends to evolve toward a ratio 0.8:0.2 for the old intershell and the H ashes. The same extended calculations should be done for different WD masses to verify these results (in particular for larger WD masses), but computational issues are a problem, as mentioned before.

In the lower panel of Fig. 3.8, after the 12th TP (green symbol in the figure) basically all the TPs are ingesting some H present at the WD surface. This specific feature will be discussed in the next section.

3.3.2   H-ingestion events in WD-accretion models

In Fig. 3.9, I compare the Kippenhahn diagrams obtained for the 6th and the 34th convective TPs , where the last one was affected by ingestion of H. The behavior of the convective region is affected in the upper part of the TP, where the H burning activated by the ingestion of H-rich material splits the He intershell in two parts: about 90% of the He intershell region is affected by the usual He burning at the bottom of the TP, while the remaining upper part undergoes a short convective episode, triggered by H burning (see horizontal blue line in Fig. 3.9). This result is qualitatively consistent with theoretical predictions of H-ingestion episodes in post-AGB stars [e.g., 71].
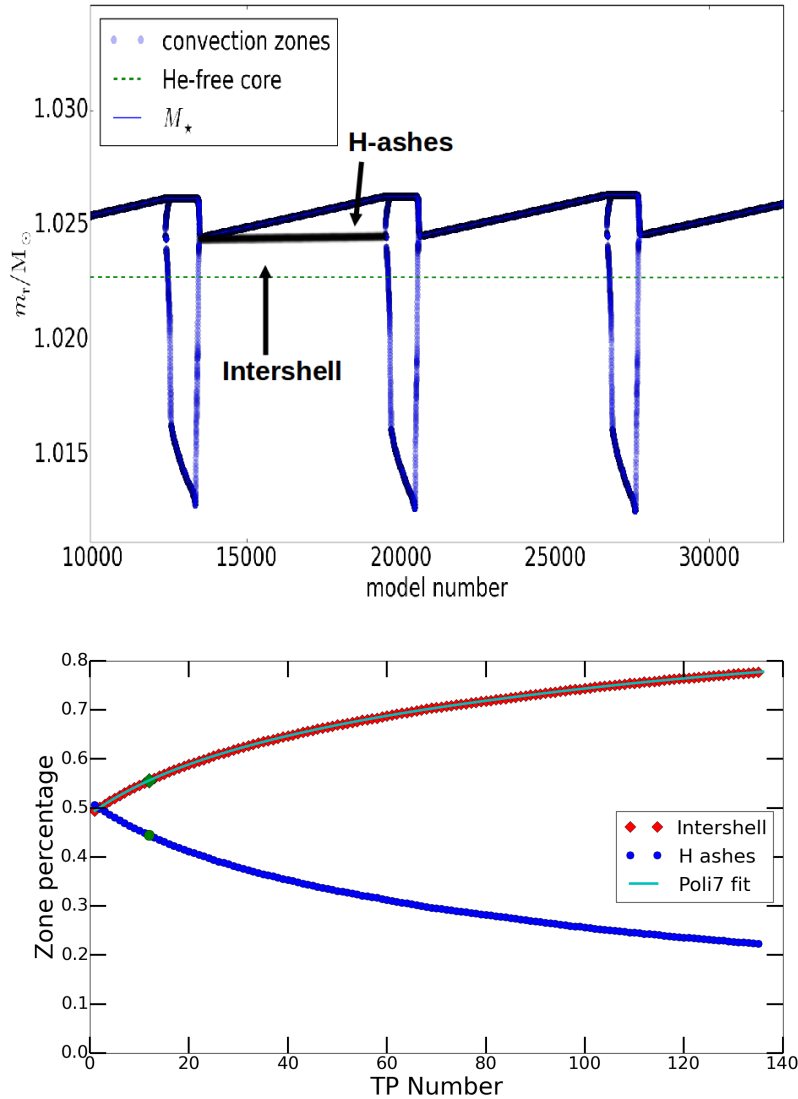
Fig. 3.8 Upper panel: Kippenhahn diagram of M1p025.Z1m2 showing the location
of H-ahes and intershell zones during the interpulse phase. Lower panel: Relative
amplitude evolution of the zones shown in the upper panel as a function of TP number.
The green symbol corresponds to the 12th TP, from which H-ingestion events start to
take place during the TPs. Continuous lines are the result of the analytical formula
reproducing the different components.
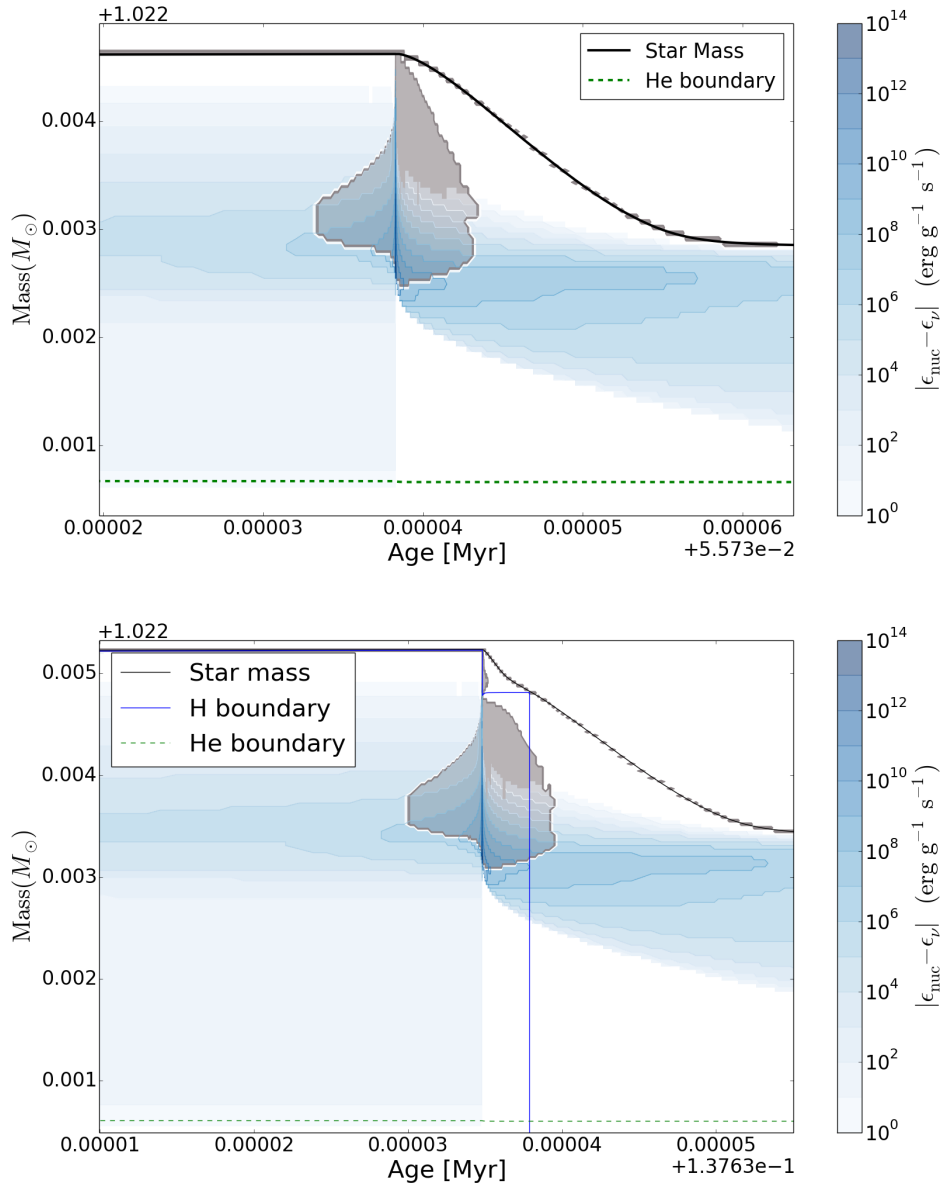
Fig. 3.9 The Kippenhahn diagrams at the 6th TP (upper panel) and at the 34th TP (lower panel) for the model M1p025.Z1m2 are shown for comparison. The 6th TP is also included in Fig. 3.4. The upper part of the 34th TP experiences H ingestion. The energy generation (blue shaded areas) and convective zones (grey-shaded areas) are indicated.

In this specific case, both the two convective regions below and above the split end before the H ingested is exhausted and the super-Eddington winds start to eject material. After about three-four months from when the split is formed, the star becomes H-free by losing a large fraction of the He intershell (the vertical blue line in Fig. 3.9 indicates when the stellar surface becomes H-free). This behavior may change for different TPs, but at least for model M1p025.Z1m2 it seems to become quite regular. For a given WD mass, similar thermodynamic conditions at the bottom of the PDCZ, He-intershell size and amount of H-rich material to accrete are the main causes of such a regular behavior. However, H-ingestion events for different WD masses may look quite different because of the differences seen in the previous sections.

It is important to keep in mind that one-dimensional hydrostatic stellar models (including the models produced in this thesis) cannot simulate the H ingestion properly, and multi-dimensional hydrodynamic calculations are needed [77, 78]. Nevertheless, one-dimensional stellar models can be adapted and constrained by gathering information from hydrodynamics simulations and observations. For instance, this was the approach followed to study the H-ingestion event in the post-AGB star Sakurai's object by Herwig et al. [77].

Unfortunately, there are no observations or specific hydrodynamics simulations available to do the same with the accreting-WD models. It would be plausible to assume that H-ingestions for WD masses of $M = 0.6 - 0.8\,M_\odot$ are similar to the VLTP observed in post-AGB stars, since the conditions of the VLTP and of the TP are in the two cases quite similar, including the amount of H available at the surface of the star [see Fig. 3.7 and e.g., 143]. However, for this work I am interested in WD masses of $M \gtrsim 1\,M_\odot$, where the TP physics properties are quite different.

In the next sections I will discuss the neutron capture nucleosynthesis in my models. I will not consider TPs affected by H ingestion in the calculations, but I will discuss its potential relevance for the conclusions of this research. In general, the occurrence of H-ingestion events is a crucial source of uncertainty that needs to be considered to provide a comprehensive picture of neutron-capture nucleosynthesis in accreting WDs.

3.4   Post-processing nucleosynthesis calculations

The nucleosynthesis during the accretion is calculated for the TPs and the relative interpulse phases indicated in table 3.2. The post-processing code `mppnp` was used (see §2.3), with the same setup and nuclear reaction rates as discussed in chapter 2.

One of the main assumptions made by Travaglio et al. [217] for their p-process calculations was a seed distribution similar to the main s-process component. As discussed in chapter 2, the production of the main s-process component in AGB stars is dominated by the ^{13}C$(\alpha,$n$)^{16}$O activation in the radiative ^{13}C-pocket. The condition to form the ^{13}C-pocket is to have CBM at the bottom of TDUs when the convective H-rich envelope penetrates the He intershell. However, during the accretion on a WD within the steady H-burning regime, there is no envelope and there are no TDU events. Thanks to the mass refinement used in these simulations (with mass resolution limit of 10^{-14} $M_\odot$), radiative ^{13}C-rich regions at the bottom of the H-burning shell are well resolved. They are in the order of 10^{-9} $M_\odot$or less, and have negligible impact for the production of heavy elements in the He intershell.

Therefore, during the interpulse phase the H burning activated on the stellar surface by the accretion is dominating the nucleosynthesis. There is no s process activated. As predicted by Iben [85], in our simulations the ^{22}Ne$(\alpha,$n$)^{25}$Mg reaction is the main neutron source at the bottom of the convective TP. As discussed in chapter 2, the ^{22}Ne$(\alpha,$n$)^{25}$Mg is partially activated in low-mass AGB stars, with neutron densities up to few 10^{11} cm^{-3}. The typical timescale of few decades of convective TPs and the temperatures at the bottom of the PDCZ in these stars do allow to fully consume the ^{22}Neby α capture.

However, the temperature at the bottom of the PDCZ increases with the increase of the CO core (and of the WD mass). This is why larger neutron densities and a more efficient ^{22}Nedestruction are obtained in massive AGB stars [e.g., 104, 202] and even more in super AGB stars [e.g., 49]. The same happens for TPs in accreting WDs. In low mass AGB stars, typical temperature conditions obtained at the bottom of TPs are about 3×10^8 K or less. According to table B.1, typical T$_{FBOT}$ ranges from 3.2×10^8 K (model M0p639.Z1m2) up to 5.9×10^8 K (model M1p376.Z1m2). The T$_{FBOT}$ variation is also shown in Fig. 3.6 excluding the model M0p639.Z1m2, which has conditions similar to low-mass AGB stars. The higher temperatures obtained cause an efficient ^{22}Nedepletion by α capture, producing neutron densities up to four orders of magnitude higher than typical TPs in low mass AGB stars.

In Fig. 3.10, I show the neutron density calculated in the temperature range of interest, by using realistic abundances from the He intershell abundances of model M1p025.Z1m2 at the onset of the TP, which is similar to the other models presented here. The initial ^{22}Ne abundance in mass fraction is X(^{22}Ne) = 0.00393 (0.393%). The neutron density peak obtained ranges from few 10^{11} cm^{-3} up to few 10^{15} cm^{-3}, that is well beyond the s-process typical conditions.
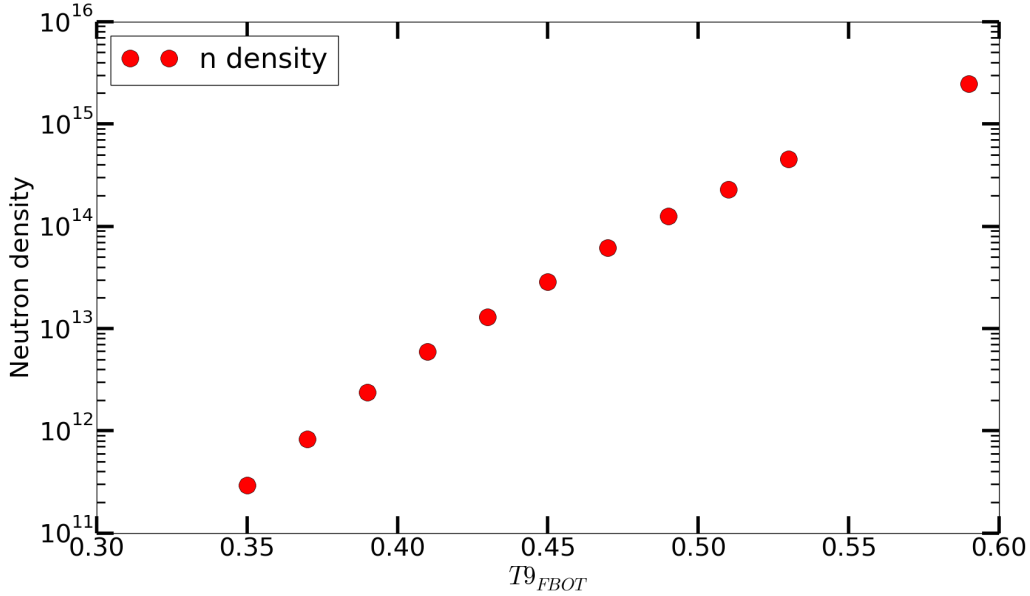
Fig. 3.10 Neutron density from ^{22}Ne$(\alpha,\text{n})^{25}$Mg as a function of temperature at the bottom of the TP during the accretion phase.

As mentioned before, I want to calculate the neutron seeds for the *p*-process, and therefore I am mostly interested in the nucleosynthesis for WD masses $M \gtrsim 1\,M_\odot$. Combining Fig. 3.6 with the results shown in Fig. 3.10, TPs for WD masses of $M \sim 1\,M_\odot$ or larger are characterized by temperatures of about 4×10^8 K or higher, which means the neutron density peaks will be few 10^{12} cm^{-3} or higher.

In the upper panel of Fig. 3.11, the abundance distribution beyond Fe in the He intershell at the end of the 7th TP of model M1p025.Z1m2 is shown. All the nucleosynthesis up to this stage has been consistently simulated trough the previous TPs by the mppnp code. The largest production is obtained for elements between Fe and Zr, in the mass region typical of the weak s process [e.g., 166]. On the other hand, neutrons are mostly released at neutron densities larger than in massive stars. The isotopes produced the most are ^{86}Kr, ^{87}Rb and ^{96}Zr. Also ^{70}Zn, ^{76}Ge and ^{82}Se, that are classically indicated as r-process isotopes, are efficiently made together with other isotopes nearby that are less neutron-rich. The heaviest isotope showing a production factor in the order of 100 is ^{123}Sb, but overall the production efficiency decreases beyond Zr. The impact of the two main neutron-source rates is also given, showing the distribution resulting setting the ^{13}C $(\alpha,\text{n})^{16}$O or the ^{22}Ne$(\alpha,\text{n})^{25}$Mg reaction rates to zero. In particular, the ^{22}Ne$(\alpha,\text{n})^{25}$Mg results to be the key reaction producing isotopes till A=130. The situation changes significantly when considering the M1p259.Z1m2

model, as shown in the lower panel: in this case the ^{13}C $(\alpha, n)^{16}$O is the main neutron source producing the bulk of the final distribution, as a result of the larger efficiency of H-ingestion producing ^{13}C in the intershell during the TP. Therefore, the main role in producing the neutrons necessary to the synthesis of the final heavy elements distribution, passes from the ^{13}C $(\alpha, n)^{16}$O to the ^{22}Ne$(\alpha,n)^{25}$Mg as soon as the WD mass overcomes a sort of critical value between 1.03 and 1.26 $M_\odot$.

The larger production of the elements at the neutron magic peak N=50 (Sr, Y and Zr) compared to heavier elements at the neutron magic peak N=82 (e.g., Ba and La) is not surprising, since the neutron source is ^{22}Ne. Even the complete depletion of ^{22}Ne by α-capture in massive stars does not allow to produce efficiently s-process elements much heavier than Sr [e.g., 101]. The main reason is that ^{22}Ne is also efficiently capturing neutrons via (n,γ), and the ^{22}Ne$(\alpha,n)^{25}$Mg efficiently produce ^{25}Mg, which is a strong neutron poison [e.g., 166]. Therefore, the impact of a stronger production of neutrons by ^{22}Neis partially compensated by the higher efficiency of light isotopes in capturing these neutrons compared to the Fe seeds.

In Fig. 3.12, upper panel, the production of the neutron-magic isotopes ^{87}Rb and ^{88}Sr, for ^{96}Zr and for the neutron-magic isotope ^{138}Ba is shown for different TPs in the M1p025.Z1m2 model. As observed in Fig. 3.11, ^{138}Ba is not efficiently produced. Interestingly, the abundances increase up to about the 3rd TP, and then they saturate to some production factor in the following TPs. This is due to the fact that at each TP the super-Eddington wind ejects a large fraction of the He intershell. During the following accretion interpulse phase, new H ashes are built until the next convective TP starts. As discussed in section 3.3.1 (see also Fig. 3.8), at this point the He intershell will be made of two components: 1) the old intershell component, rich of heavy isotopes made by neutron capture in the previous TPs, Fe-poor and ^{22}Ne-poor; 2) the H-ashes component, where the heavy abundances are representative of the accreted material, and the initial CNO has been mostly converted to ^{14}N by the CNO cycle. As soon as the convective TP mixes these two components, the ^{14}N in the H ashes will be converted into ^{22}Ne by α captures, becoming available to produce neutrons. Since the different TPs are quite similar, the ^{22}Ne and the Fe seeds available will be more or less the same, yielding a similar production of heavy elements by neutron captures TP after TP. To this fresh neutron-capture products, the old enriched intershell component needs to be accounted for. The first TP in Fig. 3.12 starts from the accreted composition, and has no memory of previous TPs by definition. Instead, the next TPs will include a fraction of the heavy abundances made in previous TPs. After 3-4 TPs, a stable balance between the two components is obtained.
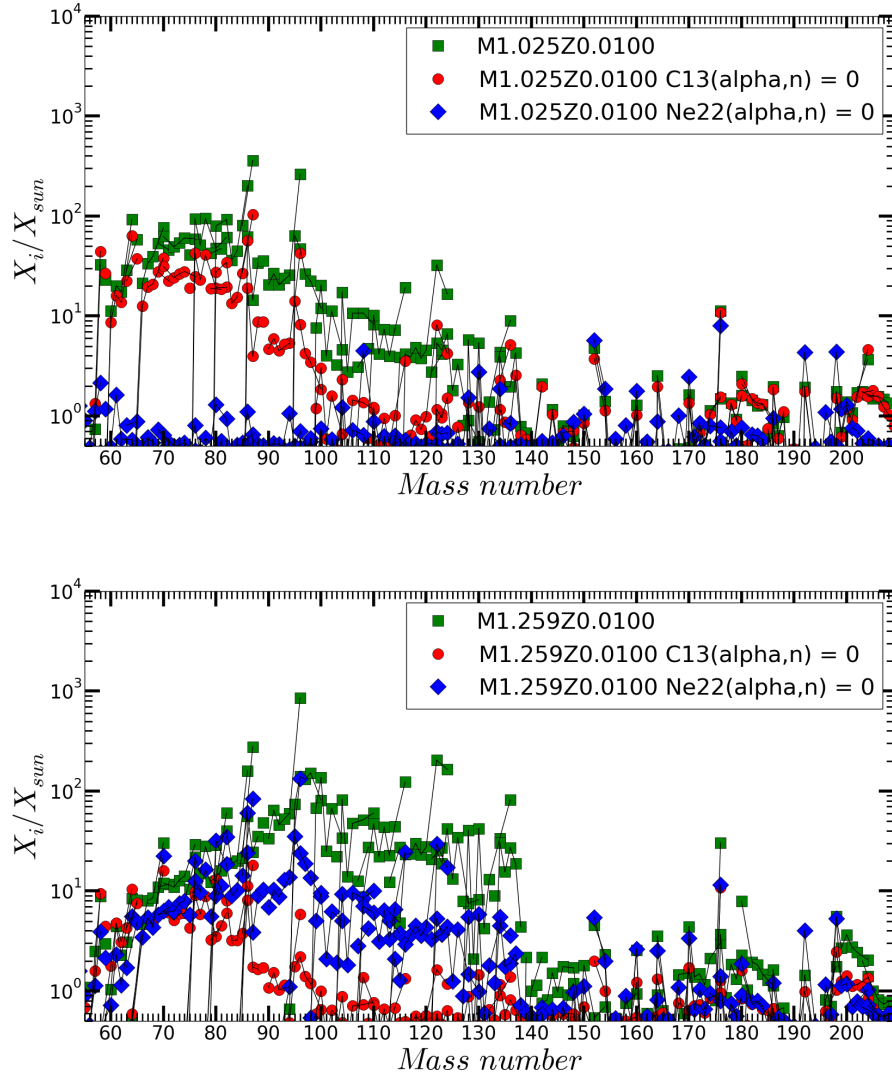
Fig. 3.11 Upper panel: Isotopic distribution beyond Fe at the 7th TP of model M1p025.Z1m2. The impact of the two main neutron-source rates is also given, showing the distribution resulting setting the ^{13}C $(\alpha, n)^{16}$O or the ^{22}Ne$(\alpha,n)^{25}$Mg reaction rates to zero. The abundances are plotted assuming complete decay of unstable isotopes. Lower panel: same as in the upper pannel, but for the M1p259.Z1m2 model.
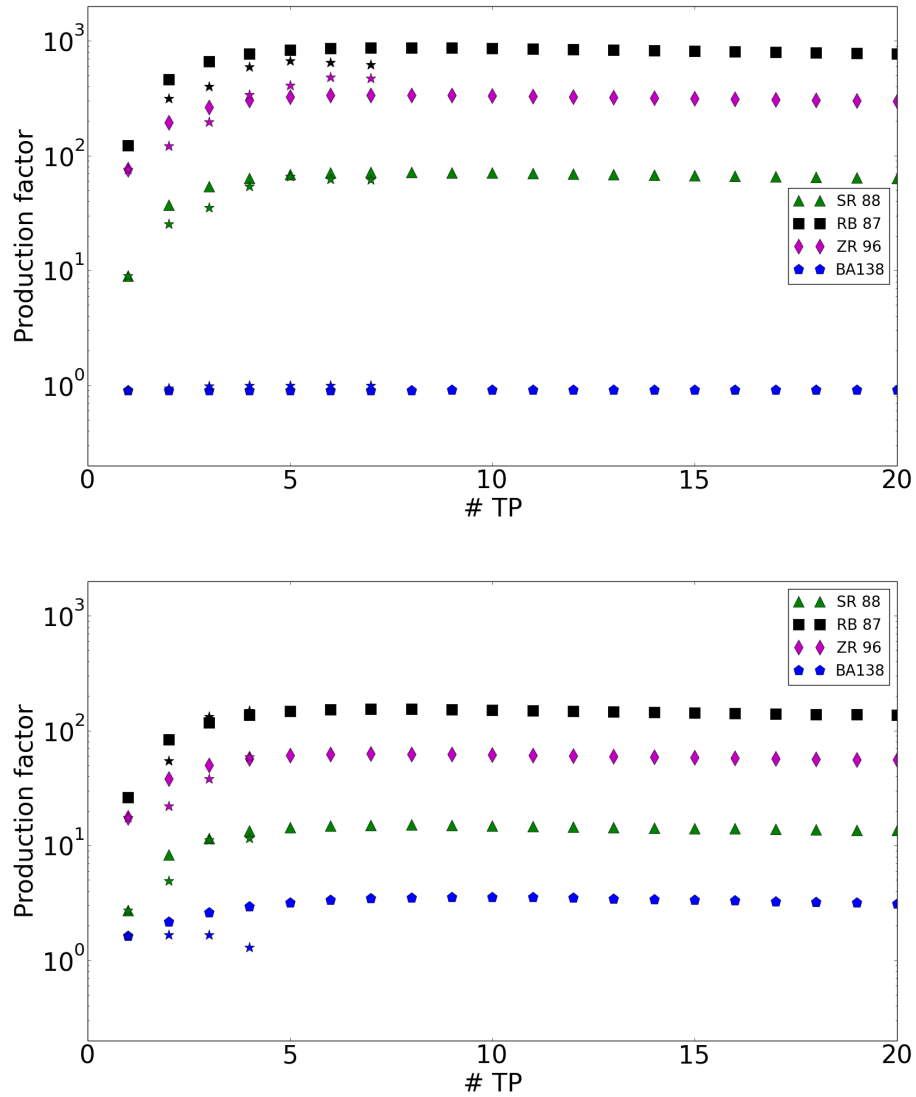
Fig. 3.12 Upper panel: the evolution of the production factors for ^{87}Rb, ^{88}Sr, ^{96}Zr and ^{138}Ba is shown as a function of the TP number for model M1p025.Z1m2 (stars). The calculations results are compared to the results from an analytical model (circles, see description in the text). Lower panel: the same as in the upper panel, but for the M0p856.Z1m2 model.

This means that there is no need to calculate with the post-processing code all
the 137 TPs of model M1p025.Z1m2 to know what is going to be the final abundance
distribution. In Fig. 3.12, upper panel, the `mppnp` results are compared with the
calculations obtained by using a simple analytical model (for the distribution in the
figure I used as a reference the 3rd TP). In this model, the distribution of production
factors of a typical TP are multiplied by the abundance distribution given by the
mixture of two components: the H-ashes (with normal heavy element abundances)
and the old intershell (already enriched by previous neutron capture processing). The
relative weight of the two components can be taken from Fig. 3.8. In Fig. 3.12 the
analytical distribution shows the same behavior observed in the full nucleosynthesis
calculations, saturating the production factors after the 5th TP. Of course the results
are not exactly the same. There are some differences due to the simplifications in the
analytical model, but the main features and the general abundance pattern are the
same.

To verify these results, in Fig. 3.12, lower panel, I also compare the `mppnp` calcula-
tions for the first 4TPs of the M0p856.Z1m2 model with the analytical calculations
using the results of the 3rd TP from the same model. Again, the saturation of the
production is obtained, and `mppnp` and the analytical model give similar results.

Therefore, for a given WD mass, by only simulating few convective TPs it is possible
to obtain a good estimation of the heavy isotope abundances in the He intershell.
As I have shown in the previous sections, the He intershell conditions during the
entire accretion phase up to the Chandrasekhar mass are evolving significantly. The
neutron density peak due to the ^{22}Ne(α,n)^{25}Mg reaction changes by four orders of
magnitude, also indicating a more and more efficient depletion of the available ^{22}Ne.
The production factors shown in Fig. 3.12 calculated for the M1p025.Z1m2 model are
larger than the ones calculated for the M0p856.Z1m2 model. This can be better seen
in Fig. 3.13, where the abundance distribution calculated for different WD masses is
shown. The complete abundance distributions are also given in Tab. B.2.

The production factors tend to increase with the increase of the WD mass, due
to the most efficient production of neutrons. The abundance distribution for the
M0p856.Z1m2 and M1p025.Z1m2 models is quite similar, with the largest efficiency in
the mass region between Fe and Zr. On the other hand, the distributions obtained
for the M1p259.Z1m2 model shows a strong production up to ^{136}Xe, while the one
obtained in M1.376.Z1m2 continues with large efficiency up to the Pb region. In the
figure, the larger neutron exposure obtained is given by the numerous H-flashes shown
in Fig. 3.14, which trigger proton captures onto the abundant ^{12}C producing ^{13}C ,
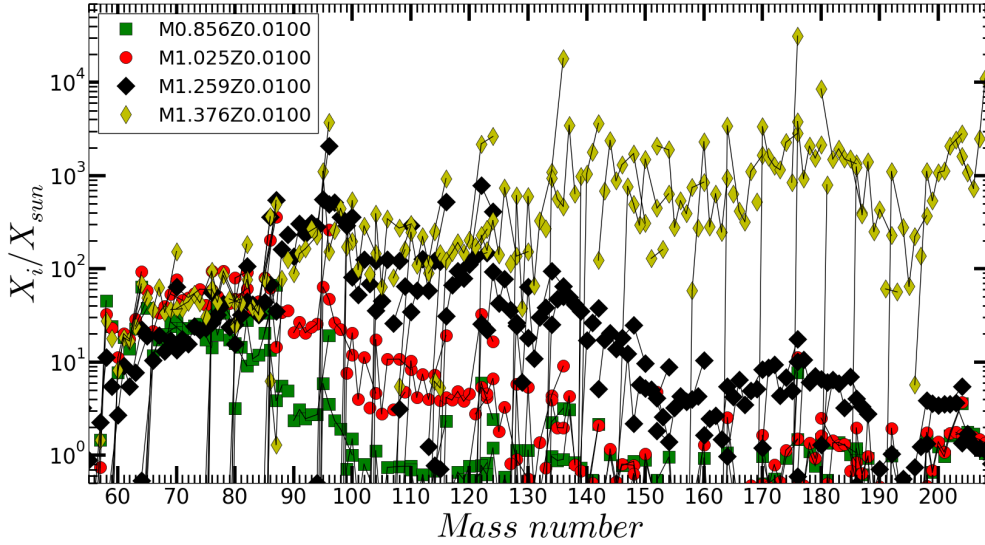
Fig. 3.13 Final abundance distribution calculated for models M0p856.Z1m2, M1p025.Z1m2, M1p259.Z1m2 and M1p376.Z1m2.

which is then completely burned radiatively via ^{13}C $(\alpha, n)^{16}$O in a region of the order of 10^{-7} $M_\odot$, concentrating all the neutron captures in a very tiny zone and with a resulting very high neutron exposure and a nuclear production reaching the Pb region. Notice that this happens during the time interval before the onset of the TP. The most produced isotopes in the Pb region is ^{204}Hg and ^{209}Bi.

Therefore, these calculations show that in the SNIa progenitor the heavy seeds of the p-process are changing between $M \sim 1\,M_\odot$ and the surface: the abundance distribution will be enriched between Fe and Zr in the deepest (and hottest) layers that will host the p-process products; instead, the abundance distribution will be enriched up to and over the Ba mass region approaching the surface [where the heaviest p-process products are made 217]. Moving from $M \sim 1\,M_\odot$ outward, the production factors are also increasing up to more than one order of magnitude between Fe and Zr, and even two orders of magnitude between Zr and Xe. Elements heavier than Ba can increase up to three order of magnitude approaching the surface, while over the mass range between 0.85 $M_\odot$ and 1.26 $M_\odot$ in the progenitor they are always less abundant compared to the lighter neutron capture products.

As example, in Fig. 3.15 I show the average production factor of ^{86}Kr, ^{87}Rb, ^{88}Sr, ^{89}Y, ^{90}Zr and ^{96}Zr for models M0p856.Z1m2, M1p025.Z1m2, M1p259.Z1m2 and M1p376.Z1m2. The production factor increases up to two orders of magnitude, as
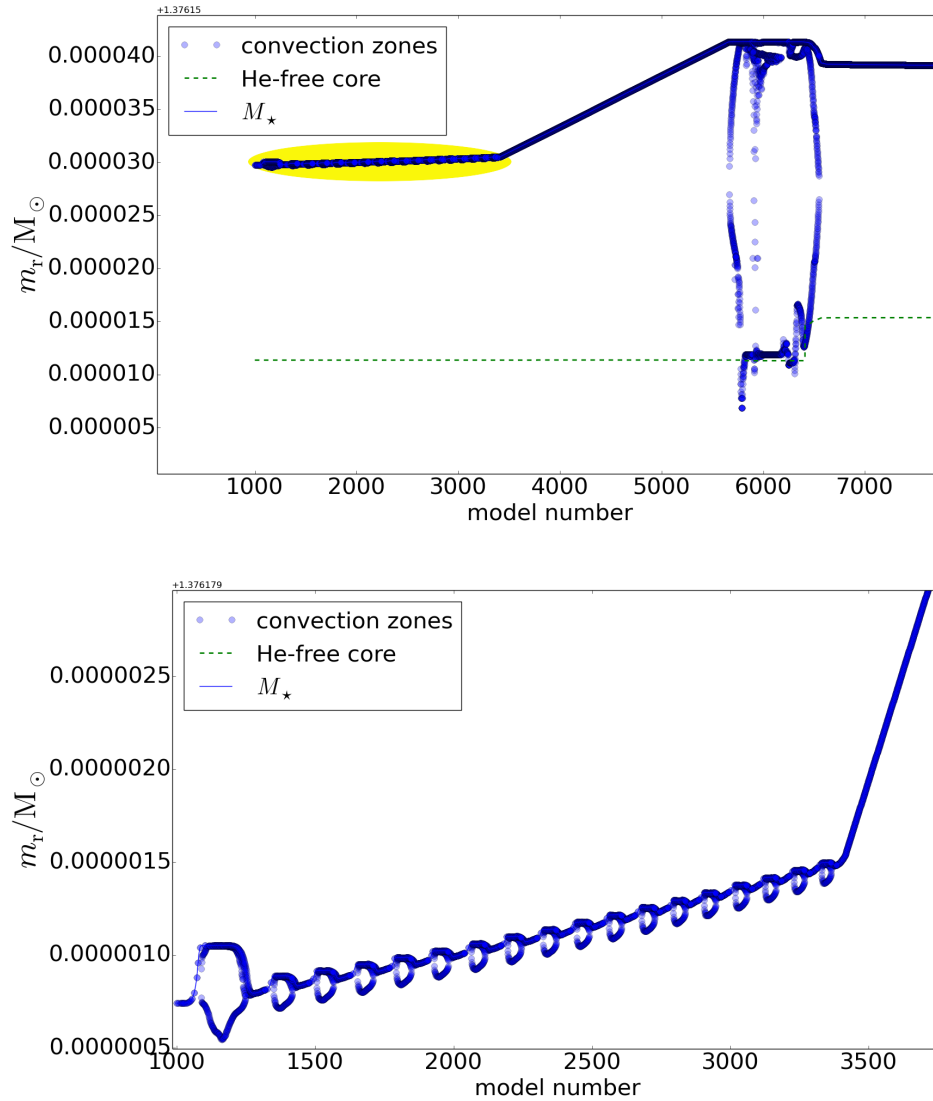
Fig. 3.14 Upper panel: Kippenhahn diagram of the accretion phase of our 1.376 M$_\odot$ accreting WD model. Indicated are the convective boundaries of the TP and the surface of the star. The zone highlighted is where the H-flashes take place. Lower panel: The highlited zone in the upper panel is zoomed in, showing in detail the sequence of H-flahes responsible of the production of ^{13}C in a tiny 10^{-7} $M_\odot$ zone just below the WD surface.

seen in Fig. 3.13. The logarithm of the production factor shown in the figure might be interpolated from the simulated data. For instance, by using a linear fit with the WD mass, the following equation is obtained:

$$Log(PF) = 4.24 \times M_{WD} - 2.49 \qquad (3.5)$$

where PF is the production factor and M_{WD} is the WD mass. Similar equations can be obtained for each single isotope by using the abundances available in Tab. B.2, providing the distribution of the p-process seeds for a given mass coordinate of the SNIa progenitor. In particular, we provide the parameters for linear fit in Tab. B.3. The validated stellar mass range is between $0.86\,M_\odot$ and $1.38\ M_\odot$, covering the needs of the p-process in SNIa.
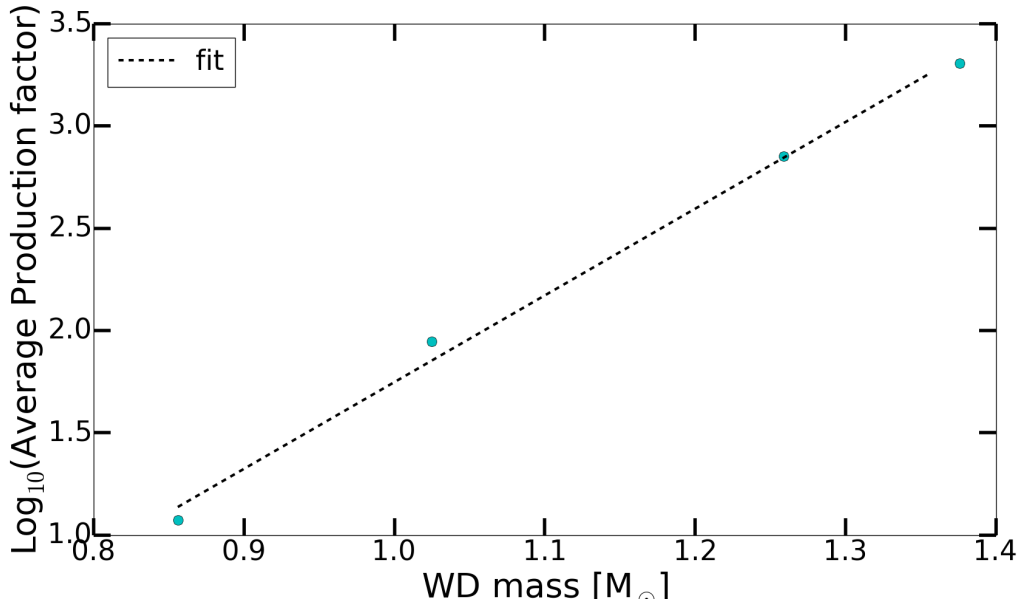
Fig. 3.15 Average logarithmic production factors as a function of WD mass. The average was calculated considering the isotopes with the highest production factor: Kr^{86}, Rb^{87}, Sr^{88}, Y^{89}, Zr^{90} and Zr^{96}. Also a linear fit is shown.

3.5 Summary of the nucleosynthesis results and stellar uncertainties

In the previous section I have analyzed the neutron capture nucleosynthesis in accreting WD models. My interest is mostly focused on WDs with masses larger than $1\,M_\odot$.

Only the external 0.2-0.3 $M_\odot$ of the SNIa progenitor are relevant for the *p*-process production [217], and realistic *p*-process seeds made by neutron captures during the accretion phase were needed.

The calculations presented in this work do not rule out the seed assumptions made by Travaglio et al. [217] and Travaglio et al. [216]: the neutron capture process activated during the accretion phase looks like the main s-process component in the very external zones of the WD when it approaches the Chandrasekhahr limit. The main neutron source is the $^{22}\text{Ne}(\alpha,\text{n})^{25}\text{Mg}$ for WD masses lower than 1.2 $M_\odot$, while for higher masses the $^{13}\text{C}(\alpha,\text{n})^{16}\text{O}$ plays a major role. Those reactions are activated at the bottom of convective TPs in the He intershell, with a possible additional and critical contribution during the interpulse period by the $^{13}\text{C}(\alpha,\text{n})^{16}\text{O}$ when the WD mass is close to Chandrasekhahr. In my simulations, the $^{22}\text{Ne}(\alpha,\text{n})^{25}\text{Mg}$ is activated in a temperature range between 4×10^8 K and 5.9×10^8 K, with neutron density peaks between few 10^{12} cm^{-3} and few 10^{15} cm^{-3}, much higher than the typical s-process conditions. The isotopic distribution obtained at the end of the TP is changing with the WD mass: the isotopes between Fe and Zr are mostly produced for WD masses of about 1 $M_\odot$, while for WD masses close to the Chandrasekhar mass also heavier isotopes are efficiently made, up to Bi. The overall production of neutron-capture species increases with the WD mass, with variations of 3-4 orders of magnitude in the external $\sim 0.4\,M_\odot$ of the SNIa progenitor.

These results will need to be tested as seeds for the *p*-process production in SNIa. But first it may be important to spend few words about the uncertainties affecting these calculations. I have explored the impact of CBM at the He intershell boundaries, and this component has likely a minor impact compared to other sources of uncertainty. I have also mentioned that the uncertainty associated to the stellar structure of the WD used to start the accretion can be considered of smaller relevance. However, I have discussed the case of the M1p025.Z1m2 model, where the relative variation of the balance between the H-burning ashes and the older He-intershell material may be due to the progenitor structure from which I started the simulations.

The major source of uncertainty for which it is difficult to set some definitive conclusions is the occurrence of H ingestion, discussed in section 3.3.2. For the M1p025.Z1m2 model, the H ingestion becomes common after 12 TPs, while for other WD masses we did not simulate the models long enough to study this event with more detail. For the case the I have discussed, the He intershell is split in two by the H burning. This is the same that is obtained for H ingestion events in post-AGB

stars. In post-AGB stars H ingestion has been shown to trigger the activation of the intermediate neutron capture process, or i-process [77].

The i-process was first proposed theoretically by Cowan and Rose [35], associated to the ingestion of fresh H in deeper and hotter He-burning stellar layers in stars. The capture of protons on the abundant ^{12}C (direct product of He-burning) produces the unstable isotope ^{13}N that decays to ^{13}C, the main neutron source of the i-process via the ^{13}C$(\alpha,n)^{16}$O reaction. The neutron densities associated with the i process are about few 10^{15} cm^{-3}, that is orders of magnitude lower than the r-process, but still higher than the s-process. The i-process has been ignored in the conventional nucleosynthesis picture. Firstly, its observational evidence was missing. Recently, observational evidences of the i-process signature are collected from different astrophysical sources, e.g., in young open stellar clusters [145] and in a sample of old Carbon Enhanced Metal Poor stars [CEMP-rs stars, 42]. Secondly, the baseline one-dimensional hydrostatic stellar models fail to simulate the H ingestion, suppressing the i-process activation. As mentioned in section 3.3.2, in order to account for the H-ingestion events and their nucleosynthesis products, one-dimensional stellar models need to be guided by full 3D-hydrodynamic simulations [e.g., 78].

H-ingestion events are found in the stellar simulations presented here, and there is the possibility that the i-process is also activated. The i-process, powered by the ^{13}C$(\alpha,n)^{16}$O during the convective TPs, could potentially change the results of this work, allowing to produce heavier abundances more easily than with the ^{22}Ne$(\alpha,n)^{25}$Mg. Multidimensional hydrodynamics simulations are made to study the H ingestion in post-AGB stars. The same events in accreting WDs represent other important candidates to study in future simulations. Finally, one more source of uncertainty is the still unknown size of the surface zone experiencing the very high neutron-exposure conditions able to produce heavy isotopes up to Bi: this aspect is critical for the p-process nucleosynthesis taking place during the WD explosion [217]. Until then, not much is possible to do to better constrain these events in accreting WDs. However, two important considerations can be made: 1) The most well known star where the H ingestion and the i-process took place is the Sakurai's object. As mentioned before, VLTP events in post AGB stars have several similarities with the TPs in accreting WD models. In the Sakurai's object, the i-process produced efficiently heavy abundances up to the Rb-Sr mass region, while heavier elements were only marginally affected. This means that if during the accretion phase the i-process episodes are similar to the VLTP case, the ^{13}C$(\alpha,n)^{16}$O should produce an amount of neutrons comparable to the ^{22}Ne$(\alpha,n)^{25}$Mg. Therefore, results could not look so much different from what I have obtained here. 2) The

^{22}Ne(α,n)^{25}Mg is efficiently activated at the high temperatures obtained for high WD masses, up to neutron densities that are also typical of the i-process. This means that similar heavy isotopic distributions would be obtained, whether the neutron source is ^{13}C or ^{22}Ne, at least in the mass region between 1 $M_\odot$ and 1.3 $M_\odot$.

Chapter 4

Conclusions

In this thesis I have presented my research in stellar evolution and nucleosynthesis of intermediate-mass stars. My work was focused on two distinct evolutionary stages. First I focused on the AGB evolution phase and on the s-process nucleosynthesis. In this case I have simulated the evolution of single stars, without considering any feedback from e.g., binary system evolution. I have also not considered the contribution from rotation and magnetic field. Instead, I have included in my simulations a new parameterization of the convective-boundary-mixing (CBM) at the He intershell boundaries, based on the best data available from multidimensional hydrodynamics simulations. Secondly, I have simulated the accretion of material with Z=0.01 and the following nucleosynthesis on the surface of a WD. The donor of this material is another star bounded with the WD in a binary system. I did not follow consistently the details of the binary evolution. Instead, I have assumed an accretion rate constant with time, but different within the range of WD mass considered. The accretion rate was previously calculated to evolve the accretion within the steady H-burning regime. This choice was made because these are the most favorable conditions for the accreting WD to reach the Chandrasekhar mass, and explode as a SNIa. My goal in this case was to simulate the neutron capture nucleosynthesis during the accretion phase, to constrain the abundance distribution of the p-process seeds made in the external part of the SNIa ejecta.

The evolution and nucleosynthesis for both the two types of stars are dominated by the interaction between H burning and shell He burning in the stellar region called He intershell. He burning is triggered by the He flash at the bottom of the He intershell, forcing the entire region to become convective in a thermal pulse (TP) and to expand. For all the work included in this research I have consistently used the same stellar code `MESA` and for the nucleosynthesis the post-processing code `mppnp`.

I have calculated eleven AGB stellar models with initial mass M $= 2\,M_\odot$ and $3\,M_\odot$, and initial metallicity Z $= 0.01$ and 0.02. Additionally, I have provided seven more stellar runs using the same stellar structures, but by using different nuclear reaction rates that are not relevant for energy generation. For the first time, these models study the impact of the CBM at the bottom of convective TPs keeping into account Kelvin-Helmholtz and gravity waves instabilities, guided by hydrodynamics simulations and by observations in post-AGB stars. The CBM at the bottom of the third dredge-up is introduced according to the simulations of Denissenkov and Tout [45]. In this case, gravity waves are the dominant physics mechanism to set the conditions to form the ^{13}C-pocket in the He intershell.

The Kelvin-Helmholtz instabilities at the bottom of convective TPs are affecting the AGB evolution and the He intershell abundances by allowing to accumulate C and O, and reducing the He abundance. My results are consistent with previous AGB simulations where overshooting was assumed to be the dominant CBM mechanism. In these models, the final C and O mass fractions in the He intershell are 0.4-0.5 and 0.2-0.1, respectively. Compared to Kelvin-Helmholtz instabilities, gravity waves have a marginal contribution.

At the end of the the AGB evolution we obtain an s-process production of 0.36 $<$[s/Fe] $<$0.78 and -0.23 $<$[hs/ls] $<$0.45, which is consistent with spectroscopic observations. I have explored the impact on the nucleosynthesis results of the uncertainty in the adopted CBM parameterization at the bottom of the TDU, considering a range of acceptable fitting of Denissenkov and Tout [45] results, and increasing up to a factor of ten their efficiency. Interestingly, the overall impact is comparable to the effect of the uncertainty of the ^{14}N(n,p)^{14}C nuclear rate. For instance, by increasing of a factor of two the mentioned rate at a relevant energy of $\sim$8 keV is reducing the final [hs/ls] by 0.05-0.1 dex. This implies that in order to better explore what is the correct CBM scenario responsible for the formation of the ^{13}C-pocket, the ^{14}N(n,p)^{14}C rate needs to be constrained with an error much lower than a factor of two.

The s-process abundance signatures in presolar C-rich grains are the most challenging and constraining observations to study the s-process nucleosynthesis in AGB stars, and crucial information are provided also about the stellar conditions in the He intershell of the parent stars. These AGB models does not have a good reproduction of a number of isotopic ratios measured in presolar grains. I have focused my analysis in the Zr isotopes. AGB models with CBM activated at the bottom of the convective TP always showed problems to reproduce the Zr abundances in presolar grains, in particular at the ^{95}Zr branching and the consequent overproduction of ^{96}Zr. I confirm

that at least part of these problems to fit the Zr measurements is still an issue also for my models. On the other hand, Piersanti et al. [164] and Liu et al. [128] showed that a physics mechanism like rotation affects the main properties and the nucleosynthesis in the ^{13}C pocket *after* its formation. From preliminary explorations on the impact of slow extra-mixing processes like e.g., molecular diffusion, I can anticipate that this could definitely solve this conundrum. With the implementation of molecular diffusion adopted in this work, I have shown that the impact on the stellar results is marginal. However, if molecular diffusion (or any other physics mechanism triggering a slow mixing between the ^{13}C-pocket and the upper ^{14}N-rich layers) would have been a factor of 2-5 higher, the resulting s-process production in the ^{13}C-pocket could be more efficient at the Sr-Y-Zr peak and produce less Ba and La. A larger s-process production in the Zr mass region would naturally solve the present overproduction of ^{96}Zr compared to the other Zr isotopes, by producing those isotopes more efficiently.

In the second part of the thesis, I have calculated a set of five accretion models considering four initial WD masses: $M = 0.639, 0.856, 1.025, 1.259$ and $1.376\,M_\odot$ accreting material with metallicity Z = 0.01. I adopted the same CBM formalism introduced in the first part of this thesis. The model with WD mass $M = 0.639\,M_\odot$ is not crucial for the purpose of this analysis, therefore in this case I did not calculate the complete nucleosynthesis. During the accretion phase, all the models go through recurrent TPs, experiencing temperatures at the bottom of the PDCZ growing with the WD mass. The largest temperature at the bottom of the TP is obtained for the model with the largest WD mass, $M = 1.376\,M_\odot$, and it is 5.9×10^8 K.

The stellar conditions during the convective TPs are crucial for neutron capture nucleosynthesis. During these events the ^{22}Ne$(\alpha,$n$)^{25}$Mg and the ^{13}C$(\alpha,$n$)^{16}$O are activated and are the main neutron sources for masses lower and higher than 1.2 $M_\odot$ respectively. In particular, with this work I have shown that the assumption made by Travaglio et al. [217] that the p-process seeds in SNIa are similar to the main s-process component, could be correct. More precisely, the ^{22}Ne$(\alpha,$n$)^{25}$Mg mostly produce heavy elements between Fe and Zr for WD masses of $M \sim 1\,M_\odot$, while elements up to Bi can be made for larger WD masses. This is due to the extra contribution coming from the production of ^{13}C during the H-flashes and his consumption during the interpulse period when the WD is close in mass to the Chandrasekhahr limit. Also the total production efficiency increases with the WD mass increase: between $M \sim 1\,M_\odot$ and the surface of the SNIa progenitor the abundances of heavy elements may increase up to 3-4 orders of magnitude, depending on the mass region. Finally, due to the temperature rise the neutron density peak also increases with the WD mass. Again,

the model with the largest WD mass, $M = 1.376\,M_\odot$, experienced the largest neutron densities, up to values in the order of few 10^{15} cm^{-3} that are well above the s-process regime.

For the first time, I presented here the results of neutron capture processes from realistic simulations of the WD-accretion phase. These can now be used as seeds for the p-process calculations in SNIa. Nevertheless, more simulations should be done in the future. First of all, the mass accretion rate should be included taking into account consistently also the evolution of the binary system during the accretion. These results were obtained by using accreted material with metallicity Z=0.01. The same calculations should be done by accreting material with different composition. If I just focus on the simulations presented in this thesis, the largest uncertainty that could affect my conclusions is the occurrence of H-ingestion events during the accretion stage. Multiple H ingestions are obtained in the model at WD mass $M = 1.025\,M_\odot$. The same did not happen for different models probably because too few TPs were simulated.

Baseline stellar codes cannot simulate properly H ingestion, and multidimensional hydrodymanics models are needed to explore this scenario. The good news is that these kind of simulations are already done for H-ingestion events in post-AGB stars, that are not too different from the models considered here. I discussed the modification of the TPs behaviour when H ingestion is obtained in my models. This was just a rough grasp of what could happens in more realistic simulations. Neglecting for now the impact on the stellar structure, the main conclusions of this work could be affected because the i-process is activated following the H ingestion, producing heavy isotopes beyond Fe at neutron densities in the order of 10^{15} cm^{-3}. The ^{13}C$(\alpha,$n$)^{16}$O activation and the consequent i-process production was observed after the Very Late Thermal Pulse in the surface of the Sakurai's object, a post-AGB star that is a close relative of the events discussed here. I do not have strong arguments at the moment to better constrain the conditions of the i-process activation in accretion WD models. There are no observations available that might help to guide this analysis further at the moment.

On the other hand, the larger temperatures experienced at the bottom of the TPs in accreting WD models compared to AGB and post-AGB phases allow to activate more efficiently the ^{22}Ne$(\alpha,$n$)^{25}$Mg, up to neutron densities similar to the i-process. Furthermore, the amount of neutrons made by the ^{13}C$(\alpha,$n$)^{16}$O in the Sakurai's object was enough to produce efficiently only up to the Rb-Sr mass region [77]. This means that in case similar i-process events are triggered during the accretion, the two neutron sources ^{22}Ne and ^{13}C could have comparable strengths, not dramatically changing the present conclusions.

Finally, one more source of uncertainty is the still unknown size of the surface zone experiencing the very high neutron-exposure conditions able to produce heavy isotopes up to Bi: this aspect is critical for the p-process nucleosynthesis taking place during the WD explosion [217].

References

[1] Abia, C., Busso, M., Gallino, R., Domínguez, I., Straniero, O., and Isern, J. (2001). The ^{85}Kr s-Process Branching and the Mass of Carbon Stars. *ApJ*, 559:1117–1134.

[2] Abia, C., Domínguez, I., Gallino, R., Busso, M., Masera, S., Straniero, O., de Laverny, P., Plez, B., and Isern, J. (2002). s-Process Nucleosynthesis in Carbon Stars. *ApJ*, 579:817–831.

[3] Alecian, G. and Michaud, G. (2005). About diffusivity, radiative viscosity and particle transport. *A&A*, 431:1–5.

[4] Amari, S. (2009). Sodium-22 from Supernovae: A Meteorite Connection. *ApJ*, 690:1424–1431.

[5] Amari, S., Anders, A., Virag, A., and Zinner, E. (1990). Interstellar graphite in meteorites. *Nature*, 345:238–240.

[6] Amari, S., Nittler, L. R., Zinner, E., Lodders, K., and Lewis, R. S. (2001). Presolar SiC Grains of Type A and B: Their Isotopic Compositions and Stellar Origins. *ApJ*, 559:463–483.

[7] Angulo, C., Arnould, M., and Rayet, M. et al. (1999). A compilation of charged-particle induced thermonuclear reaction rates. *Nucl. Phys.*, A 656:3–183. NACRE compilation.

[8] Arcones, A. and Montes, F. (2011). Production of Light-element Primary Process Nuclei in Neutrino-driven Winds. *ApJ*, 731:5–+.

[9] Arlandini, C., Käppeler, F., Wisshak, K., Gallino, R., Lugaro, M., Busso, M., and Straniero, O. (1999). Neutron capture in low-mass asymptotic giant branch stars: Cross sections and abundance signatures. *ApJ*, 525:886–900.

[10] Arnett, W. D. and Thielemann, F.-K. (1985). Hydrostatic nucleosynthesis. I - Core helium and carbon burning. *ApJ*, 295:589–619.

[11] Arnould, M. (1976). Possibility of synthesis of proton-rich nuclei in highly evolved stars. II. *A&A*, 46:117–125.

[12] Arnould, M. and Goriely, S. (2003). The p-process of stellar nucleosynthesis: astrophysics and nuclear physics status. *Phys. Rep.*, 384:1–84.

[13] Asplund, M. (1999). Sakurai's object - stellar evolution in real time. In Bertre, T. L., Lebre, A., and Waelkens, C., editors, *AGB Stars*, IAU Symp. 191, page 481.

[14] Ávila, J. N., Lugaro, M., Ireland, T. R., Gyngard, F., Zinner, E., Cristallo, S., Holden, P., Buntain, J., Amari, S., and Karakas, A. (2012). Tungsten Isotopic Compositions in Stardust SiC Grains from the Murchison Meteorite: Constraints on the s-process in the Hf-Ta-W-Re-Os Region. *ApJ*, 744:49.

[15] Bao, Z. Y., Beer, H., Käppeler, F., Voss, F., Wisshak, K., and Rauscher, T. (2000). . *ADNDT*, 76:70.

[16] Barzyk, J. G., Savina, M. R., Davis, A. M., Gallino, R., Pellin, M. J., Lewis, R. S., Amari, S., and Clayton, R. N. (2006). Multi-element isotopic analysis of single presolar SiC grains. *New Astronomy Review*, 50:587–590.

[17] Benacquista, M. (2013). *An Introduction to the Evolution of Single and Binary Stars.*

[18] Besmehn, A. and Hoppe, P. (2003). A NanoSIMS study of Si- and Ca-Ti-isotopic compositions of presolar silicon carbide grains from supernovae. *Geochim. Cosmochim. Acta*, 67:4693–4703.

[19] Bisterzo, S., Gallino, R., Käppeler, F., Wiescher, M., Imbriani, G., Straniero, O., Cristallo, S., Görres, J., and deBoer, R. J. (2015). The branchings of the main s-process: their sensitivity to α-induced reactions on ^{13}C and ^{22}Ne and to the uncertainties of the nuclear network. *MNRAS*, 449:506–527.

[20] Bisterzo, S., Gallino, R., Straniero, O., Cristallo, S., and Käppeler, F. (2010). s-Process in low-metallicity stars - I. Theoretical predictions. *MNRAS*, 404:1529–1544.

[21] Bisterzo, S., Gallino, R., Straniero, O., Cristallo, S., and Käppeler, F. (2011). The s-Process in Low Metallicity Stars. II. Interpretation of High-Resolution Spectroscopic Observations with AGB models. *ArXiv e-prints*.

[22] Bisterzo, S., Travaglio, C., Gallino, R., Wiescher, M., and Käppeler, F. (2014). Galactic Chemical Evolution and Solar s-process Abundances: Dependence on the ^{13}C-pocket Structure. *ApJ*, 787:10.

[23] Blöcker, T. (1995). Stellar evolution of low and intermediate mass stars. i. *A&A*, 297:727.

[24] Bloecker, T. (1995). Stellar evolution of low and intermediate-mass stars. I. Mass loss on the AGB and its consequences for stellar evolution. *A&A*, 297:727.

[25] Bowen, G. H. (1988). Dynamical modeling of long-period variable star atmospheres. *ApJ*, 329:299.

[26] Brachwitz, F., Dean, D. J., Hix, W. R., Iwamoto, K., Langanke, K., Martínez-Pinedo, G., Nomoto, K., Strayer, M. R., Thielemann, F.-K., and Umeda, H. (2000). The Role of Electron Captures in Chandrasekhar-Mass Models for Type IA Supernovae. *ApJ*, 536:934–947.

[27] Buchler, J.-R. and Mazurek, T. J. (1975). On presupernova dynamical mass ejection by non-detonated stellar cores. *Memoires of the Societe Royale des Sciences de Liege*, 8:435–445.

[28] Burbidge, E. M., Burbidge, G. R., Fowler, W. A., and Hoyle, F. (1957). Synthesis of the Elements in Stars. *Reviews of Modern Physics*, 29:547–650.

[29] Busso, M., Gallino, R., Lambert, D. L., Travaglio, C., and Smith, V. V. (2001). Nucleosynthesis and Mixing on the Asymptotic Giant Branch. III. Predicted and Observed s-Process Abundances. *ApJ*, 557:802–821.

[30] Busso, M., Wasserburg, G. J., Nollett, K. M., and Calandra, A. (2007). Can Extra Mixing in RGB and AGB Stars Be Attributed to Magnetic Mechanisms? *ApJ*, 671:802–810.

[31] Cameron, A. G. W. (1956). The evolution of the cosmic mixture of elements produced by capture of neutrons. *AJ*, 61:2–2.

[32] Cameron, A. G. W. (1957). Nuclear Reactions in Stars and Nucleogenesis. *PASP*, 69:201.

[33] Caughlan, G. R. and Fowler, W. A. (1988). *Atom. Data Nucl. Data Tables*, 40:283. CF88.

[34] Couch, R. G., Schmiedekamp, A. B., and Arnett, W. D. (1974). S-PROCESS Nucleosynthesis in Massive Stars: Core Helium Burning. *ApJ*, 190:95–100.

[35] Cowan, J. J. and Rose, W. K. (1977). Production of C-14 and neutrons in red giants. *ApJ*, 212:149–158.

[36] Cox, J. P. and Giuli, R. T. (1968). *Principles of stellar structure.* New York, Gordon and Breach [1968].

[37] Cristallo, S., Abia, C., Straniero, O., and Piersanti, L. (2015). On the need of the Light Elements Primary Process (LEPP). *ArXiv e-prints*.

[38] Cristallo, S., Piersanti, L., Straniero, O., Gallino, R., Domínguez, I., Abia, C., Di Rico, G., Quintini, M., and Bisterzo, S. (2011). Evolution, Nucleosynthesis, and Yields of Low-mass Asymptotic Giant Branch Stars at Different Metallicities. II. The FRUITY Database. *ApJS*, 197:17.

[39] Cristallo, S., Straniero, O., Gallino, R., Herwig, F., Chieffi, A., Limongi, M., and Busso, M. (2001). The formation of the ^{13}C pocket in AGB stars and related nucleosynthesis. *Nucl. Phys. A*, 688:217.

[40] Cristallo, S., Straniero, O., Gallino, R., Piersanti, L., Domínguez, I., and Lederer, M. T. (2009). Evolution, Nucleosynthesis, and Yields of Low-Mass Asymptotic Giant Branch Stars at Different Metallicities. *ApJ*, 696:797–820.

[41] Cyburt, R. H., Amthor, A. M., Ferguson, R., Meisel, Z., Smith, K., Warren, S., Heger, A., Hoffman, R. D., Rauscher, T., Sakharuk, A., Schatz, H., Thielemann, F. K., and Wiescher, M. (2010). The JINA REACLIB Database: Its Recent Updates and Impact on Type-I X-ray Bursts. *ApJS*, 189:240–252.

[42] Dardelet, L., Ritter, C., Prado, P., Heringer, E., Higgs, C., Sandalski, S., Jones, S., Denissenkov, P., Venn, K., Bertolli, M., Pignatari, M., Woodward, P., and Herwig, F. (2015). The i-process and CEMP-r/s stars. *ArXiv e-prints*.

[43] De Smedt, K., Van Winckel, H., Kamath, D., Karakas, A. I., Siess, L., Goriely, S., and Wood, P. (2014). The lead discrepancy in intrinsically s-process enriched post-AGB stars in the Magellanic Clouds. *A&A*, 563:L5.

[44] Delgado-Inglada, G., Rodríguez, M., Peimbert, M., Stasińska, G., and Morisset, C. (2015). Oxygen enrichment in carbon-rich planetary nebulae. *ArXiv e-prints*.

[45] Denissenkov, P. A. and Tout, C. A. (2003). Partial mixing and formation of the $^{13}C pocket by internal gravity waves in asymptotic giant branch stars. MNRAS, 340 : 722 - -732.$

[46] Denissenkov, P. A., Truran, J. W., Herwig, F., Jones, S., Paxton, B., Nomoto, K., Suzuki, T., and Toki, H. (2015). Hybrid C-O-Ne white dwarfs as progenitors of Type Ia supernovae: dependence on Urca process and mixing assumptions. *MNRAS*, 447:2696–2705.

[47] Denissenkov, P. A., Truran, J. W., Pignatari, M., Trappitsch, R., Ritter, C., Herwig, F., Battino, U., and Setoodehnia, K. (2013). MESA and NuGrid Simulations of Classical Nova Outbursts: ONe Nova and Nucleosynthesis. *ArXiv e-prints*.

[48] Dillmann, I., Plag, R., Heil, M., Käppeler, F., and Rauscher, T. (2008). Present status of the KADoNiS database. *ArXiv e-prints*.

[49] Doherty, C. L., Gil-Pons, P., Lau, H. H. B., Lattanzio, J. C., and Siess, L. (2014). Super and massive AGB stars - II. Nucleosynthesis and yields - Z = 0.02, 0.008 and 0.004. *MNRAS*, 437:195–214.

[50] Dziembowski, W. A. and Pamiatnykh, A. A. (1993). The opacity mechanism in B-type stars. I - Unstable modes in Beta Cephei star models. *MNRAS*, 262:204–212.

[51] Farouqi, K., Kratz, K.-L., Pfeiffer, B., Rauscher, T., Thielemann, F.-K., and Truran, J. W. (2010). Charged-particle and Neutron-capture Processes in the High-entropy Wind of Core-collapse Supernovae. *ApJ*, 712:1359–1377.

[52] Ferguson, J. W., Alexander, D. R., Allard, F., Barman, T., Bodnarik, J. G., Hauschildt, P. H., Heffner-Wong, A., and Tamanai, A. (2005). Low-Temperature Opacities. *Astrophysical Journal*, 623:585–596.

[53] Filippenko, A. V. (1997). Optical Spectra of Supernovae. *ARA&A*, 35:309–355.

[54] Freiburghaus, C., Rosswog, S., and Thielemann, F.-K. (1999). R-Process in Neutron Star Mergers. *ApJ*, 525:L121–L124.

[55] Freytag, B., Ludwig, H.-G., and Steffen, M. (1996). Hydrodynamical models of stellar convection. the role of overshoot in da white dwarfs, a-type stars, and the sun. *A&A*, 313:497.

[56] Fröhlich, C., Hix, W. R., Martínez-Pinedo, G., Liebendörfer, M., Thielemann, F.-K., Bravo, E., Langanke, K., and Zinner, N. T. (2006). Nucleosynthesis in neutrino-driven supernovae. *New Astr. Rev.*, 50:496–499.

[57] Fuller, G. M., Fowler, W. A., and Newman, M. J. (1985). Stellar weak interaction rates for intermediate-mass nuclei. IV - Interpolation procedures for rapidly varying lepton capture rates using effective log (ft)-values. *ApJ*, 293:1–16.

[58] Fynbo, H. O. U., Diget, C. A., Bergmann, U. C., Borge, M. J. G., Cederkäll, J., Dendooven, P., Fraile, L. M., Franchoo, S., Fedosseev, V. N., Fulton, B. R., Huang, W., Huikari, J., Jeppesen, H. B., Jokinen, A. S., Jones, P., Jonson, B., Köster, U., Langanke, K., Meister, M., Nilsson, T., Nyman, G., Prezado, Y., Riisager, K., Rinta-Antila, S., Tengblad, O., Turrion, M., Wang, Y., Weissman, L., Wilhelmsen, K., Äystö, J., and The ISOLDE Collaboration, a. (2005). Revised rates for the stellar triple-α process from measurement of $^{12}C nuclear resonances. Nature, 433: 136--139$.

[59] Gallino, R., Arlandini, C., Busso, M., Lugaro, M., Travaglio, C., Straniero, O., Chieffi, A., and Limongi, M. (1998). Evolution and Nucleosynthesis in Low-Mass Asymptotic Giant Branch Stars. II. Neutron Capture and the s-Process. *ApJ*, 497:388–+.

[60] Gallino, R., Straniero, O., Zinner, E., Jadhav, M., Piersanti, L., Cristallo, S., and Bisterzo, S. (2011). Nucleosynthesis Origin of PG 1159 Stars, Sakurai's Object, and Rare Subclasses of Presolar Grains. In Kerschbaum, F., Lebzelter, T., and Wing, R. F., editors, *Why Galaxies Care about AGB Stars II: Shining Examples and Common Inhabitants*, volume 445 of *Astronomical Society of the Pacific Conference Series*, page 143.

[61] Gonzalez, G., Lambert, D. L., Wallerstein, G., Rao, N. K., Smith, V. V., and McCarthy, J. K. (1998). FG Sagittae: A Newborn R Coronae Borealis Star? *ApJS*, 114:133–+.

[62] Goriely, S. (1999). Uncertainties in the solar system r-abundance distribution. *A&A*, 342:881–891.

[63] Goriely, S., José, J., Hernanz, M., Rayet, M., and Arnould, M. (2002). He-detonation in sub-Chandrasekhar CO white dwarfs: A new insight into energetics and p-process nucleosynthesis. *A&A*, 383:L27–L30.

[64] Goriely, S. and Siess, L. (2004). S-process in hot AGB stars: A complex interplay between diffusive mixing and nuclear burning. *A&A*, 421:L25–L28.

[65] Grevesse, N. and Noels, A. (1993). Cosmic abundances of the elements. In N. Prantzos, E. Vangioni-Flam, & M. Casse, editor, *Origin and Evolution of the Elements*, pages 15–25.

[66] Hansen, C. J., Bergemann, M., Cescutti, G., François, P., Arcones, A., Karakas, A. I., Lind, K., and Chiappini, C. (2013). LTE or non-LTE, that is the question. The NLTE chemical evolution of strontium in extremely metal-poor stars. *A&A*, 551:A57.

[67] Hansen, C. J. and Primas, F. (2011). The origin of palladium and silver. *A&A*, 525:L5.

[68] Heil, M., Plag, R., Uberseder, E., Gallino, R., Bisterzo, S., Juseviciute, A., Käppeler, F., Lederer, C., Mengoni, A., and Pignatari, M. (2014). Stellar neutron capture cross sections of ^{20,21,22}Ne. *Phys. Rev. C*, 90(4):045804.

[69] Heil, M., Winckler, N., Dababneh, S., Käppeler, F., Wisshak, K., Bisterzo, S., Gallino, R., Davis, A. M., and Rauscher, T. (2008). $^{176}Lu/^{176}Hf : ASensitiveTestofs - ProcessTemperatureandNeutronDensityinAGBStars. ApJ, 673 : 434 - -444.$

[70] Herwig, F. (2000). The evolution of AGB stars with convective overshoot. *A&A*, 360:952–968.

[71] Herwig, F. (2001). Internal mixing and surface abundance of [WC]-CSPN. *APSS*, 275:15–26.

[72] Herwig, F. (2005). Evolution of Asymptotic Giant Branch Stars. *ARA&A*, 43:435–479.

[73] Herwig, F., Blöcker, T., Langer, N., and Driebe, T. (1999). On the origin of hydrogen-deficient post-AGB stars. *A&A*, 349:L5–L8.

[74] Herwig, F., Blöcker, T., Schönberner, D., and El Eid, M. F. (1997). Stellar evolution of low and intermediate-mass stars. IV. Hydrodynamically-based overshoot and nucleosynthesis in AGB stars. *A&A*, 324:L81–L84.

[75] Herwig, F., Freytag, B., Fuchs, T., Hansen, J. P., Hueckstaedt, R. M., Porter, D. H., Timmes, F. X., and Woodward, P. R. (2007). Convective and Non-Convective Mixing in AGB Stars. In Kerschbaum, F., Charbonnel, C., and Wing, R. F., editors, *Why Galaxies Care About AGB Stars: Their Importance as Actors and Probes*, volume 378 of *Astronomical Society of the Pacific Conference Series*, page 43.

[76] Herwig, F., Langer, N., and Lugaro, M. (2003). The s-Process in Rotating Asymptotic Giant Branch Stars. *ApJ*, 593:1056–1073.

[77] Herwig, F., Pignatari, M., Woodward, P. R., Porter, D. H., Rockefeller, G., Fryer, C. L., Bennett, M., and Hirschi, R. (2011). Convective-reactive Proton-$^{12}CCombustioninSakurai'sObject(V4334Sagittarii)andImplicationsfortheEvolutionandYieldsfr$ $89 - -+ .$

[78] Herwig, F., Woodward, P. R., Lin, P.-H., Knox, M., and Fryer, C. (2014). Global Non-spherical Oscillations in Three-dimensional 4π Simulations of the H-ingestion Flash. *ApJ*, 792:L3.

[79] Hillebrandt, W., Kromer, M., Röpke, F. K., and Ruiter, A. J. (2013). Towards an understanding of Type Ia supernovae from a synthesis of theory and observations. *Frontiers of Physics*, 8:116–143.

[80] Hillebrandt, W. and Niemeyer, J. C. (2000). Type IA Supernova Explosion Models. *ARA&A*, 38:191–230.

[81] Hoppe, P., Amari, S., Zinner, E., and Lewis, R. S. (1995). Isotopic compositions of C, N, O, Mg, and Si, trace element abundances, and morphologies of single circumstellar graphite grains in four density fractions from the Murchison meteorite. *Geochim. Cosmochim. Acta*, 59:4029–4056.

[82] Hoppe, P., Fujiya, W., and Zinner, E. (2012). Sulfur Molecule Chemistry in Supernova Ejecta Recorded by Silicon Carbide Stardust. *ApJ*, 745:L26.

[83] Howard, W. M. and Meyer, B. S. (1993). The p-process and type Ia supernovae. In F. Käppeler & K. Wisshak, Bristol: IOP Publ., editor, *Nuclei in the Cosmos, Proc. of the 2nd International Symposium on Nuclear Astrophysics*, page 575.

[84] Howard, W. M., Meyer, B. S., and Woosley, S. E. (1991). A new site for the astrophysical gamma-process. *ApJ*, 373:L5–L8.

[85] Iben, Jr., I. (1981). On intermediate-mass single stars and accreting white dwarfs as sources of neutron-rich isotopes. *ApJ*, 243:987–993.

[86] Iben, Jr., I. and Renzini, A. (1982). The role of semiconvection in bringing carbon to the surface of asymptotic giant branch stars of small core mass. *ApJ*, 259:L79.

[87] Iglesias, C. A. and Rogers, F. J. (1996). Updated Opal Opacities. *ApJ*, 464:943.

[88] Iliadis, C., D'Auria, J. M., Starrfield, S., Thompson, W. J., and Wiescher, M. (2001). Proton-induced Thermonuclear Reaction Rates for A=20-40 Nuclei. *ApJS*, 134:151.

[89] Imbriani, G., Costantini, H., Formicola, A., Bemmerer, D., Bonetti, R., Broggini, C., Corvisiero, P., Cruz, J., Fülöp, Z., Gervino, G., Guglielmetti, A., Gustavino, C., Gyürky, G., Jesus, A. P., Junker, M., Lemut, A., Menegazzo, R., Prati, P., Roca, V., Rolfs, C., Romano, M., Rossi Alvarez, C., Schümann, F., Somorjai, E., Straniero, O., Strieder, F., Terrasi, F., Trautvetter, H. P., Vomiero, A., and Zavatarelli, S. (2004). The bottleneck of CNO burning and the age of Globular Clusters. *A&A*, 420:625–629.

[90] Imbriani, G., Costantini, H., Formicola, A., Vomiero, A., Angulo, C., Bemmerer, D., Bonetti, R., Broggini, C., Confortola, F., Corvisiero, P., Cruz, J., Descouvemont, P., Fülöp, Z., Gervino, G., Guglielmetti, A., Gustavino, C., Gyürky, G., Jesus, A. P., Junker, M., Klug, J. N., Lemut, A., Menegazzo, R., Prati, P., Roca, V., Rolfs, C., Romano, M., Rossi-Alvarez, C., Schümann, F., Schürmann, D., Somorjai, E., Straniero, O., Strieder, F., Terrasi, F., and Trautvetter, H. P. (2005). S-factor of ^{14}N(p,γ)^{15}O at astrophysical energies. *European Physical Journal A*, 25:455–466.

[91] Ivanova, L. N., Imshennik, V. S., and Chechetkin, V. M. (1974). Pulsation regime of the thermonuclear explosion of a star's dense carbon core. *Ap&SS*, 31:497–514.

[92] Iwamoto, K., Brachwitz, F., Nomoto, K., Kishimoto, N., Umeda, H., Hix, W. R., and Thielemann, F.-K. (1999). Nucleosynthesis in Chandrasekhar Mass Models for Type IA Supernovae and Constraints on Progenitor Systems and Burning-Front Propagation. *ApJS*, 125:439–462.

[93] Jadhav, M., Zinner, E., Amari, S., Maruoka, T., Marhas, K. K., and Gallino, R. (2013). Multi-element isotopic analyses of presolar graphite grains from Orgueil. *Geochim. Cosmochim. Acta*, 113:193–224.

[94] Jaeger, M., Kunz, R., Mayer, A., Hammer, J. W., Staudt, G., Kratz, K. L., and Pfeiffer, B. (2001). $^{22}Ne(\alpha,n)^{25}Mg$: $The Key Neutron Source in Massive Stars.$ $Physical Review Letters, 87(20)$: $202501 - - +$.

[95] Janka, H.-T. (2012). Explosion Mechanisms of Core-Collapse Supernovae. *Annual Review of Nuclear and Particle Science*, 62:407–451.

[96] Jeffery, C. S. and Saio, H. (2006). Fe-bump instability: the excitation of pulsations in subdwarf B and other low-mass stars. *MNRAS*, 371:659–672.

[97] Jones, S., Hirschi, R., Nomoto, K., Fischer, T., Timmes, F. X., Herwig, F., Paxton, B., Toki, H., Suzuki, T., Martínez-Pinedo, G., Lam, Y. H., and Bertolli, M. G. (2013). Advanced Burning Stages and Fate of 8-10 M $_{sun}$ Stars. *ApJ*, 772:150.

[98] José, J. and Hernanz, M. (2007). TOPICAL REVIEW: Nucleosynthesis in classical nova explosions. *Journal of Physics G Nuclear Physics*, 34:431.

[99] Jose, J., Hernanz, M., and Isern, J. (1993). Hydrogen and helium shell flashes on massive accreting white dwarfs. *A&A*, 269:291–300.

[100] Kappeler, F., Beer, H., and Wisshak, K. (1989). s-process nucleosynthesis-nuclear physics and the classical model. *Reports on Progress in Physics*, 52:945–1013.

[101] Käppeler, F., Gallino, R., Bisterzo, S., and Aoki, W. (2011). The s process: Nuclear physics, stellar models, and observations. *Reviews of Modern Physics*, 83:157–194.

[102] Käppeler, F., Wiescher, M., Giesen, U., Goerres, J., Baraffe, I., El Eid, M., Raiteri, C. M., Busso, M., Gallino, R., Limongi, M., and Chieffi, A. (1994). Reaction rates for O-18(alpha, gamma)Ne-22, Ne-22(alpha, gamma)Mg-26, and Ne-22(alpha, n)Mg-25 in stellar helium burning and s-process nucleosynthesis in massive stars. *ApJ*, 437:396–409.

[103] Karakas, A. I. (2010). Updated stellar yields from AGB models (Karakas, 2010). *VizieR Online Data Catalog*, 740:31413.

[104] Karakas, A. I. and Lattanzio, J. C. (2014). The Dawes Review 2: Nucleosynthesis and Stellar Yields of Low- and Intermediate-Mass Single Stars. *Publ. Astronom. Soc. Aus.*, 31:30.

[105] Karakas, A. I., Lugaro, M. A., Wiescher, M., Görres, J., and Ugalde, C. (2006). The Uncertainties in the ^{22}Ne+α-Capture Reaction Rates and the Production of the Heavy Magnesium Isotopes in Asymptotic Giant Branch Stars of Intermediate Mass. *ApJ*, 643:471–483.

[106] Kato, M. and Hachisu, I. (1999). A New Estimation of Mass Accumulation Efficiency in Helium Shell Flashestoward Type IA Supernova Explosions. *ApJ*, 513:L41–L44.

[107] Khokhlov, A. M. (1991). Delayed detonation model for type IA supernovae. *A&A*, 245:114–128.

[108] Kippenhahn, R. and Weigert, A. (1990). *Stellar structure and evolution*. Springer, Berlin.

[109] Knigge, C., Baraffe, I., and Patterson, J. (2011). The Evolution of Cataclysmic Variables as Revealed by Their Donor Stars. *ApJS*, 194:28.

[110] Kobayashi, C., Karakas, A. I., and Umeda, H. (2011). The evolution of isotope ratios in the Milky Way Galaxy. *MNRAS*, 414:3231–3250.

[111] Koehler, P. E. and O'brien, H. A. (1989). ^{14}N(n,p)^{14}C cross section from 61 meV to 34.6 keV and its astrophysical implications. *Phys. Rev. C*, 39:1655–1657.

[112] Koike, O., Hashimoto, M., Arai, K., and Wanajo, S. (1999). Rapid proton capture on accreting neutron stars - effects of uncertainty in the nuclear process. *A&A*, 342:464–473.

[113] Kunz, R., Fey, M., Jaeger, M., Mayer, A., Hammer, J. W., Staudt, G., Harissopulos, S., and Paradellis, T. (2002). Astrophysical Reaction Rate of $^{12}C(\alpha, \gamma)^{16}O$. *ApJ*, $567: 643--650$.

[114] Kusakabe, M., Iwamoto, N., and Nomoto, K. (2011). Production of the p-process Nuclei in the Carbon-deflagration Model for Type Ia Supernovae. *ApJ*, 726:25.

[115] Kwok, S. (1990). Transition from red giant to planetary nebula. In Wallerstein, G., editor, *Cool Stars, Stellar Systems, and the Sun*, volume 9 of *Astronomical Society of the Pacific Conference Series*, pages 438–449.

[116] Lamb, S. A., Howard, W. M., Truran, J. W., and Iben, Jr., I. (1977). Neutron-capture nucleosynthesis in the helium-burning cores of massive stars. *ApJ*, 217:213–221.

[117] Lambert, D. L., Smith, V. V., Busso, M., Gallino, R., and Straniero, O. (1995). The Chemical Composition of Red Giants. IV. The Neutron Density at the s-Process Site. *ApJ*, 450:302.

[118] Langanke, K. and Martínez-Pinedo, G. (2000). Shell-model calculations of stellar weak interaction rates: II. Weak rates for nuclei in the mass range /A=45-65 in supernovae environments. *Nuclear Physics A*, 673:481–508.

[119] Langer, N., Deutschmann, A., Wellstein, S., and Höflich, P. (2000). The evolution of main sequence star + white dwarf binary systems towards Type Ia supernovae. *A&A*, 362:1046–1064.

[120] Langer, N., Heger, A., Wellstein, S., and Herwig, F. (1999). Mixing and nucleosynthesis in rotating AGB stars. *A&A*, 346:L37–L40.

[121] Lattanzio, J. C. (1989). Carbon dredge-up in low-mass stars and solar metallicity stars. *ApJ*, 344:L25–L27.

[122] Lau, H. H. B., Gil-Pons, P., Doherty, C., and Lattanzio, J. (2012). The end of super AGB and massive AGB stars. I. The instabilities that determine the final mass of AGB stars. *A&A*, 542:A1.

[123] Lawlor, T. M. and MacDonald, J. (2006). The mass of helium in white dwarf stars and the formation and evolution of hydrogen-deficient post-AGB stars. *MNRAS*, 371:263–282.

[124] Lederer, C., Massimi, C., Berthoumieux, E., Colonna, N., Dressler, R., Guerrero, C., Gunsing, F., Käppeler, F., Kivel, N., Pignatari, M., Reifarth, R., Schumann, D., Wallner, A., Altstadt, S., Andriamonje, S., Andrzejewski, J., Audouin, L., Barbagallo, M., Bécares, V., Bečvář, F., Belloni, F., Berthier, B., Billowes, J., Boccone, V., Bosnar, D., Brugger, M., Calviani, M., Calviño, F., Cano-Ott, D., Carrapiço, C., Cerutti, F., Chiaveri, E., Chin, M., Cortés, G., Cortés-Giraldo, M. A., Dillmann, I., Domingo-Pardo, C., Duran, I., Dzysiuk, N., Eleftheriadis, C., Fernández-Ordóñez, M., Ferrari, A., Fraval, K., Ganesan, S., García, A. R., Giubrone, G., Gómez-Hornillos, M. B., Gonçalves, I. F., González-Romero, E., Gramegna, F., Griesmayer, E., Gurusamy, P., Harrisopulos, S., Heil, M., Ioannides, K., Jenkins, D. G., Jericha, E., Kadi, Y., Karadimos, D., Korschinek, G., Krtička, M., Kroll, J., Langer, C., Lebbos, E., Leeb, H., Leong, L. S., Losito, R., Lozano, M., Manousos, A., Marganiec, J., Marrone, S., Martinez, T., Mastinu, P. F., Mastromarco, M., Meaze, M., Mendoza, E., Mengoni, A., Milazzo, P. M., Mingrone, F., Mirea, M., Mondalaers, W., Paradela, C., Pavlik, A., Perkowski, J., Plag, R., Plompen, A., Praena, J., Quesada, J. M., Rauscher, T., Riego, A., Roman, F., Rubbia, C., Sarmento, R., Schillebeeckx, P., Schmidt, S., Tagliente, G., Tain, J. L., Tarrío, D., Tassan-Got, L., Tsinganis, A., Tlustos, L., Valenta, S., Vannini, G., Variale, V., Vaz, P., Ventura, A., Vermeulen, M. J., Versaci, R., Vlachoudis, V., Vlastou, R., Ware, T., Weigand, M., Weiß, C., Wright, T. J., Žugec, P., and n TOF Collaboration (2014). Ni62(n,γ) and Ni63(n,γ) cross sections measured at the n_TOF facility at CERN. *Phys. Rev. C*, 89(2):025810.

[125] Lewis, R. S., Amari, S., and Anders, E. (1994). Interstellar grains in meteorites: II. SiC and its noble gases. *Geochim. Cosmochim. Acta*, 58:471–494.

[126] Lewis, R. S., Ming, T., Wacker, J. F., Anders, E., and Steel, E. (1987). Interstellar diamonds in meteorites. *Nature*, 326:160–162.

[127] Lin, Y., Gyngard, F., and Zinner, E. (2010). Isotopic Analysis of Supernova SiC and Si_3N_4 Grains from the Qingzhen (EH3) Chondrite. *ApJ*, 709:1157–1173.

[128] Liu, N., Davis, A. M., Gallino, R., Savina, M. R., Bisterzo, S., Gyngard, F., Pellin, M. J., and Dauphas, N. (2015). The ^{13}C-pockets in AGB Stars and Their Fingerprints in Mainstream SiC Grains. *ArXiv e-prints*.

[129] Liu, N., Gallino, R., Bisterzo, S., Davis, A. M., Savina, M. R., and Pellin, M. J. (2014a). The ^{13}C-Pocket Structure in AGB Models: Constraints from Zirconium Isotope Abundances in Single Mainstream SiC Grains. *ApJ*, 788:163.

[130] Liu, N., Savina, M. R., Davis, A. M., Gallino, R., Straniero, O., Gyngard, F., Pellin, M. J., Willingham, D. G., Dauphas, N., Pignatari, M., Bisterzo, S., Cristallo, S., and Herwig, F. (2014b). Barium Isotopic Composition of Mainstream Silicon Carbides from

Murchison: Constraints for s-process Nucleosynthesis in Asymptotic Giant Branch Stars. *ApJ*, 786:66.

[131] Luck, R. E. and Bond, H. E. (1991). Subgiant CH stars. II - Chemical compositions and the evolutionary connection with barium stars. *ApJS*, 77:515–540.

[132] Lugaro, M., Davis, A. M., Gallino, R., Pellin, M. J., Straniero, O., and Käppeler, F. (2003a). Isotopic Compositions of Strontium, Zirconium, Molybdenum, and Barium in Single Presolar SiC Grains and Asymptotic Giant Branch Stars. *ApJ*, 593:486–508.

[133] Lugaro, M., Herwig, F., Lattanzio, J. C., Gallino, R., and Straniero, O. (2003b). s-Process Nucleosynthesis in Asymptotic Giant Branch Stars: A Test for Stellar Evolution. *ApJ*, 586:1305–1319.

[134] Lugaro, M., Karakas, A. I., Stancliffe, R. J., and Rijs, C. (2012). The s-process in Asymptotic Giant Branch Stars of Low Metallicity and the Composition of Carbon-enhanced Metal-poor Stars. *ApJ*, 747:2.

[135] Lugaro, M., Tagliente, G., Karakas, A. I., Milazzo, P. M., Käppeler, F., Davis, A. M., and Savina, M. R. (2014). The Impact of Updated Zr Neutron-capture Cross Sections and New Asymptotic Giant Branch Models on Our Understanding of the S Process and the Origin of Stardust. *ApJ*, 780:95.

[136] Lugaro, M., Ugalde, C., Karakas, A. I., Görres, J., Wiescher, M., Lattanzio, J. C., and Cannon, R. C. (2004). Reaction Rate Uncertainties and the Production of ^{19}F in Asymptotic Giant Branch Stars. *ApJ*, 615:934–946.

[137] Ma, X., Chen, X., Chen, H.-l., Denissenkov, P. A., and Han, Z. (2013). A Super-Eddington Wind Scenario for the Progenitors of Type Ia Supernovae. *ApJ*, 778:L32.

[138] Matteucci, F. and Greggio, L. (1986). Relative roles of type I and II supernovae in the chemical enrichment of the interstellar gas. *A&A*, 154:279–287.

[139] Mattsson, L. and Höfner, S. (2011). Dust-driven mass loss from carbon stars as a function of stellar parameters. II. Effects of grain size on wind properties. *A&A*, 533:A42.

[140] Meyer, B. S. (1994). The r-, s-, and p-Processes in Nucleosynthesis. *ARA&A*, 32:153–190.

[141] Meyer, B. S., Weaver, T. A., and Woosley, S. E. (1995). Isotope source table for a 25 Msun supemova. *Meteoritics*, 30:325.

[142] Miller, D. L. and Branch, D. (1990). Supernova absolute-magnitude distributions. *AJ*, 100:530–539.

[143] Miller Bertolami, M. M. and Althaus, L. G. (2007). The born-again (very late thermal pulse) scenario revisited: the mass of the remnants and implications for V4334 Sgr. *MNRAS*, 380:763–770.

[144] Miller Bertolami, M. M., Althaus, L. G., Serenelli, A. M., and Panei, J. A. (2006). New evolutionary calculations for the born again scenario. *A&A*, 449:313–326.

[145] Mishenina, T., Pignatari, M., Carraro, G., Kovtyukh, V., Monaco, L., Korotin, S., Shereta, E., Yegorova, I., and Herwig, F. (2015). New insights on Ba overabundance in open clusters. Evidence for the intermediate neutron-capture process at play? *MNRAS*, 446:3651–3668.

[146] Morel, P. and Thévenin, F. (2002). Atomic diffusion in star models of type earlier than G. *A&A*, 390:611–620.

[147] Nishimura, S., Kotake, K., Hashimoto, M.-a., Yamada, S., Nishimura, N., Fujimoto, S., and Sato, K. (2006). r-Process Nucleosynthesis in Magnetohydrodynamic Jet Explosions of Core-Collapse Supernovae. *ApJ*, 642:410–419.

[148] Nittler, L. R. and Hoppe, P. (2005). Are Presolar Silicon Carbide Grains from Novae Actually from Supernovae? *ApJ*, 631:L89–L92.

[149] Nomoto, K. (1982). Accreting white dwarf models for type I supernovae. I - Presupernova evolution and triggering mechanisms. *ApJ*, 253:798–810.

[150] Nomoto, K. (1984). Evolution of 8-10 solar mass stars toward electron capture supernovae. I - Formation of electron-degenerate O + NE + MG cores. *ApJ*, 277:791–805.

[151] Nomoto, K., Saio, H., Kato, M., and Hachisu, I. (2007). Thermal Stability of White Dwarfs Accreting Hydrogen-rich Matter and Progenitors of Type Ia Supernovae. *ApJ*, 663:1269–1276.

[152] Nucci, M. C. and Busso, M. (2014). Magnetohydrodynamics and Deep Mixing in Evolved Stars. I. Two- and Three-dimensional Analytical Models for the Asymptotic Giant Branch. *ApJ*, 787:141.

[153] Oda, T., Hino, M., Muto, K., Takahara, M., and Sato, K. (1994). Rate Tables for the Weak Processes of sd-Shell Nuclei in Stellar Matter. *Atomic Data and Nuclear Data Tables*, 56:231–+.

[154] Otsuka, M. and Tajitsu, A. (2013). Chemical Abundances in the Extremely Carbon-rich and Xenon-rich Halo Planetary Nebula H4-1. *ApJ*, 778:146.

[155] Ott, U. and Begemann, F. (1990). Discovery of s-process barium in the Murchison meteorite. *ApJ*, 353:L57–L60.

[156] Ott, U., Besmehn, A., Farouqi, K., Hallmann, O., Hoppe, P., Kratz, K.-L., Melber, K., and Wallner, A. (2012). New Attempts to Understand Nanodiamond Stardust. *Publ. Astronom. Soc. Aus.*, 29:90–97.

[157] Paczynski, B. (1974). Helium-Shell Flashes in Population i Stars. *ApJ*, 192:483–486.

[158] Paczynski, B. (1983). A one-zone model for shell flashes on accreting compact stars. *ApJ*, 264:282–295.

[159] Paczynski, B. and Proszynski, M. (1986). Models of radiation-driven winds from general relativistic neutron stars. *ApJ*, 302:519–529.

[160] Paxton, P., Bildsten, L., Timmes, F., Nelson, L., Lesaffre, P., Herwig, F., Dotter, A., VandenBerg, D., Sigur?son, S., Hirschi, R., and Tomshine, J. (2010). MESA: modules for experiments in stellar astrophysics. http://mesa.sourceforge.net.

[161] Péquignot, D., Walsh, J. R., Zijlstra, A. A., and Dudziak, G. (2000). Third-dredge-up oxygen in planetary nebulae. *A&A*, 361:L1–L4.

[162] Perego, A., Hempel, M., Fröhlich, C., Ebinger, K., Eichler, M., Casanova, J., Liebendoerfer, M., and Thielemann, F.-K. (2015). Pushing 1D CCSNe to explosions: model and SN 1987A. *ArXiv e-prints*.

[163] Peters, J. G. (1968). Nucleosynthesis by the s-PROCESS in Stars of 9 and 15 Solar Masses. *ApJ*, 154:225–+.

[164] Piersanti, L., Cristallo, S., and Straniero, O. (2013). The Effects of Rotation on s-process Nucleosynthesis in Asymptotic Giant Branch Stars. *ApJ*, 774:98.

[165] Piersanti, L., Tornambé, A., and Yungelson, L. R. (2014). He-accreting white dwarfs: accretion regimes and final outcomes. *MNRAS*, 445:3239–3262.

[166] Pignatari, M., Gallino, R., Heil, M., Wiescher, M., Käppeler, F., Herwig, F., and Bisterzo, S. (2010). The Weak s-Process in Massive Stars and its Dependence on the Neutron Capture Cross Sections. *ApJ*, 710:1557–1577.

[167] Pignatari, M., Gallino, R., Käppeler, F., and Wiescher, M. (2005). Effects of uncertainties of the ^{22}Ne(α, n)^{25}Mg and ^{13}C(α, n)^{16}O reaction rates in the s-process yields. *Nuclear Physics A*, 758:541–544.

[168] Pignatari, M., Herwig, F., Hirschi, R., Bennett, M., Rockefeller, G., Fryer, C., Timmes, F. X., Heger, A., Jones, S., Battino, U., Ritter, C., Dotter, A., Trappitsch, R., Diehl, S., Frischknecht, U., Hungerford, A., Magkotsios, G., Travaglio, C., and Young, P. (2013a). NuGrid stellar data set. I. Stellar yields from H to Bi for stars with metallicities Z = 0.02 and Z = 0.01. *ArXiv e-prints*.

[169] Pignatari, M., Hirschi, R., Wiescher, M., Gallino, R., Bennett, M., Beard, M., Fryer, C., Herwig, F., Rockefeller, G., and Timmes, F. X. (2013b). The ^{12}C + ^{12}C Reaction and the Impact on Nucleosynthesis in Massive Stars. *ApJ*, 762:31.

[170] Pignatari, M., Wiescher, M., Timmes, F. X., de Boer, R. J., Thielemann, F.-K., Fryer, C., Heger, A., Herwig, F., and Hirschi, R. (2013c). Production of Carbon-rich Presolar Grains from Massive Stars. *ApJ*, 767:L22.

[171] Piro, A. L. and Bildsten, L. (2008). Neutronization during Type Ia Supernova Simmering. *ApJ*, 673:1009–1013.

[172] Prantzos, N., Arnould, M., and Arcoragi, J.-P. (1987). Neutron capture nucleosynthesis during core helium burning in massive stars. *ApJ*, 315:209–228.

[173] Prantzos, N., Hashimoto, M., and Nomoto, K. (1990). The s-process in massive stars - Yields as a function of stellar mass and metallicity. *A&A*, 234:211–229.

[174] Pruet, J., Hoffman, R. D., Woosley, S. E., Janka, H.-T., and Buras, R. (2006). Nucleosynthesis in Early Supernova Winds. II. The Role of Neutrinos. *ApJ*, 644:1028–1039.

[175] Qian, Y.-Z. and Wasserburg, G. J. (2008). Abundances of Sr, Y, and Zr in Metal-Poor Stars and Implications for Chemical Evolution in the Early Galaxy. *ApJ*, 687:272–286.

[176] Raiteri, C. M., Busso, M., Picchio, G., and Gallino, R. (1991a). S-process nucleosynthesis in massive stars and the weak component. II - Carbon burning and galactic enrichment. *ApJ*, 371:665–672.

[177] Raiteri, C. M., Busso, M., Picchio, G., Gallino, R., and Pulone, L. (1991b). S-process nucleosynthesis in massive stars and the weak component. I - Evolution and neutron captures in a 25 solar mass star. *ApJ*, 367:228–238.

[178] Rapp, W., Görres, J., Wiescher, M., Schatz, H., and Käppeler, F. (2006). Sensitivity of p-Process Nucleosynthesis to Nuclear Reaction Rates in a 25 $M_{solar} Supernova Model. ApJ, 653 : 474 - -489.$

[179] Rauscher, T. (2006). Branchings in the γ process path revisited. *Phys. Rev. C*, 73(1):015804–+.

[180] Rauscher, T., Heger, A., Hoffman, R. D., and Woosley, S. E. (2002). Nucleosynthesis in Massive Stars with Improved Nuclear and Stellar Physics. *ApJ*, 576:323–348.

[181] Rayet, M., Arnould, M., Hashimoto, M., Prantzos, N., and Nomoto, K. (1995). The p-process in Type II supernovae. *A&A*, 298:517–+.

[182] Reddy, B. E., Lambert, D. L., Gonzalez, G., and Yong, D. (2002). Spectroscopic Analysis of Two Carbon-rich Post-Asymptotic Giant Branch Stars. *ApJ*, 564:482–494.

[183] Reimers, D. (1975). Circumstellar absorption lines and mass loss from red giants. *Memoires of the Societe Royale des Sciences de Liege*, 8:369–382.

[184] Renzini, A. (1983). Red giants as precursors of planetary nebulae. In Flower, D. R., editor, *Planetary Nebulae*, volume 103 of *IAU Symposium*, pages 267–279.

[185] Reyniers, M., van de Steene, G. C., van Hoof, P. A. M., and van Winckel, H. (2007). IRAS08281-4850 and IRAS14325-6428: two A-type post-AGB stars with s-process enrichment. *A&A*, 471:247–254.

[186] Reyniers, M., Van Winckel, H., Gallino, R., and Straniero, O. (2004). A study of the s-process in the carbon-rich post-AGB stars IRAS 06530-0213 and IRAS 08143-4406 on the basis of VLT-UVES spectra. *A&A*, 417:269–281.

[187] Roberts, L. F., Woosley, S. E., and Hoffman, R. D. (2010). Integrated Nucleosynthesis in Neutrino-driven Winds. *ApJ*, 722:954–967.

[188] Rodríguez, M. and Delgado-Inglada, G. (2011). An Overabundance of Oxygen in Planetary Nebulae of the Solar Neighborhood. In *Revista Mexicana de Astronomia y Astrofisica Conference Series*, volume 40 of *Revista Mexicana de Astronomia y Astrofisica, vol. 27*, pages 179–180.

[189] Rybicki, G. B. and Lightman, A. P. (1979). *Radiative processes in astrophysics.*

[190] Savina, M. R., Davis, A. M., Tripa, C. E., Pellin, M. J., Clayton, R. N., Lewis, R. S., Amari, S., Gallino, R., and Lugaro, M. (2003). Barium isotopes in individual presolar silicon carbide grains from the Murchison meteorite. *Geochim. Cosmochim. Acta*, 67:3201–3214.

[191] Schatz, H., Aprahamian, A., Goerres, J., Wiescher, M., Rauscher, T., Rembges, J. F., Thielemann, F.-K., Pfeiffer, B., Moeller, P., Kratz, K.-L., Herndl, H., Brown, B. A., and Rebel, H. (1998). rp-Process Nucleosynthesis at Extreme Temperature and Density Conditions. *Phys. Rep.*, 294:167–264.

[192] Schatz, H., Bildsten, L., and Cumming, A. (2003). Photodisintegration-triggered Nuclear Energy Release in Superbursts. *ApJ*, 583:L87–L90.

[193] Schatz, H. and Rehm, K. E. (2006). X-ray binaries. *Nuclear Physics A*, 777:601–622.

[194] Sharpee, B., Zhang, Y., Williams, R., Pellegrini, E., Cavagnolo, K., Baldwin, J. A., Phillips, M., and Liu, X.-W. (2007). s-Process Abundances in Planetary Nebulae. *ApJ*, 659:1265–1290.

[195] Shen, K. J. and Bildsten, L. (2007). Thermally Stable Nuclear Burning on Accreting White Dwarfs. *ApJ*, 660:1444–1450.

[196] Sion, E. M., Acierno, M. J., and Tomczyk, S. (1979). Hydrogen shell flashes in massive accreting white dwarfs. *ApJ*, 230:832–838.

[197] Sneden, C., Cowan, J. J., and Gallino, R. (2008). Neutron-Capture Elements in the Early Galaxy. *ARA&A*, 46:241–288.

[198] Spitzer, L. (1962). *Physics of Fully Ionized Gases.* Dover Books on Physics.

[199] Starrfield, S., Iliadis, C., Timmes, F. X., Hix, W. R., Arnett, W. D., Meakin, C., and Sparks, W. M. (2012). Theoretical studies of accretion of matter onto white dwarfs and the single degenerate scenario for supernovae of Type Ia. *Bulletin of the Astronomical Society of India*, 40:419.

[200] Sterling, N. C., Dinerstein, H. L., and Bowers, C. W. (2002). Discovery of Enhanced Germanium Abundances in Planetary Nebulae with the Far Ultraviolet Spectroscopic Explorer. *ApJ Lett.*, 578:L55–L58.

[201] Sterling, N. C., Dinerstein, H. L., Hwang, S., Redfield, S., Aguilar, A., Witthoeft, M. C., Esteves, D., Kilcoyne, A. L. D., Bautista, M., Phaneuf, R., Bilodeau, R. C., Ballance, C. P., McLaughlin, B., and Norrington, P. H. (2009). Improved Neutron-Capture Element Abundances in Planetary Nebulae. *Publ. Astronom. Soc. Aus.*, 26:339–344.

[202] Straniero, O., Cristallo, S., and Piersanti, L. (2014). Heavy Elements in Globular Clusters: The Role of Asymptotic Giant Branch Stars. *ApJ*, 785:77.

[203] Straniero, O., Gallino, R., Busso, M., Chiefei, A., Raiteri, C. M., Limongi, M., and Salaris, M. (1995). Radiative C-13 burning in asymptotic giant branch stars and s-processing. *ApJ*, 440:L85–L87.

[204] Straniero, O., Gallino, R., and Cristallo, S. (2006). s process in low-mass asymptotic giant branch stars. *Nuclear Physics A*, 777:311–339.

[205] Surman, R., McLaughlin, G. C., Ruffert, M., Janka, H.-T., and Hix, W. R. (2008). r-Process Nucleosynthesis in Hot Accretion Disk Flows from Black Hole-Neutron Star Mergers. *ApJ*, 679:L117–L120.

[206] Tagliente, G., Lugaro, M., Karakas, A. I., Milazzo, P. M., and n TOF Collaboration (2012). New 90,91,92,93,94,96Zr neutron capture cross-sections. In *Nuclei in the Cosmos (NIC XII)*.

[207] Takahashi, K., Witti, J., and Janka, H.-T. (1994). Nucleosynthesis in neutrino-driven winds from protoneutron stars II. The r-process. *A&A*, 286:857–869.

[208] The, L., El Eid, M. F., and Meyer, B. S. (2007). s-Process Nucleosynthesis in Advanced Burning Phases of Massive Stars. *ApJ*, 655:1058–1078.

[209] Thielemann, F. K. and Arnett, W. D. (1985). Hydrostatic Nucleosynthesis - Part Two - Core Neon to Silicon Burning and Presupernova Abundance Yields of Massive Stars. *ApJ*, 295:604–+.

[210] Thielemann, F.-K., Hirschi, R., Liebendörfer, M., and Diehl, R. (2011). Massive Stars and Their Supernovae. In Diehl, R., Hartmann, D. H., and Prantzos, N., editors, *Lecture Notes in Physics, Berlin Springer Verlag*, volume 812 of *Lecture Notes in Physics, Berlin Springer Verlag*, pages 153–232.

[211] Thielemann, F.-K., Nomoto, K., and Yokoi, K. (1986). Explosive nucleosynthesis in carbon deflagration models of Type I supernovae. *A&A*, 158:17–33.

[212] Tornambé, A., Iben, Jr., I., Piersanti, L., and Cassisi, S. (2000). Hydrogen-accreting low mass CO white dwarfs and sub-Chandrasekhar Supernovae. *Mem. Soc. Astron. Italiana*, 71:471.

[213] Tosi, M. (2007). AGB Stars and the Chemical Evolution of Galaxies. In F. Kerschbaum, C. Charbonnel, & R. F. Wing, editor, *Why Galaxies Care About AGB Stars: Their Importance as Actors and Probes*, volume 378 of *Astronomical Society of the Pacific Conference Series*, page 353.

[214] Travaglio, C., Gallino, R., Arnone, E., Cowan, J., Jordan, F., and Sneden, C. (2004). Galactic Evolution of Sr, Y, And Zr: A Multiplicity of Nucleosynthetic Processes. *ApJ*, 601:864–884.

[215] Travaglio, C., Gallino, R., Busso, M., and Gratton, R. (2001). Lead: Asymptotic Giant Branch Production and Galactic Chemical Evolution. *ApJ*, 549:346–352.

[216] Travaglio, C., Gallino, R., Rauscher, T., Röpke, F. K., and Hillebrandt, W. (2015). Testing the Role of SNe Ia for Galactic Chemical Evolution of p-nuclei with Two-dimensional Models and with s-process Seeds at Different Metallicities. *ApJ*, 799:54.

[217] Travaglio, C., Röpke, F. K., Gallino, R., and Hillebrandt, W. (2011). Type Ia Supernovae as Sites of the p-process: Two-dimensional Models Coupled to Nucleosynthesis. *ApJ*, 739:93–+.

[218] van Aarle, E., Van Winckel, H., De Smedt, K., Kamath, D., and Wood, P. R. (2013). Detailed abundance study of four s-process enriched post-AGB stars in the Large Magellanic Cloud. *A&A*, 554:A106.

[219] van den Heuvel, E. P. J., Bhattacharya, D., Nomoto, K., and Rappaport, S. A. (1992). Accreting white dwarf models for CAL 83, CAL 87 and other ultrasoft X-ray sources in the LMC. *A&A*, 262:97–105.

[220] van Winckel, H. (2003). Post-AGB Stars. *ARA&A*, 41:391–427.

[221] Wallner, A., Buczak, K., Dillmann, I., Feige, J., Käppeler, F., Korschinek, G., Lederer, C., Mengoni, A., Ott, U., Paul, M., Schätzel, G., Steier, P., and Trautvetter, H. P. (2012). AMS Applications in Nuclear Astrophysics: New Results for ^{13}C(n,γ)^{14}C and ^{14}N(n,p)^{14}C. *Publ. Astronom. Soc. Aus.*, 29:115–120.

[222] Wanajo, S. (2006). The rp-Process in Neutrino-driven Winds. *ApJ*, 647:1323–1340.

[223] Wanajo, S., Janka, H.-T., and Müller, B. (2011). Electron-capture Supernovae as The Origin of Elements Beyond Iron. *ApJ*, 726:L15.

[224] Webbink, R. F. (1984). Double white dwarfs as progenitors of R Coronae Borealis stars and Type I supernovae. *ApJ*, 277:355–360.

[225] Werner, K. and Herwig, F. (2006). The Elemental Abundances in Bare Planetary Nebula Central Stars and the Shell Burning in AGB Stars. *PASP*, 118:183–204.

[226] Werner, K., Rauch, T., and Kepler, S. O. (2014). New hydrogen-deficient (pre-) white dwarfs in the Sloan Digital Sky Survey Data Release 10. *A&A*, 564:A53.

[227] Whelan, J. and Iben, Jr., I. (1973). Binaries and Supernovae of Type I. *ApJ*, 186:1007–1014.

[228] Winteler, C., Käppeli, R., Perego, A., Arcones, A., Vasset, N., Nishimura, N., Liebendörfer, M., and Thielemann, F.-K. (2012). Magnetorotationally Driven Supernovae as the Origin of Early Galaxy r-process Elements? *ApJ*, 750:L22.

[229] Wolf, W. M., Bildsten, L., Brooks, J., and Paxton, B. (2013). Hydrogen Burning on Accreting White Dwarfs: Stability, Recurrent Novae, and the Post-nova Supersoft Phase. *ApJ*, 777:136.

[230] Woosley, S. E., Hartmann, D. H., Hoffman, R. D., and Haxton, W. C. (1990). The nu-process. *ApJ*, 356:272–301.

[231] Woosley, S. E., Heger, A., and Weaver, T. A. (2002). The evolution and explosion of massive stars. *Rev. Mod. Phys.*, 74(4):1015.

[232] Woosley, S. E. and Hoffman, R. D. (1992). The alpha-process and the r-process. *ApJ*, 395:202–239.

[233] Woosley, S. E. and Howard, W. M. (1978). The p-process in supernovae. *ApJS*, 36:285–304.

[234] Woosley, S. E. and Weaver, T. A. (1995). The evolution and explosion of massive stars. II. explosive hydrodynamics and nucleosynthesis. *APJS*, 101:181+.

[235] Zamora, O., Abia, C., Plez, B., Domínguez, I., and Cristallo, S. (2009). The chemical composition of carbon stars. The R-type stars. *A&A*, 508:909–922.

[236] Zinner, E. (2014). Presolar Grains. *Treatise on Geochemistry, 2nd edition*, 1:181–213.

Appendix A

Tables of AGB stellar models properties and isotopic distributions

Table A.1 List of AGB stellar models not included in Tab. 2.1 and their relevant parameters: initial mass, initial metallicity, CBM parameterization (see Tab. 2.1 for details) and respective modification for the reaction rate reported in the last column, compared to the default nuclear reaction network.

name	mass [$M_\odot$]	metallicity	CBM	f1	D2	f2	f1*	D2*	f2*	rate test
M3.z2m2.zrtest	3.0	0.02	df	0.024	10^5	0.14	0.014	10^{11}	0.25	^{95}Zr (n,γ) ^{96}Zr / 2
M3.z1m2.zrtest	3.0	0.01	df	0.024	10^5	0.14	0.014	10^{11}	0.25	^{95}Zr (n,γ) ^{96}Zr / 2
M2.z2m2 .zrtest	2.0	0.02	df	0.024	10^5	0.14	0.014	10^{11}	0.25	^{95}Zr (n,γ) ^{96}Zr / 2
M2.z1m2.zrtest	2.0	0.01	df	0.024	10^5	0.14	0.014	10^{11}	0.25	^{95}Zr (n,γ) ^{96}Zr / 2
M3.z1m2.hCBM.ntest	3.0	0.01	df	0.024	10^5	0.14	0.014	10^{12}	0.27	^{14}N (n,p) ^{14}C x 2
M2.z2m2.hCBM.ntest	2.0	0.02	df	0.024	10^5	0.14	0.014	10^{12}	0.27	^{14}N (n,p) ^{14}C x 2
Pi13.newnet	3.0	0.02	sf	0.008	-	-	0.126	-	-	Present work network test

Table A.2 TP-AGB evolution properties of stellar models presented in this work.

TP	DUP_λ	t_{TP} [yrs]	T_{FBOT} [K]	T_{HES} [K]	T_{HS} [K]	T_{CEB} [K]	m_{FBOT} [$M_\odot$]	m_{HTP} [$M_\odot$]	$m_{D,max}$ [$M_\odot$]	M_* [$M_\odot$]
					M2.z1m2					
1	0.00	0.00E+00	8.31	8.15	7.09	6.25	0.4452	0.4948	0.4961	1.978
2	0.00	7.43E+05	8.36	8.15	7.14	6.31	0.4574	0.5056	0.5063	1.978
3	0.00	1.15E+06	8.38	8.16	7.16	6.27	0.4677	0.5131	0.5138	1.978
4	0.00	1.33E+06	8.37	8.15	7.17	6.33	0.4721	0.5165	0.5174	1.978
5	0.00	1.50E+06	8.38	7.75	7.15	6.33	0.4758	0.5208	0.5215	1.977
6	0.00	1.68E+06	8.41	7.76	7.16	6.33	0.4808	0.5261	0.5267	1.977
7	0.00	1.86E+06	8.41	7.78	7.18	6.36	0.4873	0.5319	0.5324	1.977
8	0.00	2.02E+06	8.43	7.79	7.25	6.37	0.4948	0.5381	0.5385	1.976
9	0.00	2.18E+06	8.42	7.79	7.27	6.37	0.5029	0.5444	0.5447	1.975
10	0.00	2.33E+06	8.44	7.79	7.31	6.40	0.5114	0.5508	0.5511	1.974
11	0.00	2.47E+06	8.43	7.80	7.32	6.39	0.5198	0.5572	0.5574	1.972
12	0.00	2.60E+06	8.45	7.80	7.57	6.41	0.5280	0.5636	0.5636	1.970
13	0.13	2.72E+06	8.44	7.79	7.64	6.41	0.5362	0.5699	0.5693	1.967
14	0.26	2.83E+06	8.46	7.81	7.66	6.43	0.5437	0.5758	0.5742	1.964
15	0.42	2.94E+06	8.45	8.11	7.66	6.43	0.5504	0.5810	0.5783	1.960
16	0.55	3.04E+06	8.46	8.13	7.67	6.45	0.5561	0.5854	0.5815	1.954
17	0.66	3.14E+06	8.47	8.13	7.70	6.47	0.5608	0.5890	0.5841	1.947
18	0.75	3.24E+06	8.47	7.93	7.46	6.29	0.5647	0.5920	0.5862	1.937
19	0.82	3.34E+06	8.47	8.13	7.71	6.55	0.5679	0.5945	0.5877	1.925
20	0.88	3.43E+06	8.47	8.13	7.70	6.50	0.5704	0.5964	0.5887	1.876
21	0.91	3.52E+06	8.48	8.12	7.68	6.56	0.5723	0.5979	0.5896	1.795
22	0.88	3.61E+06	8.48	8.12	7.68	6.49	0.5739	0.5990	0.5907	1.682
23	0.75	3.70E+06	8.46	8.12	7.68	6.49	0.5759	0.6001	0.5931	1.522
24	0.46	3.78E+06	8.44	8.21	7.68	6.34	0.5800	0.6023	0.5941	1.233
					M2.z2m2					
1	0.00	0.00E+00	8.23	8.15	7.16	6.28	0.4737	0.5145	0.5151	1.951
2	0.00	3.19E+05	8.26	8.17	7.17	6.37	0.4796	0.5203	0.5209	1.951
3	0.00	4.77E+05	8.27	8.16	7.19	6.27	0.4824	0.5233	0.5240	1.950
4	0.00	6.11E+05	8.30	8.07	7.18	6.41	0.4854	0.5269	0.5275	1.950
5	0.00	7.51E+05	8.30	7.83	7.22	6.39	0.4895	0.5315	0.5320	1.950
6	0.00	8.94E+05	8.30	7.84	7.22	6.50	0.4949	0.5368	0.5372	1.949
7	0.00	1.03E+06	8.30	7.85	7.29	6.50	0.5016	0.5425	0.5429	1.948
8	0.00	1.17E+06	8.29	7.86	7.30	6.46	0.5091	0.5484	0.5487	1.947
9	0.00	1.29E+06	8.29	7.86	7.36	6.45	0.5168	0.5544	0.5547	1.945
10	0.00	1.41E+06	8.28	7.87	7.34	6.49	0.5246	0.5604	0.5606	1.943
11	0.00	1.52E+06	8.28	7.87	7.44	6.49	0.5323	0.5664	0.5665	1.940
12	0.00	1.62E+06	8.27	7.85	7.56	6.61	0.5399	0.5724	0.5722	1.936
13	0.13	1.72E+06	8.27	7.86	7.73	6.62	0.5471	0.5782	0.5776	1.932
14	0.25	1.81E+06	8.27	7.91	7.72	6.91	0.5541	0.5837	0.5823	1.927
15	0.38	1.90E+06	8.28	8.05	7.74	7.12	0.5602	0.5886	0.5863	1.920
16	0.49	1.98E+06	8.27	8.11	7.72	7.39	0.5657	0.5929	0.5897	1.911
17	0.59	2.06E+06	8.27	8.11	7.74	7.47	0.5704	0.5965	0.5925	1.900
18	0.68	2.14E+06	8.27	8.11	7.69	7.58	0.5743	0.5997	0.5948	1.886
19	0.75	2.22E+06	8.27	8.11	7.69	7.63	0.5778	0.6023	0.5967	1.869
20	0.77	2.30E+06	8.29	8.11	7.71	7.58	0.5806	0.6045	0.5985	1.848
21	0.80	2.37E+06	8.26	8.11	7.72	7.64	0.5831	0.6064	0.6001	1.822
22	0.82	2.45E+06	8.26	8.11	7.70	7.62	0.5854	0.6082	0.6015	1.793
23	0.83	2.52E+06	8.25	8.11	7.72	7.42	0.5875	0.6097	0.6029	1.683
24	0.79	2.59E+06	8.29	8.21	7.41	7.46	0.5894	0.6113	0.6035	1.437
					M3.z1m2					
1	0.00	0.00E+00	8.39	8.20	7.59	6.37	0.6192	0.6397	0.6393	2.973
2	0.39	4.85E+04	8.41	8.17	7.68	6.54	0.6218	0.6421	0.6411	2.972
3	0.59	9.69E+04	8.31	8.16	7.68	6.53	0.6243	0.6450	0.6428	2.970
4	0.75	1.48E+05	8.42	8.15	7.69	6.63	0.6268	0.6477	0.6440	2.967
5	0.91	2.03E+05	8.46	8.14	7.70	6.64	0.6293	0.6498	0.6445	2.963
6	1.04	2.59E+05	8.43	8.13	7.67	6.75	0.6310	0.6512	0.6443	2.957
7	1.08	3.18E+05	8.46	8.12	7.65	6.76	0.6319	0.6517	0.6437	2.909
8	1.12	3.78E+05	8.46	8.12	7.63	6.82	0.6321	0.6517	0.6427	2.832
9	1.18	4.40E+05	8.47	8.12	7.60	6.77	0.6318	0.6513	0.6411	2.731
10	1.17	5.02E+05	8.48	8.11	7.60	6.79	0.6308	0.6501	0.6395	2.601
11	1.20	5.65E+05	8.45	8.11	7.60	6.79	0.6297	0.6489	0.6376	2.426
12	1.18	6.29E+05	8.46	8.11	7.65	6.91	0.6280	0.6474	0.6358	2.168
13	1.23	6.93E+05	8.46	8.10	7.65	7.11	0.6265	0.6458	0.6336	1.713
					M3.z2m2					
1	0.00	0.00E+00	8.31	8.19	7.21	6.32	0.5644	0.5879	0.5888	2.978
2	0.00	5.72E+04	8.37	8.18	7.26	6.51	0.5645	0.5903	0.5906	2.978

3	0.00	1.22E+05	8.39	8.18	7.30	6.45	0.5670	0.5936	0.5937	2.978
4	0.10	1.89E+05	8.42	8.17	7.57	6.61	0.5706	0.5977	0.5974	2.977
5	0.18	2.57E+05	8.43	8.15	7.59	6.53	0.5751	0.6021	0.6015	2.976
6	0.31	3.25E+05	8.43	8.11	7.67	6.62	0.5803	0.6067	0.6052	2.974
7	0.46	3.93E+05	8.42	8.14	7.68	6.56	0.5853	0.6109	0.6084	2.972
8	0.60	4.59E+05	8.44	8.14	7.72	6.55	0.5899	0.6145	0.6109	2.969
9	0.73	5.25E+05	8.46	8.14	7.71	6.64	0.5937	0.6174	0.6127	2.966
10	0.83	5.91E+05	8.44	8.14	7.69	6.64	0.5967	0.6196	0.6139	2.962
11	0.89	6.58E+05	8.46	8.13	7.70	6.73	0.5990	0.6213	0.6147	2.956
12	0.96	7.24E+05	8.46	8.13	7.69	6.66	0.6006	0.6225	0.6150	2.950
13	1.02	7.92E+05	8.45	7.76	7.64	6.30	0.6017	0.6233	0.6148	2.943
14	1.04	8.60E+05	8.45	7.51	7.66	6.08	0.6021	0.6236	0.6145	2.935
15	1.08	9.29E+05	8.39	8.12	7.66	6.73	0.6022	0.6235	0.6138	2.877
16	1.09	9.98E+05	8.49	8.11	7.63	6.99	0.6019	0.6233	0.6129	2.787
17	1.11	1.07E+06	8.42	8.09	7.65	7.71	0.6014	0.6229	0.6119	2.672
18	1.09	1.14E+06	8.34	8.10	7.67	7.66	0.6006	0.6219	0.6109	2.531
19	1.10	1.21E+06	8.33	8.10	7.67	7.68	0.5999	0.6212	0.6099	2.349
20	1.06	1.28E+06	8.21	8.10	7.73	7.52	0.5991	0.6203	0.6092	2.103
21	1.19	1.35E+06	8.23	8.04	7.79	7.54	0.5985	0.6197	0.6079	1.721
					M2.z2m2.hCBM					
1	0.00	0.00E+00	8.31	8.21	7.39	6.22	0.4743	0.5141	0.5153	1.950
2	0.00	2.36E+05	8.16	8.24	7.42	6.27	0.4783	0.5177	0.5187	1.950
3	0.00	4.71E+05	8.19	8.18	7.23	6.25	0.4840	0.5233	0.5238	1.950
4	0.00	7.16E+05	8.28	8.13	7.25	6.35	0.4922	0.5308	0.5311	1.949
5	0.00	8.40E+05	8.25	8.22	7.36	6.55	0.4980	0.5341	0.5347	1.949
6	0.00	9.63E+05	8.26	8.10	7.52	6.85	0.5021	0.5388	0.5392	1.948
7	0.00	1.09E+06	8.27	8.20	7.61	7.21	0.5078	0.5440	0.5443	1.947
8	0.00	1.21E+06	8.25	8.09	7.49	7.41	0.5142	0.5495	0.5497	1.945
9	0.00	1.32E+06	8.25	8.11	7.39	7.55	0.5212	0.5552	0.5553	1.944
10	0.06	1.43E+06	8.28	7.81	7.62	7.61	0.5285	0.5610	0.5608	1.941
11	0.11	1.54E+06	8.28	7.75	7.65	7.21	0.5357	0.5667	0.5662	1.938
12	0.22	1.64E+06	8.23	7.76	7.66	7.15	0.5426	0.5724	0.5711	1.934
13	0.35	1.74E+06	8.29	8.02	7.62	7.19	0.5491	0.5776	0.5753	1.928
14	0.47	1.83E+06	8.28	8.13	7.63	7.37	0.5549	0.5823	0.5791	1.921
15	0.57	1.92E+06	8.28	8.14	7.63	7.21	0.5599	0.5865	0.5823	1.911
16	0.65	2.01E+06	8.27	8.14	7.63	7.07	0.5643	0.5902	0.5851	1.899
17	0.71	2.11E+06	8.27	8.14	7.64	6.83	0.5682	0.5934	0.5875	1.883
18	0.76	2.19E+06	8.26	8.13	7.63	6.67	0.5717	0.5963	0.5897	1.863
19	0.77	2.28E+06	8.26	8.16	7.68	6.32	0.5748	0.5988	0.5918	1.759
20	0.72	2.37E+06	8.47	8.13	7.61	6.60	0.5777	0.6011	0.5944	1.598
21	0.53	2.45E+06	8.47	8.08	7.47	6.42	0.5815	0.6038	0.5958	1.311
					M3.z1m2.hCBM					
1	0.00	0.00E+00	8.39	8.20	7.56	6.46	0.6251	0.6445	0.6437	2.972
2	0.65	4.59E+04	8.40	8.17	7.59	6.63	0.6271	0.6466	0.6448	2.970
3	0.83	9.31E+04	8.41	8.16	7.64	6.66	0.6287	0.6489	0.6455	2.968
4	0.98	1.44E+05	8.43	8.14	7.65	6.63	0.6304	0.6508	0.6456	2.965
5	1.10	1.99E+05	8.43	8.13	7.66	6.69	0.6318	0.6519	0.6450	2.960
6	1.17	2.57E+05	8.46	8.12	7.65	6.71	0.6323	0.6523	0.6437	2.913
7	1.23	3.18E+05	8.45	8.11	7.62	6.75	0.6330	0.6518	0.6418	2.837
8	1.26	3.81E+05	8.46	8.11	7.59	6.78	0.6308	0.6505	0.6395	2.738
9	1.25	4.46E+05	8.47	8.10	7.54	6.80	0.6291	0.6490	0.6371	2.604
10	1.26	5.13E+05	8.46	8.10	7.55	6.80	0.6272	0.6472	0.6344	2.417
11	1.21	5.80E+05	8.49	8.10	7.55	6.81	0.6248	0.6448	0.6322	2.143
12	1.28	6.47E+05	8.46	8.14	7.55	7.04	0.6229	0.6427	0.6304	1.685
					M3.z2m2.st					
1	0.00	0.00E+00	8.35	8.19	7.17	6.43	0.5689	0.5928	0.5933	2.975
2	0.00	5.48E+04	8.37	8.18	7.20	6.44	0.5710	0.5951	0.5955	2.973
3	0.00	1.17E+05	8.37	8.18	7.25	6.46	0.5741	0.5988	0.5988	2.968
4	0.20	1.81E+05	8.38	8.17	7.45	6.49	0.5787	0.6029	0.6022	2.960
5	0.37	2.45E+05	8.41	8.16	7.46	6.51	0.5833	0.6071	0.6054	2.948
6	0.56	3.11E+05	8.44	8.14	7.46	6.56	0.5877	0.6111	0.6079	2.930
7	0.71	3.79E+05	8.41	8.13	7.47	6.55	0.5915	0.6144	0.6098	2.903
8	0.81	4.49E+05	8.42	8.12	7.42	6.62	0.5948	0.6172	0.6112	2.866
9	0.88	5.22E+05	8.39	8.11	7.44	6.65	0.5973	0.6195	0.6123	2.815
10	0.91	5.96E+05	8.47	8.11	7.42	6.61	0.5995	0.6214	0.6131	2.746
11	0.95	6.73E+05	8.48	8.10	7.42	6.66	0.6013	0.6229	0.6136	2.652
12	0.97	7.50E+05	8.48	8.09	7.42	6.68	0.6024	0.6239	0.6139	2.527
13	0.92	8.28E+05	8.39	8.10	7.42	6.62	0.6033	0.6247	0.6147	2.348
14	0.94	9.02E+05	8.49	8.10	7.47	6.67	0.6045	0.6253	0.6154	2.094
15	1.05	9.76E+05	8.49	8.11	7.48	6.76	0.6056	0.6261	0.6262	1.668
					M2.z1m2.he07					

1	0.00	0.00E+00	8.30	8.15	7.12	6.25	0.4490	0.4975	0.4993	1.978
2	0.00	5.50E+05	8.34	8.15	7.12	6.29	0.4590	0.5051	0.5061	1.978
3	0.00	9.09E+05	8.37	8.16	7.15	6.29	0.4674	0.5117	0.5124	1.978
4	0.00	1.10E+06	8.35	8.15	7.18	6.31	0.4722	0.5149	0.5159	1.977
5	0.00	1.26E+06	8.37	8.15	7.18	6.33	0.4752	0.5190	0.5198	1.977
6	0.00	1.43E+06	8.37	8.13	7.17	6.34	0.4805	0.5240	0.5247	1.977
7	0.00	1.60E+06	8.39	7.76	7.17	6.34	0.4866	0.5296	0.5301	1.977
8	0.00	1.76E+06	8.41	7.78	7.20	6.36	0.4936	0.5354	0.5359	1.976
9	0.00	1.92E+06	8.40	7.79	7.23	6.37	0.5013	0.5415	0.5419	1.975
10	0.00	2.06E+06	8.42	7.84	7.23	6.38	0.5092	0.5477	0.5480	1.974
11	0.00	2.20E+06	8.42	8.11	7.27	6.40	0.5175	0.5541	0.5543	1.973
12	0.00	2.33E+06	8.41	8.13	7.31	6.40	0.5257	0.5603	0.5604	1.971
13	0.04	2.45E+06	8.43	8.14	7.53	6.41	0.5334	0.5666	0.5665	1.968
14	0.08	2.56E+06	8.41	8.14	7.63	6.42	0.5412	0.5727	0.5724	1.966
15	0.20	2.67E+06	8.42	8.14	7.64	6.44	0.5487	0.5788	0.5777	1.962
16	0.34	2.77E+06	8.43	8.14	7.68	6.45	0.5556	0.5843	0.5822	1.957
17	0.47	2.87E+06	8.45	8.14	7.68	6.47	0.5615	0.5893	0.5860	1.951
18	0.51	2.97E+06	8.42	8.14	7.68	6.48	0.5668	0.5934	0.5897	1.943
19	0.51	3.06E+06	8.42	8.14	7.68	6.49	0.5715	0.5969	0.5932	1.934
20	0.51	3.14E+06	8.45	8.15	7.66	6.50	0.5758	0.6005	0.5969	1.923
21	0.53	3.22E+06	8.44	8.14	7.69	6.51	0.5802	0.6039	0.6002	1.873
22	0.56	3.30E+06	8.45	8.15	7.65	6.51	0.5844	0.6077	0.6036	1.804
23	0.54	3.37E+06	8.44	8.14	7.65	6.49	0.5884	0.6106	0.6069	1.722
24	0.52	3.44E+06	8.46	8.15	7.70	6.47	0.5925	0.6142	0.6104	1.602
25	0.36	3.51E+06	8.46	8.15	7.70	6.50	0.5970	0.6174	0.6222	1.428
					M2.z2m2.he07					
1	0.00	0.00E+00	8.29	8.16	7.13	6.29	0.4686	0.5097	0.5112	1.959
2	0.00	2.72E+05	8.33	8.16	7.18	6.34	0.4722	0.5139	0.5149	1.959
3	0.00	6.42E+05	8.36	8.18	7.19	6.34	0.4836	0.5230	0.5236	1.958
4	0.00	7.79E+05	8.36	8.16	7.19	6.37	0.4884	0.5257	0.5265	1.958
5	0.00	9.04E+05	8.38	8.16	7.20	6.38	0.4906	0.5298	0.5303	1.958
6	0.00	1.04E+06	8.39	8.15	7.21	6.39	0.4954	0.5343	0.5348	1.957
7	0.00	1.17E+06	8.38	8.14	7.24	6.40	0.5008	0.5396	0.5399	1.956
8	0.00	1.29E+06	8.40	8.12	7.25	6.41	0.5076	0.5452	0.5455	1.955
9	0.00	1.41E+06	8.40	8.09	7.30	6.42	0.5146	0.5508	0.5511	1.954
10	0.00	1.53E+06	8.40	8.13	7.29	6.43	0.5217	0.5567	0.5569	1.952
11	0.00	1.64E+06	8.40	8.14	7.35	6.44	0.5292	0.5625	0.5627	1.949
12	0.00	1.74E+06	8.41	8.15	7.41	6.45	0.5366	0.5683	0.5684	1.946
13	0.00	1.84E+06	8.43	8.15	7.53	6.46	0.5437	0.5741	0.5741	1.943
14	0.08	1.93E+06	8.43	8.15	7.71	6.47	0.5509	0.5799	0.5796	1.938
15	0.10	2.01E+06	8.43	8.15	7.70	6.47	0.5580	0.5857	0.5852	1.932
16	0.12	2.10E+06	8.43	8.15	7.71	6.47	0.5646	0.5911	0.5905	1.925
17	0.19	2.17E+06	8.44	8.15	7.73	6.48	0.5711	0.5964	0.5953	1.917
18	0.31	2.25E+06	8.45	8.15	7.74	6.49	0.5771	0.6014	0.5996	1.907
19	0.41	2.32E+06	8.42	8.15	7.74	6.49	0.5824	0.6060	0.6035	1.894
20	0.45	2.39E+06	8.46	8.15	7.74	6.49	0.5873	0.6100	0.6071	1.879
21	0.46	2.46E+06	8.42	8.15	7.74	6.51	0.5918	0.6138	0.6107	1.860
22	0.46	2.52E+06	8.46	8.15	7.75	6.52	0.5960	0.6172	0.6143	1.839
23	0.46	2.59E+06	8.44	8.15	7.74	6.51	0.6002	0.6208	0.6178	1.814
24	0.40	2.64E+06	8.44	8.16	7.75	6.49	0.6044	0.6242	0.6217	1.786
25	0.48	2.70E+06	8.44	8.15	7.76	6.52	0.6088	0.6279	0.6249	1.753
26	0.58	2.76E+06	8.44	8.15	7.77	6.52	0.6127	0.6317	0.6278	1.710
27	0.46	2.81E+06	8.46	8.15	7.76	6.52	0.6164	0.6345	0.6346	1.463
					M3.z1m2.he07					
1	0.00	0.00E+00	8.22	8.23	7.49	6.79	0.6275	0.6467	0.6468	2.971
2	0.20	4.42E+04	8.24	8.20	7.60	6.75	0.6304	0.6494	0.6490	2.970
3	0.40	8.76E+04	8.24	8.19	7.63	6.73	0.6333	0.6526	0.6513	2.968
4	0.50	1.34E+05	8.23	8.18	7.68	6.69	0.6363	0.6557	0.6535	2.965
5	0.69	1.81E+05	8.14	8.18	7.71	6.72	0.6397	0.6586	0.6551	2.961
6	0.78	2.31E+05	8.17	8.17	7.71	6.61	0.6426	0.6610	0.6564	2.956
7	0.90	2.80E+05	8.21	8.15	7.65	6.60	0.6448	0.6626	0.6570	2.949
8	0.57	3.31E+05	8.25	8.16	7.66	6.44	0.6463	0.6638	0.6599	2.885
9	0.85	3.75E+05	8.07	8.14	7.78	6.57	0.6493	0.6655	0.6608	2.821
10	0.95	4.22E+05	8.06	8.13	7.76	6.58	0.6509	0.6674	0.6611	2.728
11	1.04	4.70E+05	8.05	8.13	7.72	6.16	0.6518	0.6682	0.6609	2.605
12	0.99	5.18E+05	8.04	8.13	7.72	6.95	0.6519	0.6682	0.6609	2.440
13	0.68	5.65E+05	8.04	8.13	7.72	6.67	0.6523	0.6683	0.6633	2.208
14	0.78	6.07E+05	7.99	8.13	7.76	7.35	0.6546	0.6694	0.6647	1.911
15	0.97	6.49E+05	7.98	8.13	7.72	7.47	0.6565	0.6712	0.6712	1.441
					M3.z2m2.he07					
1	0.00	0.00E+00	8.36	8.20	7.22	6.41	0.5681	0.5925	0.5930	2.978
2	0.00	5.60E+04	8.35	8.18	7.31	6.45	0.5700	0.5944	0.5949	2.978
3	0.00	1.16E+05	8.38	8.18	7.31	6.46	0.5722	0.5980	0.5982	2.977
4	0.00	1.79E+05	8.42	8.17	7.35	6.48	0.5764	0.6020	0.6020	2.976

TP	DUP_λ	t_{TP}	T_{FBOT}	T_{HES}	T_{CEB}	m_{FBOT}	$m_{D,max}$	M_*		
5	0.09	2.43E+05	8.41	8.17	7.59	6.51	0.5810	0.6064	0.6062	2.975
6	0.15	3.05E+05	8.42	8.16	7.67	6.52	0.5864	0.6111	0.6105	2.973
7	0.25	3.67E+05	8.44	8.16	7.67	6.54	0.5920	0.6158	0.6146	2.971
8	0.40	4.27E+05	8.42	8.15	7.67	6.56	0.5972	0.6201	0.6180	2.969
9	0.52	4.87E+05	8.44	8.15	7.72	6.58	0.6019	0.6239	0.6209	2.965
10	0.54	5.46E+05	8.46	8.15	7.74	6.59	0.6059	0.6271	0.6238	2.961
11	0.63	6.03E+05	8.43	8.15	7.73	6.62	0.6096	0.6300	0.6262	2.956
12	0.68	6.60E+05	8.46	8.15	7.71	6.63	0.6128	0.6327	0.6283	2.951
13	0.66	7.15E+05	8.47	8.15	7.73	6.64	0.6156	0.6350	0.6306	2.945
14	0.75	7.69E+05	8.45	8.14	7.73	6.67	0.6185	0.6373	0.6324	2.938
15	0.81	8.23E+05	8.44	8.14	7.71	6.68	0.6207	0.6393	0.6337	2.930
16	0.85	8.77E+05	8.47	8.14	7.73	6.64	0.6226	0.6409	0.6350	2.827
17	0.89	5.46E+05	8.49	8.14	7.74	6.59	0.6253	0.6429	0.6430	2.718
18	0.90	6.03E+05	8.48	8.12	7.73	6.62	0.6258	0.6439	0.6439	2.585
19	0.92	6.60E+05	8.26	8.14	7.71	6.63	0.6263	0.6444	0.6445	2.436
20	0.94	7.15E+05	8.34	8.15	7.73	6.64	0.6285	0.6455	0.6456	2.247
21	0.95	7.69E+05	8.48	8.14	7.73	6.67	0.6293	0.6465	0.6466	1.993
22	0.94	8.23E+05	8.26	8.16	7.71	6.68	0.6301	0.6480	0.6481	1.767
23	1.00	8.77E+05	8.26	8.04	7.71	6.63	0.6309	0.6500	0.6501	0.735

TP: TP number.

DUP_λ: DUP Lambda parameter.

t_{TP}: Time since first TP.

T_{FBOT}: Largest temperature at the bottom of the flash-convective zone.

T_{HES}: Temperature in the He-burning shell during deepest extend of TDUP.

T_{CEB}: Temperature at the bottom of the convective envelope during deepest extend of TDUP.

m_{FBOT}: Mass coordinate at the bottom of the He-flash convective zone.

$m_{D,max}$: Mass coordinate of the H-free core at the time of the TP.

M_*: Stellar mass at the TP.

Table A.3 Final isotopic ratio values of Zr and Ba isotopes calculated in the He-intershell region (final values on the surface are shown in brackets for comparison).

name	$\delta(^{90}Zr/^{94}Zr)$	$\delta(^{91}Zr/^{94}Zr)$	$\delta(^{92}Zr/^{94}Zr)$	$\delta(^{96}Zr/^{94}Zr)$	$\delta(^{134}Ba/^{136}Ba)$	$\delta(^{135}Ba/^{136}Ba)$	$\delta(^{137}Ba/^{136}Ba)$	$\delta(^{138}Ba/^{136}Ba)$
M3.z2m2	-393.51 (-335.08)	-181.45 (-161.41)	-154.83 (-135.18)	-426.57 (-392.59)	83.87 (46.89)	-878.02 (-789.77)	-387.23 (-349.64)	-52.89 (-72.07)
M3.z1m2	-463.92 (-347.54)	-219.91 (-165.14)	-125.72 (-112.07)	650.29 (122.05)	81.64 (32.13)	-875.29 (-760.49)	-184.04 (-231.80)	597.95 (483.26)
M2.z2m2	-382.17 (-216.94)	-188.69 (-107.80)	-147.67 (-100.41)	-598.55 (-456.40)	87.22 (68.68)	-865.73 (-647.20)	-415.13 (-323.87)	-129.00 (-161.59)
M2.z1m2	-396.44 (-276.76)	-229.26 (-146.97)	-195.42 (-126.68)	-580.93 (-474.66)	21.78 (37.41)	-874.24 (-744.11)	-412.71 (-350.00)	264.87 (146.90)
M3.z1m2.hCBM	-488.00 (-395.95)	-245.69 (-190.77)	-157.98 (-129.68)	631.22 (162.06)	76.56 (48.45)	-875.28 (-805.50)	-187.77 (-239.85)	280.46 (217.94)
M2.z2m2.hCBM	-349.64 (-220.55)	-191.38 (-95.05)	-166.33 (-103.31)	-741.10 (-584.30)	116.10 (111.88)	-859.01 (-680.29)	-448.36 (-359.08)	-342.55 (-332.49)
M3.z1m2.hCBM.ntest	-474.68 (-387.64)	-224.84 (-182.62)	-142.25 (-123.04)	639.19 (159.53)	91.50 (60.64)	-872.71 (-792.65)	-194.13 (-239.59)	102.04 (60.02)
M2.z2m2.hCBM.ntest	-291.93 (-161.23)	-133.05 (-44.19)	-127.27 (-66.49)	-751.27 (-533.73)	172.91 (124.98)	-851.96 (-567.77)	-463.02 (-310.92)	-470.00 (-352.22)
M3.z2m2.zrtest	-410.72 (-337.39)	-182.78 (-161.47)	245.82 (-133.07)	-592.46 (-581.47)	75.29 (46.49)	-872.68 (-789.63)	-357.73 (-344.24)	-75.47 (-57.02)
M3.z1m2.zrtest	-465.18 (-350.91)	-215.45 (-167.77)	-129.23 (-111.21)	6.88 (-230.81)	70.13 (33.72)	-874.00 (-758.98)	-158.26 (-216.71)	585.02 (494.77)
M2.z2m2.zrtest	-379.70 (-210.93)	-187.06 (-105.88)	-159.57 (-100.20)	-802.90 (-526.57)	94.57 (69.21)	-864.86 (-636.15)	-417.91 (-319.34)	-130.13 (-159.15)
M2.z1m2.zrtest	-411.85 (-273.40)	-227.21 (-142.87)	-172.50 (-122.68)	-745.62 (-588.58)	49.90 (40.31)	-871.84 (-738.79)	-397.75 (-347.05)	275.06 (122.01)
M3.z2m2.he07	-400.18 (-343.19)	-219.03 (-166.66)	-193.04 (-135.04)	-357.52 (-235.48)	49.65 (24.19)	-876.58 (-788.31)	-393.20 (-324.14)	-119.29 (-7.66)
M3.z1m2.he07	-446.17 (-349.71)	-208.80 (-161.26)	-134.09 (-110.59)	419.98 (188.82)	58.55 (10.67)	-874.39 (-769.64)	-210.50 (-214.39)	434.86 (464.19)
M2.z2m2.he07	-398.38 (-188.99)	-203.37 (-95.98)	-162.19 (-87.74)	-538.58 (-362.46)	48.18 (38.41)	-872.15 (-582.18)	-407.46 (-285.89)	-43.56 (-91.69)
M2.z1m2.he07	-412.08 (-237.36)	-223.41 (-126.75)	-166.87 (-110.76)	-479.08 (-402.85)	34.92 (22.64)	-873.79 (-684.83)	-395.16 (-321.61)	367.92 (163.60)
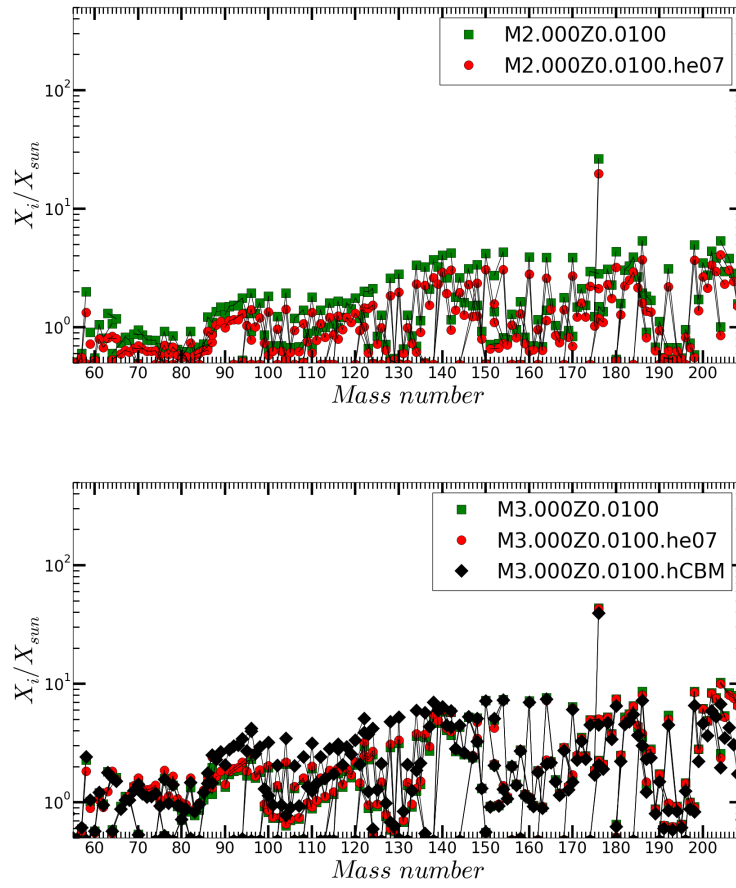
Fig. A.1 Upper panel: Isotopic abundance distribution after the last TDU event in our models with initial M=2 $M_\odot$ and Z=0.01. Lower Panel: same as in the upper panel, but for models with initial M=3 $M_\odot$ and Z=0.01.

Table A.4 Comparison between the present work, [38] (Cr11) and [103] (Ka10) for the $2\,M_\odot$ and Z=0.02 stellar yields. Also the surface mass fraction (X0) of a given isotope in M2.z2m2.he07 is given

Isotopes	X0	Z	A	Yields M2.z2m2.he07	Yields M2.z2m2	Yields M2.z2m2.hCBM	Yields Cr11	Yields Ka10
H-1	7.064E-01	1	1	9.175E-01	9.232E-01	9.257E-01	9.24950E-01	1.2335814E+00
He-4	2.735E-01	2	4	4.004E-01	4.045E-01	4.074E-01	3.95700E-01	5.6186771E-01
C-12	3.425E-03	6	12	1.462E-02	2.289E-02	2.392E-02	9.33420E-03	2.7675023E-03
C-13	4.156E-05	6	13	1.360E-04	1.368E-04	1.376E-04	1.31110E-04	1.2363438E-04
N-14	1.059E-03	7	14	3.549E-03	3.469E-03	3.476E-03	3.26650E-03	3.0212691E-03
N-15	4.171E-06	7	15	2.752E-06	2.755E-06	2.768E-06	2.80090E-06	3.0777028E-06
O-16	9.624E-03	8	16	1.767E-02	2.376E-02	2.445E-02	1.18310E-02	1.3041234E-02
O-17	3.813E-06	8	17	5.434E-05	4.492E-05	3.996E-05	4.03320E-05	2.4374334E-05
O-18	2.171E-05	8	18	2.146E-05	2.152E-05	2.160E-05	1.91220E-05	2.2738323E-05
F-19	5.611E-07	9	19	1.686E-06	2.760E-06	3.332E-06	1.71410E-06	5.5231231E-07
Ne-20	1.818E-03	10	20	2.485E-03	2.547E-03	2.564E-03	2.09900E-03	2.2048058E-03
Ne-21	4.575E-06	10	21	6.631E-06	6.855E-06	6.949E-06	5.34460E-06	5.6205986E-06
Ne-22	1.470E-04	10	22	9.618E-04	1.771E-03	2.096E-03	9.87250E-04	1.6960394E-04
Na-23	4.000E-05	11	23	7.384E-05	8.433E-05	9.051E-05	9.54390E-05	5.3539075E-05
Mg-24	5.862E-04	12	24	8.047E-04	8.229E-04	8.283E-04	1.05810E-03	7.0122938E-04
Mg-25	7.733E-05	12	25	1.338E-04	1.620E-04	1.628E-04	1.38140E-04	9.2150629E-05
Mg-26	8.848E-05	12	26	1.771E-04	2.462E-04	2.523E-04	1.61950E-04	1.0570988E-04
Al-27	6.481E-05	13	27	8.974E-05	9.203E-05	9.244E-05	1.19650E-04	7.9080222E-05
Si-28	7.453E-04	14	28	1.015E-03	1.034E-03	1.039E-03	1.36490E-03	8.8968419E-04
Si-29	3.919E-05	14	29	5.394E-05	5.537E-05	5.570E-05	7.18800E-05	4.6674944E-05
Si-30	2.673E-05	14	30	3.822E-05	4.052E-05	4.106E-05	4.95380E-05	3.2046293E-05
P-31	7.106E-06	15	31	9.934E-06	1.035E-05	1.056E-05	1.30750E-05	1.1111028E-05
S-33	3.265E-06	16	33	4.595E-06	4.785E-06	4.818E-06	5.94620E-06	4.3899581E-06
S-34	1.890E-05	16	34	2.623E-05	2.701E-05	2.721E-05	3.41060E-05	2.5454728E-04
Fe-54	8.118E-05	26	54	1.091E-04	1.098E-04	1.102E-04	1.44260E-04	9.7166812E-05
Fe-56	1.322E-03	26	56	1.790E-03	1.812E-03	1.820E-03	2.35860E-03	1.5932062E-03
Co-59	3.991E-06	27	59	6.846E-06	8.251E-06	8.511E-06	7.55400E-06	4.5764918E-06
Ni-58	5.711E-05	28	58	7.676E-05	7.722E-05	7.751E-05	9.91850E-05	6.7378882E-05
Ni-60	2.276E-05	28	60	3.188E-05	3.336E-05	3.380E-05	4.00250E-05	2.6685300E-05
Ni-61	1.006E-06	28	61	1.873E-06	2.372E-06	2.506E-06	1.94490E-06	4.7256694E-06
Ni-62	3.259E-06	28	62	5.328E-06	6.176E-06	6.498E-06	6.01960E-06	1.7063927E-07
Sr-86	5.845E-09	38	86	1.194E-08	1.496E-08	2.320E-08	6.51720E-08	-
Sr-87	4.443E-09	38	87	8.666E-09	1.057E-08	1.588E-08	4.31680E-08	-
Sr-88	5.011E-08	38	88	1.103E-07	1.368E-07	2.094E-07	7.07640E-07	-
Y-89	1.229E-08	39	89	2.845E-08	3.544E-08	5.359E-08	1.38720E-07	-
Zr-90	1.534E-08	40	90	3.248E-08	3.931E-08	5.588E-08	1.47450E-07	-
Zr-96	8.903E-10	40	96	1.511E-09	1.629E-09	1.821E-09	2.50880E-09	-
Ba-136	1.409E-09	56	136	5.004E-09	6.510E-09	7.325E-09	1.35020E-08	-
Ba-138	1.305E-08	56	138	4.215E-08	5.070E-08	4.608E-08	7.93670E-08	-
La-139	1.790E-09	57	139	5.132E-09	6.008E-09	5.299E-09	9.42830E-09	-
Pb-208	8.850E-09	82	208	1.294E-08	1.303E-08	1.289E-08	2.52760E-08	-

Table A.5 Comparison between the present work, [38] (Cr11) and [103] (Ka10) for the $3\,M_\odot$ stellar yields. Also the surface mass fraction (X0) of a given isotope in M3.z2m2.he07 is given

| Isotopes	X0	Z	A	Yields M3.z2m2.he07	Yields M3.z2m2	Yields Cr11	Yields Ka10
H-1	7.064E-01	1	1	1.540E+00	1.536E+00	1.57880E+00	1.5249571E+00
He-4	2.735E-01	2	4	7.148E-01	7.337E-01	7.04700E-01	7.3096633E-01
C-12	3.425E-03	6	12	3.916E-02	5.150E-02	1.86110E-02	2.0739544E-02
C-13	4.156E-05	6	13	2.300E-04	2.338E-04	2.20200E-04	1.9436399E-04
N-14	1.059E-03	7	14	7.197E-03	7.327E-03	6.64840E-03	5.6565693E-03
N-15	4.171E-06	7	15	4.382E-06	4.289E-06	4.29400E-06	5.0818235E-06
O-16	9.624E-03	8	16	3.600E-02	4.259E-02	1.94360E-02	2.1144016E-02
O-17	3.813E-06	8	17	6.205E-05	6.310E-05	7.91850E-05	5.5763638E-05
O-18	2.171E-05	8	18	3.490E-05	3.457E-05	3.12110E-05	3.6596495E-05
F-19	5.611E-07	9	19	5.937E-06	1.012E-05	3.68770E-06	4.3487280E-06
Ne-20	1.818E-03	10	20	4.327E-03	4.407E-03	3.63520E-03	3.7571993E-03
Ne-21	4.575E-06	10	21	1.355E-05	1.444E-05	9.90460E-06	1.0039988E-05
Ne-22	1.470E-04	10	22	3.360E-03	5.387E-03	2.32210E-03	2.1113991E-03
Na-23	4.000E-05	11	23	1.599E-04	1.929E-04	1.87730E-04	1.2845088E-04
Mg-24	5.862E-04	12	24	1.404E-03	1.442E-03	1.84710E-03	1.1949923E-03
Mg-25	7.733E-05	12	25	3.379E-04	3.680E-04	2.43210E-04	1.6784266E-04
Mg-26	8.848E-05	12	26	5.377E-04	6.289E-04	2.88120E-04	1.9374024E-04
Al-27	6.481E-05	13	27	1.583E-04	1.617E-04	2.08100E-04	1.3861095E-04
Si-28	7.453E-04	14	28	1.754E-03	1.780E-03	2.36270E-03	1.5164100E-03
Si-29	3.919E-05	14	29	9.452E-05	9.652E-05	1.24570E-04	7.9920115E-05
Si-30	2.673E-05	14	30	7.082E-05	7.378E-05	8.60130E-05	5.5390818E-05
P-31	7.106E-06	15	31	1.808E-05	1.857E-05	2.28230E-05	1.9017965E-05
S-33	3.265E-06	16	33	8.144E-06	8.462E-06	1.04160E-05	7.6937777E-06
S-34	1.890E-05	16	34	4.651E-05	4.761E-05	5.91400E-05	4.3391171E-04
Fe-54	8.118E-05	26	54	1.856E-04	1.865E-04	2.49280E-04	1.6390771E-04
Fe-56	1.322E-03	26	56	3.065E-03	3.098E-03	4.08090E-03	2.7071363E-03
Co-59	3.991E-06	27	59	1.519E-05	1.703E-05	1.33220E-05	8.5931824E-06
Ni-58	5.711E-05	28	58	1.306E-04	1.311E-04	1.71330E-04	1.1363259E-04
Ni-61	1.006E-06	28	61	4.501E-06	5.167E-06	3.46150E-06	8.8770785E-06
Ni-62	3.259E-06	28	62	1.214E-05	1.280E-05	1.04870E-05	5.0042019E-08
Sr-86	5.845E-09	38	86	3.391E-08	3.824E-08	1.51990E-07	-
Sr-87	4.443E-09	38	87	2.294E-08	2.592E-08	1.01840E-07	-
Sr-88	5.011E-08	38	88	3.357E-07	3.860E-07	1.63060E-06	-
Y-89	1.229E-08	39	89	9.175E-08	1.055E-07	3.17410E-07	-
Zr-90	1.534E-08	40	90	9.561E-08	1.104E-07	3.24600E-07	-
Zr-96	8.903E-10	40	96	6.089E-09	5.654E-09	5.17810E-09	-
Ba-136	1.409E-09	56	136	2.074E-08	2.437E-08	2.79920E-08	-
Ba-138	1.305E-08	56	138	1.945E-07	2.128E-07	1.68590E-07	-
La-139	1.790E-09	57	139	2.273E-08	2.452E-08	2.00170E-08	-
Pb-208	8.850E-09	82	208	3.234E-08	3.023E-08	4.82470E-08	-
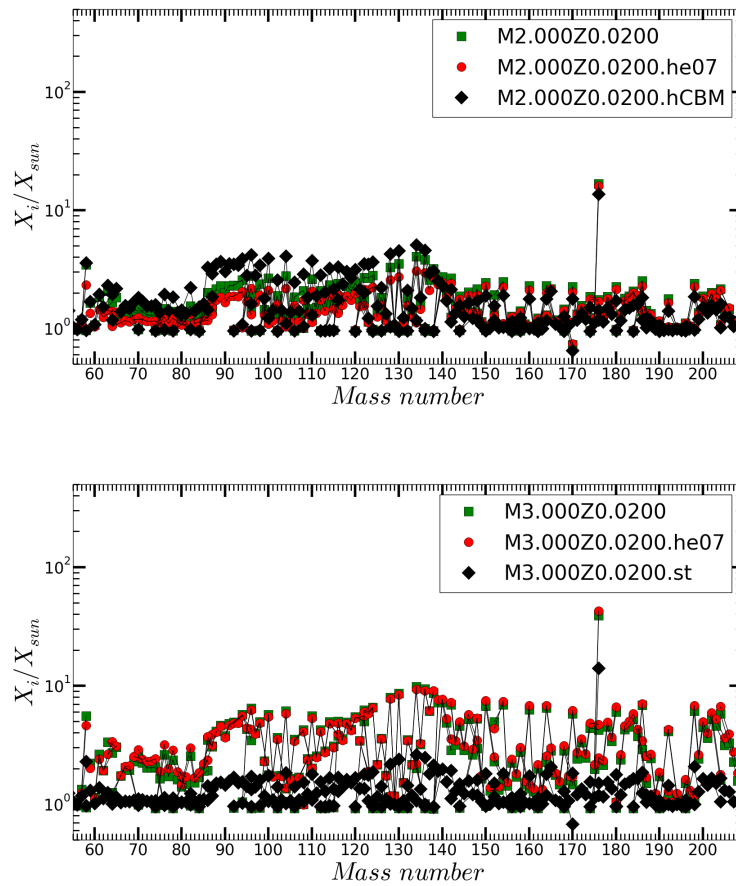
Fig. A.2 Upper panel: Isotopic abundance distribution after the last TDU event in our models with initial M=2 $M_\odot$ and Z=0.02. Lower Panel: same as in the upper panel, but for models with initial M=3 $M_\odot$ and Z=0.02.

Appendix B

Tables of accreting WD models properties

Table B.1 Evolution properties of stellar models presented in this work.

TP	t_{TP}	T_{FBOT}	m_{FBOT}	m_{HTP}	M_*	M_{**}
	[yrs]	[K]	[$M_\odot$]	[$M_\odot$]	[$M_\odot$]	[$M_\odot$]
			M0p639.Z1m2			
1	0.00E+00	8.51	0.6035	0.6500	0.650	0.638
2	1.43E+05	8.51	0.6040	0.6521	0.652	0.640
3	2.86E+05	8.51	0.6068	0.6543	0.654	0.642
4	4.32E+05	8.51	0.6087	0.6568	0.657	0.645
			M0p856.Z1m2			
1	0.00E+00	8.58	0.8380	0.8608	0.861	0.855
2	2.60E+04	8.58	0.8368	0.8606	0.861	0.856
3	5.21E+04	8.59	0.8354	0.8609	0.861	0.855
4	8.02E+04	8.59	0.8351	0.8609	0.861	0.855
			M1p025.Z1m2			
1	0.00E+00	8.65	1.0144	1.0265	1.026	1.024
2	5.53E+03	8.64	1.0149	1.0261	1.026	1.025
3	1.11E+04	8.64	1.0148	1.0262	1.026	1.025
4	1.68E+04	8.64	1.0145	1.0263	1.026	1.025
5	2.24E+04	8.64	1.0145	1.0264	1.026	1.025
6	2.81E+04	8.64	1.0144	1.0264	1.026	1.025
7	3.38E+04	8.64	1.0141	1.0265	1.026	1.025
136	7.88E+05	8.66	1.0155	1.0308	1.031	1.029
137	7.94E+05	8.66	1.0155	1.0309	1.031	1.029
			M1p259.Z1m2			
1	0.00E+00	8.74	1.2591	1.2595	1.2595	1.2592
2	5.90E+02	8.71	1.2587	1.2595	1.2595	1.2592
			M1p376.Z1m2			
1	0.00E+00	8.77	1.37616	1.37619	1.37619	1.37618
2	2.50E+01	8.73	1.37618	1.37620	1.37620	-

TP: TP number.
t_{TP}: Time since first TP.
T_{FBOT}: Largest temperature (in logarithm) at the bottom of the flash-convective zone.
m_{FBOT}: Mass coordinate at the bottom of the He-flash convective zone.
m_{HTP}: Mass coordinate at the top of the He-flash convective zone.
M_*: Stellar mass at the TP.
M_{**}: Stellar mass after the TP.

Table B.2 Isotopic production factors resulting from the listed models.

Specie	M0.856Z0.0100	M1.025Z0.0100	M1.259Z0.0100	M1.376Z0.0100
H 1	3.937E-24	1.123E-26	2.762E-11	3.505E-20
HE 4	2.570E+00	1.612E+00	2.309E+00	6.669E-03
C 12	8.454E+01	1.460E+02	6.898E+01	5.285E+01
C 13	3.014E-09	1.013E-10	3.472E-03	5.501E-09
N 14	1.252E-05	4.970E-14	3.234E-06	7.233E-14
N 15	1.699E-06	9.052E-16	2.505E-04	4.761E-20
O 16	2.544E+00	5.937E+00	1.264E+00	1.446E+00
O 17	4.231E-02	7.832E-04	2.730E-04	2.389E-06
O 18	6.711E-03	3.306E-10	7.771E-03	7.448E-14
F 19	2.302E+00	3.672E-05	6.389E-02	7.184E-11
NE 20	8.191E-01	2.789E+00	5.474E+00	5.008E+00
NE 21	1.724E+01	2.761E+01	1.685E+01	3.187E-02
NE 22	2.908E+01	1.685E+00	1.047E+00	2.713E-08
NA 23	2.004E+00	1.445E+00	4.368E-01	1.943E-03
MG 24	1.807E-01	2.884E+00	1.679E+02	5.649E+02
MG 25	3.439E+01	6.340E+01	2.417E+02	2.365E+02
MG 26	4.187E+01	7.874E+01	9.273E+01	7.327E+01
AL 27	5.947E+00	4.774E+00	8.718E+00	2.184E+01
SI 28	8.315E-01	1.227E+00	1.421E+01	5.637E+02
SI 29	2.183E+01	4.361E+00	1.496E+01	2.887E+02
SI 30	5.753E+00	1.085E+01	5.818E+00	4.520E+01
P 31	4.295E+00	1.007E+01	4.287E+00	1.681E+01
S 32	2.639E-01	2.093E-01	4.188E-01	6.946E+00
S 33	1.131E+00	1.630E+00	1.620E+00	2.405E+01
S 34	1.844E+00	2.109E+00	9.197E-01	4.270E+00
S 36	4.085E+01	5.919E+01	2.347E+01	5.080E+02
CL 35	2.319E-01	2.512E-01	4.515E-01	6.859E-01
CL 37	3.632E+00	3.741E+00	2.187E+00	4.926E+00
AR 36	1.292E-01	7.500E-02	3.435E-01	1.164E-01
AR 38	1.282E+00	1.320E+00	7.559E-01	1.201E+00
AR 40	1.103E+02	1.835E+02	8.611E+01	2.853E+02
K 39	1.184E+00	1.398E+00	7.571E-01	1.476E+00
K 40	2.067E+02	1.211E+02	4.748E+02	1.492E+02
K 41	2.588E+00	2.844E+00	3.343E+00	6.129E+00
CA 40	2.020E-01	1.385E-01	3.676E-01	1.672E-01
CA 42	2.065E+00	2.044E+00	1.580E+00	6.810E+00
CA 43	3.260E+00	3.929E+00	2.673E+00	9.033E+00
CA 44	8.785E-01	1.096E+00	6.825E-01	1.557E+00
CA 46	2.147E+02	3.745E+02	1.119E+02	9.987E+02
CA 48	6.579E-01	1.442E+00	9.258E-01	5.873E+01
SC 45	1.038E+01	1.432E+01	5.187E+00	2.594E+01
TI 46	2.678E-01	3.137E-01	5.616E-01	2.389E-01
TI 47	4.680E-01	1.009E+00	7.648E-01	5.812E+00
TI 48	6.225E-02	8.580E-02	3.036E-01	2.882E-01
TI 49	1.534E+00	1.024E+00	2.353E+00	6.908E+00
TI 50	6.319E+00	6.096E+00	3.649E+00	2.540E+01
V 50	1.500E-03	1.508E-04	1.727E-01	1.183E-02
V 51	3.113E-01	3.436E-01	6.414E-01	1.900E+00
CR 50	1.701E-03	1.858E-04	1.745E-01	8.549E-03
CR 52	1.613E-01	1.017E-01	3.618E-01	2.371E-01
CR 53	2.402E-01	1.631E-01	4.747E-01	4.470E-01
CR 54	8.310E+00	7.501E+00	3.204E+00	1.003E+01
MN 55	1.209E-01	7.577E-02	8.921E-01	2.473E-01
FE 54	1.052E-02	2.187E-03	2.306E-01	2.154E-02
FE 56	1.001E-01	4.599E-02	3.295E-01	9.443E-02
FE 57	1.462E+00	7.410E-01	2.250E+00	1.448E+00
FE 58	4.540E+01	3.254E+01	1.120E+01	2.761E+01
CO 59	2.397E+01	2.300E+01	5.437E+00	1.775E+01
NI 58	6.789E-03	9.958E-04	2.265E-01	2.080E-02
NI 60	7.688E+00	1.118E+01	2.710E+00	8.167E+00
NI 61	1.846E+01	2.003E+01	9.056E+00	1.818E+01
NI 62	1.375E+01	1.747E+01	5.490E+00	1.673E+01
NI 64	6.405E+01	9.247E+01	2.222E+01	6.872E+01
CU 63	2.253E+01	2.890E+01	7.727E+00	2.414E+01
CU 65	3.780E+01	5.815E+01	1.883E+01	4.852E+01
ZN 64	2.002E-02	7.244E-02	5.343E-01	2.019E-02
ZN 66	1.170E+01	2.127E+01	1.034E+01	3.587E+01
ZN 67	1.744E+01	3.350E+01	1.923E+01	6.314E+01
ZN 68	1.975E+01	3.958E+01	1.307E+01	3.408E+01
ZN 70	2.397E+01	7.627E+01	6.375E+01	1.536E+02
GA 69	2.690E+01	5.354E+01	1.698E+01	3.627E+01

GA 71	2.077E+01	4.597E+01	1.761E+01	3.722E+01
GE 70	3.122E+01	6.257E+01	1.341E+01	3.726E+01
GE 72	2.298E+01	4.912E+01	1.558E+01	4.420E+01
GE 73	2.431E+01	5.398E+01	2.404E+01	5.316E+01
GE 74	2.557E+01	6.031E+01	2.189E+01	4.316E+01
GE 76	1.428E+01	5.912E+01	5.569E+01	9.378E+01
AS 75	1.719E+01	4.086E+01	2.307E+01	3.055E+01
SE 74	3.177E-07	1.461E-07	1.240E-02	2.067E-05
SE 76	3.798E+01	9.387E+01	2.628E+01	6.123E+01
SE 77	1.951E+01	5.112E+01	3.199E+01	4.370E+01
SE 78	3.353E+01	9.435E+01	4.170E+01	8.444E+01
SE 80	1.574E+01	4.748E+01	2.530E+01	4.362E+01
SE 82	9.012E+00	6.126E+01	1.068E+02	1.836E+02
BR 79	1.737E+01	4.238E+01	2.373E+01	4.752E+01
BR 81	1.446E+01	4.728E+01	3.213E+01	4.272E+01
KR 78	1.781E-07	7.127E-08	8.860E-03	9.433E-06
KR 80	3.176E+00	7.953E+01	1.567E+01	2.432E+01
KR 82	2.797E+01	9.210E+01	4.443E+01	7.674E+01
KR 83	1.077E+01	3.604E+01	4.119E+01	3.814E+01
KR 84	1.185E+01	4.464E+01	3.198E+01	3.337E+01
KR 86	3.360E+01	2.016E+02	7.178E+02	2.548E+03
RB 85	2.044E+01	8.024E+01	8.767E+01	5.423E+02
RB 87	6.639E+01	3.607E+02	1.086E+03	3.432E+03
SR 84	1.097E-07	3.703E-08	9.325E-03	4.282E-05
SR 86	1.344E+01	6.203E+01	1.359E+02	4.373E+01
SR 87	3.843E+00	1.449E+01	6.969E+01	9.074E+00
SR 88	5.568E+00	3.397E+01	3.233E+02	5.454E+02
Y 89	4.926E+00	3.557E+01	4.651E+02	8.790E+02
ZR 90	2.350E+00	2.059E+01	2.696E+02	6.207E+02
ZR 91	3.087E+00	2.658E+01	6.101E+02	1.019E+03
ZR 92	2.449E+00	2.056E+01	4.721E+02	1.146E+03
ZR 94	2.722E+00	2.566E+01	5.633E+02	1.585E+03
ZR 96	1.912E+01	2.614E+02	4.164E+03	2.614E+04
NB 93	2.727E+00	2.383E+01	6.186E+02	1.876E+03
MO 92	2.795E-04	2.489E-05	2.560E-01	2.262E-02
MO 94	1.170E-03	2.732E-04	1.007E+00	1.011E-01
MO 95	5.843E+00	6.368E+01	1.103E+03	7.787E+03
MO 96	3.535E+00	4.727E+01	9.904E+02	1.067E+03
MO 97	2.336E+00	2.630E+01	1.027E+03	1.817E+03
MO 98	1.903E+00	2.245E+01	7.185E+02	3.116E+03
MO100	1.004E+00	1.191E+01	7.141E+02	1.383E+03
RU 96	7.644E-07	4.278E-07	5.250E-02	5.175E-04
RU 98	1.638E-05	9.022E-06	4.967E-01	1.070E-02
RU 99	7.075E-01	7.639E+00	5.852E+02	1.203E+03
RU100	1.489E+00	2.038E+01	1.625E+02	3.758E+03
RU101	2.936E-01	3.995E+00	1.050E+02	6.869E+02
RU102	7.989E-01	1.121E+01	2.503E+02	2.017E+03
RU104	3.804E-01	4.625E+00	2.422E+02	1.027E+03
RH103	2.538E-01	3.243E+00	1.384E+02	6.154E+02
PD102	1.083E-07	3.709E-08	9.394E-03	4.314E-05
PD104	1.113E+00	1.732E+01	7.072E+01	2.724E+03
PD105	1.961E-01	2.776E+00	9.010E+01	4.475E+02
PD106	7.363E-01	1.066E+01	2.494E+02	2.404E+03
PD108	7.561E-01	1.071E+01	2.427E+02	1.913E+03
PD110	7.606E-01	8.246E+00	5.800E+02	2.110E+03
AG107	2.045E-01	3.076E+00	5.181E+01	5.584E+02
AG109	3.352E-01	4.733E+00	1.290E+02	1.119E+03
CD106	2.124E-07	8.936E-08	1.792E-02	9.050E-05
CD108	3.030E-04	8.025E-02	6.273E+00	3.805E+01
CD110	6.971E-01	1.021E+01	6.926E+01	1.723E+03
CD111	3.238E-01	4.173E+00	1.169E+02	7.735E+02
CD112	6.155E-01	7.374E+00	2.542E+02	1.550E+03
CD113	3.387E-01	3.979E+00	1.167E+02	7.967E+02
CD114	6.797E-01	7.279E+00	2.451E+02	1.746E+03
CD116	2.319E+00	1.926E+01	1.039E+03	6.519E+03
IN113	9.305E-05	2.800E-02	2.480E+00	6.275E+02
IN115	4.175E-01	3.876E+00	2.398E+02	1.028E+03
SN112	7.031E-07	3.411E-07	3.995E-02	3.954E-04
SN114	5.500E-05	4.798E-03	1.555E+00	4.336E+01
SN115	6.401E-05	5.875E-03	1.414E+00	3.678E+01
SN116	4.075E-01	4.166E+00	6.255E+01	8.547E+02
SN117	4.395E-01	3.893E+00	1.334E+02	1.046E+03
SN118	6.571E-01	4.822E+00	1.895E+02	1.338E+03
SN119	5.464E-01	3.779E+00	1.581E+02	1.035E+03
SN120	7.678E-01	4.539E+00	2.219E+02	1.428E+03

SN122	6.003E+00	3.230E+01	1.562E+03	1.533E+04
SN124	2.431E+00	1.663E+01	8.205E+02	1.839E+04
SB121	5.394E-01	2.761E+00	2.686E+02	1.220E+03
SB123	8.262E-01	4.157E+00	2.981E+02	1.857E+03
TE120	3.418E-08	7.564E-09	2.696E-03	1.257E-05
TE122	7.709E-01	5.331E+00	5.143E+01	1.595E+03
TE123	6.143E-01	4.550E+00	4.388E+01	1.103E+03
TE124	1.190E+00	6.611E+00	1.858E+02	2.305E+03
TE125	3.288E-01	1.799E+00	8.527E+01	9.978E+02
TE126	5.859E-01	3.295E+00	1.548E+02	5.174E+03
TE128	1.905E-01	8.984E-01	4.920E+01	9.556E+02
TE130	2.030E-01	5.534E-01	3.626E+01	1.068E+03
I 127	1.707E-01	8.054E-01	7.240E+01	7.911E+02
XE124	1.627E-08	2.556E-09	1.216E-03	6.122E-06
XE126	4.135E-07	1.434E-07	2.353E-02	1.511E-04
XE128	1.118E+00	5.799E+00	5.261E+01	4.277E+03
XE129	5.817E-02	2.713E-01	1.210E+01	2.629E+02
XE130	1.130E+00	5.361E+00	1.280E+02	4.163E+03
XE131	1.087E-01	4.366E-01	2.165E+01	4.640E+02
XE132	3.901E-01	1.375E+00	6.042E+01	2.313E+03
XE134	2.261E+00	4.326E+00	1.892E+02	7.681E+03
XE136	3.185E+00	9.014E+00	1.296E+02	1.270E+05
CS133	2.516E-01	7.340E-01	7.627E+01	1.877E+03
BA130	9.708E-09	1.235E-09	7.751E-04	3.752E-06
BA132	2.930E-07	8.867E-08	1.554E-02	1.017E-04
BA134	9.702E-01	3.943E+00	5.011E+01	6.608E+03
BA135	8.749E-01	1.977E+00	9.504E+01	3.928E+03
BA136	9.003E-01	1.957E+00	1.009E+02	3.268E+03
BA137	3.071E+00	4.294E+00	9.954E+01	2.423E+04
BA138	8.352E-01	7.874E+00	8.228E+01	4.468E+03
LA138	2.618E-08	1.234E-09	8.211E-03	2.218E-05
LA139	7.265E-01	6.774E-01	7.044E+01	6.838E+03
CE136	2.184E-07	8.550E-08	1.612E-02	7.521E-05
CE138	3.209E-06	1.749E-06	1.212E-01	1.769E-03
CE140	3.759E-01	3.138E+00	3.431E+01	7.299E+03
CE142	2.153E+00	2.093E+00	7.568E+01	2.549E+04
PR141	5.360E-01	4.977E-01	5.280E+01	1.256E+04
ND142	1.623E-01	1.416E-01	1.028E+01	8.633E+02
ND143	4.248E-01	3.823E-01	3.477E+01	4.824E+03
ND144	1.010E+00	1.158E+00	4.063E+01	1.669E+04
ND145	4.298E-01	5.126E-01	2.780E+01	6.148E+03
ND146	7.728E-01	7.989E-01	3.635E+01	9.122E+03
ND148	8.569E-01	7.784E-01	4.974E+01	1.205E+04
ND150	1.420E-01	1.444E-01	1.923E+01	2.158E+03
SM144	5.544E-05	7.724E-06	1.980E-01	1.168E-02
SM147	3.581E-01	3.075E-01	2.448E+01	5.359E+03
SM148	3.539E-01	6.312E-01	4.361E+00	3.469E+03
SM149	1.454E-01	1.484E-01	1.142E+01	2.055E+03
SM150	8.918E-01	1.026E+00	1.042E+01	1.051E+04
SM152	2.818E-01	2.494E-01	8.153E+00	3.135E+03
SM154	3.322E-01	2.846E-01	1.771E+01	4.464E+03
EU151	7.701E-02	5.844E-02	1.018E+01	9.026E+02
EU153	8.935E-02	8.726E-02	5.117E+00	1.127E+03
GD152	5.365E-01	4.772E+00	3.637E+00	1.463E+04
GD154	9.492E-01	1.398E+00	2.784E+00	1.321E+04
GD155	1.413E-01	1.164E-01	6.404E+00	1.953E+03
GD156	2.796E-01	3.316E-01	8.561E+00	3.758E+03
GD157	1.693E-01	1.982E-01	7.480E+00	2.730E+03
GD158	3.727E-01	4.255E-01	7.986E+00	5.212E+03
GD160	3.080E-01	2.940E-01	2.065E+01	5.953E+03
TB159	1.253E-01	1.274E-01	8.583E+00	1.916E+03
DY156	5.443E-10	1.372E-11	1.976E-04	9.686E-08
DY158	8.688E-03	2.962E-01	1.431E-01	4.091E+02
DY160	9.322E-01	1.280E+00	3.282E+00	1.613E+04
DY161	9.850E-02	9.959E-02	4.940E+00	1.979E+03
DY162	2.477E-01	2.892E-01	5.284E+00	4.465E+03
DY163	8.529E-02	7.540E-02	2.971E+00	1.736E+03
DY164	3.347E-01	3.151E-01	1.092E+01	6.577E+03
HO165	2.123E-01	3.047E-01	8.455E+00	4.418E+03
ER162	4.570E-10	1.005E-11	1.810E-04	7.203E-08
ER164	1.069E+00	2.525E+00	1.945E+00	2.392E+04
ER166	1.482E-01	2.364E-01	1.283E+01	2.937E+03
ER167	1.228E-01	1.281E-01	6.941E+00	2.238E+03
ER168	4.353E-01	4.716E-01	9.883E+00	7.735E+03
ER170	4.932E-01	4.837E-01	1.670E+01	1.164E+04

TM169	1.933E-01	1.499E-01	1.025E+01	3.673E+03
YB168	1.239E-09	5.178E-11	2.509E-04	3.481E-07
YB170	9.695E-01	1.629E+00	2.403E+00	2.338E+04
YB171	4.945E-01	4.555E-01	1.734E+01	1.110E+04
YB172	5.535E-01	7.894E-01	1.880E+01	8.883E+03
YB173	4.305E-01	5.131E-01	8.717E+00	8.096E+03
YB174	9.310E-01	1.129E+00	1.355E+01	1.591E+04
YB176	1.480E+00	1.489E+00	3.515E+01	1.995E+04
LU175	3.269E-01	3.531E-01	9.848E+00	5.914E+03
LU176	7.663E+00	1.127E+01	2.008E+01	2.204E+05
HF174	2.749E-09	1.745E-10	3.189E-04	8.401E-07
HF176	2.023E-01	5.476E-01	1.177E+00	2.663E+04
HF177	4.456E-01	4.727E-01	2.099E+01	6.501E+03
HF178	1.100E+00	1.348E+00	1.210E+01	1.446E+04
HF179	7.671E-01	9.214E-01	1.413E+01	1.080E+04
HF180	1.482E+00	1.614E+00	1.305E+01	1.492E+04
TA180	7.131E-09	4.466E-10	6.649E-01	8.576E-01
TA181	5.379E-01	4.941E-01	1.218E+01	5.586E+03
W 180	6.463E-02	2.497E+00	2.598E+00	5.973E+04
W 182	1.354E+00	1.440E+00	1.278E+01	1.052E+04
W 183	1.364E+00	1.269E+00	1.173E+01	1.358E+04
W 184	1.275E+00	1.305E+00	6.472E+00	1.055E+04
W 186	1.057E+00	8.393E-01	8.132E+00	9.391E+03
RE185	1.015E+00	6.754E-01	1.395E+01	1.061E+04
RE187	2.403E-01	1.931E-01	6.688E+00	2.801E+03
OS184	1.952E-08	3.226E-09	1.310E-03	6.412E-06
OS186	1.183E+00	1.956E+00	9.392E-01	8.665E+03
OS187	6.221E-01	6.355E-01	4.070E-01	2.655E+03
OS188	9.317E-01	9.767E-01	5.575E+00	9.798E+03
OS189	1.713E-01	1.834E-01	7.940E-01	1.749E+03
OS190	4.041E-01	4.591E-01	1.409E+00	3.030E+03
OS192	2.251E-01	1.914E-01	2.066E+00	1.591E+03
IR191	5.234E-02	5.640E-02	3.101E-01	4.246E+02
IR193	5.198E-02	4.422E-02	8.091E-01	3.943E+02
PT190	3.725E-08	8.188E-09	2.682E-03	1.213E-05
PT192	9.917E-01	1.940E+00	4.886E-01	7.733E+03
PT194	2.426E-01	2.453E-01	1.105E+00	1.962E+03
PT195	6.432E-02	8.889E-02	2.352E-01	4.525E+02
PT196	2.740E-01	3.226E-01	1.475E+00	1.555E+03
PT198	4.243E-01	4.623E-01	7.737E+00	2.597E+03
AU197	1.563E-01	1.654E-01	2.472E+00	9.575E+02
HG196	3.634E-05	1.921E-03	5.216E-02	3.973E+01
HG198	1.473E+00	1.750E+00	2.671E+00	7.754E+03
HG199	6.518E-01	6.861E-01	7.212E+00	3.769E+03
HG200	1.238E+00	1.384E+00	6.868E+00	7.551E+03
HG201	9.629E-01	1.081E+00	7.039E+00	7.864E+03
HG202	1.609E+00	1.714E+00	7.100E+00	1.449E+04
HG204	3.557E+00	3.687E+00	1.083E+01	1.967E+04
TL203	1.658E+00	1.755E+00	7.218E+00	1.696E+04
TL205	1.770E+00	1.499E+00	3.357E+00	7.514E+03
PB204	1.511E+00	1.634E+00	2.709E+00	1.123E+04
PB206	1.678E+00	1.561E+00	1.262E+00	7.277E+02
PB207	1.295E+00	1.466E+00	1.176E+00	2.494E+03
PB208	1.041E+00	1.348E+00	2.247E+00	7.750E+04
BI209	7.343E-01	9.990E-01	1.613E+00	8.102E+04

Table B.3 Linear fitting parameters A and B, where LOG(PF) = A × WDmass + B, to interpolate production factors of each single tabulated isotope as a function of the WD mass. This fitting is valid in the mass range between 0.86 $M_\odot$ and 1.38 $M_\odot$.

Specie	A	B
H 1	2.19939481635e-11	-1.79261674585e-11
H 2	1.70768899512e-06	-1.64435172548e-06
HE 3	2.4949511687e-16	-2.0335288703e-16
HE 4	-3.47581520576	5.54861260157
LI 7	987.936713827	-945.693868781
B 11	-0.00135372979452	0.501103357469
C 12	-99.4895672605	200.416222505

C 13	0.00276477459491	-0.00225342838987
N 14	-1.83612046502e-05	2.46683001525e-05
N 15	0.000196633290801	-0.000158949238671
O 16	-4.84201273437	8.2643823187
O 17	-0.0710304346132	0.0910355078045
O 18	-0.00503432130668	0.00930424881575
F 19	-3.79864585868	4.88015286658
NE 20	8.78952850994	-6.40085267928
NE 21	-32.95225882	52.6360678985
NE 22	-48.8684501449	63.1254801996
NA 23	-3.92093345339	5.39866961988
MG 24	986.242493898	-929.50160212
MG 25	452.389709356	-366.750482397
MG 26	64.5198338183	-1.19039234266
AL 27	26.9996020239	-20.1628005334
SI 28	862.010073302	-828.21724775
SI 29	442.281334452	-421.78462655
SI 30	56.4872591107	-46.868865535
P 31	15.2496418723	-8.35134568621
S 32	10.268012402	-9.63308600071
S 33	34.7474915755	-32.1221679782
S 34	2.76564746815	-0.83674099755
S 36	681.265331754	-611.271060446
CL 35	0.849466469535	-0.553922645202
CL 37	0.737697205511	2.78863984067
AR 36	0.185809836832	-0.0437543088107
AR 38	-0.565695096703	1.77839477004
AR 40	198.87720513	-58.2298636757
K 39	-0.0344800505598	1.24270297789
K 40	181.02404477	33.5738492583
K 41	5.79558825459	-2.81721911559
CA 40	0.119668717287	0.0837190196793
CA 42	6.80625895403	-4.55951635648
CA 43	7.84081875828	-4.12853438096
CA 44	0.731923930488	0.227157868889
CA 46	1002.51633057	-706.890937599
CA 48	87.575736623	-83.4340816392
SC 45	16.8967986954	-5.11973582529
TI 46	0.160989034998	0.163743385305
TI 47	7.97706646611	-6.99265805259
TI 48	0.519043649221	-0.4010377769
TI 49	9.10781956091	-7.32797828093
TI 50	26.8850933767	-19.9872704495
V 50	0.15281602386	-0.125984090237
V 51	2.64595473462	-2.18820789689
CR 50	0.148926870036	-0.121904485398
CR 52	0.312310859523	-0.13712396311
CR 53	0.548733878532	-0.288270547343
CR 54	-0.948240824197	8.33181397635
MN 55	0.834100957927	-0.607682488419
FE 54	0.197232361438	-0.156463586232
FE 56	0.20856424744	-0.092964036775
FE 57	1.06561552527	0.272170074234
FE 58	-45.95716207	81.0731365397
CO 59	-23.5507236504	44.1280167791
NI 58	0.199845887078	-0.161854805432
NI 60	-5.46384824858	13.604934809
NI 61	-8.91224627397	26.4934259251
NI 62	-4.43860461822	18.3711843851
NI 64	-44.3486288198	111.934602834
CU 63	-13.4097793441	35.9638910149
CU 65	-11.8506129119	54.2043421493
ZN 64	0.376387186837	-0.263203626864
ZN 66	29.3892341033	-13.3854451977
ZN 67	60.3376321235	-34.7936866484
ZN 68	3.72909558049	22.4098514711
ZN 70	194.487182774	-140.178530363
GA 69	-10.6935820904	45.4955541991
GA 71	6.31868026157	23.2587105569
GE 70	-25.0151285766	64.3570798769
GE 72	9.56044094561	22.1762617719
GE 73	24.5333670993	11.1743285259
GE 74	1.55199787537	35.9802945132
GE 76	124.691829943	-85.0595766823
AS 75	9.81684829194	16.8342784882

SE 74	0.0099048330197	-0.0080772729402
SE 76	-9.74438648616	65.8414130867
SE 77	26.3999045588	6.77450748607
SE 78	44.7865938423	12.9409350562
SE 80	29.5747731199	-0.354919214721
SE 82	308.732922614	-258.391469267
BR 79	34.7483651261	-6.48090386497
BR 81	35.9197340059	-6.40587972124
KR 78	0.00706919261283	-0.00576369776509
KR 80	-6.70138493031	38.2398633298
KR 82	46.0415694918	8.32906756689
KR 83	49.5357516587	-24.3908636227
KR 84	27.7002701301	-0.813605148591
KR 86	4242.04490055	-3914.01869463
RB 85	805.003980535	-726.186994883
RB 87	5716.53208434	-5217.69222032
SR 84	0.00749012459267	-0.00611435886826
SR 86	112.389708357	-63.1129826706
SR 87	53.5660955253	-36.2018713112
SR 88	1051.67318614	-960.279529937
Y 89	1669.37363123	-1538.57382818
ZR 90	1136.74391319	-1055.07387645
ZR 91	2005.45729883	-1849.46954653
ZR 92	2092.61754004	-1952.28795134
ZR 94	2825.73322835	-2646.08231792
ZR 96	42666.6093352	-40524.4719407
NB 93	3311.20343658	-3108.05943602
MO 92	0.237594481726	-0.198513069328
MO 94	0.952710948867	-0.79822486891
MO 95	12609.5602006	-11996.3127164
MO 96	2366.98560588	-2145.2754928
MO 97	3546.2290179	-3285.53356141
MO 98	5269.10630626	-4984.10776957
MO100	2651.82638622	-2466.4084962
RU 96	0.0425874350063	-0.0348265414819
RU 98	0.411680501069	-0.337930937997
RU 99	2280.06295771	-2125.05445123
RU100	5799.70465102	-5562.27430122
RU101	1119.84188574	-1065.25433903
RU102	3242.51816611	-3090.97578377
RU104	1743.11288178	-1649.4230943
RH103	1038.80603111	-983.487810635
PD102	0.00754555596622	-0.00615961126726
PD104	4164.77679678	-3998.74475332
PD105	746.709180174	-707.891639794
PD106	3827.77971336	-3655.36422295
PD108	3079.50643966	-2934.97124613
PD110	3647.71933415	-3443.52347819
AG107	883.802955394	-844.440911301
AG109	1792.17206572	-1710.09521225
CD106	0.0144063011233	-0.0117620134085
CD108	62.512472895	-59.4756937069
CD110	2654.34630685	-2545.96520489
CD111	1260.17807107	-1199.01684189
CD112	2541.81258715	-2416.65903665
CD113	1295.21860717	-1232.87238323
CD114	2831.06341473	-2696.50591875
CD116	10674.3287942	-10156.4224586
IN113	951.351652025	-916.573991869
IN115	1743.12984005	-1649.97021367
SN112	0.0324092282764	-0.0265034081092
SN114	66.8379089404	-64.2300359568
SN115	56.7695219091	-54.5428054744
SN116	1339.61733503	-1281.97209647
SN117	1685.5889823	-1607.09683757
SN118	2171.09610601	-2067.92272868
SN119	1688.50881195	-1606.97009715
SN120	2333.05973397	-2220.22274118
SN122	24407.1935826	-23323.145805
SN124	28462.4071514	-27326.6674241
SB121	2057.06200526	-1949.44790244
SB123	3042.95221057	-2895.47224419
TE120	0.00216579488006	-0.00176802947369
TE122	2449.47150056	-2352.32034909
TE123	1699.83275274	-1631.10010252

TE124	3629.1704116	-3472.6831439
TE125	1575.85628017	-1507.84229115
TE126	7948.34656233	-7640.51304309
TE128	1484.09080327	-1424.06629169
TE130	1644.04441659	-1579.87204675
I 127	1253.7722659	-1199.38986282
XE124	0.000977540638794	-0.000798108188198
XE126	0.0189648891151	-0.0154909453808
XE128	6507.34432292	-6262.65999046
XE129	407.127570787	-390.814659827
XE130	6395.15703134	-6145.75953837
XE131	718.802715097	-689.97944044
XE132	3546.10669546	-3409.75818464
XE134	11765.3217845	-11313.8515454
XE136	192240.564028	-185254.147036
CS133	2899.70890001	-2785.20744894
BA130	0.000622875814796	-0.0005085110534
BA132	0.0125279055704	-0.0102334849586
BA134	10033.5389238	-9662.10964483
BA135	6015.94291364	-5785.52657428
BA136	5022.01287741	-4826.91321321
BA137	36730.8932159	-35384.9521905
BA138	6823.61535177	-6565.88608245
LA138	0.0065719747778	-0.00536145769785
LA139	10400.2010133	-10014.3659684
CE136	0.0129498102971	-0.0105714573976
CE138	0.0991821664517	-0.0812331757414
CE140	11069.7321001	-10664.2276157
CE142	38621.185141	-37210.8365241
PR141	19043.8574926	-18347.0566843
ND142	1313.9798453	-1265.01227041
ND143	7325.34804941	-7055.42367267
ND144	25281.5596441	-24359.681338
ND145	9322.89165411	-8981.35907767
ND146	7.48346923493	-7.12104825385
ND148	7.70701201082	-7.30076010667
ND150	8.01976252325	-8.32184031584
SM150	6.97120025578	-6.62026378076
SM152	7.31945811577	-7.45007010914
SM154	7.66393324977	-7.68418632959
EU151	7.92170081141	-8.53947512875
EU153	7.61086178856	-8.17945069339
GD152	6.76831566879	-6.35786393795
GD154	6.53410385	-6.20489401206
GD155	7.63714340665	-8.04402272775
GD156	7.3823242432	-7.4659858406
GD157	7.63238424133	-7.90800559754
GD158	7.29547962101	-7.28169831638
GD160	7.95212922309	-7.96631539688
TB159	7.78814924444	-8.18803172599
DY156	8.85038904	-17.7033084372
DY158	7.06252271706	-8.17909467598
DY160	6.75976016868	-6.43164621783
DY161	7.86127191737	-8.37991980399
DY162	7.45454711065	-7.60920653436
DY163	7.78090789022	-8.40446456857
DY164	7.71774156351	-7.7434915643
HO165	7.70771578675	-7.85622069038
ER162	8.83850766108	-17.7843567389
ER164	6.55032930972	-6.12059181116
ER166	7.91491080868	-8.15577774159
ER167	7.82990957414	-8.24296051285
ER168	7.48737708676	-7.40432084025
ER170	7.83963828493	-7.684384471
TM169	7.91729204245	-8.17917814897
YB168	8.80869540391	-17.2579077389
YB170	6.80066178751	-6.44093036114
YB171	7.83613854661	-7.68774373129
YB172	7.48370488372	-7.23331975091
YB173	7.45865246635	-7.37261545889
YB174	7.27676634023	-6.87665592941
YB176	7.34189482046	-6.74174307953
LU175	7.59781258954	-7.62104493219
LU176	6.97251872256	-5.72639911304
HF174	8.55564592263	-16.6320853325

|		
HF176	8.07900908154	-8.23604951193
HF177	7.616038675	-7.48387681815
HF178	7.00464129885	-6.55473096187
HF179	7.23355600933	-6.90846820347
HF180	6.78505114525	-6.24328998961
TA180	19.3378298976	-26.2676324465
TA181	7.17917986636	-7.04097791263
W 180	9.29252945513	-9.39159466702
W 182	6.64538271258	-6.14800512849
W 183	6.81312958802	-6.33190485581
W 184	6.482846308	-6.05528057568
W 186	6.74363640233	-6.40584013959
RE185	7.10002060438	-6.76434410231
RE187	7.36341971713	-7.57851450445
OS184	8.14908446402	-15.2694642374
OS186	5.62840845698	-5.28575309366
OS187	5.33979784987	-5.37097310031
OS188	6.69064916939	-6.37963802066
OS189	6.57709123345	-7.01559423689
OS190	6.25935622591	-6.34212572986
OS192	6.63542087816	-6.95361068132
IR191	6.5090696754	-7.45134102877
IR193	6.86440668564	-7.78359416719
PT190	8.08877739444	-14.8830738176
PT192	5.45801451902	-5.19672751141
PT194	6.43371689868	-6.73600396974
PT195	6.17972896404	-7.03085029428
PT196	6.21665238281	-6.44186619891
PT198	6.7096805145	-6.67631893599
AU197	6.66911122053	-7.08275613585
HG196	10.5526620535	-13.6238633839
HG198	5.78843496852	-5.35328295024
HG199	6.50910601513	-6.32758478956
HG200	6.28875343727	-5.86282974922
HG201	6.57481496385	-6.23282575406
HG202	6.47898705172	-5.95155298748
HG204	6.03777833699	-5.20510429907
TL203	6.55978403274	-6.01807008609
TL205	5.75626811524	-5.29242733726
PB204	6.03716635847	-5.59703450366
PB206	3.9114376941	-3.57071151473
PB207	4.90192461712	-4.59784602285
PB208	7.5655978934	-7.19454867199
BI209	7.81650966244	-7.57942299576
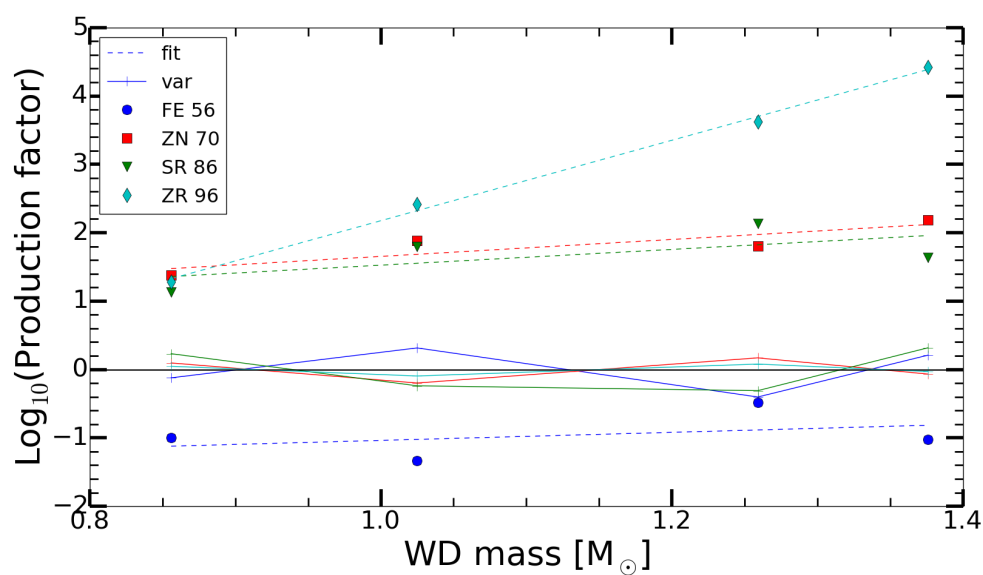
Fig. B.1 Logarithmic production factors relative as a function of WD mass. I show Fe^{56}, Zn^{70}, Zr^{96} and Sr^{86}, i.e. one Fe-seed, one r-only, one major product and one s-only respectively. Also the difference between the fit and each data-point is plotted. A linear fit is shown for each one of the isotopes considered, whose fitting parameters are taken from Tab. B.3.

Curriculum Vitae

Umberto Battino

16 Dimsdale-Parade East

ST58BS Newcastle-Under-Lyme

07809905409

<u>ubattino@gmail.com</u>

SHORT PROFILE

Computational physicist with deep experience in scientific data analysis and programming skills.

More than 7 years experience in research and development.

PERSONAL INFORMATIONS

Date of birth: 08/04/1986

Place of birth: Torino (Italy)

Nationality: Italian

LinkedIn: <u>https://ch.linkedin.com/in/ubattino</u>

WORK EXPERIENCE

1/10/2016 – Present	Postdoc position in Keele University, Dr Raphael Hirschi's Astrophysics Group
1/7/2011 – 30/4/2016	PhD position in University of Basel, Department of Physics

Supervisor: Prof. Friedrich-Karl Thielemann

Main activities:
1) Calculations of stellar models of low, intermediate and massive stars and related Nucleosynthesis.

2) Numerical simulations.

3) Statistical data analysis and comparison with scientific observations

1/9/2008 – 30/6/2011	Scientific guide in Turin Planetarium and Astronomical Museum INFINI-TO (http://www.planetarioditorino.it/infinito/)
2005 – 2010	Scientific guide in different public science and astronomy communication events like "ESOF" (http://www.esof2010.org/index.php?section=24-esof2010) and "La Notte Dei Ricercatori" (http://piemonte.nottedeiricercatori.it/)

EDUCATION AND TRAINING

24/9/2015	**PhD Degree in Theoretical Physics**
	University of Basel
	<u>Final mark:</u> Magna Cum Laude
	<u>Project title:</u> "Evolution and nucleosynthesis of Asymptotic Giant Branch stars and accreting White Dwarfs" (Supervisor: Prof. Friedrich-Karl Thielemann)

6/4/2011	**Master Degree in Astrophysics**
	University of Turin
	<u>Master Thesis title:</u> "The p-process in Type-Ia supernovae" (Supervisor: Dott. Claudia Travaglio)

1/7/2008	**Bachelor Degree in Physics**
	University of Turin
	<u>Thesis title:</u> "Light curve and spectra reproduction of blazars 3C279 and PKS1510" (Supervisor: Dott. Claudia M. Raiteri)

PERSONAL SKILLS

Communication skills	Very good communication and presentation skills gained also through my experience as scientific guide in Turin Planetarium and Astronomical Museum INFINI-TO and during my volunteering activity as educator in the Scout Movement.

Mother tongue	Italian
Other languages	English: Fluent
	German: Good knowledge
	French: Good knowledge

Computer skills	Deep experience in data-related sciences such as Statistics, Applied Mathematics, Computer Science, and Physics.
	UNIX/Linux (system administration), **Fortran,Python** (advanced user), **Java,C++** (5 years of practice during Bachelor and Master courses).
	Very good knowledge of **LaTeX** and **Pandas** data analysis library.
	Experienced in Microsoft products: Word, Excel, Power Point

ADDITIONAL INFORMATION

Publications list

- **U. Battino, M. Pignatari, C. Ritter, F. Herwig, P. Denissenkov, J.W. den Hartogh, R. Trappitsch, R. Hirschi, B. Freytag, F. Thielemann, B. Paxton,** *"Application of a theory and simulation based convective boundary mixing model for AGB star evolution and nucleosynthesis".* **The Astrophysical Journal, Volume 827, Issue 1, article id. 30, pp. (2016).**

- **Pavel A. Denissenkov, Falk Herwig, Umberto Battino, Christian Ritter, Marco Pignatari, Sam Jones and Bill Paxton,** *"i-process Nucleosynthesis and Mass Retention Efficiency in He-shell Flash Evolution of Rapidly Accreting White Dwarfs".* **The Astrophysical Journal Letters, Volume 834, Issue 2, article id. L10, pp. (2017).**

- **Pignatari, M.; Herwig, F.; Hirschi, R.; Bennett, M.; Rockefeller, G.; Fryer, C.; Timmes, F. X.; Heger, A.; Jones, S.; Battino, U.; C. Ritter, A. Dotter, R. Trappitsch, S. Diehl, U. Frischknecht, A. Hungerford, G. Magkotsios, C. Travaglio, P. Young,** *"NuGrid stellar data set. I. Stellar yields from H to Bi for stars with metallicities Z = 0.02 and Z = 0.01".* **The Astrophysical Journal Supplement Series, Volume 225, Issue 2, article id. 24, pp. (2016).**

- Denissenkov, P. A.; Truran, J. W.; Pignatari, M.; Trappitsch, R.; Ritter, C.; Herwig, F.; Battino, U.; Setoodehnia, K.; Paxton, B. 2014, *"MESA and NuGrid simulations of classical novae: CO and ONe nova nucleosynthesis",* Monthly Notices of the Royal Astronomical Society, Volume 442, Issue 3, p.2058-2074

- U. Battino, M. Pignatari, P. Denissenkov, F. Herwig, F. Thielemann, B. Paxton 2016, *"Production of the p-process seeds for thermonuclear supernovae in the single-degenerate scenario: neutron capture nucleosynthesis during the late accretion phase before reaching Chandrasekhar mass",* in preparation.

Invited seminars

Hungarian Academy of Sciences, Konkoly Observatory, Budapest H-1121 Hungary. "Introduction to the MESA stellar evolution code". 14th April 2015

Astronimical observatory of Teramo, Collurania. "Evolution and nucleosynthesis of AGB stars and accreting white dwarfs". 27Th April 2016.

Memberships

Member of the NuGrid Collaboration (http://www.nugridstars.org/)
Member of the Swiss Society of Astronomy and Astrophysics (SSAA)